UNIVERSITY OF BIRMINGHAM

The Behaviour of Double Oxide Film Defects in the Processing of Liquid Mg Alloys

By

Tian Li

A thesis submitted to the College of Engineering
and Physical Sciences of
The University of Birmingham
For the degree of
Doctor of Philosophy

School of Metallurgy and Materials
College of Engineering and Physical Sciences
University of Birmingham
Birmingham B15 2TT
United Kingdom

SYNOPSIS

The global demand for Mg alloys continually grew in the last 20 years, motivating a wide interest in the improvement of the mechanical properties of Mg-alloy castings. In addition, the existence of double oxide film defects, which were widely recognised as a major factor in the quality and reproducibility of the properties of light-alloy castings, has been demonstrated in Mg-alloy castings. Thus it became important to understand the behaviour of double oxide film defects formed in Mg-alloys.

In the work reported here, three different Mg alloys (commercial pure Mg, AZ91 alloy, and Mg-Y alloys) and two cover gases (SF_6/air and SF_6/CO_2), were used, in order to involve different doubled oxide films which may have different behaviours. Direct and cross-sectional observations of the double oxide film defects formed the Mg-alloy castings protected by different cover gases were obtained via a Scanning Electron Microscope (SEM), and the focus ion beam milling (FIB) technique. In addition, the oxide films growing on the corresponding Mg-alloy melt surfaces was also investigated. Based on the observed film structures in conjunction with a thermochemical calculation, evolution processes of the different double oxide film defects were suggested.

The quality of Mg-alloy castings was evaluated by the Weibull modulus, which is popularly used to discriminate “good” and “bad” castings. A shortcoming of the traditional Weibull estimation method (i.e. linear least square method) was demonstrated, and a new estimation method was therefore proposed. The Weibull modulus result revealed that air can confer an improvement in the quality of AZ91 castings, compared with CO_2. Thus the European Mg-alloy foundries, which did not use air as a carrier gas according to an EU commission survey, were recommended to consider the use of air in Mg-alloy casting process.

ACKNOWLEDGEMENTS

I would like to deeply and sincerely acknowledge my supervisor, Dr Bill Griffiths, for his exceptional supervision, help and guidance. I can hardly make this work without his patience and motivation. I feel deeply honoured to be able to work under his supervision.

I also would like to appreciate Dr KeeHyun Kim's help of focused ion beam milling process, Dr Yang Yue's and Dr Dmytro Shevchenko's simulation support during the mould design.

Thank you to Mr. Adrian Caden and Mr. Peter Cranmer for their technical support. The experimental work could not be carried out without their help.

I particularly acknowledge my wife, Dr Jing Chen, for her love, encouragement, and support during my PhD period.

Contents

List of Figures

List of Tables

List of Equations

1. Introduction

As the lightest structural metal available on Earth, magnesium became one of the most attractive light metals over the last few decades. The magnesium industry has consequently experienced a rapid development in the last 20 years. As shown in Fig 1-1, the primary annual production of Mg metal in the word grew continually between 1994 ~ 2013, increasing from 267,000 tons/year to 878,000 tons/year [1-20], indicating a large growth in demand for Mg alloys all over the world. Nowadays, the use of Mg alloys can be found in the fields of automobiles, aerospace, electronics and etc., due to their low density and relatively good mechanical properties [21]. In the future, it has been predicted that the global consumption of Mg metals will further increase, especially in the automotive industry, as the fuel efficiency standard makes the manufactures seek to reduce the vehicle weight [1].

Due to the sustained growth in demand for Mg alloys, improvement in quality of Mg-alloy castings has become a significant issue to be addressed, motivating the investigation of double oxide film defects formed in Mg alloys, which have been widely accepted to be a major factor in the quality and reproducibility of the properties of light alloy castings [22]. Entrainment of the oxidised surface of the liquid metal can result in the entrapment of a doubled-over surface film containing a small quantity of the local atmosphere, forming a double oxide film defect in the final castings. The random nature of fluid flow, involved in their formation, their subsequent random size and orientation, contributes greatly to the variable nature of

casting properties.

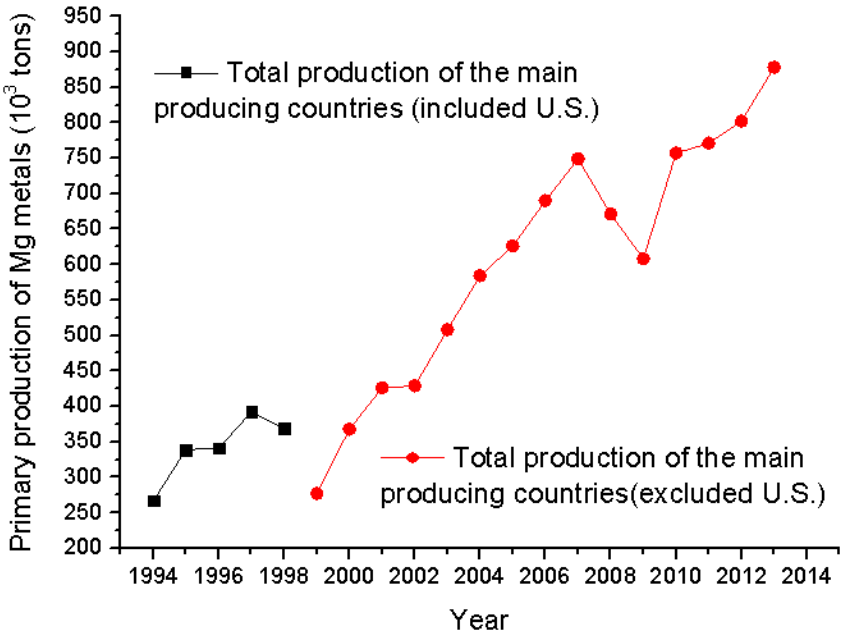

Fig 1-1, primary annual production of magnesium metals of the main producing countries in the world, according to [1-20]. The data of the U.S. has been withheld since 1998, due to the proprietary of some companies. The total value of the global production consequently excludes the production of the U.S. from 1998

Most of the previous investigations into double oxide film defects were carried out on aluminium alloys, and research into the defects in Mg alloys has been relatively small. Compared with aluminium castings, the behaviour of double oxide film defects formed in Mg-alloy castings is more complicated, since during the casting of Mg alloys, they should be protected by a cover gas, to avoid their well-known rapid oxidation and burning of molten magnesium in air. This cover gas causes the surface film formed on a Mg-alloy melt to have a more complicated structure, in contrast to the film formed on an Al melt. In addition, many of the protective gases (e.g. SF_6,

SO_2, HFC-134a etc.) and carrier gases (such as CO_2, air, N_2 etic.) have been developed for the protection of the Mg-alloy melt in industry, further complicating the issue of the surface film structure, as well as the behaviour of double oxide film defects.

The alloying elements contained in Mg alloys could also make the structure of double oxide film defects different. For example, in the oxidation of Mg-Y alloys, yttrium could react with magnesium oxide to produce yttrium oxide, thus forming a compact doubled oxide film composed of Y_2O_3, rather than MgO.

Therefore, more investigation is required to understand the behaviour of double oxide film defects formed in magnesium alloys, in order to improve the quality of Mg-alloy castings. The work reported here is aimed characterising the behaviour of double oxide film defects formed in different Mg alloys (i.e. pure Mg, Mg-Al alloy, and Mg-Y alloy), and varied atmospheres (i.e. SF_6/Air, SF_6/CO_2). In addition, the classical statistical methods used to determine the quality of castings (i.e. the Weibull modulus) have been improved by a new estimation approach.

2. Literature Review

2.1 The formation of double oxide film defects.

A solid oxide film can easily form on the surface of a light alloy melt due to a reaction with the surrounding atmosphere. If the film is skimmed off, a new oxide film will almost immediately reform. As a result, the melt is always covered by a solid oxide layer.

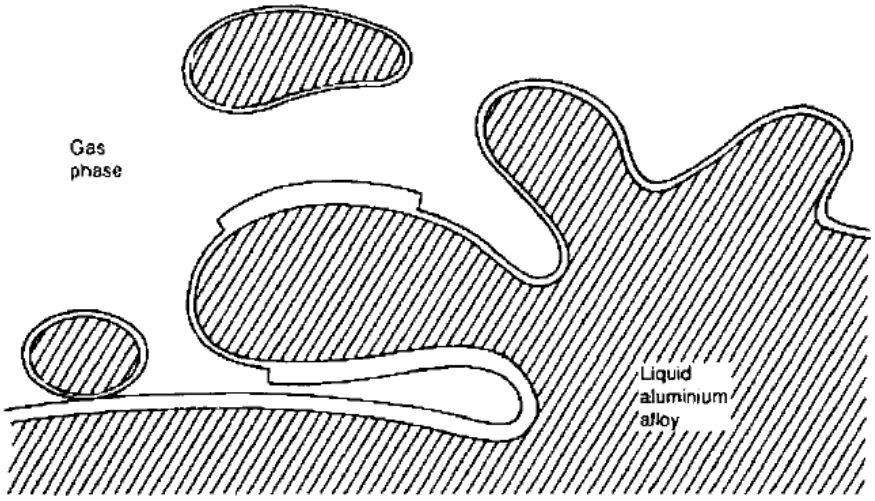

Fig 2-1, sketch of the entrainment process [22].

In casting processes, surface turbulence (i.e. a wave or vortex) can make the film fold as shown in Fig 2-1. Since the folding action necessarily folds over the layer dry side to dry side, films of the folded surface must be double, hence “double oxide film ”, or “bifilm”. When double oxide films are submerged into the bulk liquid, it becomes a double oxide film defect, or “entrainment defect” [22]. The entrainment process in the liquid magnesium melt can also be described in this way [23, 24].

2.2 Evidence of the existence of double oxide film defects

Fox and Campbell [25] developed a reduced pressure test to observe the behaviour of entrainment defects in Al-7Mg-0.4Si alloys. Fig 2-2 shows radiographs of plate castings from a series of reduced pressure tests. It can be seen that small grey 'specks' in the samples, cast under a pressure of 1000 mbar, were elongated into discrete "streaks", under the effect of the pressure decrease. This suggests that there was a reservoir of gas being trapped in the expanded "speck", which suggested that the "specks" were double oxide defects.

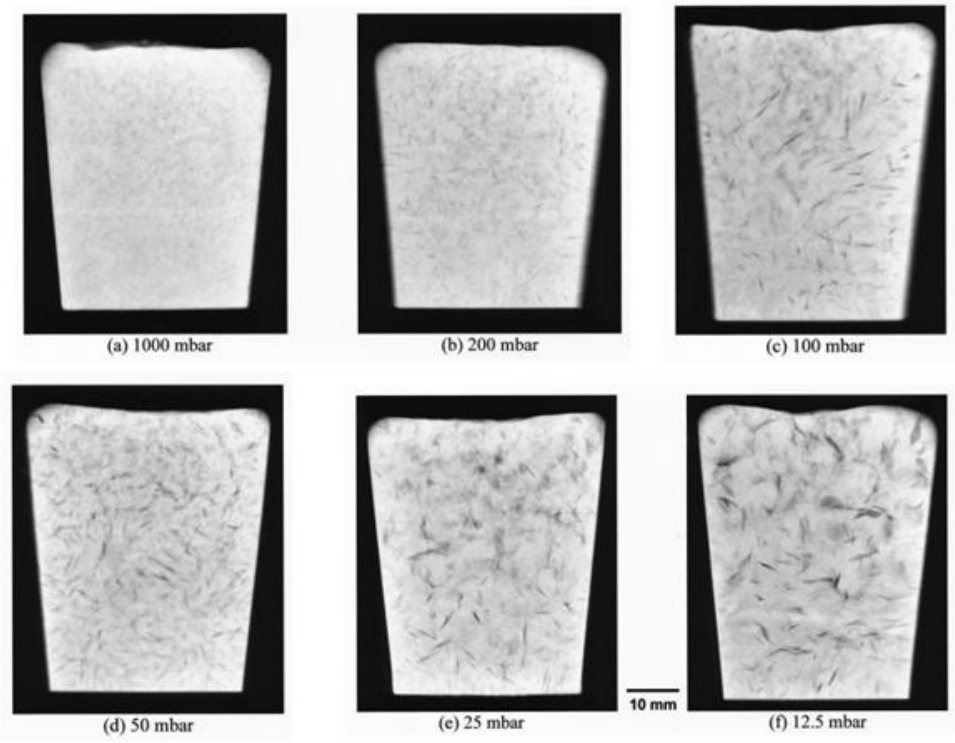

Fig 2-2, radiographs of internal defects of plate castings [25]

Cox et al. [26] provided direct evidence of the existence of double oxide defects on the fracture surface of bend test bars that had been cast by investment casting in an Al-7Si-Mg alloy. They detected oxygen in a discoloured area on the fracture surface

by EDX analysis, but no oxygen was found in the other regions, suggesting that the oxygen-rich region was a double oxide film defect.

Cao and Campbell [27] found a symmetrical oxide films on the opposing fracture surfaces of Al-11.5Si-0.4Mg alloy castings. The symmetrical nature of the oxide films indicated that they were a double oxide film defect.

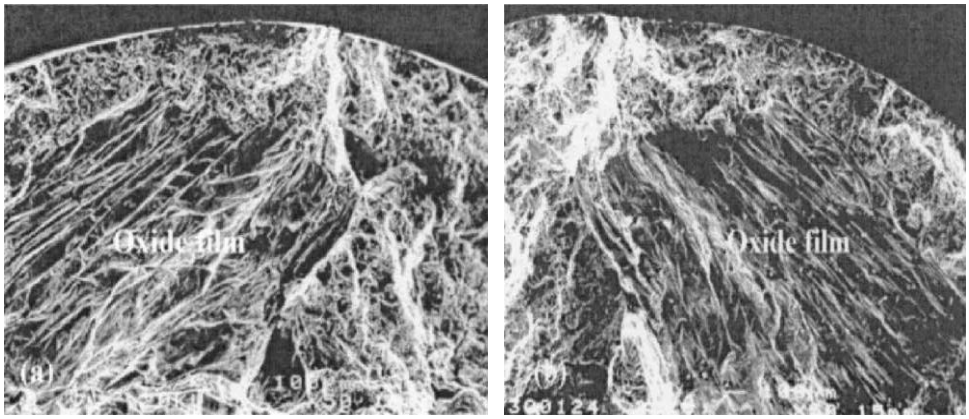

Fig 2-3, symmetrical oxide films on the fracture surface of Al-alloy castings.

For magnesium alloys, Griffiths and Lai [23] found black symmetrical areas on the fracture surfaces of commercial purity Mg test bars, cast under a protective gas of 96%CO_2/4%SF_6. This black area presented a wrinkled film-like appearance and contained oxygen, which agreed well with the feature being a double oxide film defect.

2.3. Effects of double oxide film defects on mechanical properties.

2.3.1 Cracks

The fracture of components comprises of three stages [28]:

(1) Micro-crack initiation into a short crack;

(2) Short crack growth and coalescence into a long crack;

(3) Long crack propagation until final rupture;

Pitcher and Forsyth [29] found that the poor fatigue properties of cast Al-alloys was generally caused by the short process of the fatigue crack initiation in stage (1). Wang et al. [28] confirmed this observation, and suggested that crack initiation could be accelerated by stress concentration around defects such as porosity and oxide films. It can be consequently suggested that the fatigue property of castings can be also reduced by double oxide film defects.

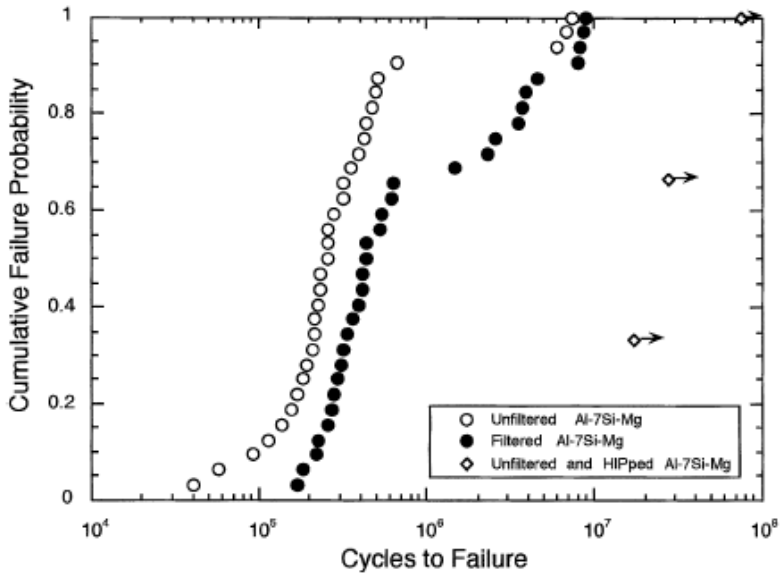

Fig 2-4, fatigue life distributions for filtered and unfiltered castings [30].

The practical experience for this suggestion comes from the work of Nyahumwa et al. [30]. They detected an entrainment defect acting as a crack initiator on the fracture

surface. In addition, Fig 2-4 shows that filtered Al-alloy castings had longer fatigue lives than unfiltered castings, since a ceramic filter could remove oxide films from liquid Al [31]. The better fatigue properties of the filtered castings revealed the negative effect of double oxide defects on casting fatigue.

2.3.2 Ductility

As shown in Fig 2-5, Edelson and Baldwin [32] examined the detrimental effects of second phase particles and pores, on the ductility of pure copper.

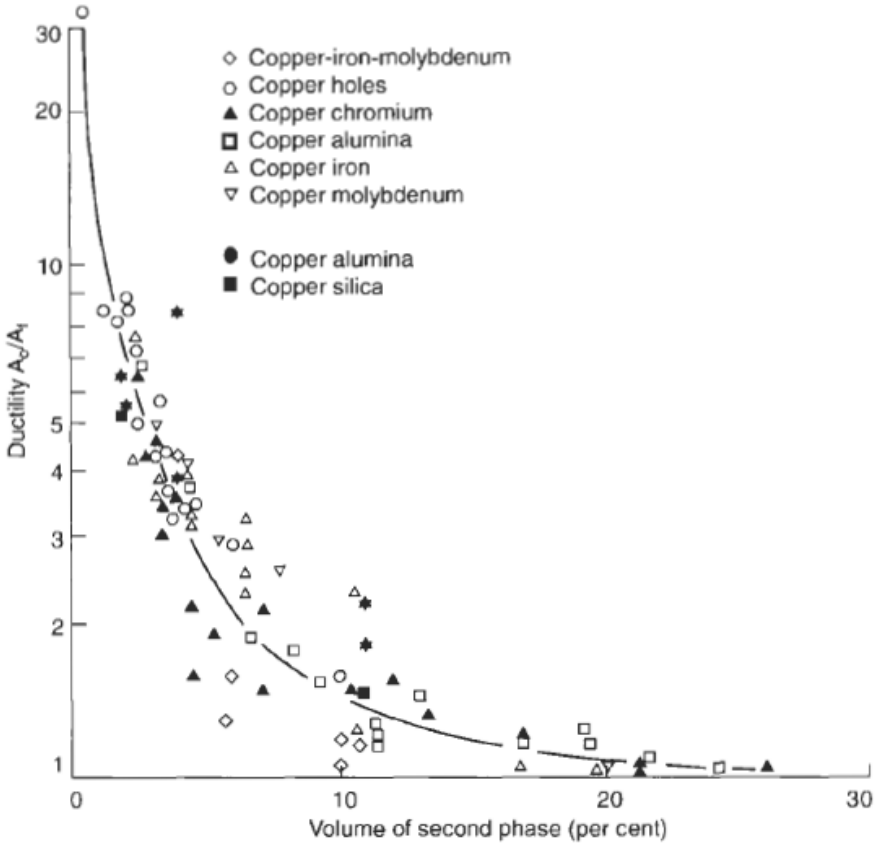

Fig 2-5, relationship between ductility and volume of second phase in copper [32].

Campbell [22] proposed an equation to approximate the relationship between elongation and micro-pore content for a space containing an array of micro-pores:

Eq. 2-1: $$Elongation = (1 - f^{\frac{1}{2}}) / n^{\frac{1}{2}}$$

where f was the area fraction of the pores on the fracture surface, and n was the amount of pores per unit area. This equation suggested that double oxide defects can effectively reduce the ductility of castings when the double oxide film defects are normal to the direction of applied tensile force, but they lead to a relatively lower effect on elongation when the double oxide film defect is parallel to the tensile force direction.

Dai et al. [33] supported Campbell's equation (Eq. 2-1). In their experiment, cast plates produced with two different runner systems were sampled in vertical and horizontal directions, respectively. The UBS Weibull modulus of the horizontally machined samples was higher (18.0 and 14.9) than that of the vertically sampled specimens (12.7 and 8.8). This difference might be due to the different angles between the double oxide films and the direction of the applied tensile force.

2.3.3 Fe-rich phase

Iron is a common impurity in Al alloys castings, and a high iron content could negatively affect the quality of the castings [34]. Cao and Campbell [27] suggested that the external wetted surface of double oxide film defects could be the site for nucleation of Fe-rich inter metallics, based on a detection of primary *α*-Fe crystals on the outer surfaces of a double oxide film defect. It was the first direct evidence that primary *α*-Fe particles nucleate and grow on the wet outer sides of double oxide

films.

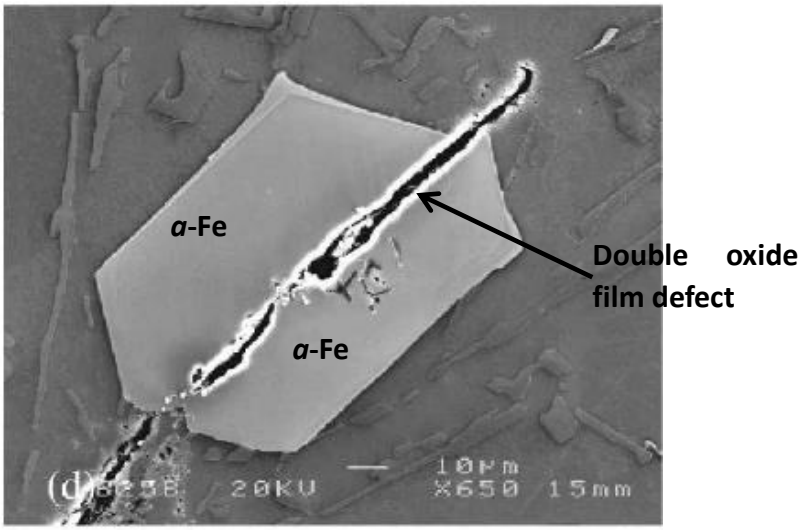

Fig 2-6 *α*-Fe crystals grown on the wetted outer side of a double oxide film defects [27].

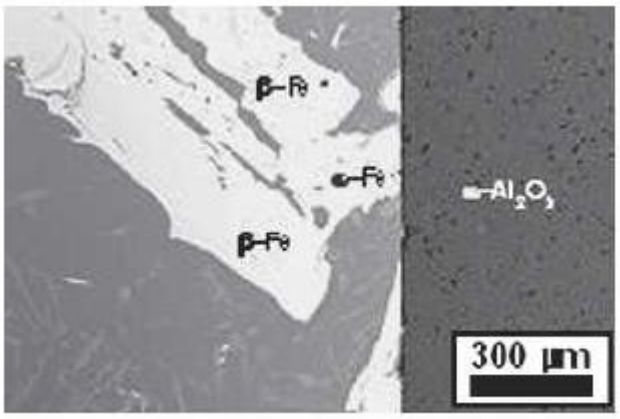

Fig 2-7 a backscattered electron SEM image of the interface between the Al-alloy melt and a polycrystalline α-Al_2O_3 substrate [35].

Further evidence was offered by Miller et al. [35], who directly inserted substrates of Al_2O_3 and $MgAl_2O_4$ into an Al-11.6Si-0.37Mg alloy melt. It was found that α-Fe phase formed close to or at the α-Al_2O_3 substrate, followed by β-Fe phase, as shown in Fig 2-8. Miller et al.[35] suggested that α-Fe could nucleate on aluminium oxide

particles, and β-Fe subsequently nucleated on the α-Fe phase. In addition, the β-Fe phase could also form directly on the surface of a $MgAl_2O_4$ substrate, as shown in Fig 2-8, indicating that this Fe-phase nucleation may also occur in a Mg-alloy melt, such AZ91 alloy.

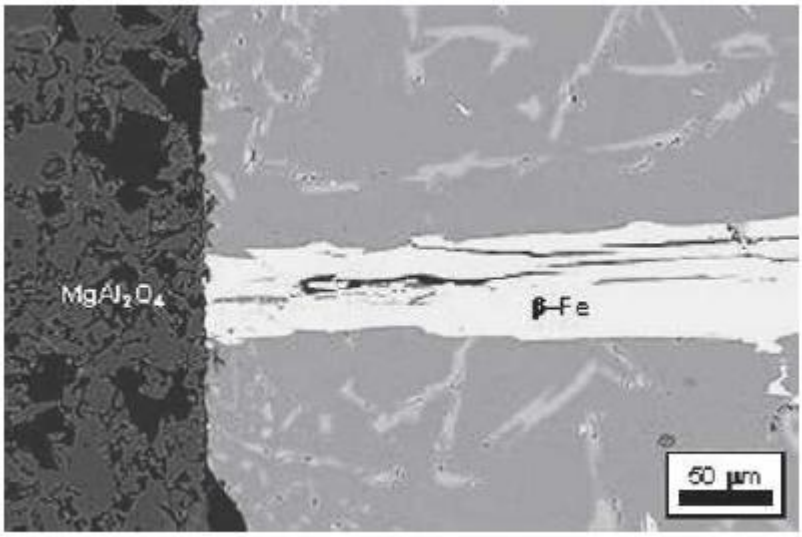

Fig 2-8 SEM image of a β-Fe particle at the surface of an MgAl2O4 substrate [35].

Zahedi et al.[36] detected a number of β-Fe phase plates near a pore formed in an Al-5Si-3Cu-1Fe-0.3Mg alloy. Since the pore in an Al-alloy casting has the same behaviour as a double oxide defect, these results further supported Cao and Campbell's suggestion that Fe-rich phase nucleates on a double oxide film defect.

2.4 Healing of double oxide film defects

As previously mentioned, a double oxide film defect acts a reservoir of a trapped gas when submerged into the melt. Many publications reported that this trapped gas could be further consumed by reaction with the surrounding melt [22, 30, 37, 38], thus creating the expectation that the folded oxide films could finally be bonded

together, due to the reaction between the trapped gas and the surrounding melt. The negative effect of double oxide film defects, referred to in section 2.3, could therefore be expected to decrease.

Aryafar et.al.[39] carried out an experiment that melted two A356 bars with oxidised surface in a steel tube. It was found that the two Al-alloy bars strongly bonded with each other, and became even stronger by bonded with an increase in the holding time. In addition, spinel ($MgAl_2O_4$) and MgO were recognized in the bonded area. This work indicated a possibility that a bonding action could occur in a doubled oxide film structure.

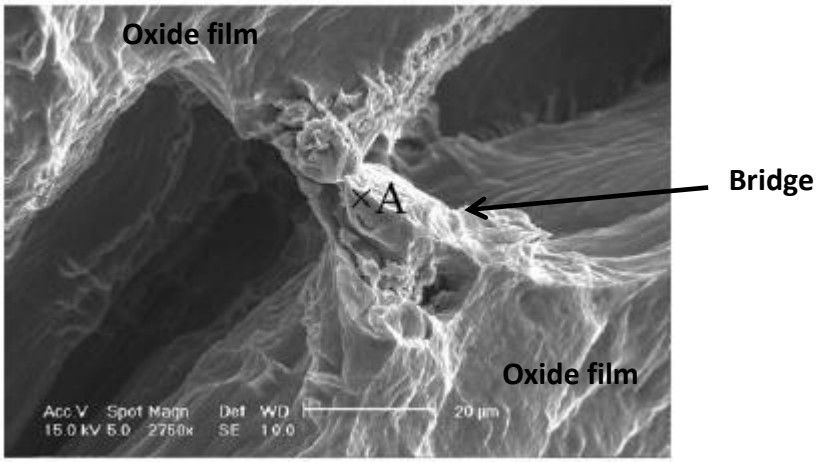

Fig 2-9 a bridge between the two oxide films of a double oxide film defect [40].

Raidszadeh and Griffiths [40] further investigated the relationship between casting reproducibility and holding time before pouring. A bridge between the two oxide films of a double oxide defect was found in their study (Fig 2-9). However, their Weibull modulus results revealed that the reproducibility of A356 alloy castings

decreased with a 10-min holding time, but increased with a 20-min holding time. Moreover, the commercial purity Al casings did not present a clear difference in their quality after a 20-min holding time. The reason for this was suggested to be due to hydrogen diffused from the surrounding melt into the double oxide film defects, which expanded the folded oxide films, making them unable to bond together.

Another potential reason for this could be that nitrogen contained in the trapped gas was difficult to consume by the reaction with Al-alloy melt [41]. This will be further discussed in section 2.7.1.

2.5 Effect of hydrogen diffusion

2.5.1 Expansion of double oxide film defects caused by H diffusion

Campbell [22] conjectured that hydrogen could precipitate into the entrained gas between the oxide interfaces, inflating the corresponding double oxide defect. This H penetration was supported by Raiszadeh and Griffiths [37], who introduced an air bubble into liquid Al with different hydrogen contents. In Fig 2-10, it can be seen that the air bubble in the liquid Al of high hydrogen content, with a short holding time (H=0.26 ml/100g, delay 15 min), experienced a significant expansion, which did not occur when the air bubble was trapped in the liquid metal with the same holding time, but lower hydrogen content (H=0.14 ml/100g, delay 15 min). The expansion was suggested to be due to hydrogen diffusion into the air bubble.

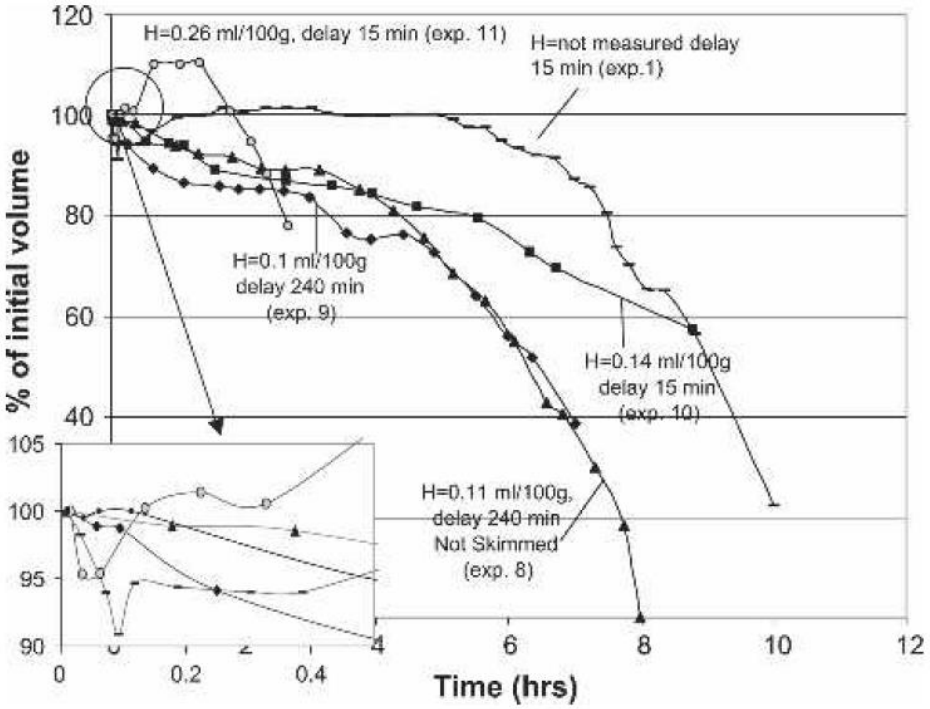

Fig 2-10 A comparison of air bubble volume with different hydrogen contents [37].

Yue et al. [42] observed the evolution of double oxide film defects in liquid A356 aluminium alloy by Synchrotron X-ray at the Swiss Light Source, supporting a result which was not fully consistent with Campbell's conjecture. According to Fig 2-11, Campbell's unfolding processes were not seen. Hydrogen did not diffuse into the internal bubble of gas of the large entrainment defects, but penetrated into some smaller defects instead, too small to be viewed clearly.

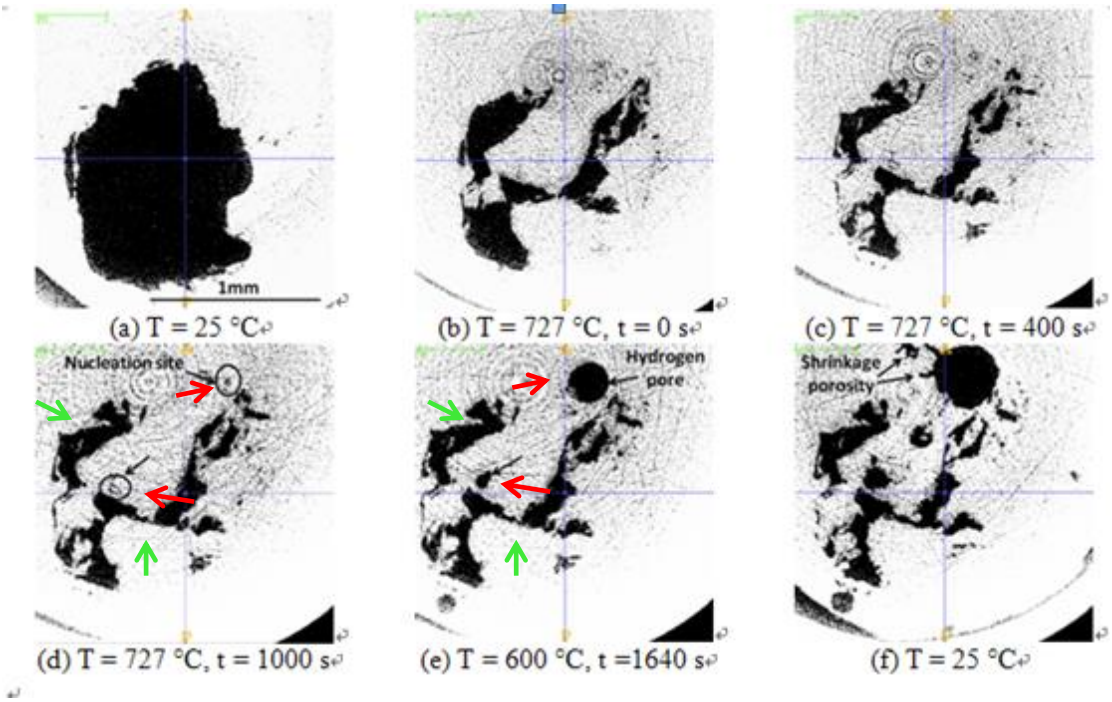

Fig 2-11 Evolution of an entrained pore [42] formed in Al alloy. The red arrows denote the small defects which hydrogen penetrated into; the green arrows denote the large double oxide film defects which were not unfolded.

2.5.2 H solubility.

Hydrogen gas porosity is a well-known defect in aluminium alloy casting, thus the H solubility in Al alloys has been studied for decades [43-45]. Harvey and Chartrand [45] summarized the H solubility in Al which had been published in previous literatures, as shown in Fig 2-12. It can be seen that the H solubility in liquid Al was no more than 30 molar ppm (≈ 1.1 ppm) at common casting temperatures from 973 K to 1073 K.

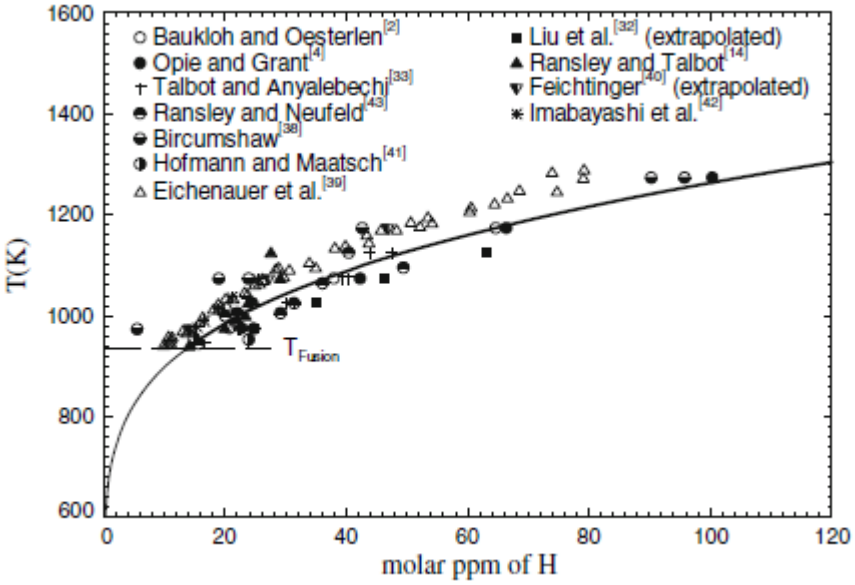

Fig 2-12 a summary of H solubility in liquid aluminium, at $P(H_2)$ = 1 atm, from [45].

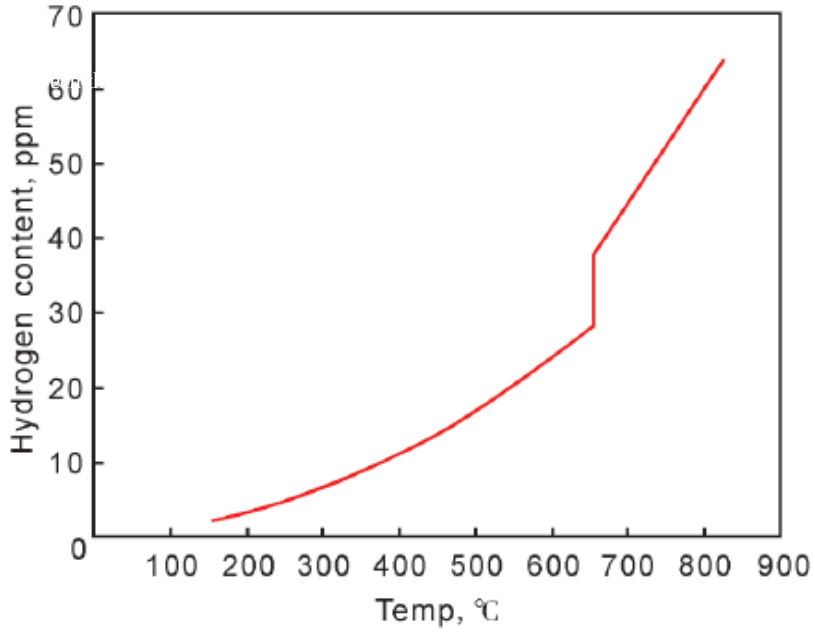

Fig 2-13 Hydrogen solubility of liquid pure Mg (at 1 atm) [46].

Compared with aluminium, magnesium has a high hydrogen solubility, which even caused widespread interest in Mg-based alloys for hydrogen storage [47-49]. Fig 2-13 shows the hydrogen solubility in liquid pure magnesium [46], revealing that hydrogen

solubility in liquid Mg (melt point = 650 ^{o}C) was 35 ppm, which was significantly higher than that in liquid Al. In conjunction with the H diffusion acting in double oxide defects (referred to in section 2.5.1), it is possible that the quality of Mg-alloy castings may be more seriously affected by double oxide defects, thanAl-alloy castings.

2.6. Protective gas

Compound	Pilling-BedWorth Ratio	Oxide film type
MgO	0.81	Porous film
MgF_2	1.45	Dense film
$MgSO_4$	3.2	Dense film
MgS	1.4	Dense film
$MgCO_3$	1.6	Dense film
Mg_3N_2	0.89	Porous film
CaO	0.64	Porous film
Al_2O_3	1.28	Dense film
Y_2O_3	1.13	Dense film

Table 2-1 P-B ratio of some compounds, summarized by [50]. Data of yttrium oxide is based on [51].

As mentioned in section 2.1, the light alloy melts are always covered by a surface film. The protective ability of this surface film can be determined by the Pilling-Bedworth ratio (P-B ratio), which is a volume ratio between the elementary cells of the oxide formed and the corresponding metal. If the P-B ratio is smaller than 1, the oxides formed on the melt surface can not cover the entire melt surface, making the

oxide film, thus the oxidation process can not be halted by the film. If the surface film has a compact structure, the film can isolate the melt from the surrounding atmosphere, thus stopping the further oxidation process.

Table 2-1 shows the P-B ratio of some compounds related to the reactions between molten Mg and cover gases. It can be seen that MgO has a P-B ratio of 0.81, thus MgO can not form a protective surface film like Al_2O_3, whose P-B ratio is 1.28. Therefore, a magnesium melt can be rapidly oxidised in air and burn.

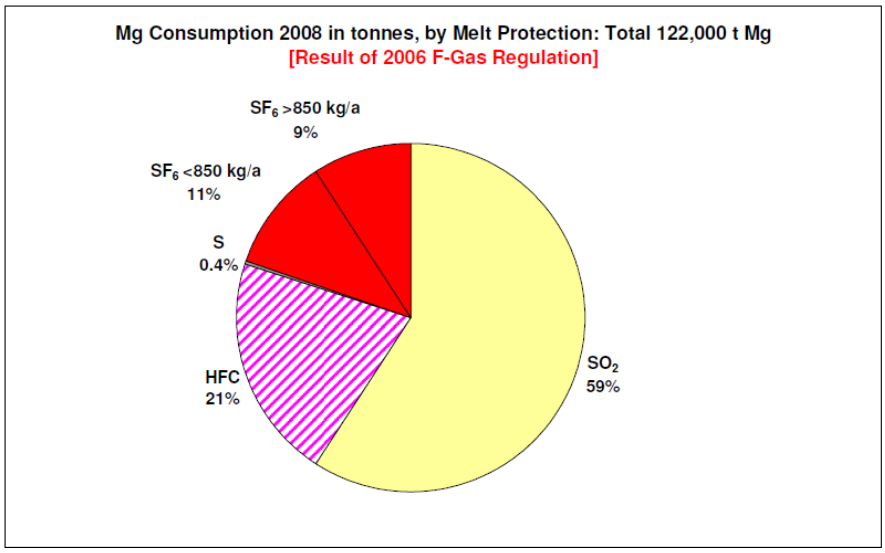

Fig 2-14 the most widely used cover gases in the Mg industry, from a survey of Europe[52].

Due to this well-known rapid oxidation of molten magnesium in air, a cover gas is required for casting Mg alloys. The gas can react with liquid Mg alloys, to form a protective surface film, halting the rapid oxidation process. Fig 2-14 shows the most widely used cover gases in the Mg industry according to a survey of 53 Mg die-casting foundries in 11 countries in Europe [52]. It can be seen that nearly all the Mg

melting process was protected by one of the three gases: SF_6, HFC-134a, and SO_2.

2.6.1 Sulphur hexafluoride (SF_6)

SF_6 is a traditional gas used for the protection of liquid magnesium [53]. It was proven to be an effective inhibitor in the early 1970s [54], but its protective mechanism was not clear for decades.

A widely accepted explanation of the protective mechanism of SF_6 was proposed by Cashion et al. [55, 56]. They suggested that MgO molecules could be wetted by liquid Mg, so that capillary forces would pull the adjacent oxide particles together to form a cohesive ‘‘raft’’ on the melt surface (Fig 2-15). The “raft” minimized the contact area between the melt and the atmosphere, decreasing further magnesium vaporization and halting rapid oxidation.

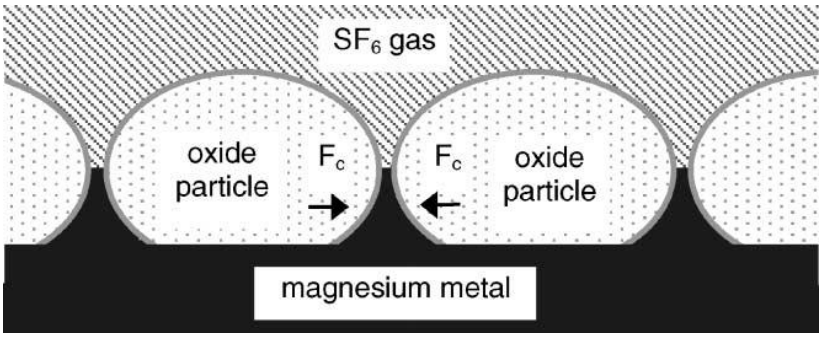

Fig 2-15 A sketch showing that the oxide particles on the magnesium melt surface can be drawn together due to the capillary forces (Fc) [56].

Pettersen et al. [57] noticed that the surface of the protective film formed under a

protective gas of 1%SF_6/air consisted of grey areas and shiny areas, as shown in Fig 2-16. The shiny area was comparatively thin, and had a relatively lower F: O ratio. They suggested that the liquid Mg firstly reacted with oxygen, forming a thin MgO film, and then SF_6 dissociated to provide atomic fluorine, as shown below:

Eq. 2-2 : $SF_6 \rightarrow SF_4 + nF + (1 - n/2\ F_2)$

The atomic fluorine could penetrate through the porous MgO layer in the grey region, forming an inner MgF_2 layer. In conjunction with Cashion's process [56], a relatively small amount of F atoms can penetrates through the cohesive "raft", forming the shiny area, while a large amount of atomic F can penetrate in the other region having a relative porous structure, forming the grey area.

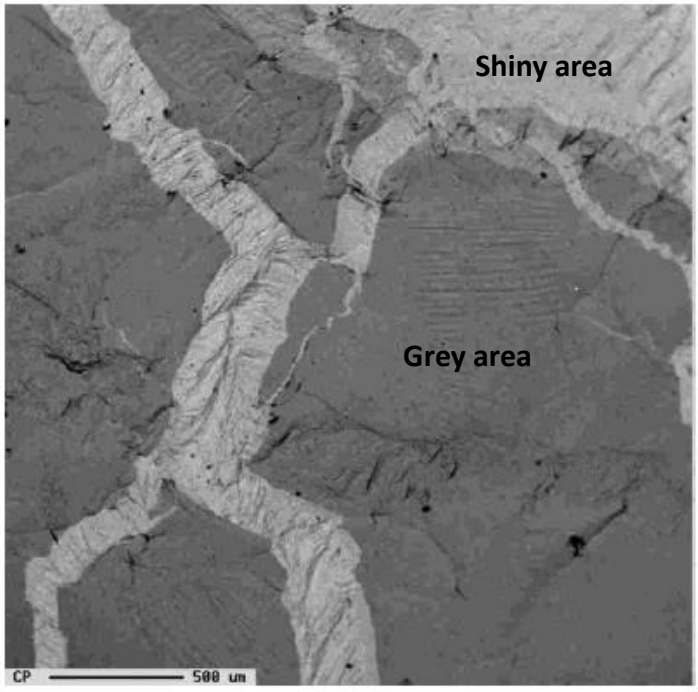

Fig 2-16 Image of backscattered electrons from a sample exposed to 1% SF_6/air for 5 min [57]

Further support for Cashion's process was produced by Xiong and Liu [58], who also

found different-coloured regions on the surface of the protective film (Fig 2-17). Their EDX results suggested that the discoloured regions corresponded to MgF_2 particles under the surface film. In addition, Xiong and Wang [59] reported that the discoloured regions appeared after the formation of a preliminary MgO film, giving support to Pettersen's process [57].

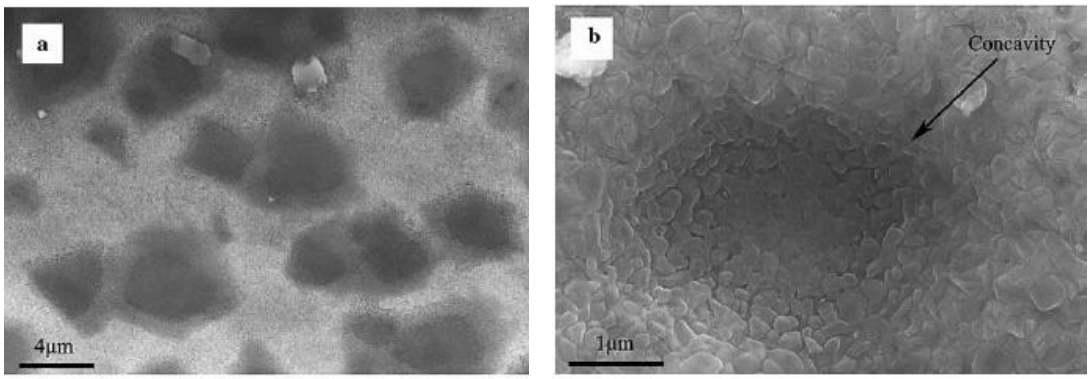

Fig 2-17 (a) the different-coloured regions on the surface of the protective film; (b) the dark region was concavities on the film surface [58].

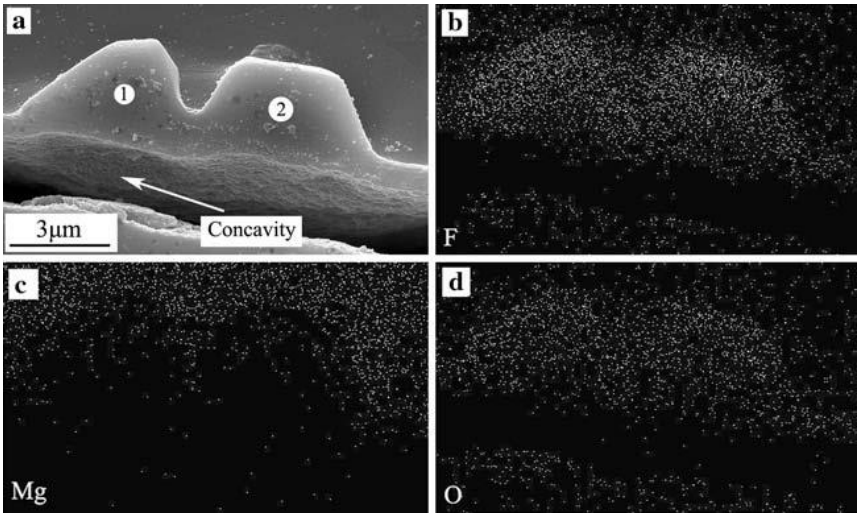

Fig 2-18 (a) cross-sections of the dark region shown in Fig 2-17, (b-d) the element map [58].

In the publications mentioned, sulphur was not detected in the protective film

formed with SF_6, but Shih et al. [60] found a layer containing MgS over the MgF_2 layer in the surface film formed in 2%SF_6/air. Aarstad [50] also detected high sulphur contents on the surface of pure magnesium castings in SF_6-containing gases (SF_6/air, SF_6/N_2, and SF_6/CO_2). The reason for the sulphur detection may be that the thermal decomposition of SF_6 was more complicated than Eq. 2-2. According to [61-63], SF_6 could decompose to various fluorides including SF_5, SF_4, SF_3, SF_2, SF, F_2, and F [62, 63]. These fluorides can further dissociate to provide sulphur in the cover gas, as S_2 ,S_3, and atomic S [61].

2.6.2 HFC -134a (CH_2FCF_3)

Due to the high global warming potential (GWP) of SF_6 [64], HFC-134a (1, 1, 1, 2-tetrafluoroethane) was developed for the protection of magnesium melts [65]. HFC-134a has a lower required inhibitor concentration and GWP than SF_6 [64, 66].

Chen et al. [67] found that MgO, MgF_2 and C comprised the surface film formed on pure liquid Mg protected by HFC-134a/air. Two layers were detected in the oxide film by the AES analysis with ion beam etching (Fig 2-19): an outer layer enriched with MgF_2 and an inner layer containing relatively less fluorine. Chen et al. proposed that HFC-134a could readily decompose into C, HF and F_2 due to its low thermal stability. The fluorine and the oxygen in air could react with liquid Mg, forming an inner F-rich layer. The carbon provided by the decomposition of CH_2FCF_3 might partly fall on the film surface.

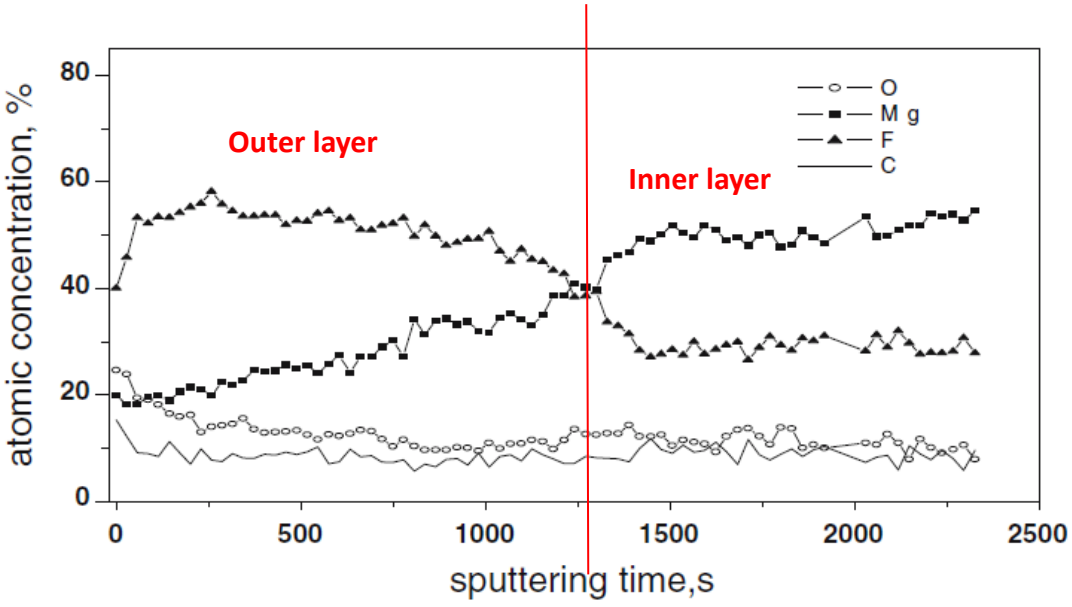

Fig 2-19 AES depth profile of the surface film formed in an atomophere of HFC-134a.

Liu and Xiong [68] found some dark areas on the surface film when they used HFC-134a/CO_2 to protect the liquid AZ91D alloy. The dark regions were corresponding to MgF_2 particles under the surface film (Fig 2-20). Thus Cashion's process [56] of MgO cohesive "raft" may also occur in the protective process of HFC-134a.

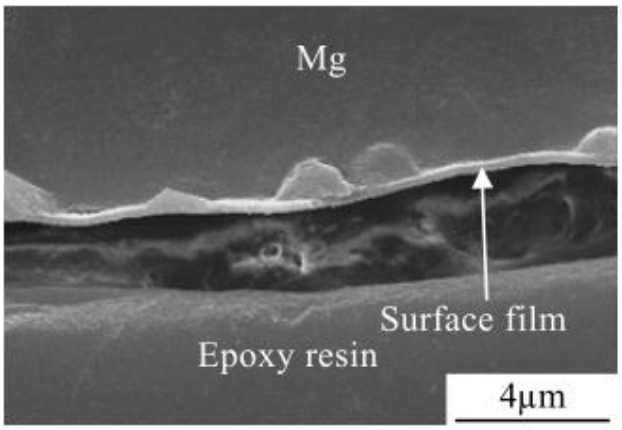

Fig 2-20 a cross-section of surface film (650℃, 10 min, 0.3%HFC-134a/CO_2) [68]

2.6.3 SO_2

Sulphur dioxide was one of the first gases applied in protecting liquid magnesium without the use of solid fluxes [69]. It was widely used for Mg casting until Fruehling [54] proved that SF_6 offered better protection at a lower concentration. However, in recent decades, due to the high GWP of SF_6, SO_2 became the focus again in the magnesium industry as a feasible alternative to SF_6.

Cashion and Ricketts [69] detected $MgSO_4$ and MgO, but no MgS on the surface film when testing the protective performance of SO_2 with different diluent gases in an unsealed environment. However, Liang et al. [70] only found MgS and MgO, but no $MgSO_4$ on the oxide film when they used SO_2/CO_2 to protect solid AZ91D alloy.

Currently, the publications of Wang and Xiong [71-76] appear to be the most detailed explanation of the mechanism of SO_2 protection. The surface film was found to contain three layers: an inner layer containing Mg, O, and S, an outer O-rich layer and an extra outer thin S-rich layer. The corresponding formation process could be described in the following steps [71-76]:

Step 1, the Mg melt was quickly oxidised, forming a MgO preliminary film.

Step 2, because of the porous structure of the MgO film, $MgSO_4$ was produced due to the reaction $Mg + SO_2 + O_2 = MgSO_4$.

Step 3, $MgSO_4$ in the inner part of the oxide film reacted with liquid Mg according to the reaction $4Mg + MgSO_4 = MgS + 4MgO$. Thus $MgSO_4$ only existed in the outermost layer, and an inner layer of MgS and MgO consequently formed.

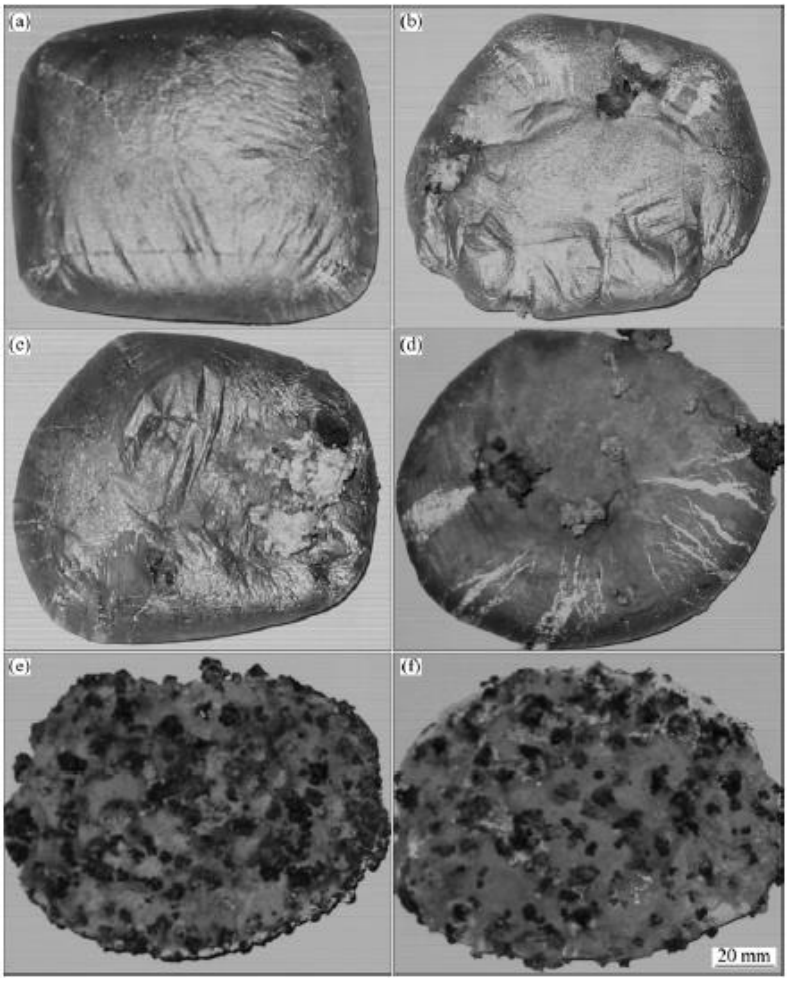

Fig 2-21, samples formed in N_2+0.5%SO_2 containing different air content: (a) 90%; (b) 80%; (c) 60%; (d) 40%; (e) 20%; (f) 5% [73].

In addition, it was reported that the oxygen content in the cover gas had a significant effect in protecting liquid Mg alloy with SO_2 [73, 76]. Fig 2-21 shows AZ91D samples

protected by the cover gases having different air contents. It can be seen that the protective ability of the cover gas could be eliminated due to a low content of oxygen. It was proposed that the active species (i.e. MgS, $MgSO_4$) needed to protect the Mg alloy melt could not be produced in an absence of oxygen in the cover gas; the SO_2 could not directly react with liquid magnesium via the reaction of $3Mg + SO_2 = 2MgO + MgS$.

2.7 Carrier Gas

The protective gases mentioned in section 2.6 are normally mixed with a diluent gas, known as a "carrier gas" in a practical application. The common carrier gases include air, CO_2, N_2, Ar, He etc. Among them, N_2, air and CO_2 were the most widely used in industrial practice for the last 30 years [52, 77, 78]. However, according to a report submitted to the European Commission in 2009 [52], air was not used as a carrier gas in the companies surveyed in Europe.

2.7.1 Air and N_2

As previously mentioned, liquid magnesium can be quickly oxidised and burn in an atmosphere of air, due to the MgO P-B ratio of 0.81. This burning phenomenon also happens when liquid magnesium is covered by nitrogen, known as "nitrogen burning" [79], since Mg_3N_2 has a P-B ratio of 0.89 (Table 2-1) making the Mg_3N_2 surface film not protective.

Compared with magnesium, aluminium is hard to efficiently react with nitrogen.

Kumari et al. [80] reported a detection of AlN in a solidified pure Al sample, after bubbling pure nitrogen into the Al melt. This revealed the possibility that aluminium reacts with nitrogen in a trapped gas. However, it should be noted that this reaction of Al and N_2 may occur very slowly. Scholz and Greil [41] found that only 16% of a cover gas of pure nitrogen had been consumed by an Al-2Mg-0.8Si alloy melt, after a holding time of 15 hours at 1273K, but a mixture of 0.7%H_2 in the cover gas can increase this consumption rate to > 95%. Swaminathan [81] further suggested that the residual oxygen in cover gas can inhibit the reaction between aluminium and nitrogen.

In a practical process, it is quite unusual to hold liquid metal for 15 hours, thus most of the nitrogen in double oxide film defects in an Al-alloy casting may not be consumed, making the folded oxide films unlikely to bond together. This may be the reason why Raiszadeh and Griffiths [40] did not find a clear effect from an extension of the holding time on the quality of Al castings. Nevertheless, this low nitrogen consumption rate does not exist for Mg alloys, thus an extension of the holding time may be an effective technique to increase the quality of Mg alloy castings.

2.7.2 CO_2 and Mg carbides

A previously widely accepted equation of the reaction between Mg and CO_2 was suggested as Mg + CO_2 = MgO + CO [79, 82]. Liang et.al [70] further suggested an equation of 2Mg + 2CO = 2MgO +C, based on a XRD detection of monoatomic carbon

in the surface film formed in AZ91D alloy under a cover gas of SO_2/CO_2.

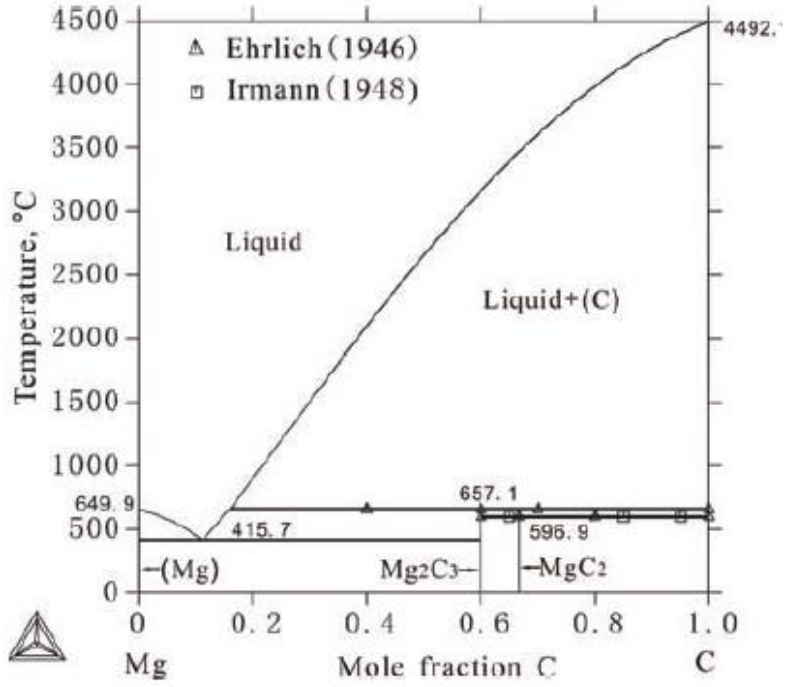

Fig 2-22, Mg-C phase diagram, calculated by [83]

In addition, an investigation into Mg combustion [84] reported a detection of Mg_2C_3 in the Mg sample after burning in CO_2. This detection not only supported Liang's equation, but also indicated the formation of Mg carbides in double oxide film defects. According to the Mg-C phase diagram shown in Fig 2-22 [83], magnesium carbides do not exist when the alloy is in a liquid state, but can be produced during solidification.

2.7.3 Protective ability of the carrier gas.

The carrier gas can also affect the protective ability of the cover gas. As shown in Fig 2-23 [85], SF_6/air required a higher content of SF_6 than did a SF_6/CO_2 and SF_6/N_2 carrier gas, to avoid the ignition of molten magnesium. In addition, the thickness of

the surface films was found to grow faster in SF_6/air, than in SF_6/CO_2 and SF_6/N_2 [85]. Thus, air has a lower protective ability than CO_2 and N_2, which may be the reason why all the surveyed companies of [52] in Europe did not use air as a carrier gas.

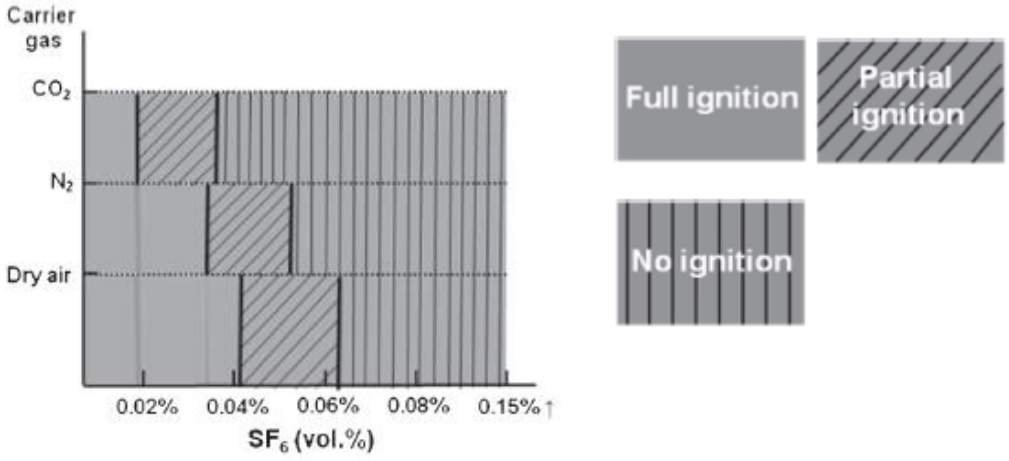

Fig 2-23, to protect magnesium, the minimum concentration of SF_6 under different carrier gases at 973K [85].

Nevertheless, according to their different protective abilities, it can be conjectured that a trapped gas of SF_6/air in a bifilm can be consumed faster than in the case of SF_6/CO_2 and SF_6/N_2 gases in a Mg-alloy melt. Thus it can be further conjectured that the folded films of a double oxide defect formed in SF_6/air can bond together earlier than the doubled oxide films formed in SF_6/CO_2 and SF_6/N_2 in the casting process. Therefore, castings produced with SF_6/air may have a better quality than those protected by SF_6/CO_2 and SF_6/N_2.

2.8 Oxidation of Mg alloys.

2.8.1 Mg-Al Alloy

A stability diagram of the Al-Mg-O system was computed by [86], as shown in Fig

2-24. It suggested that aluminium oxides may not be produced when the Mg content was high, which suggestion was supported by the experimental results of [87, 88]. Czerwinski [87] reported that the surface film of AZ91D alloy formed in air at 800K contained $MgAl_2O_4$, MgO, AlN and Mg_3N_2, but no Al_2O_3. Barrena et al. [88] also found the same absence of alumina in the oxide film of AM60 and AZ91 alloys.

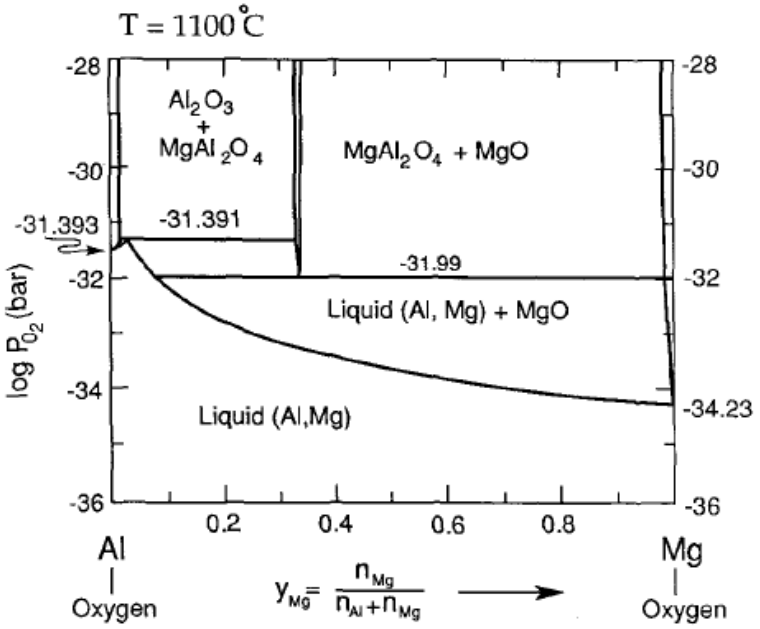

Fig 2-24 a stability diagram of the Al-Mg-0 system at 1100 °C [86].

In addition, Zeng et al. [89] found that the oxide film on a sample of an AZ91 alloy exposed to air at 650 ^{o}C had an outermost layer consisting only of Mg and O, indicating that a porous MgO film formed in this oxidation process, and then Al reacted with the oxygen which penetrated through the MgO layer.

Furthermore, Wang and Xiong [75] revealed that the aluminium concentration in the

oxide film reduced with an increase in the sample holding time at 680^{o}C, when they used SO_2 to protect liquid AZ91D alloy. This reduction in Al content may be caused by the reaction between liquid Mg and $MgAl_2O_4$ as: $3Mg + MgAl_2O_4 = 4MgO + 2Al$ ΔG (680^{o}C) = -106.619 kJ.

Therefore, the oxidation process of an Mg-Al alloy can be summarized as following steps:

Step (1), a MgO porous film is firstly produced on the melt surface.

Step (2), Al subsequently reacts with the oxygen passing through the MgO film, producing $MgAl_2O_4$.

Step (3), Spinel ($MgAl_2O_4$) can react with liquid Mg to form MgO and Al, decreasing the Al concentration in the oxide film.

2.8.2 Mg-Y alloy

An yttrium-enriched surface film was found on a sample of a Mg-Y binary alloy after oxidation testing using air [90], which indicated that yttrium could react with MgO, forming Y_2O_3 and Mg. This reaction was supported by many oxidation tests of various Mg-Y alloys [91-95]. In addition, the Pilling-Bedworth ratio of Y_2O_3 is 1.13 [51], suggesting the possibility that Mg-Y alloys may have a protective oxide surface film at high temperature.

Wang et al. [90] reported that an increase in Y concentration could result in a

positive effect on the oxidation resistance of a Mg-Y melt. Fan et al. [91] also found that Mg-Y alloys had a significant resistance to oxidation in air, even not burning at 1173 K, as shown in Fig 2-25. It should be noted that the widely used Mg-Y alloys, such as WE43 and WE54 alloys, do not have an yttrium content higher than 6%, thus they can still burn at 950K, which is a normal pouring temperature of a Mg-Y alloy casting process. A protective gas is therefore still required for casting Mg-Y alloys.

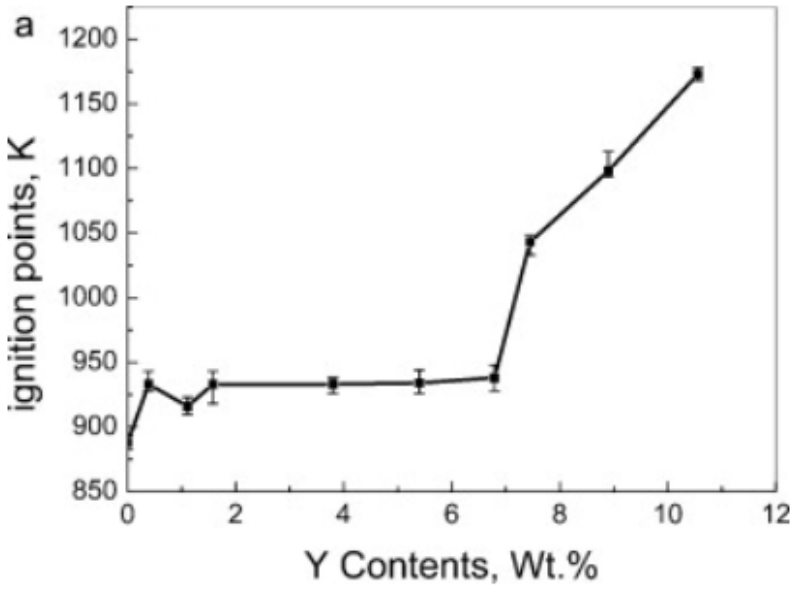

Fig 2-25 Ignition points of Mg–Y alloys [91]

2.9 Weibull distribution to characterize the quality of castings

The Weibull distribution has been widely used to analyse the variability of the fracture properties of brittle materials for over 30 years. It also later became a popular method in the prediction of the quality and reproducibility of castings [23, 96, 97]. It was considered to be one of the best methods to describe the scatter of data in mechanical property tests and allow discrimination between “good” and “bad” casting process [96].

The cumulative probability function of the Weibull distribution was given by [98]:

$$\text{Eq. 2-3:} \qquad \mathbf{P = 1 - exp}[-\left(\frac{x - x_u}{\mathbf{x_0}}\right)^{\boldsymbol{m}}]$$

where P is the probability of failure at value of x, x_u is the minimum possible value of x, and the probability scale parameter x_0 characterises the value of x at which 62.8% of the population of specimens have failed. The shape parameter m describes the variability in the measured properties. The greater the value of m, the narrower the range will be of the distribution. If all the castings were perfectly produced without any defects, all the x values would be the same, making m value infinite. Thus, the value of m is itself a direct index of casting quality, which is also widely known as the Weibull modulus.

In a practical application, x could be substituted by the symbol σ for the properties of materials (e.g. Ultimate Tensile Strength (UTS)), and the lowest possible value of properties, such as UTS, could be assumed to be 0, making x_u = 0, so that Eq. 2-3 could be re-written as a 2-parameter Weibull function:

$$\text{Eq. 2-4:} \qquad \mathbf{P = 1 - exp}[-\left(\frac{\sigma}{\boldsymbol{\sigma_0}}\right)^{\boldsymbol{m}}]$$

2.10 Estimation of Weibull moduli.

There are different approaches to obtain the Weibull modulus of Eq. 2-4, with the usual methods being the Linear Least Squares method (LLS) (or known as the linear regression method), the Maximum Likelihood method (ML).

2.10.1 Linear Least Squares (LLS) methods

The Linear Least Squares method is also known as linear regression method. Taking the natural logarithm of Eq. 2-3 twice gives the linearized form of cumulative Weibull function:

Eq. 2-5: $$\mathbf{Ln}[-\mathbf{Ln}(\mathbf{1}-\mathbf{P})] = \mathbf{mLn}(\boldsymbol{\sigma}) - \mathbf{mLn}(\boldsymbol{\sigma_0})$$

The Weibull modulus can accordingly be determined according to the slope of a simple linear regression (i.e. ordinary least squares) of Ln [-Ln (1-P)] against Ln (σ), where the P value is assigned via a probability estimator. The probability estimators reported in the literature were generally written in the form:

Eq. 2-6: $$\boldsymbol{P} = \frac{\boldsymbol{i-a}}{\boldsymbol{N+b}}$$

where i is the number of the result when all results are ranked in an ascending order, N is the total sample size, a and b are constants, whose values depend on the estimator used. The common estimators were summarized by Tiryakioglu [6], and shown in Table 2-2. Among them, Eq. 2-7 to 2-9 have been most widely used for the prediction of Weibull parameters, and are also known as the Modified Kaplan-Meier (Hazen) method, the Mean Rank (Herd-Johnson) method, and the Median Rank (Bernard) method, respectively.

However, in a practical process, it is apparent that the true probability, written as P_{true}, does not necessarily equal the P values computed by the estimators. Thus there is a bias in the estimated Weibull modulus (referred to as m_{esi}) compared with

the true Weibull modulus (referred to as m_{true}).

a	b	
0.5	0	Eq. 2-7
0	1	Eq. 2-8
0.3	0.4	Eq. 2-9
0.375	0.250	Eq. 2-10
0.44	0.12	Eq. 2-11
0.25	0.50	Eq. 2-12
0.4	0.2	Eq. 2-13
0.333	0.333	Eq. 2-14
0.50	0.25	Eq. 2-15
0.31	0.38	Eq. 2-16

Table 2-2, probability estimators published in previous papers, summarized by [99].

Monte Carlo simulation has been used to study the bias level of the estimators shown in Table 2-2 [99-102]. Eq. 2-7 and Eq. 2-15 were less biased than the others, and recommended as the default Weibull estimators. In addition, based on their results, all the estimators were inevitably biased for a sample size smaller than 20, suggesting that it was not appropriate to obtain Weibull moduli from less than 20 specimens, such as [103, 104].

2.10.2 The Maximum likelihood (ML) method.

In statistics, the likelihood is a function of the parameters of a given observed dataset and the underlying statistical model. "Likelihood" is related to, but is not equivalent to "probability"; the former is used after the outcome data are available to describe that something that is likely to have happened, while the latter describes possible future outcomes before the data are available.

The basic principles can be described as follows [105, 106]. If there is a dataset of N independent and identically distributed observations, namely x_1, x_2, …, x_N, coming from a underlying probability density function f(θ). The true value of θ is unknown and it is desirable to find an estimator $\widehat{\boldsymbol{\theta}}$ which would be as close to θ_{true} as possible. First the joint density function for all observations can be calculated as

Eq. 2-17: $$f\left(x_1, x_2, ..., x_n \middle| \theta\right) = f\left(x_1 \middle| \theta\right) f\left(x_2 \middle| \theta\right) \cdots f\left(x_n \middle| \theta\right) = \prod_{i=1}^{n} f\left(x_i \middle| \theta\right)$$

From a different perspective, Eq. 2-17 can be considered to have the observed data x_1, x_2, …, x_N, as the fixed parameters and θ as the function's variable. This will be called the likelihood function as follows

Eq. 2-18: $$L\left(\theta \middle| x_1, x_2, ..., x_n\right) = f\left(x_1, x_2, ..., x_n \middle| \theta\right) = \prod_{i=1}^{n} f\left(x_i \middle| \theta\right)$$

The maximum likelihood estimate (MLE) of θ can be obtained by maximizing the likelihood function given the observed data as

Eq. 2-19: $$\hat{\theta}_{MLE} = \arg\max_{\theta} L\left(\theta \middle| x_1, x_2, ..., x_n\right)$$

For a Weibull estimation, the likelihood function of the observed dataset, x_1, x_2, …, x_N, can be written as

Eq. 2-20: $$L\left(m, s \middle| x_1, x_2, ..., x_n\right) = \prod_{i=1}^{n} f\left(x_i \middle| m, s\right) = \prod_{i=1}^{n} \left(\frac{m}{s} \left(\frac{x}{s} \right)^{m-1} \exp\left(-\left(\frac{x_i}{s} \right)^{m} \right) \right)$$

Here $f(x_i|m, s)$ is the probability density function of Weibull distribution. According to Eq. 2-19, the MLE of a Weibull parameter can then be obtained by maximizing Eq. 2-20 given the data set as

Eq. 2-21: $$\hat{\theta}_{MLE} = \arg\max_{\theta} \prod_{i=1}^{n} \left(\frac{m}{s} \left(\frac{x}{s} \right)^{m-1} \exp\left(-\left(\frac{x_i}{s} \right)^{m} \right) \right)$$

The MLE can be obtained either as an explicit function or by using numerical optimization methods, which would depend on the statistical model under study.

The estimated Weibull modulus obtained by the Maximum Likelihood method were also biased from the value of m_{true}. Khalili [102] reported that the bias level of the ML Method was higher than Eq. 2-7 of the linear least square method. This suggestion was also supported by a following study of [100, 107].

2.10.3 The Non-linear Least Squares (Non-LS) method

The Non-LS method has many similarities to the LLS method. The observed data is also sorted in an ascending fashion, and subsequently paired with the failure probabilities, obtained by the estimators shown in Table 2-2. Then, which is different from the LLS method, a non-linear regression, using a Gauss-Newton algorithm, is directly carried out to achieve the best fitted curve of a 2-parameter Weibull function, determining the estimated Weibull modulus.

This method was used to estimate Weibull parameters in publications in other fields

[108, 109], but has not been applied in the Weibull estimation in metallurgy and material.

2.11 Goodness-of-fit.

2.11.1 R^2

R^2 , also known as the coefficient of determination, is defined by the following equations [110]:

Eq. 2-22: $SS_{tot} = \sum_i (y_i - \bar{y})^2$

Eq. 2-23: $\boldsymbol{SS_{res} = = \sum_i (y_i - f_i)^2}$

Eq. 2-24: $\boldsymbol{R^2 = 1 - \frac{SS_{res}}{SS_{tot}}}$

where y_i is the observed values, such UTS of a casting, $\bar{y}$ is the corresponding mean; $SS_{tot}$is the total sum of squares; f_i denotes the predicted values, such as data points computed by the estimated Weibull function, and SS_{res} is the residual sum of squares. Thus R^2 can describe the variance proportion in the dependent variable. It has been therefore widely used to determine the goodness-of-fit of a linear regression, including the linear regression of the LLS method for Weibull moduli estimation [34, 39, 96, 111, 112].

Doremus [110] suggested that a good fit should have an $R^2 \geq 0.95$, and $R^2 < 0.9$ denoted a poor fit, but they did not suggest a goodness-of-fit level for $0.9 \leq R^2 < 0.95$. No evidence was provided to support this suggestion.

Tiryakioglu [113] further pointed out that $R^2 \geq 0.95$ was a quite conservative standard when the sample size was smaller than 80. Tiryakioglu [113] randomly generated datasets from a determined Weibull function to compute the corresponding values of R^2. For each sample size, 20,000 datasets was generated. As shown in Table 2-3, for $15 \leq n \leq 40$, which was a common sample size for practical tests, less than 90% of datasets had a R^2 value ≥ 0.95, suggesting that the standard of [110] was too strict.

n	$f_{R^2 \geq 0.95}$	$f_{R^2 < 0.90}$
5	0.371	0.283
7	0.386	0.236
10	0.467	0.157
15	0.584	0.092
20	0.730	0.051
25	0.743	0.041
30	0.799	0.029
40	0.857	0.018
50	0.902	0.013
60	0.923	0.008
70	0.942	0.007
80	0.952	0.005
90	0.964	0.003
100	0.968	0.003

Table 2-3, fraction of R^2 values larger than 0.95, and smaller than 0.90. n denotes the sample size.

Tiryakioglu [113] therefore proposed the following equation:

Eq. 2-25: $$\boldsymbol{R^2_{0.05} = 1.0637 - \frac{0.4174}{n^{0.3}}}$$

and suggested:

"If the R^2 of the linear regression from the Weibull probability plot is less than the $R^2_{0.05}$, value, then it can be concluded that the data do not come from a Weibull distribution. If $R^2 \geq R^2_{0.05}$, then the distribution of the mechanical testing data is indeed Weibull."

Two concerns of this suggestion are:

(1) A common and serious misunderstanding is that a high R^2 value indicates a good fit of the estimated linear regression line [114]. It should be noted that R^2 can not indicate the regression relationship, and data points following a non-linear curve may also present a high R^2. A residual plot is required to confirm the linear behaviour of data points in a Weibull estimation, such as [103, 114-116].

(2) The Goodness-of-fit of the linear regression line does not necessarily show whether the data points follow a Weibull distribution. This will be further discussed in section 4.5.

2.11.2 Residual plot and a misunderstanding of R^2

As mentioned in section 2.11.1, R^2 does not indicate the linearity of a dataset, and is thus not able to suggest whether a linear regression is appropriate. Consequently, a residual plot, which is normally used to study the linearity of data points, has been applied for a Weibull estimation in previous publications [103, 114-116].

Residual can be computed using the following equation, denoting the difference between the predicted value f_i, and the observed value y_i.

Eq. 2-26: $$\mathbf{e} = \boldsymbol{y_i} - \boldsymbol{f_i}$$

Using residuals on the y axis, and independent variables on the x axis, gives a residual plot as shown in Fig 2-26. If the linear regression model is appropriate, the residual

would randomly fall in a horizontal band centred on 0, presenting a random pattern, as shown in Fig 2-26 (a). Otherwise, a non-linear model would be more appropriate. An example of an inverted U pattern is shown in Fig 2-26 (b), indicating a non-linear regression relationship.

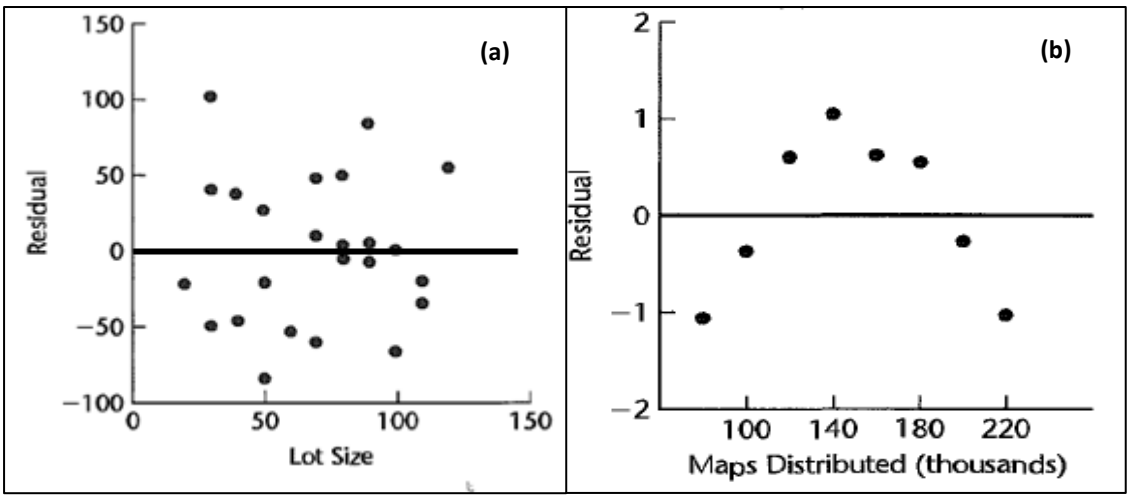

Fig 2-26, (a) a random pattern of residual plot, indicating an appropriate linear regression. (b) a inverted U pattern, suggesting a non-linear relationship [114].

2.12 Summary

It has been shown that double oxide film defects played a significant role in the failure of Al alloy castings. Double oxide film defects can accelerate the crack initiation process, and consequently reduce the reliability and reproducibility of castings. In addition, this defect can also become a nucleation site for Fe-rich phase and hydrogen porosity.

It was suggested that an extension of the holding time can deactivate double oxide film defects, since the entrained gas in the bifilms could be consumed by the surrounding melt. However, the Weibull modulus results of Al-alloy castings did not successfully demonstrate that the casting quality can be improved by an extension of the holding time. The deactivation of double oxide film defects may not widely occur in the Al-alloy castings, since nitrogen is very hard to be consumed by the Al-alloy melt, and hydrogen can diffuse into the entrained gas, expanding the double oxide film defects.

In contrast to Al-alloy castings, the behaviour of double oxide film defects formed in Mg-alloys is more complicated, due to the use of cover gases. The oxide film can have different structures, depending on the holding time and the use of cover gases. In addition, it was expected that the quality of Mg-alloy castings can be clearly improved due to the deactivation of double oxide film defects, since Mg-alloy melt can efficiently consume the entrained gas, especially for nitrogen (i.e. the “nitrogen burning”).

Therefore, the main issue, which was addressed in this research, was to determine the evolution of double oxide film defects in molten Mg-alloy, such as the reactions between an entrained gas and the surrounding Mg-alloy melt, the compositions of the oxide film and the residual trapped gas, methods to deactivate double oxide film defects, etc.. According to this evolution process, a technique was accordingly

proposed to reduce the negative effect of double oxide film defects and therefore increase on the quality of castings.

In addition, the traditional method (i.e. linear least square method) to evaluate the reproducibility of casting may not be necessarily reliable. A further investigation was carried out to propose a new estimation method.

3. Experimental procedure

3.1 Casting process

3.1.1 Mould design

Fig 3-1 shows the design and dimensions of the mould for the casting experiments reported in this section. In order to explore the effect of double oxide film defects, the casting was deliberately designed to introduce a large amount of double oxide films. Thus the top-filling system, which was expected to create more double oxide films than the bottom-filling system[96], was used for this mould. The running system contains the following three parts:

(1) *A pouring basin*. A round offset weir design was used to for achieve a good metal filling of the sprue of the metal flow, and a uniform inlet velocity field [117].

(2) *A tapered down-sprue and a runner bar*. The ratio between the entrance area and the exit area of the down-sprue was 1.25, making the flow velocity at the exit be higher than 0.48 m/s, which was the critical velocity for pure liquid Mg suggested by Campbell [22]. It was suggested that at a velocity lower than this critical value, the Mg melt surface film would not be broken, thus avoiding surface turbulence and the creation of double oxide film defects.

A flow simulation, using Flow-3D software, was carried out by Yang Yue (a PhD

student in the University of Birmingham) and has been shown in Fig 3-2. The black particles in the figure denote the predicted location of the double oxide film defects. From Fig 3-2 (a - b), it can be seen that a flow velocity of over 0.7 m/s occurred at the down-sprue exit, and larger than 1.5 m/s in the middle of the mould cavity. This high flow velocity would be expected to create more double oxide film defects as the critical velocity was exceeded. As shown in Fig 3-2 (c), a large amount of double oxide film defects were predicted to be contained in the final casting.

(3) *A 210 mm * 110 mm * 14 mm mould cavity with a 2mm thick cooling fin*. The cooling fin was designed to make the final casting gradually solidify from the bottom to the top [118], avoiding shrinkage porosity. A solidification simulation, using ProCAST software, was carried out by Dmytro Shevchenko (a PhD student in the University of Birmingham), as shown in Fig 3-3. It can be seen that no shrinkage pores were predicted to occur in the final casting.

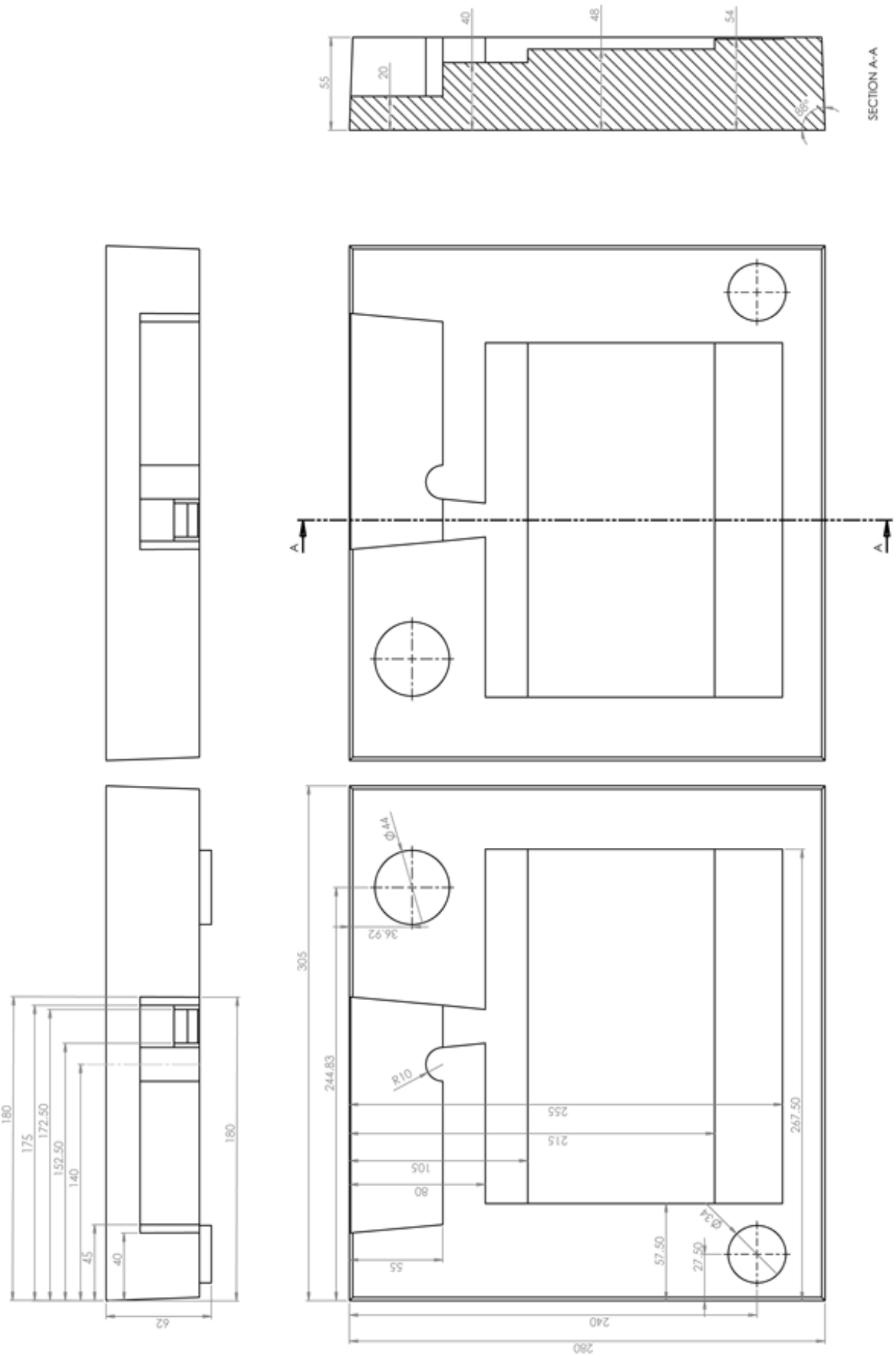

Fig 3-1, dimensions of the mould used for the casting process, unit: mm.

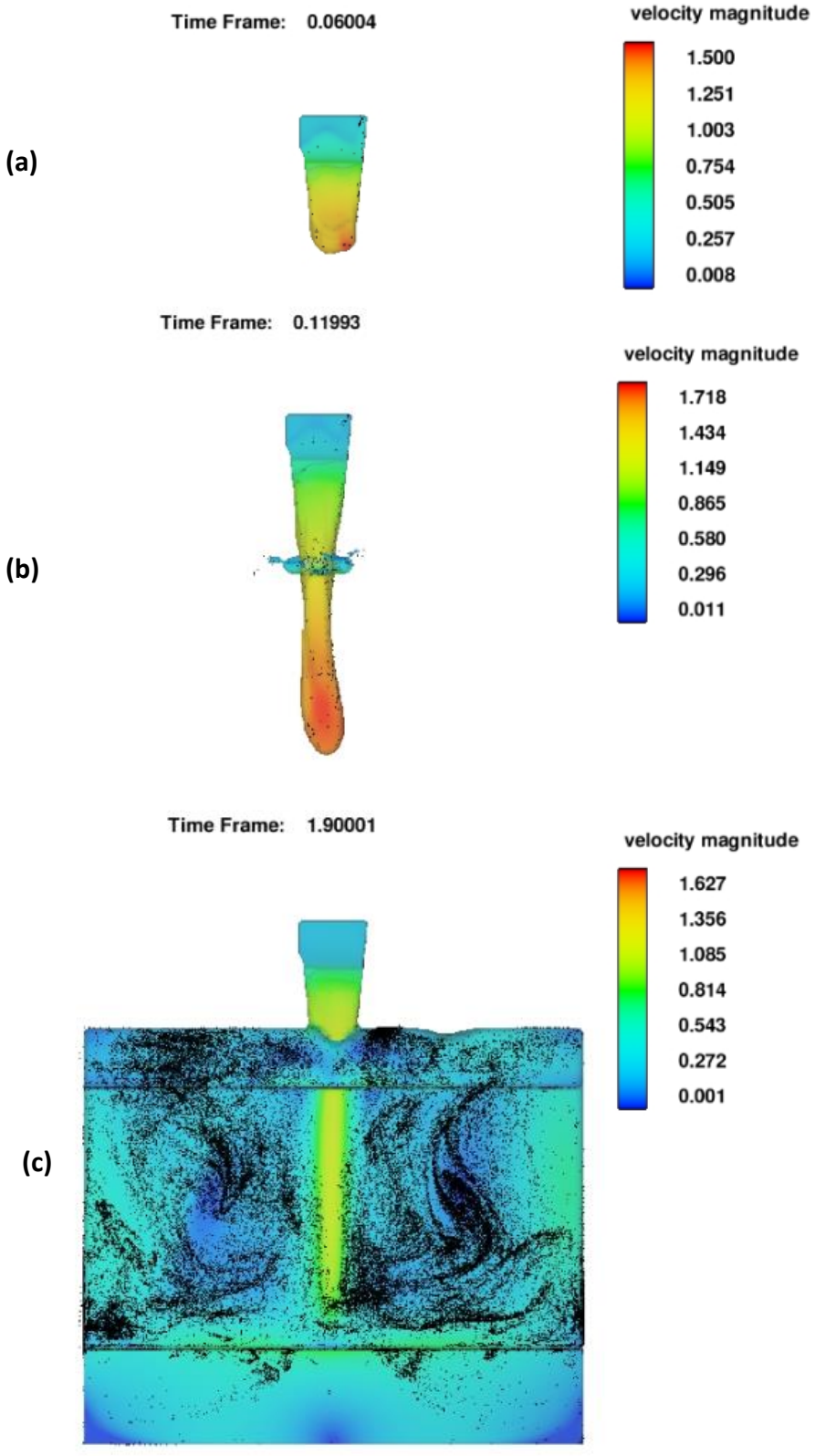

Fig 3-2, a melt flow simulation of the mould shown in Fig 3-1. The black particles denote the predicted location of the double oxide films defects.

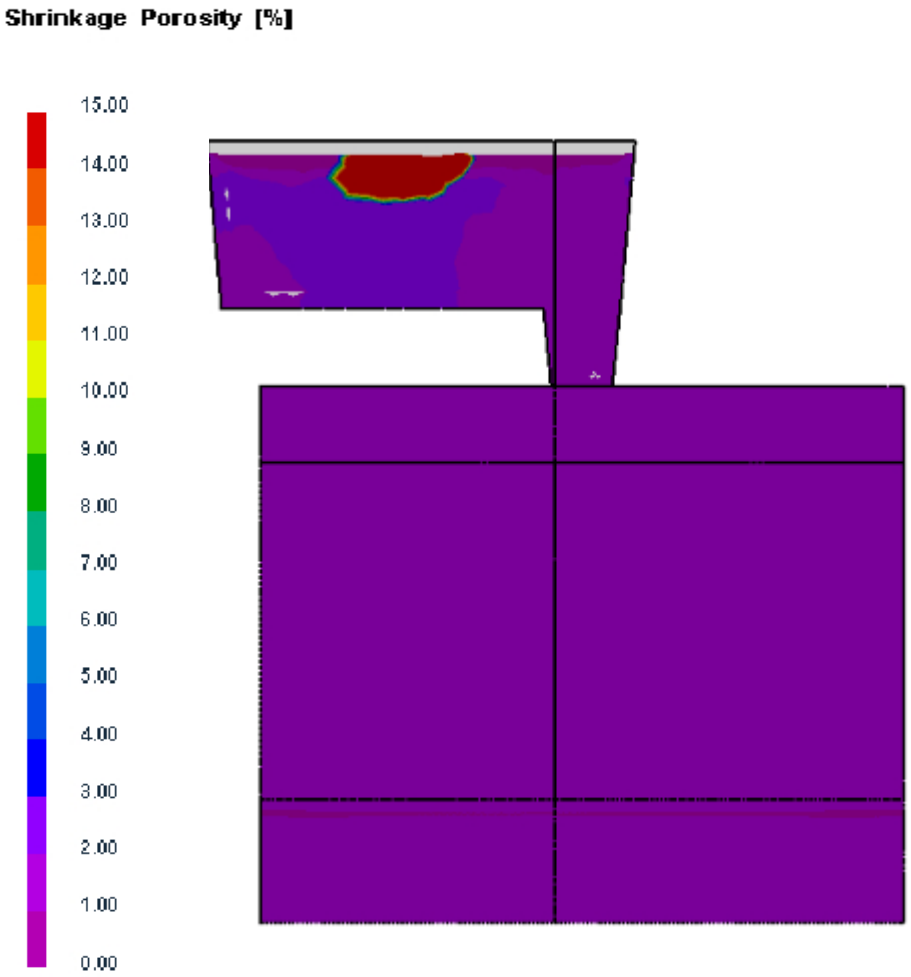

Fig 3-3, a solidification simulation of the designed mould shown in Fig 3-1.

3.1.2 Preparation of the sand mould

The sand moulds were made from resin-bonded silica sand, mixing with 1wt. % PEPSET 5230 resin and 1wt. % PEPSET 5112 catalyst. Due to the reaction between the Mg-alloy melt and the silica sand [119], the sand also contained 2 wt.% Na_2SiF_6 acting as an inhibitor, according to [120].

3.1.3 Facilities used in the casting process.

Fig 3-4 shows the facilities used for the casting and alloying process. The crucible was a mild steel cylindrical crucible of 16 cm diameter and 20 cm height. Prior to heating, it was cleaned by a shot-blaster, to remove any residual oxides and metal.

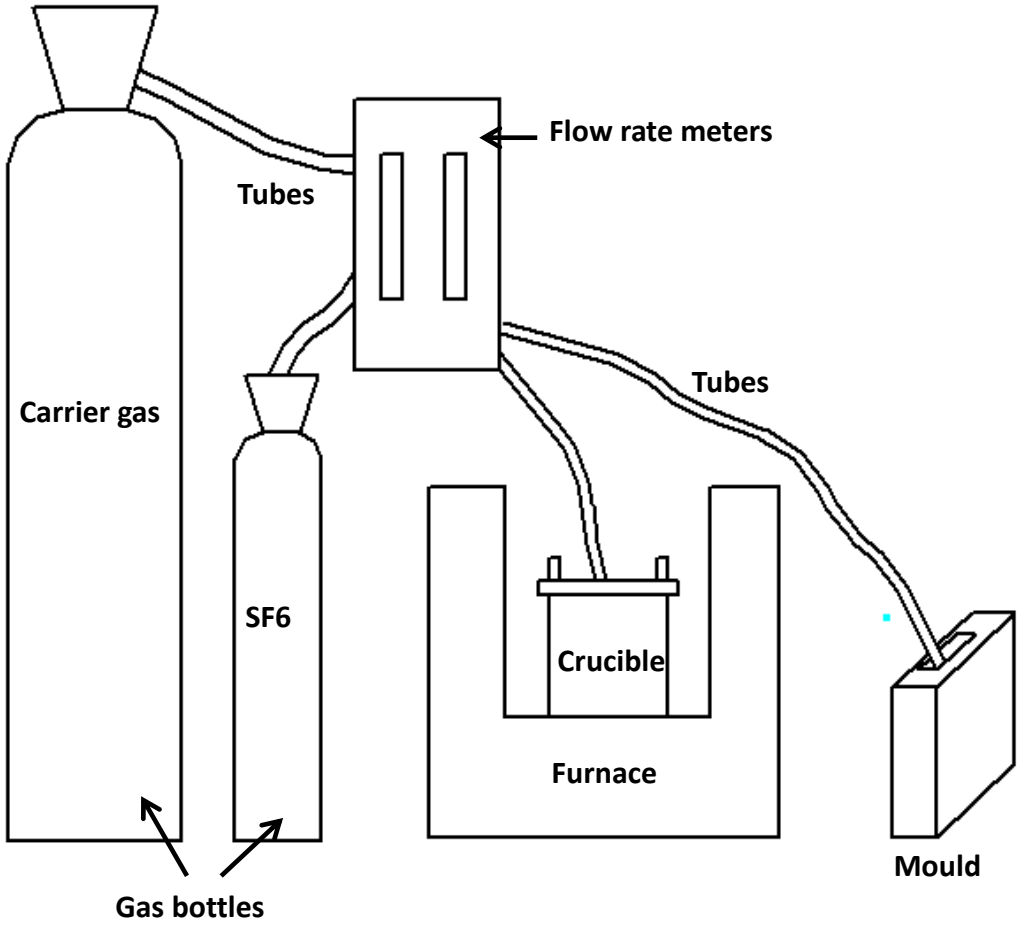

Fig 3-4, facilities of the casting and alloying process.

Since a Mg-alloy melt should be protected by a cover gas, the crucible was connected to a gas flow system. As can be seen from Fig 3-4, the carrier gas and the SF_6 gas were mixed in the tube, and their concentrations were controlled by the flowrate meter. The bottle pressure of both SF_6 and the carrier gas was 2 bar, and the total

flow rate of the mixed 0.5%SF_6/air, or 0.5%SF_6/CO_2, was 6 L/min.

For the casting process, half the amount of the protective gas (i.e. 3L/min) was introduced into the sand mould during the melting process, to displace the air in the mould cavity. However, for the alloying process, all of the gas was introduced into the crucible (i.e. 6L/min).

3.1.4 Preparation of Mg-alloys

Three Mg-alloys were used for the casting experiments, including a commercial purity Mg alloy, an AZ91 alloy (Mg-9%Al-1%Zn) alloy, and a binary Mg-Y alloy. The commercial purity Mg and AZ91 alloys were obtained from the Stone Foundry Ltd., following the British Standard of [121, 122], but the binary Mg-Y alloy was produced inhouse. The alloying process can be described in the following steps:

(1) 3 kg of commercial purity Mg alloy and 0.75 kg Mg-35%Y master alloy were placed in a mild steel crucible. Prior to heating, all of the oxide scale on the ingot surface was removed by cutting. The material was heated in a medium frequency induction furnace of 12 kW. The whole alloying process was carried out under a cover gas of 0.5%SF_6/air or 0.5SF_6/CO_2. The cover gas used depended on the intended use of the final alloy. For example, if the alloy was planned to be used for producing a casting protected by 0.5%SF_6/air, the corresponding alloying process was also protected by 0.5%SF_6/air.

(2) When the metal was completely melted, its temperature was kept at 700 ^{o}C ± 20 ^{o}C, and the liquid alloy was stirred by an air-driven stirrer for 5 min, at 60 r/min.

(3) Since most fluxes can react with rare-earth metals [120],a fluxless refining technique was applied based on [120, 123]. Argon was sparged through the melt at 0.3 L/min, for 15 min.

(4) The argon sparging process caused a sponge-like froth to form on the melt surface, which was skimmed off at the end of this process. After refining, the furnace was switched off, and the melt was solidified in the crucible. After solidification, a 10 mm thick disc was removed from the bottom and top, and a 5 mm cut was taken from around the rest of the surface of the solidified ingot. The remaining approximately 2 kg alloy ingot was used for the further experiments.

3.1.4 The Casting process

A Mg-alloy ingot with the oxide surface removed, was melted in a medium frequency induction furnace of 12 kW, under a cover gas of 0.5%SF_6/carrier gas. During this process, as previously stated, the cover gas was also led into the sand mould.

When the molten Mg-alloy was heated to 730^{o}C, the melt was poured into the sand mould. The temperature in the pouring basin was 700 ^{o}C ± 20 ^{o}C. After the pouring

process, the protective gas was still fed onto the melt surface, to inhibite the ignition of the Mg-alloy. Six castings were produced, using the three different Mg-alloys (commercial pure Mg, AZ91, Mg-Y) under the two cover gases (0.5%SF_6/air, 0.5%SF6/CO_2), respectively.

3.1.5 Mechanical property test

Each cast plate, produced from the mould shown in Fig 3-1, was machined into 40 test bars. The dimensions of the test bar were designed based on BS EN ISO 6892-1 [124], as shown in Fig 3-5, where L_0 is the original gauge length, Lc is the parallel length, and Lt is the total length of the test bar. Their tensile strength was determined using on a Zwick 1484 tensile test machine with a clip extensometer. The test speed of the cross head was 1mm/min.

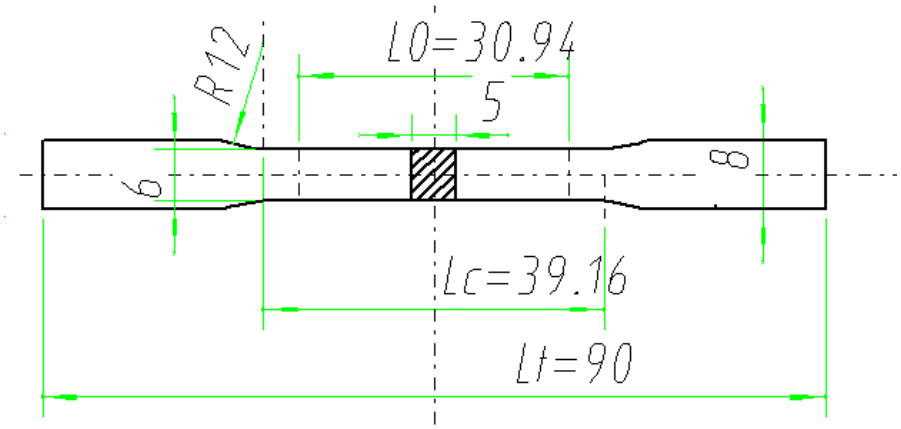

Fig 3-5, dimensions of test bar, used for the tensile strength test (unit mm).

The ultimate tensile strength (UTS) and %Elongation of the test bars was recorded for a Weibull analysis. The fracture surfaces of the broken test bars were inspected using Scanning Electron Microscopy (SEM). During this inspection, Energy Dispersive X-ray

Spectroscopy (EDS) was carried out, using a Philips JEOL6060 SEM, and a Philips JEOL7000 SEM with Oxford INCA.

3.2 Cross sectional observation of double oxide film defects.

3.2.1 Sampling double oxide film defects from ingots.

This cross sectional observation experiment was carried out to analyse the structure of a folded double oxide film defect. Most steps of this experiment is the same with alloying process referred to in section 3.1.4, except the last step in skimming off the sponge-like froth. This froth on the liquid metal surface was not removed, since many double oxide film defects may be contained in it for study.

After solidification, 10 ~ 20 mm thick disc cut from the top and bottom of the final cylindrical ingot was sectioned into small pieces, and polished for an SEM observation. Double oxide film defects and bubble trails could be found on the polished surface.

3.2.2 Focused ion beam milling (FIB)

Focused ion beam milling was another technique used to obtain a cross-section of double oxide films defects. Fig 3-6 (a) shows the surface of a double oxide film on the fracture surface of a broken test bar. The area required to be analysed was coated

with platinum layer. Then, as shown in Fig 3-6 (b), a gallium ion beam, accelerated to 30 kV, milled the material substrate surrounding the platinum coated area, to expose the cross section of the oxide film. EDS analysis of the oxide film's cross section was carried out using Transmission Electron Microscopy (TEM) with a FEI Tecnai F20 TEM. The whole FIB process and TEM observation was carried out by Dr. KeeHyun Kim (in the University of Birmingham).

Observation of the double oxide film defects formed in an AZ91 casting protected by 0.5%SF_6/CO_2 was obtained by this technique. For the samples of the other alloys and cover gas (i.e. AZ91 protected by 0.5%SF_6/air, Mg and Mg-Y alloy samples), the cross sectional observations were achieved via the technique referred to in section 3.2.1.

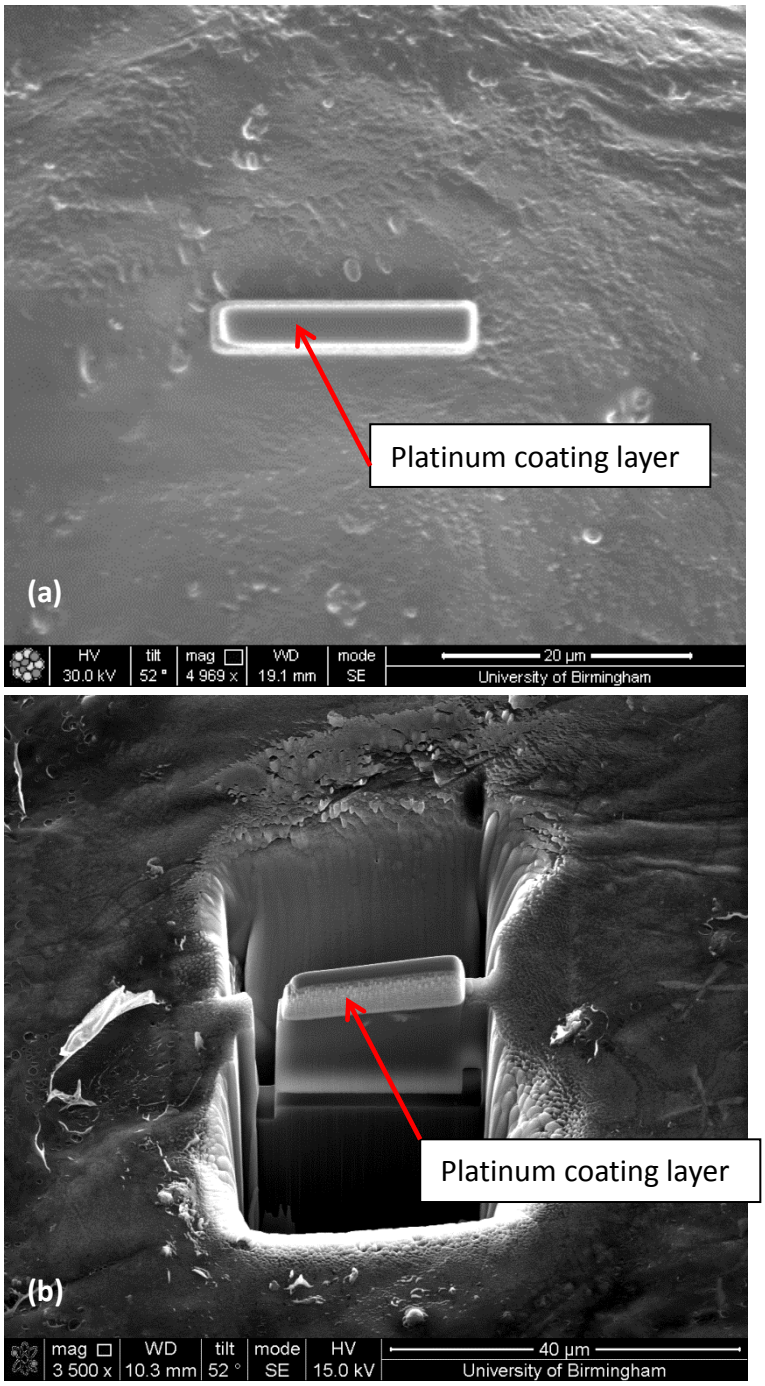

Fig 3-6, an example of the FIB process. (a) a surface of a double oxide film defect coated by a platinum layer, (b) ion beam milled the substrate surrounding the coated area.

3.3 Investigation of the growth of oxide films

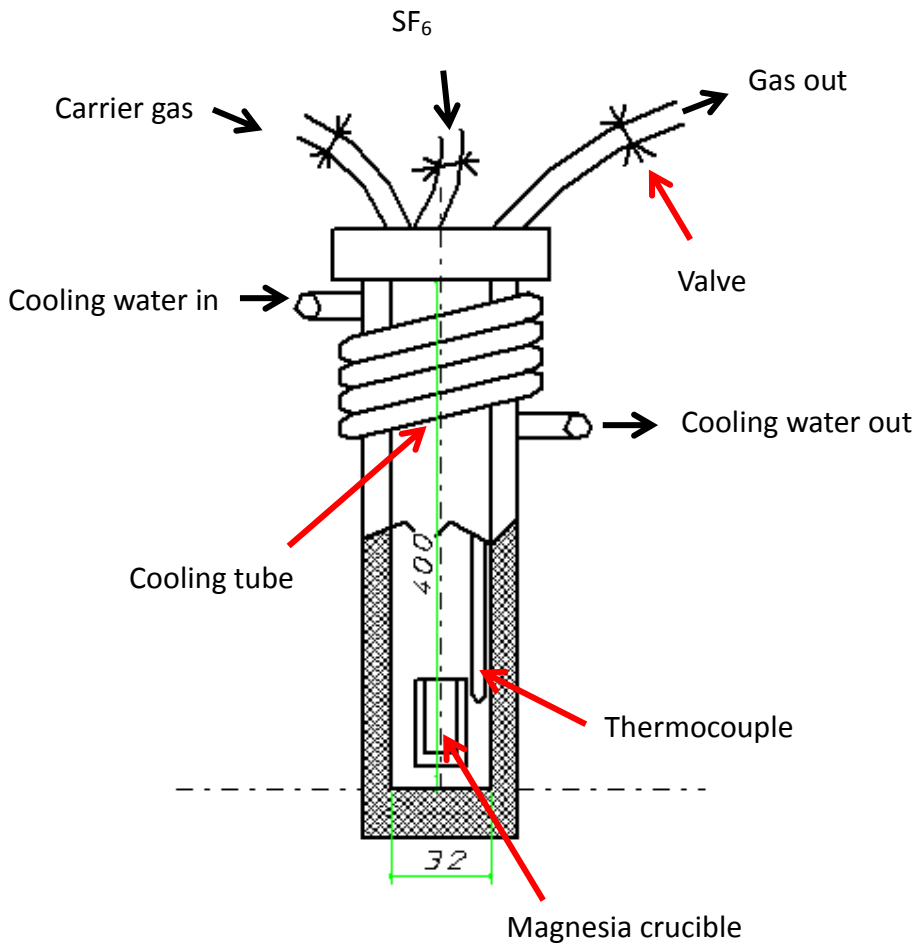

Fig 3-7, oxidation cell used for study the growth of oxide films on a Mg alloy melt (unit mm).

Fig 3-7 shows a sketch of an oxidation cell, used for studying the growth of oxide films on a Mg alloy melt under different cover gases (i.e. 0.5%SF_6/air, 0.5%SF_6/CO_2). A closed-end mild steel tube was used which had an inner length of 400 mm, and an inner diameter of 32 mm. A water-cooled tube was wrapped around the upper half of the cell. When the cell was heated, this cooling system created a temperature difference between the upper and bottom parts, making the interior gas to convect

in the cell. The temperature was controlled by a thermocouple inserted at the bottom of the cell.

During the experiment process, a cylinder of the Mg-alloy, of 15mm diameter and 15 mm height, was placed in a magnesia crucible which was subsequently placed at the bottom of the cell, as shown in Fig 3-7. Then, the whole cell was heated to 100 ^{o}C in an electric resistance furnace under a total gas flow rate of 1L/min. The cell was held at this temperature for 20 min, to remove the air originally contained within it.

After the degassing process, the oxidation cell was further heated to 700 ^{o}C. Once the temperature reached 700 ^{o}C, the valves of the gas inlet and exit were closed, creating a sealed environment for oxidation to tale place, which limited the amount of SF_6 in the cell. Then, the cell was held at 700 ^{o}C ± 10 ^{o}C for 5 min to 30 min. At the end of this holding process, the whole cell was lifted from the furnace and quenched in cooling water. After cooling to room temperature, the oxidised sample was sectioned, and subsequently polished for an SEM observation.

3.4 Pore gas analyser

This experiment is to analyse the components of the trapped residual gas in pore defects. As shown in Fig 3-8, a sample containing a pore was firstly place in the fracture vessel. Then the pumps are operated to evacuate the fracture vessel to a pressure of about 10^{-6} mbar. After that, a needle is driven through the surface layer

above the pore, releasing the inner trapped gas. The left pump (i.e. Pump P1) is subsequently operated, making the released gas pass through the spectrometer. Thus the components of the gas can be detected.

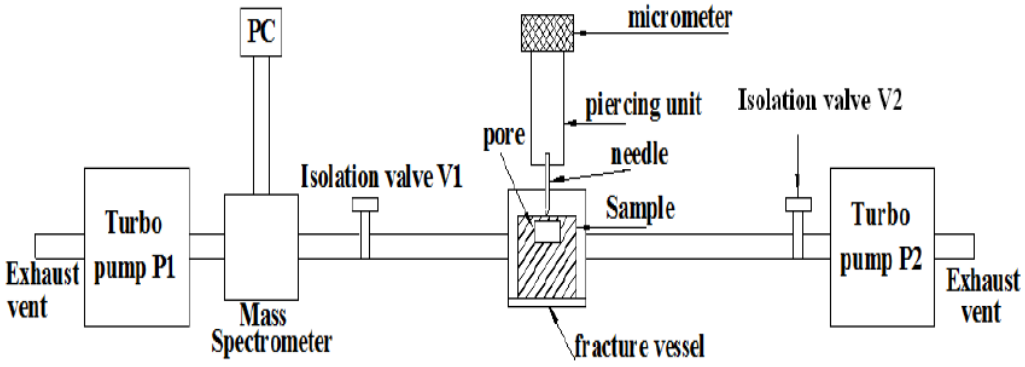

Fig 3-8 Structure of the Pore Gas Analyser [125].

4. Results

4.1 Double oxide film defects on the fracture surfaces of Mg-alloy castings.

Observation of the fracture surfaces of the Mg-alloy tensile test bars showed symmetrical black or brown areas occurring on many of them. Examples and SEM images of these fracture surfaces, formed in different Mg-alloys and protective gases will be shown in this section.

4.1.1 Commercial purity Mg in SF_6/air.

Fig 4-1 shows an example of a fracture surface of a commercial purity Mg tensile test bar, cast in an atmosphere of 0.5%SF_6/air. Two symmetrical black regions were seen on the bright fracture surfaces.

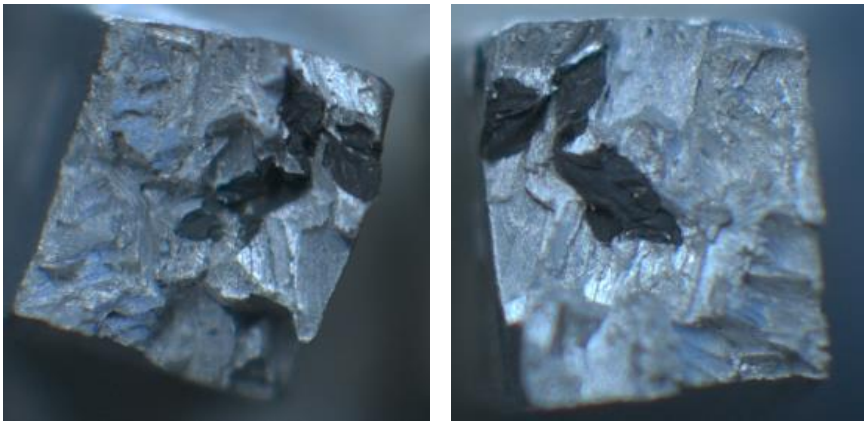

Fig 4-1, Fracture surface of a tensile test bar, machined from a commercial purity Mg casting protected by 0.5%SF_6/air. The symmetrical black regions were double oxide film defects. The dimensions of the fracture surface are 5mm * 6mm.

Fig 4-2 shows a section of the boundary between the black and bright areas shown in Fig 4-1. It can be seen that the bright region was relatively rough and full of ridges and lines; the black region was comparatively smooth, and of a creased nature. EDS analysis results (Fig 4-3 and Table 4-1) corresponding to both the regions indicated that fluorine was only detected in the black area. In addition, according to Table 4-1, the oxygen content of the black region was significantly higher than that of the bright area, revealing that most oxygen in the black area was originally contained in the material, rather than produced by oxidation after the tensile test. Thus it can be concluded that the black region was a part of the protective surface film, entrained into the melt during the casting process.

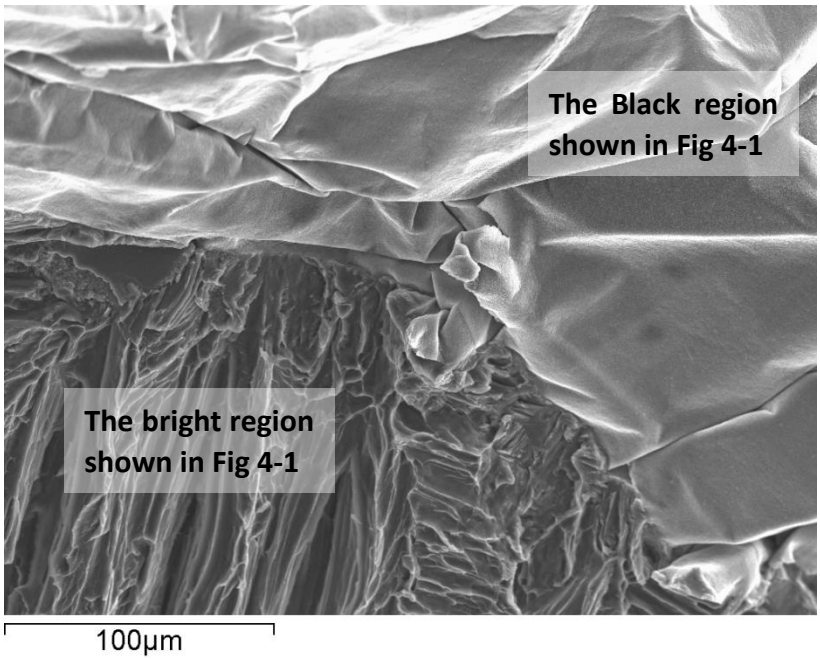

Fig 4-2 The boundary between the black and bright regions shown in Fig 4-1.

In addition, the structure of the films (i.e. the pair of symmetrical oxide films on each side of the fracture surfaces) was consistent with the description of double oxide film

defects from [22, 23] , indicating that the black area shown in Fig 4-1 was a double oxide film defect.

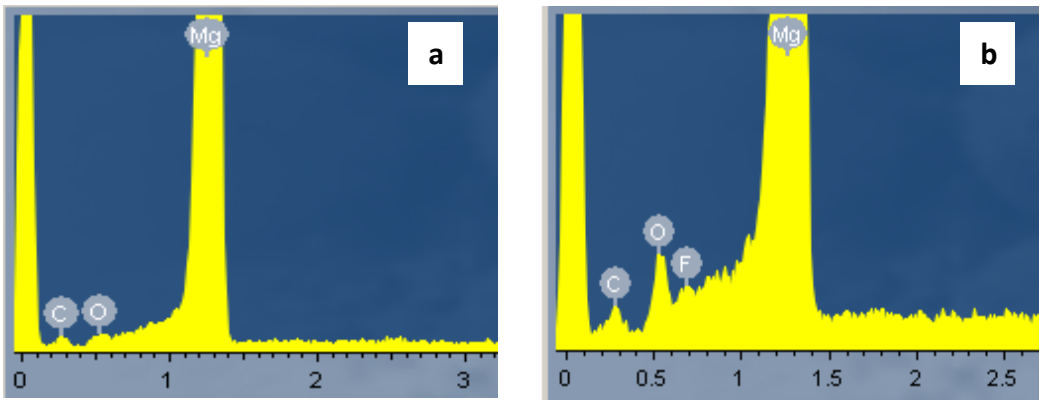

Fig 4-3, spectrum of SEM scanning of both bright and black areas shown in Fig 4-2, (a) the bright region, (b) the black region.

	C	O	Mg	F	S
Black area (weight %)	3.43	2.22	94.02	0.33	-
Bright area (weight %)	3.72	0.53	95.74	-	-

Table 4-1 Element contents of the EDS results corresponding to the regions shown in Fig 4-2.

A closer observation (Fig 4-4(a)) of the black region revealed some dark areas on the film surface. Further examination, shown in Fig 4-4(b ~ d), indicated that the film surface consisted of white granules, and the dark areas consisted of relatively larger granules (Fig 4-4(c)) compared with the surrounding area (Fig 4-4(d)). The corresponding EDS spectra (Table 4-2) indicated that a clear difference between the carbon content in the two areas. Thus the dark areas may have a higher content of

Mg carbides.

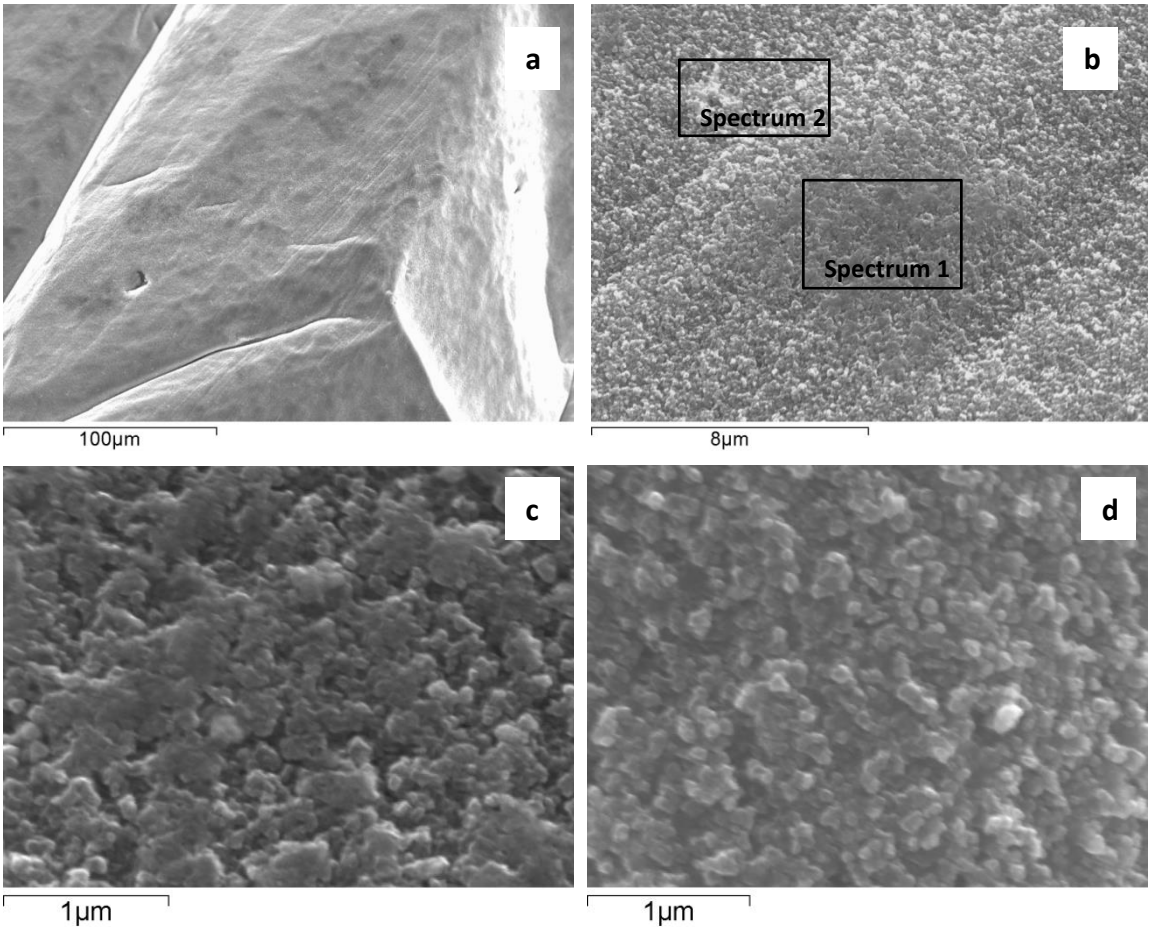

Fig 4-4 (a) A closer observation of the surface of the double oxide films shown in Fig 4-1, (b) A closer observation of the dark areas shown in (a). (c) a closer observation of the spectrum 1 area shown in (b) ; (d) a closer observation of the spectrum 2 area shown in (b).

	C	O	Mg	F	S
Spectrum 1 (Weight%)	3.62	3.85	92.17	0.36	-
Spectrum 2 (Weight%)	0.97	3.24	95.23	0.56	-

Table 4-2, element contents of the EDS results corresponding to the spectrum regions shown in Fig 4-4(b).

4.1.2 Commercial purity Mg in SF_6/CO_2.

Fig 4-5 exhibits an example of the fracture surfaces of commercial purity Mg casting produced under a cover gas of 0.5%SF_6/CO_2. As with the Mg casting protected by 0.5%SF_6/air shown in Fig 4-1, two symmetrical brown areas were also found on the bright fracture surfaces.

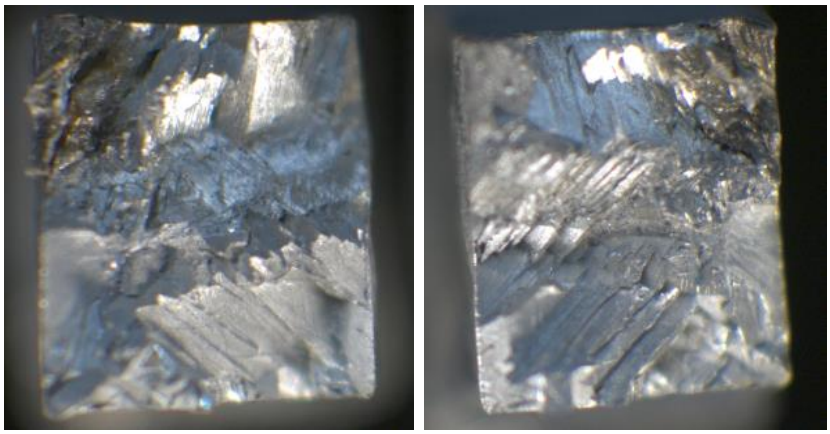

Fig 4-5 Fracture surface of a commercial pure Mg tensile test bar produced under a cover gas of 0.5%SF_6/CO_2. The symmetrical brown regions were double oxide film defects. The dimensions of the fracture surface are 5 mm × 6 mm.

The SEM image of the boundary between the bright and brown areas (Fig 4-6(a)) presented a similar appearance to the area shown in Fig 4-2: the bright area was full of ridges and lines; the brown region also presented a wrinkled film-like nature.

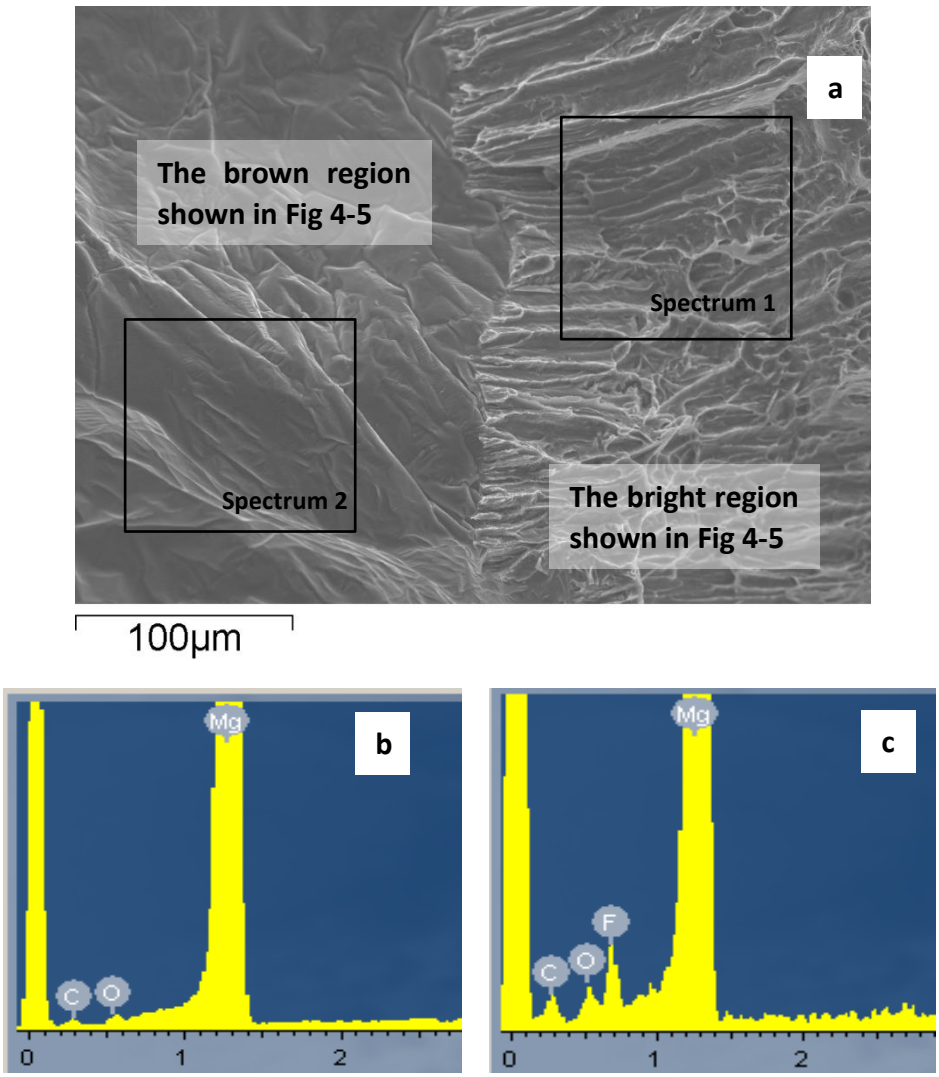

Fig 4-6 (a) the boundary between the bright and brown region shown in Fig 4-5; (b ~ c) the EDS spectrum corresponding to the spectrum regions shown in (a): (b) spectrum 1; (c) spectrum 2.

The corresponding EDS analysis (Fig 4-6(b - c), Table 4-3) revealed that fluorine only occurred in the brown area, and the bright region contained comparatively less

oxygen, suggesting that the brown regions shown in Fig 4-5 were a double oxide film defect and the composition of the oxide films were MgO and MgF_2. However, this oxide film had a higher content of fluorine in contrast to the black oxide film defect shown in Fig 4-1, and Table 4-2.

	C	O	Mg	F	S
Spectrum 1 (Weight%)	2.93	0.53	96.54	-	-
Spectrum 2 (Weight%)	6.06	1.17	90.31	2.46	-

Table 4-3 Element contents of the EDS results corresponding to the spectrum regions shown in Fig 4-6 (a).

An SEM image at higher magnification (Fig 4-7(a)) showed that the oxide film formed in 0.5%SF_6/CO_2 had a smoother surface, compared with the film formed in 0.5%SF_6/air shown in Fig 4-4. In addition, according to a further observation (Fig 4-7 (b)), this oxide film surface was more compact and composed of smaller granules. Dark spots were seen on the film surface (Fig 4-7(b)). The corresponding element map (Fig 4-7 (c ~ e)) indicated that the spots were concentrations of MgF_2.

This smooth surface appearance and the relative higher fluorine content of the oxide film, in contrast to the film formed in 0.5%SF_6/air shown in Fig 4-4, indicated a greater protectability of SF_6/CO_2 than SF_6/air.

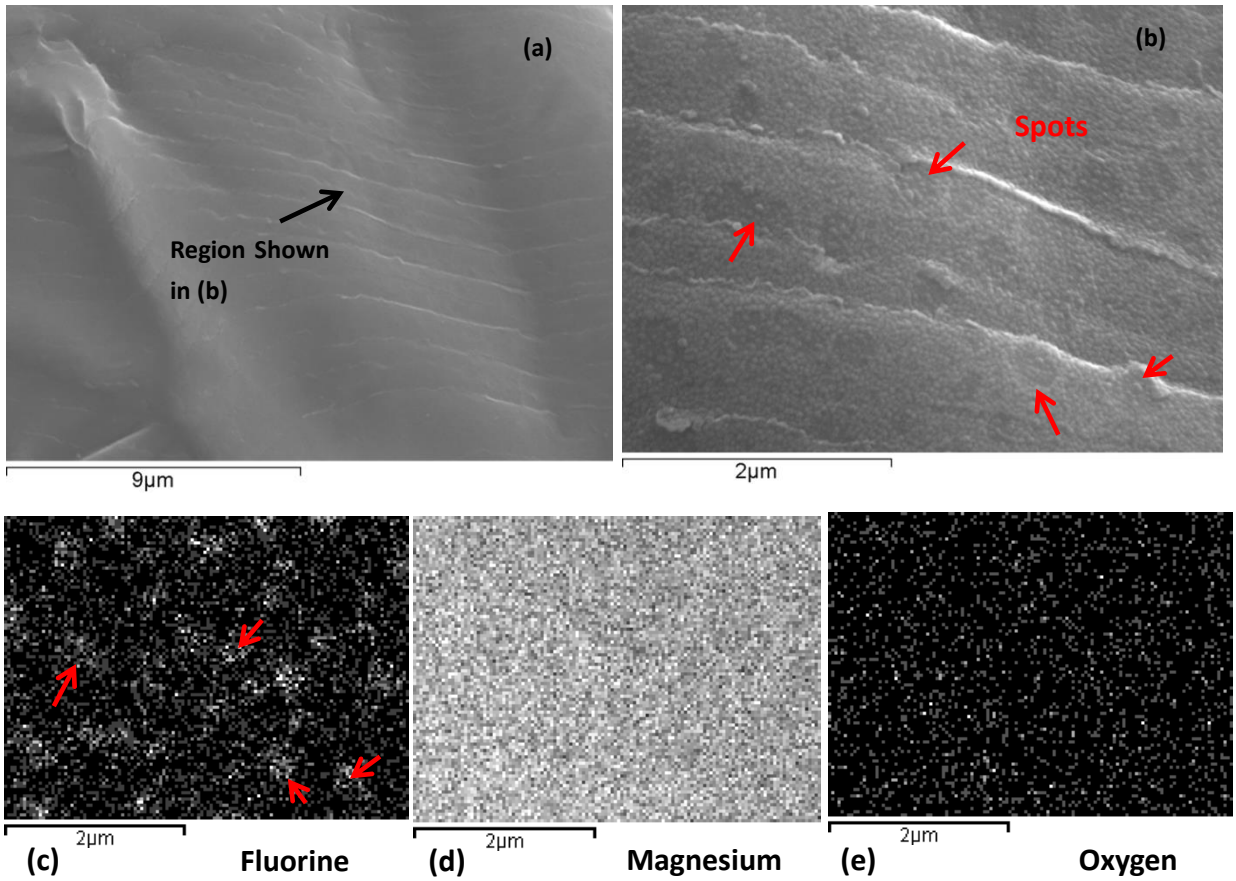

Fig 4-7 (a) an observation of the oxide film, shown in Fig 4-6, at a higher magnification; (b) an closer image corresponding to area denoted in (a); (c) ~(e), element map corresponding to (b), (c) Fluorine, (d) magnesium, (e) oxygen. The red arrows denote the spots shown in (b).

4.1.3 AZ91 in SF_6/air

Fig 4-8 shows a pair of symmetrical oxide films on the fracture surfaces of an AZ91 tensile test bar cast in 0.5%SF_6/air. Fig 4-9 shows a section of the boundary between the oxide films and the surrounding bright region. As it can be seen, the bright region consisted of jagged and broken features, while the surface of the oxide film was relatively smooth and flat. Wrinkles were observed on the film surface, but they

were much less creased, compared with the oxide films formed in commercial purity Mg (Fig 4-2).

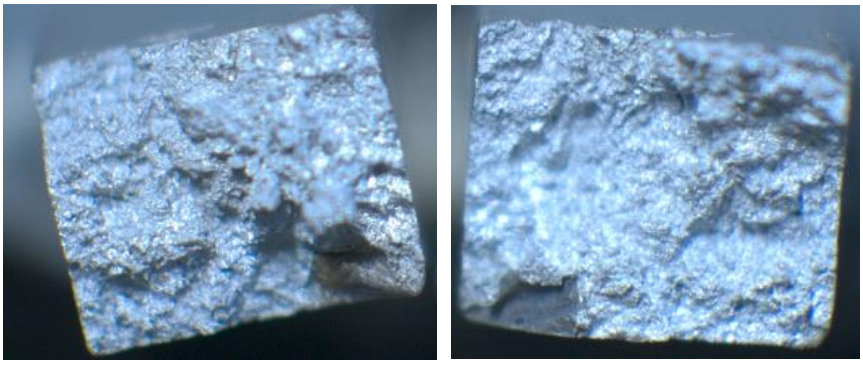

Fig 4-8 Double oxide film defects on the fracture surface of an AZ91 tensile test bar produced under a cover gas of 0.5%SF_6/air. The dimension of the fracture surface is 5 mm × 6 mm.

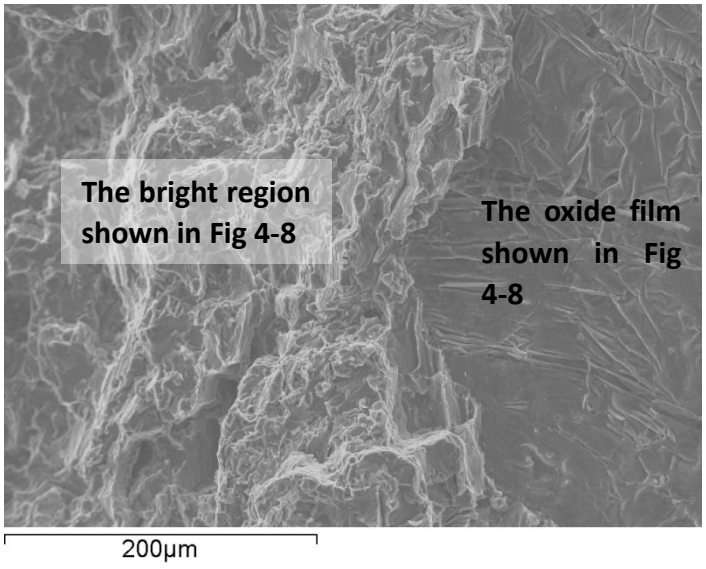

Fig 4-9, a section of the boundary between the brown and bright regions shown in Fig 4-8.

Fig 4-10 and Table 4-4 shows the element contents of the bright and oxide-film regions. Fluorine was only detected in the oxide film, and the oxygen content in the film was higher than the bright area. Al and Zn were found in both regions, but not

with a significant difference. Thus it could not be distinguished whether the determination of Al and Zn came from the alloy matrix under the oxide film or from the film itsself.

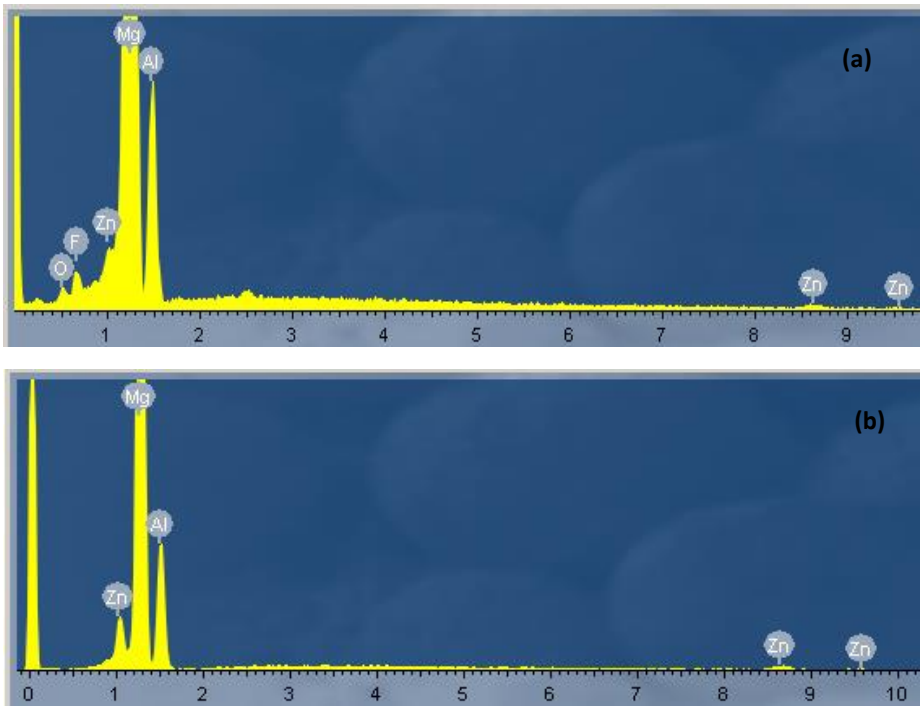

Fig 4-10 Spectrum corresponding to the different regions shown in Fig 4-9, (a) oxide-film region, (b) Bright region.

	C	O	Mg	F	Al	Zn	S
Oxide film (Weight%)	2.65	1.51	83.12	0.63	11.45	0.64	-
Bright region (Weight%)	0.71	-	91.53	-	8.86	1.36	-

Table 4-4 Element contents of the EDS results corresponding to bright and brown regions shown in Fig 4-9.

Fig 4-11(a) shows a further image of the oxide film, indicating “spots” distributed on

the film surface. A closer SEM image Fig 4-11(b) subsequently showed that the "spots" were holes or depressions.

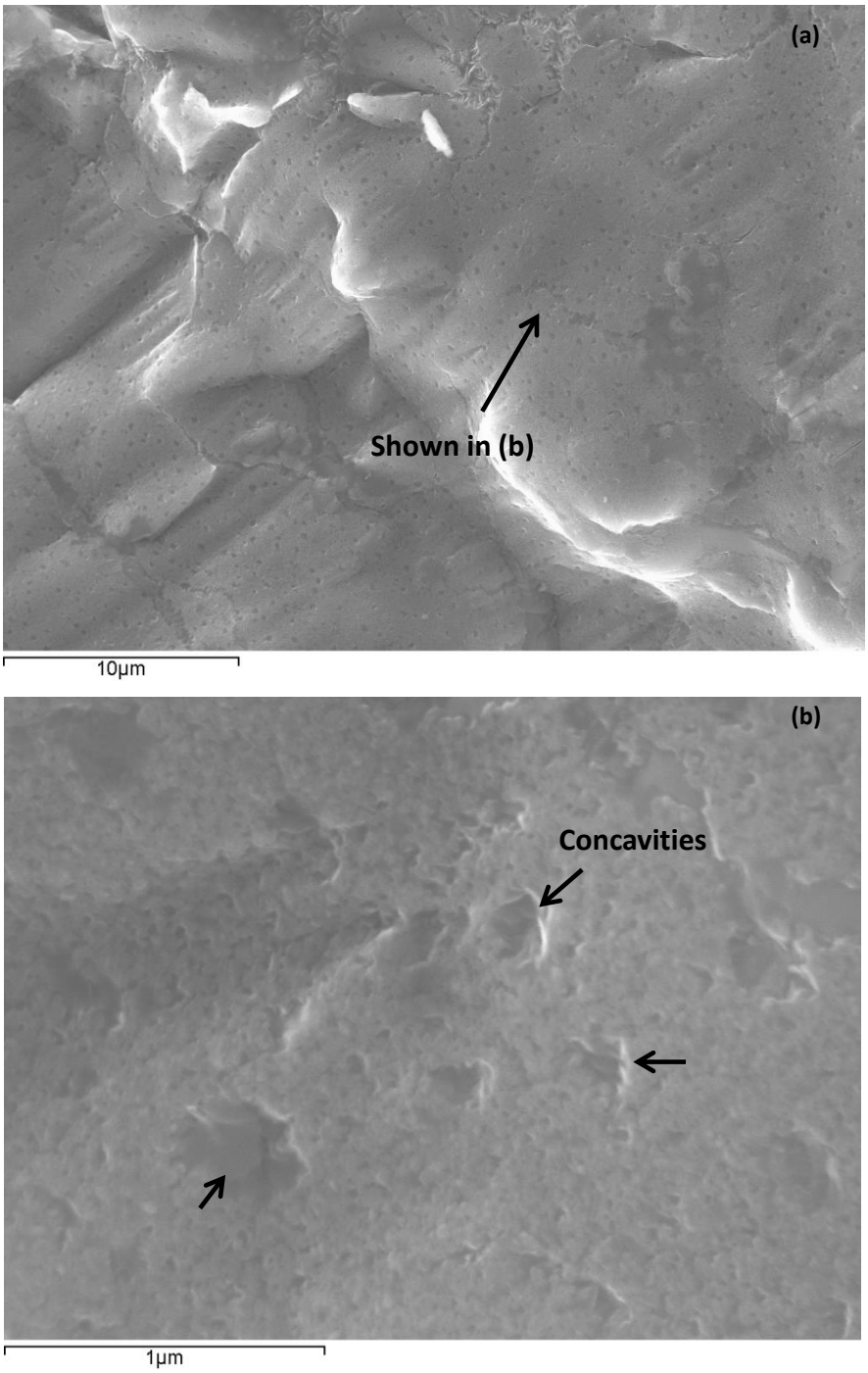

Fig 4-11 (a) an observation of the oxide film shown in Fig 4-9, indicating "spots" on the film surface; (b) A closer observation revealed that the "spots" was actually holes or depressions.

4.1.4 AZ91 in SF_6/CO_2

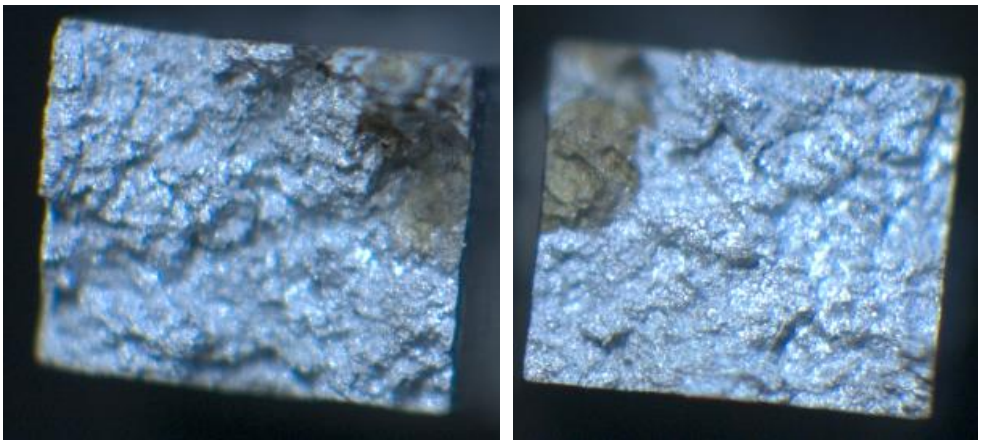

Fig 4-12 Double oxide film defect on the fracture surface of an AZ91 tensile test bar produced under a cover gas of 0.5%SF_6/CO_2. The dimensions of the fracture surface are 5 mm × 6 mm.

Fig 4-12 shows fracture surfaces of an AZ91 tensile test bar, cast in an atmosphere of 0.5%SF_6/CO_2. A pair of symmetrical brown regions, indicating a double oxide film defect, could be seen by the naked eye. Fig 4-13 shows a section of the boundary between the brown and bright areas shown in Fig 4-12, revealing the wrinkled nature of the oxide films surface. EDS examination of both regions (Fig 4-14,Table 4-5) showed a similar result, compared with the previous oxide films, where the oxide films contained more oxygen than the surrounding area, and fluorine only occured in the films.

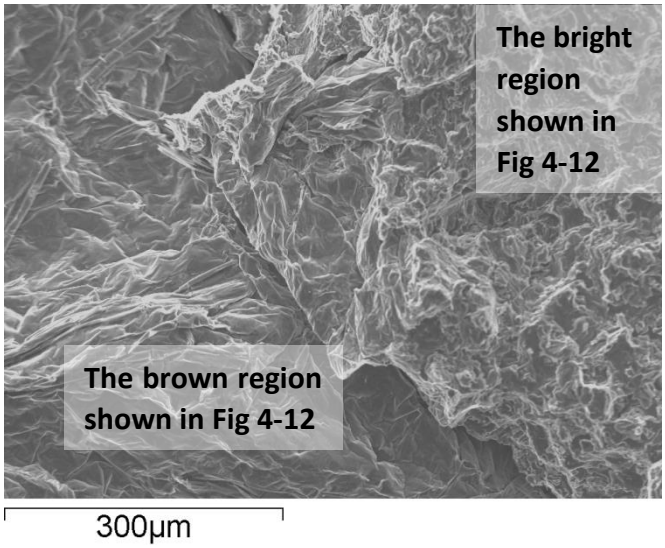

Fig 4-13 a section of the boundary between the brown and bright areas shown in Fig 4-12.

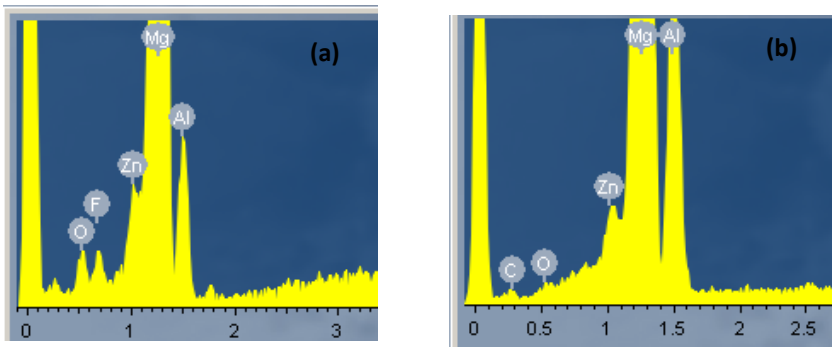

Fig 4-14 EDS spectrum corresponding to the (a) brown area, (b) bright area, shown in Fig 4-13.

	C	O	Mg	F	Al	Zn	S
Brown region (Weight%)	1.85	1.44	90.80	0.95	4.00	0.96	-
Bright region (Weight%)	2.10	0.44	82.83	-	13.26	1.36	-

Table 4-5 Element contents of the EDS results corresponding to bright and black regions shown in Fig 4-13.

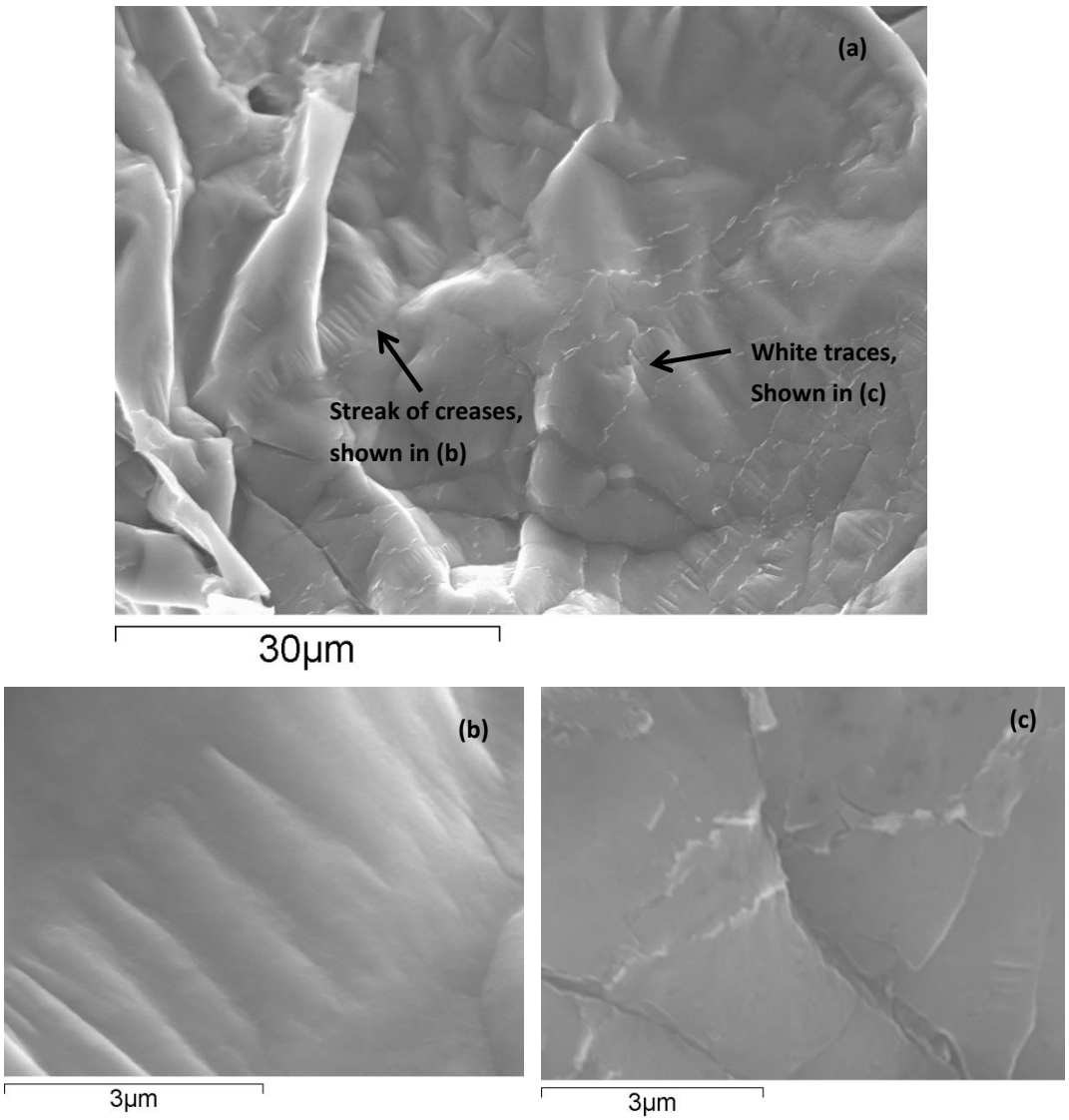

Fig 4-15 (a) a closer observation of the oxide film shown in in Fig 4-13., (b) the creased streak corresponding to (a), presenting a compact smooth surface; (c) corresponding to the white traces shown in (a), indicating cracks on the film surface.

A closer observation of the oxide films (Fig 4-15(a)) showed a more compact film surface in contrast to the oxide films formed in the AZ91 casting protected by 0.5%SF_6/air. This revealed white traces and a streak of creases on the film surface. Fig 4-15 (b) shows the film around the streak, showing a compact and smooth surface, but the white traces (Fig 4-15 (c)) indicated edges of cracked flakes elsewhere in the

film.

4.1.5 Mg-Y alloy in SF_6/Air.

Fig 4-16 shows a pair of fracture surfaces of a tensile test bar cut from a Mg-Y casting cast in 0.5%SF_6/air. A black wedge-like feature was seen on the bright fracture surfaces.

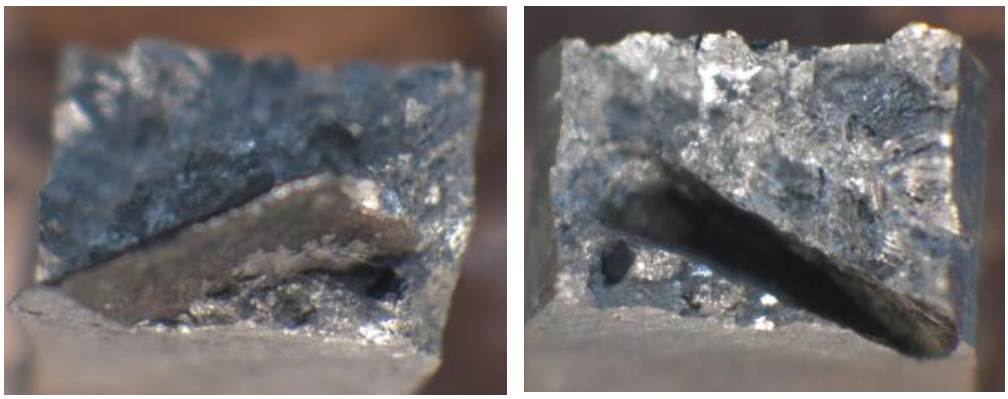

Fig 4-16 Fracture surface of a Mg-Y tensile test bar produced under a cover gas of 0.5%SF_6/air. The dimensions of the fracture surface are 5 mm × 6 mm.

The SEM images (Fig 4-17 (a - b)) revealed a highly wrinkled nature of the surface of the black region. The corresponding EDS spectrum (Fig 4-17 (c-d), Table 4-6) showed that fluorine and sulphur existed in the black region only, and its oxygen content was much higher than the bright regions, indicating that the black region of the wedge-like feature was the oxide surface of a double oxide film defect.

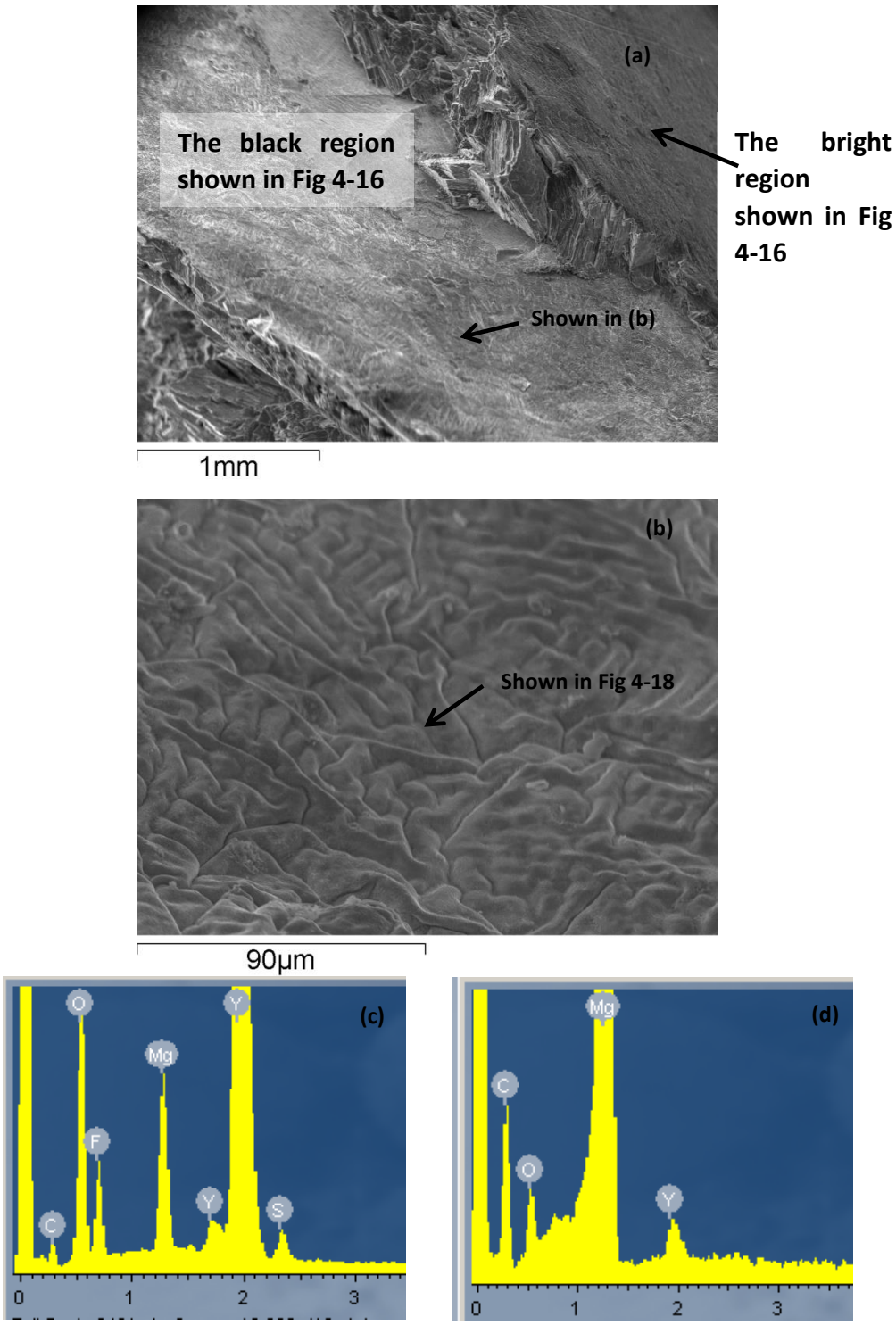

Fig 4-17 (a) a SEM image of the wedge-like feature shown in Fig 4-16, (b) a closer observation of the corresponding area pointed out in (a); (c~ d) the EDS spectrum corresponding to the black and bright regions respectively.

In addition, the Y content of the oxide film was 51.78%, while the Mg content was only 4.4%. In conjunction with the Mg and Y contents of the bright area, it can be suggested that the oxide films were mainly composed of yttrium fluorides and oxides, rather than magnesium compounds.

	C	O	Mg	F	Y	S
Black region (Weight%)	5.81	25.70	4.40	11.15	51.78	1.16
Bright region (Weight%)	5.17	1.22	89.59	-	4.02	-

Table 4-6 Element contents of the EDS results corresponding to bright and black regions shown in Fig 4-17(a)

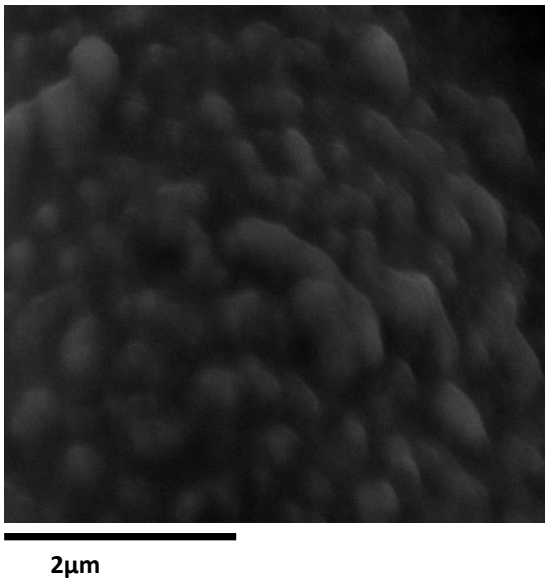

Fig 4-18, a closer observation of the area pointed out in Fig 4-17 (b)

Fig 4-18 shows a closer observation of the area pointed out in Fig 4-17(b), revealing that the oxide film surface consisted of white granules.

4.1.6 Mg-Y alloy in SF_6/CO_2.

Fig 4-19 shows the fracture surfaces of an Mg-Y casting formed in 0.5%SF_6/CO_2, indicating a double oxide film defect.

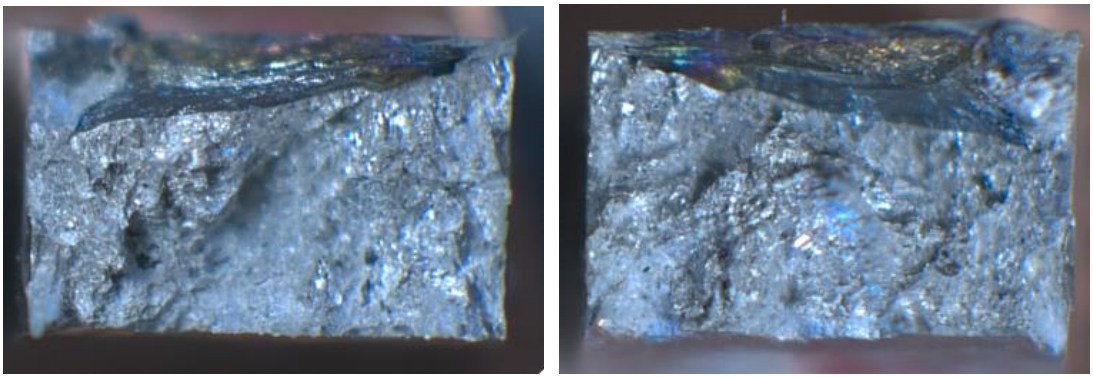

Fig 4-19 Double oxide film defects on the fracture surface of an Mg-Y tensile test bar produced under a cover gas of 0.5%SF_6/CO_2. The size of the test bar is 5 mm × 8 mm.

Fig 4-20(a) shows a section of the boundary between the oxide film and the bright region. Some traces could be found on the oxide film surface. According to the corresponding EDS results (Fig 4-20 (b-c), Table 4-7), fluorine was detected in the oxide film only, while the oxygen content of the bright area was relatively lower (0.71wt% in the bright area, 18.15wt% in the oxide film).

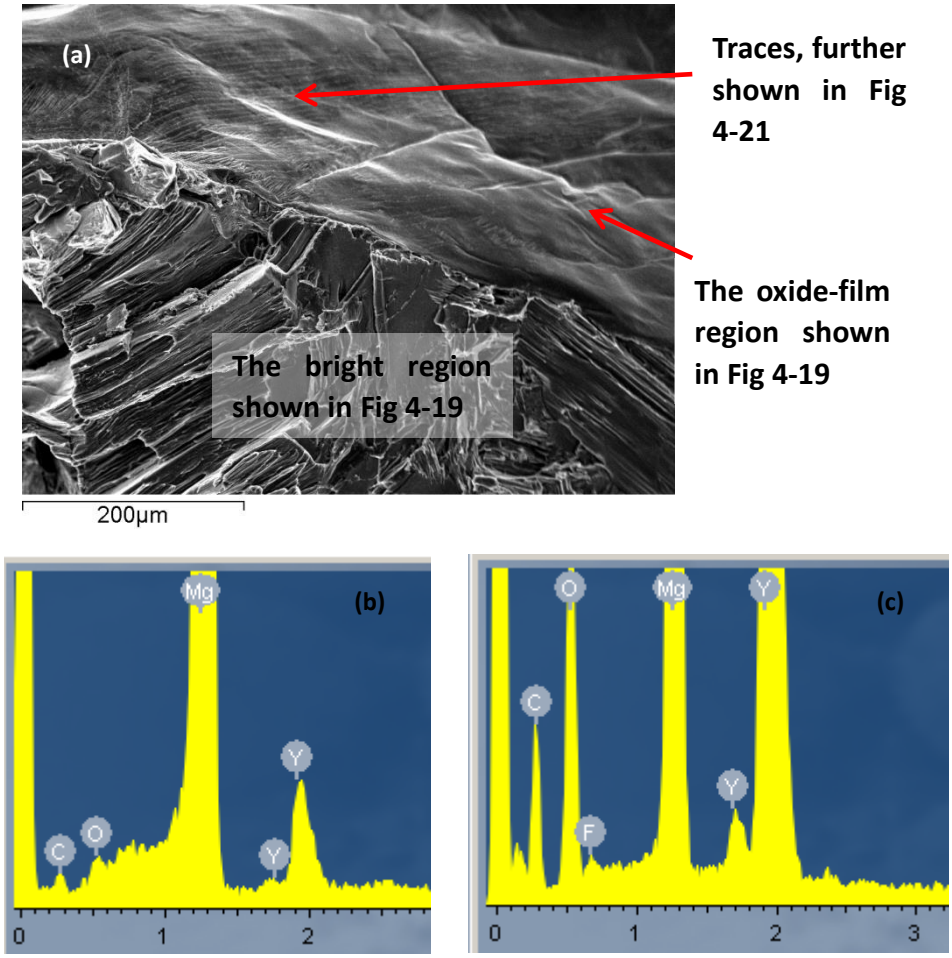

Fig 4-20 (a) a SEM image of a section of the boundary between the oxide-film and bright regions shown in Fig 4-19, (b ~c) the EDS spectrum corresponding to the bright and oxide-film regions respectively.

As in the Mg-Y oxide film formed in 0.5%SF_6/air, this Mg-Y oxide film formed in SF_6/CO_2 also contained more yttrium (40%) than magnesium (23%), indicating that the oxide film mainly consisted of yttrium compounds. The EDS results also revealed a higher carbon content in the oxide film of 17.64%, in contrast to that of the bright fracture surface of 3.47%, suggesting that carbon might exist in oxide films. Nevertheless, this carbon content required a further confirmation, since the carbon

background signal can be significant due to the hydrocarbon contamination which is common for EDS analysis [126].

	C	O	Mg	F	Y	S
Oxide films (Weight%)	17.64	18.15	22.77	0.85	40.59	-
Bright region (Weight%)	3.47	0.71	89.69	-	6.13	-

Table 4-7 Element contents of the EDS results corresponding to bright and oxide-film regions shown in Fig 4-20(a).

Fig 4-21 shows a closer observation of the traces pointed out in Fig 4-20 (a). It can be seen that the traces consisted of cracked flakes.

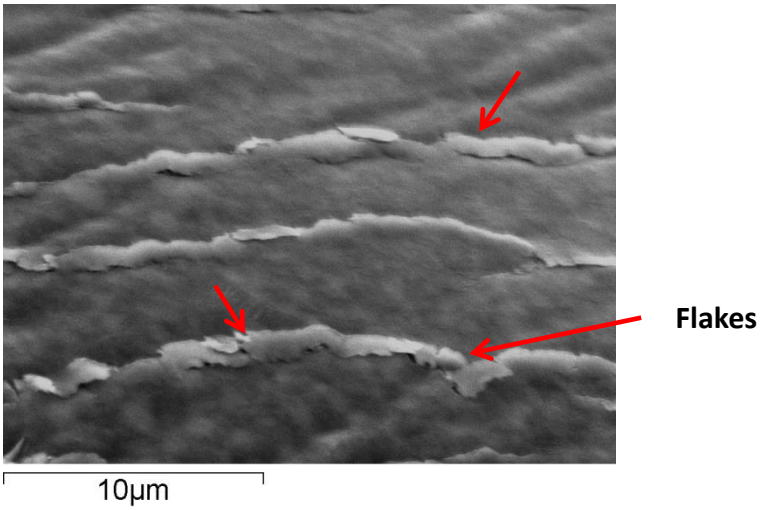

Fig 4-21 a closer observation of the corresponding area pointed out in Fig 4-20(a);

4.1.7 Summary

Several double oxide film defects on the fracture surfaces of Mg-alloy castings have been shown in this section. It indicated that this kind of defect can act as a crack initiator of Mg-alloy castings, as do double oxide film defects in Al-alloy castings. The oxide film normally consisted of oxides and fluorides.

In addition, the observation of the film surface (Fig 4-4, Fig 4-7, Fig 4-11, Fig 4-15, Fig 4-18, Fig 4-21) indicated that the oxide films formed in SF_6/CO_2 (Fig 4-7, Fig 4-15, Fig 4-21) had a relatively compact and smooth surface, in contrast to the films formed in $0.5SF_6$/air (Fig 4-4, Fig 4-11, Fig 4-18). Thus the oxide films formed in SF_6/air may have a more porous structure compared with that produced in SF_6/CO_2.

4.2 Cross-sectional examination of the double oxide film defect formed in the Mg alloy melt

4.2.1 Commercial purity Mg in SF_6/air.

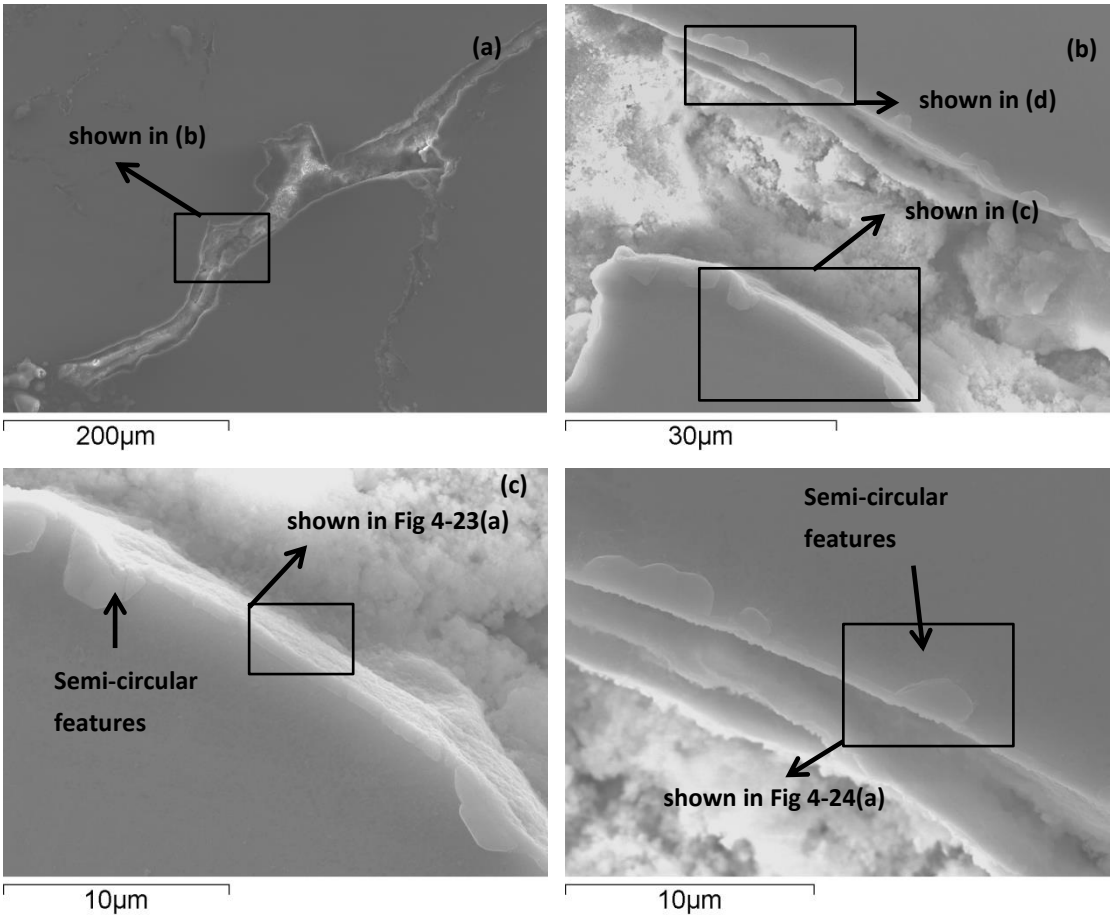

Fig 4-22 (a) A double oxide film defect formed in Mg + 0.5%SF_6/air; (b) a further observation corresponding to the area pointed out in (a), indicating the tube-liked nature; (c) a further observation corresponding to the area pointed out in (b); (d) a further observation corresponding to the area pointed out in (b);

Fig 4-22(a) shows a bubble trail, which has been defined as a particular type of

double oxide film defect [22], formed in a pure Mg sample under a cover gas of 0.5%SF_6/air. Further examination of the defect (Fig 4-22 (b)) indicated that the trail was covered by a continuous surface film having a tube-like structure. Fig 4-22 (c - d) showed some semi-circular features found at the interface between the Mg substrate and the oxide film. These features were a few microns in diameter and embedded in the material substrate.

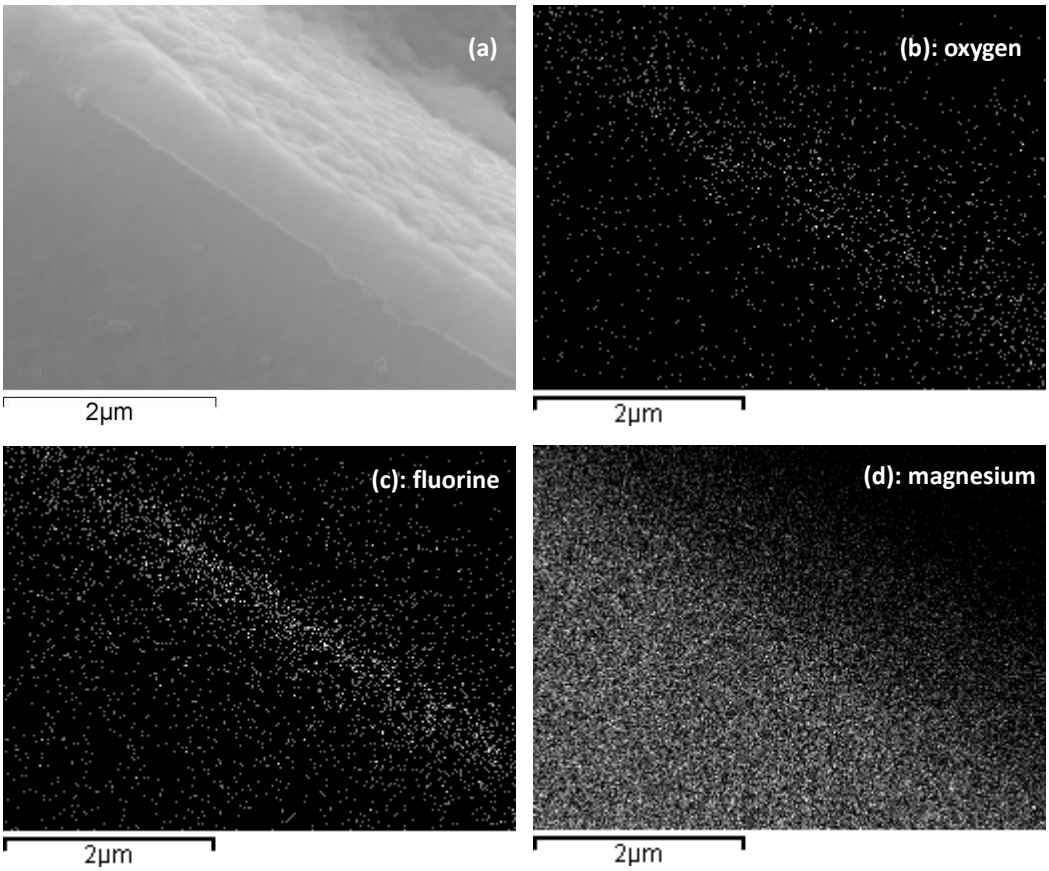

Fig 4-23 (a) a section of the surface film, corresponding to the region pointed out in Fig 4-22(c), no semi-circular feature existed in this section of the surface film; (b ~ d) Element map of (a): (b) oxygen, (c) fluorine, (d) magnesium.

Fig 4-23 shows a element map corresponding to the region pointed out in Fig 4-22 (c), in which the semi-circular features were excluded. It can be seen that the oxide

film was compact and uniform, consisting of a mixture of MgF_2 and MgO. In contrast, the element map of a semi-circular feature, shown in Fig 4-24, indicated a comparative lack of oxygen, suggesting that these features were MgF_2 particles attached to the oxide film. This structure was similar to Wang and Xiong's observation of the protective film formed on an AZ91 melt surface in an atmosphere of SF_6/CO_2/air[58].

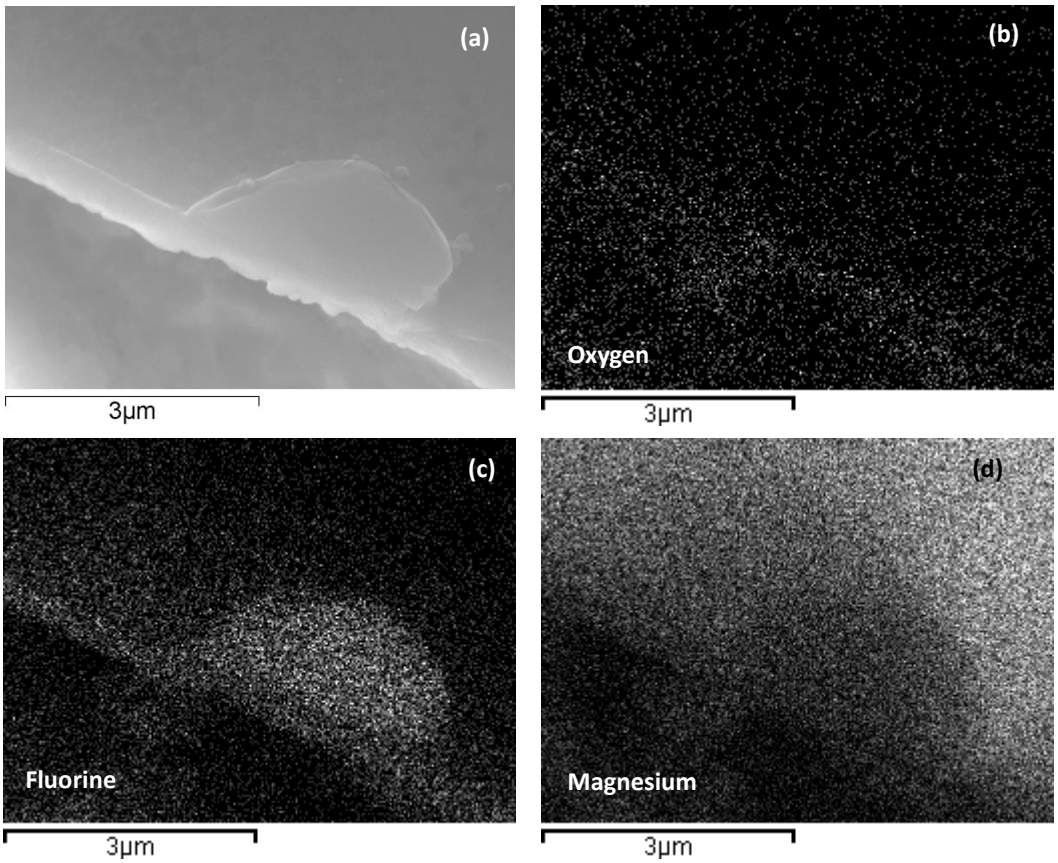

Fig 4-24, (a) a section of the surface film, corresponding to the region pointed out in Fig 4-22(d), a semi-circle feature existed in this section of the surface film; (b ~ d) element map of (a): (b) oxygen, (c) fluorine, (d) magnesium.

4.2.2 Commercial purity Mg in SF_6/CO_2.

Fig 4-25 (a) shows a double oxide film defect formed in commercial purity Mg alloy protected by 0.5%SF_6/CO_2. Fig 4-25(b) showed a tube-liked structure of this defect, similar to the defect shown in Fig 4-22.

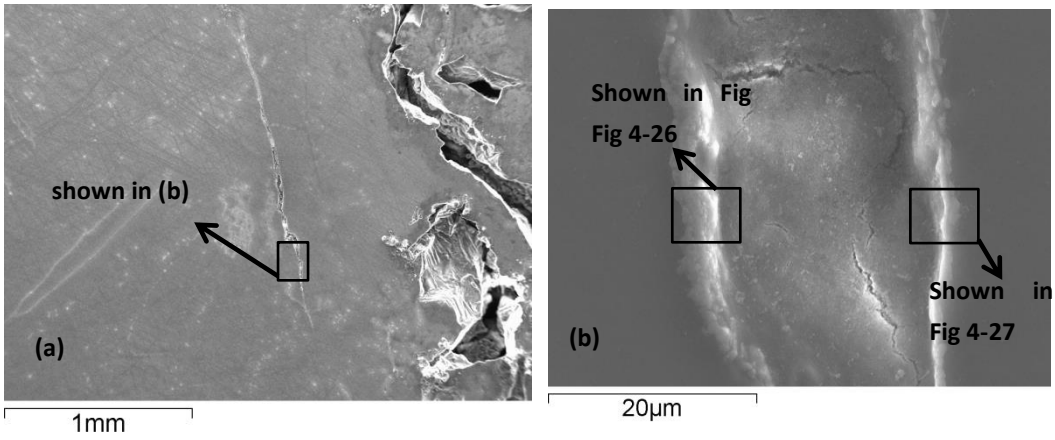

Fig 4-25 (a) A tube-liked double oxide film defect formed in Mg + 0.5%SF_6/CO_2; (b) A further observation corresponding to the area pointed out in (a);

Fig 4-26 and Fig 4-27 show element maps of both sides of the tube-like defect, corresponding to the regions pointed out in Fig 4-25 (b). Fig 4-26 indicates a double-layer structure of the oxide film, having an inner F-enriched layer and an outer MgO enriched layer.

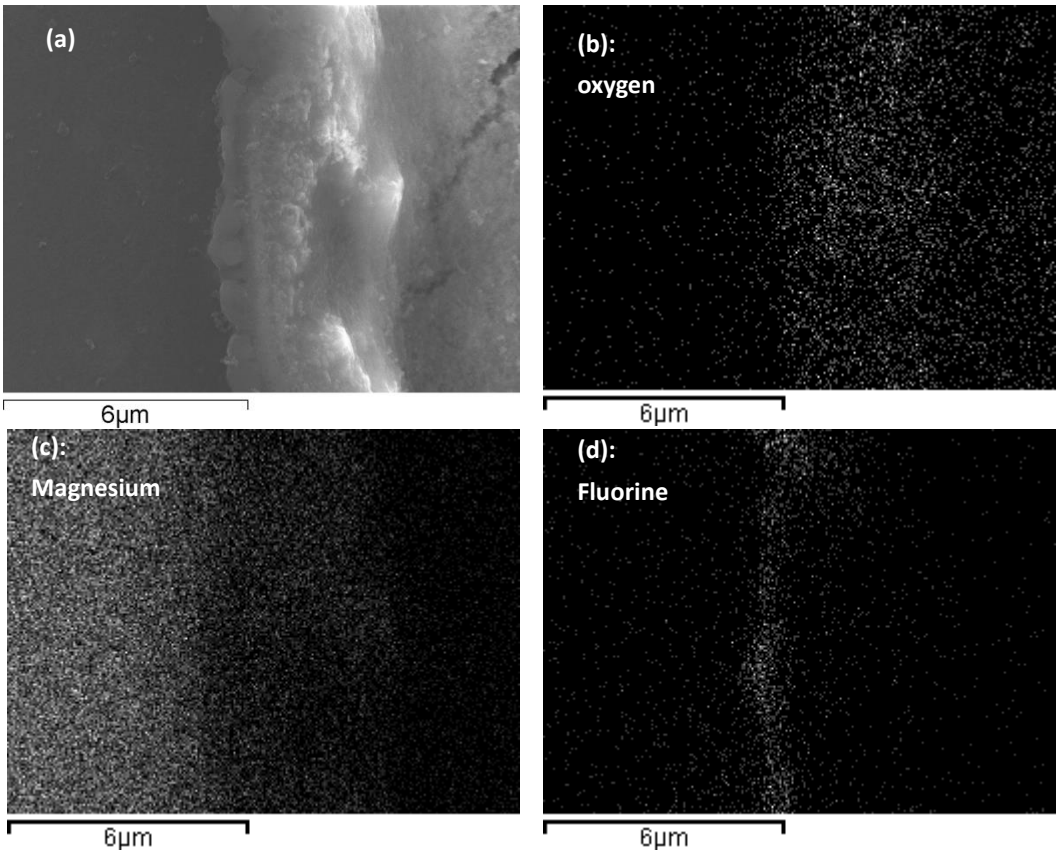

Fig 4-26 (a) an oxide film, corresponding to the region pointed out in Fig 4-25 (b),; (b ~ d) Element map of (a): (b) oxygen, (c) fluorine, (d) magnesium.

Fig 4-27 revealed a similar double-layer structure on the other side of the film, and the locations of the boundary of the two layers are denoted by red points. It can be seen that the inner layer was also enriched with fluorine, and had a lack of oxygen, but the outer layer consisted of a mixture of MgF_2 and MgO, which was different from the outer layer shown in Fig 4-26. In addition, the inner MgF_2 layer did not have a uniform structure, but consisted of MgF_2 particles.

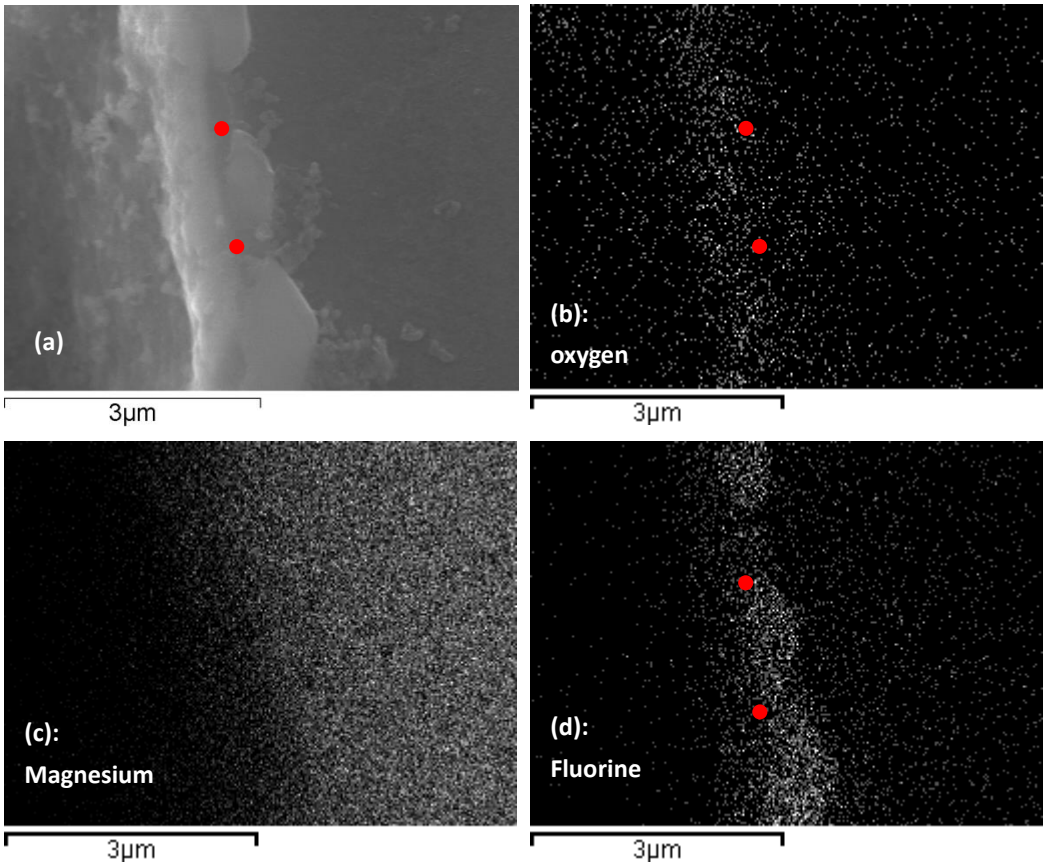

Fig 4-27 (a) a oxide film, corresponding to the region pointed out in Fig 4-25 (b); (b ~ d) Element map of (a): (b) oxygen, (c) fluorine, (d) magnesium. The reds points in (a), (b) and (d) denote the boundary of the two layers.

4.2.3 AZ91 in SF_6/air.

Fig 4-28 (a) shows a bubble trail found in an AZ91 casting produced in an atmosphere of 0.5%SF_6/air. Fig 4-28 (b) shows a tube-like structure to this defect.

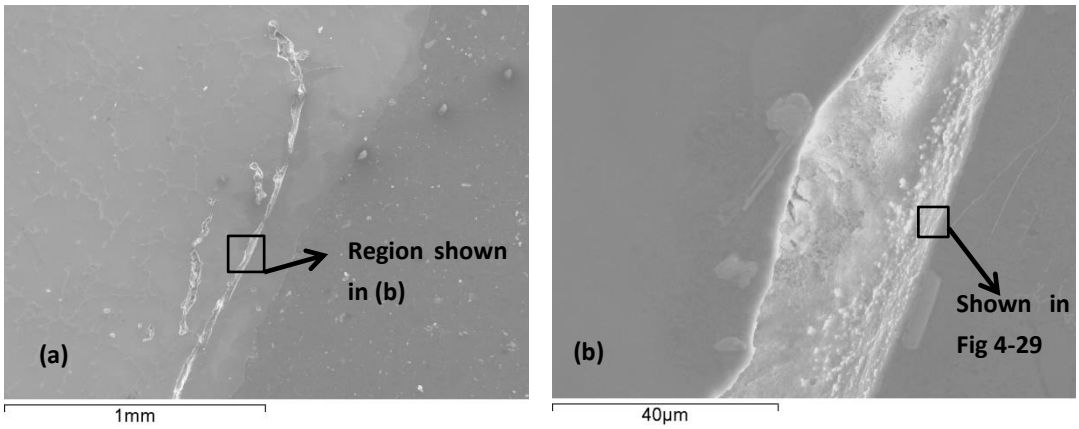

Fig 4-28 (a) A tube-liked double oxide film defect formed in AZ91 + 0.5%SF6/air; (b) A further observation corresponding to the area pointed out in (a);

Fig 4-29 shows the element map of the region pointed out in Fig 4-28 (b), and the locations of the oxide film in the different element maps are denoted by red points. It can be seen that the film contained two layers: an inner layer enriched with fluorine, and an outer thin layer enriched with oxygen. An aluminium concertation was also detected in the film. However, the existence of sulphur and zinc could not be confirmed in the element map.

Fig 4-30(a) shows pores contained in the same AZ91 casting, and the element map of its oxide film is shown in Fig 4-30(b - h), revealing a homogenous Al-enriched layer inside the oxide film. Oxygen and fluorine were uniformly distributed in this film as a mixture.

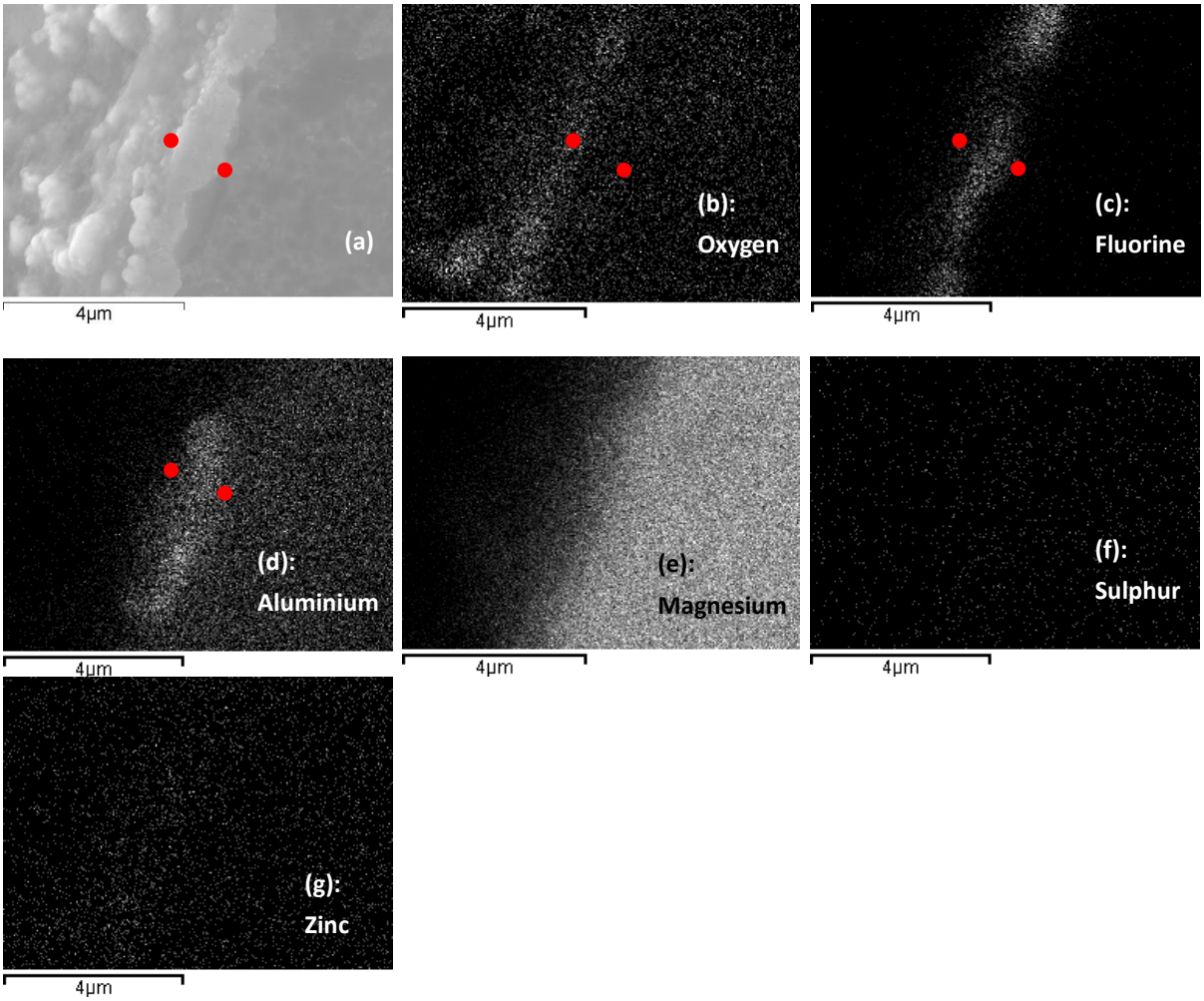

Fig 4-29 (a) A section of oxide film corresponding to the region pointed out in Fig 4-28(b); (b ~ g) element maps corresponding to (a): (b) oxygen, (c) fluorine, (d) aluminium, (e) magnesium, (f) sulphur, (g) zinc. The reds points are the location reference, denoting the oxide films in (a ~d).

Therefore, it can be suggested that aluminium could be contained in the surface film as oxides or fluorides, which was different to the observation of Xiong and Wang [58, 59], who did not see aluminium in the film formed on an AZ91 melt surface protected by SF_6+10%Air/90%CO_2.

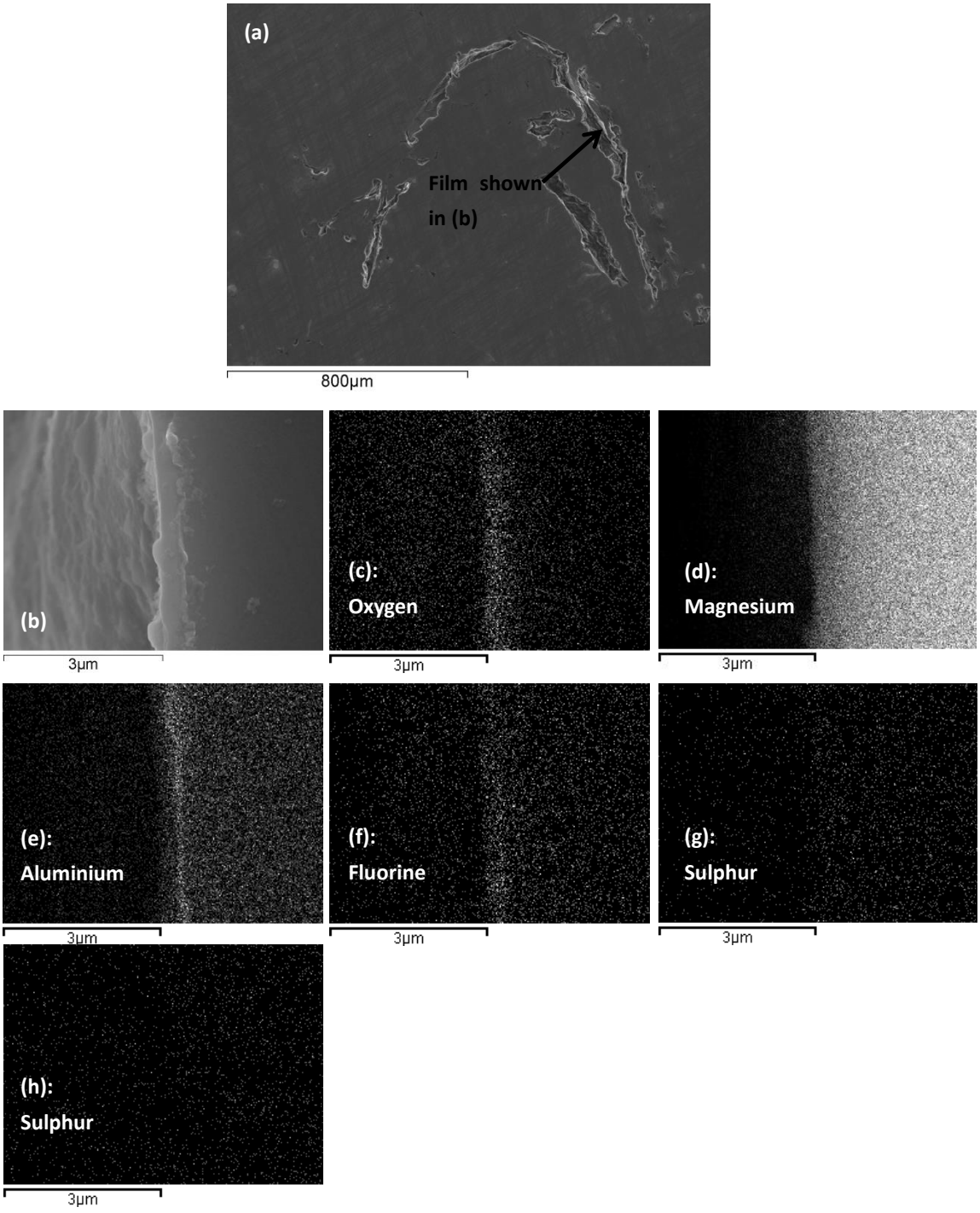

Fig 4-30 (a) Micro bubbles formed in AZ91 + 0.5%SF_6/air (b) a section of oxide film corresponding to the region pointed out in Fig 4-29; (c ~ h) element maps corresponding to (b): (c) oxygen, (d) magnesium, (e) aluminium, (f) fluorine, (g) sulphur, (h) zinc

4.2.4 AZ91 in SF_6/CO_2.

The cross-section structure of an oxide film, cut from a double oxide film defect formed in an AZ91 sample cast in 0.5%SF_6/CO_2, was observed using the FIB technique, with Keyhum Kim's help. According to Fig 4-31, a continuous oxide film was found between the platinum coating layer and the Mg-Al alloy substrate. Some white spots, which may be inclusions contained in the casting, could be seen in the area close to the oxide film.

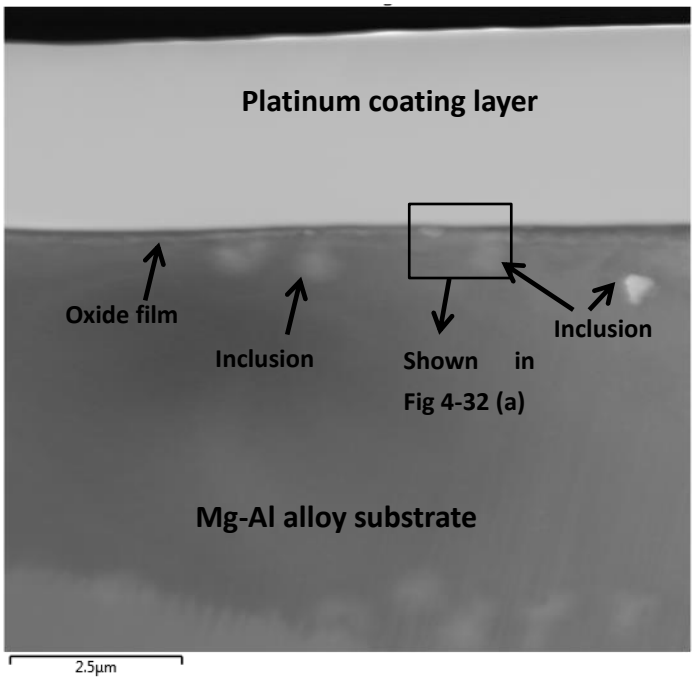

Fig 4-31 a cross-sectional SEM image of a double oxide film defect, achieved by FIB, indicating a continuous oxide film, and some inclusions.

Fig 4-32 shows the element map corresponding to the region denoted in Fig 4-31 . It can be seen that fluorine and oxygen were uniformly distributed in the oxide film, but aluminium existed as a concentration. The existence of sulphur and zinc could not be confirmed according to the EDS element map. In addition, Fig 4-32 (d) showed

a concentration of carbon in the film, revealing that CO_2 was able to react with the melt, forming carbon or carbides. The inclusion attached to the film, denoted in Fig 4-32 (a), was found to be a MgO particle.

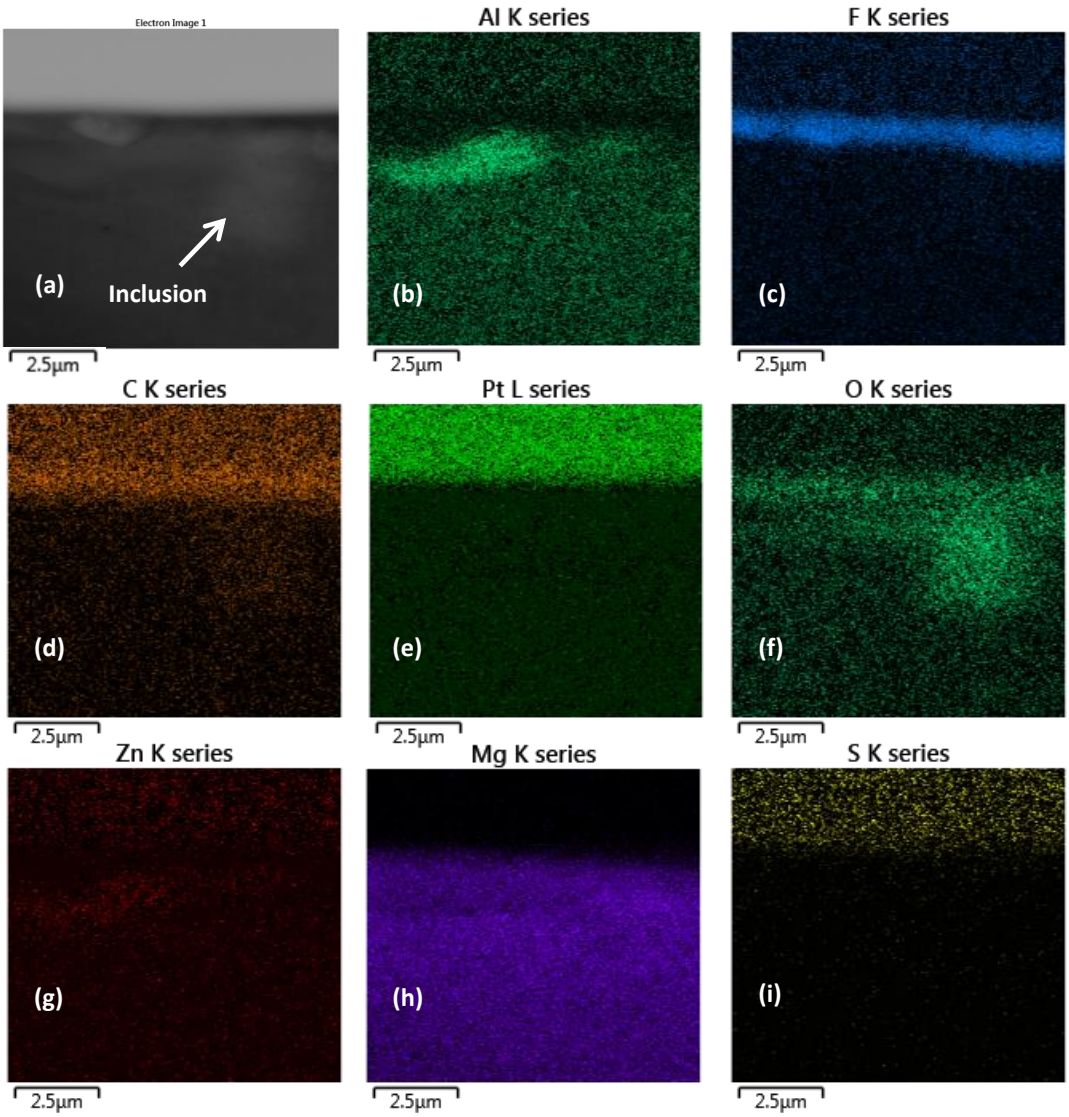

Fig 4-32 (a)SEM image corresponding to the area pointed out in Fig 4-30; (b ~ i) element map corresponding to (a): (b) aluminium, (c) fluorine, (d) carbon; (e) platinum; (f) oxygen; (g) Zinc; (h) magnesium; (i) sulphur.

4.2.5 Mg-Y alloy in SF_6/air.

Fig 4-33(a) shows a double film defect found in an Mg-Y sample formed in 0.5%SF_6/air. Fig 4-33(b) shows a closer observation of the area denoted in (a), indicating the doubled nature of the oxide films.

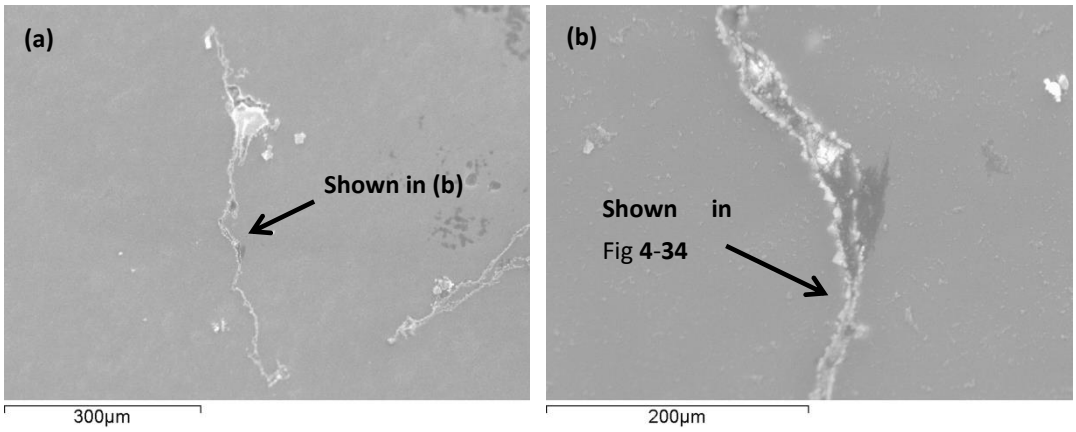

Fig 4-33 (a) a double film defect found in an Mg-Y sample formed in 0.5%SF_6/air. (b) a closer observation of the area denoted in (a), indicated a doubled nature of the oxide films.

Fig 4-34 shows the element map of a section of the double oxide films, denoted in Fig 4-33(b). Fluorine and oxygen were detected in the oxide films, while sulphur could not be found. According to Fig 4-34(d ~ e), the films mainly contained yttrium oxides and fluorides, and the amount of magnesium compounds was small. The concentration of Y in the oxide films was consistent with the EDS results in Table 4-6, which indicated a high Y-content and a low Mg-content in the double oxide film defect formed in the Mg-Y casting.

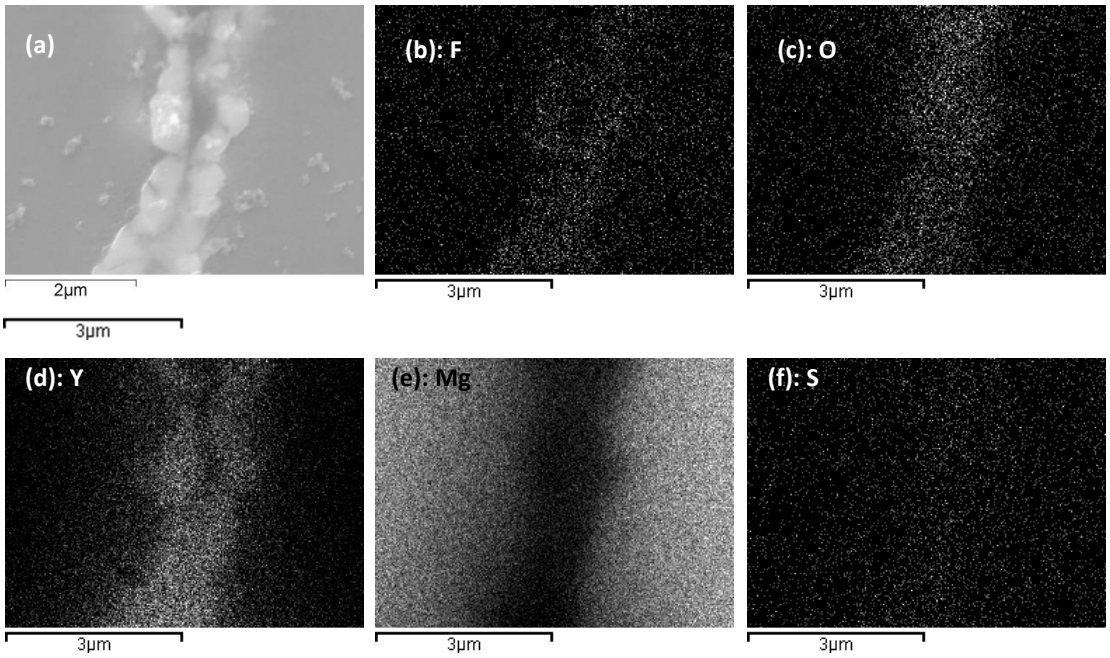

Fig 4-34 (a)SEM image corresponding to the area pointed out in Fig 4-33; (b ~ f) element map corresponding to (a): (b) fluorine, (c) oxygen; (d) yttrium; (e) magnesium, (f) sulphur.

4.2.6 Mg-Y alloy in SF_6/CO_2.

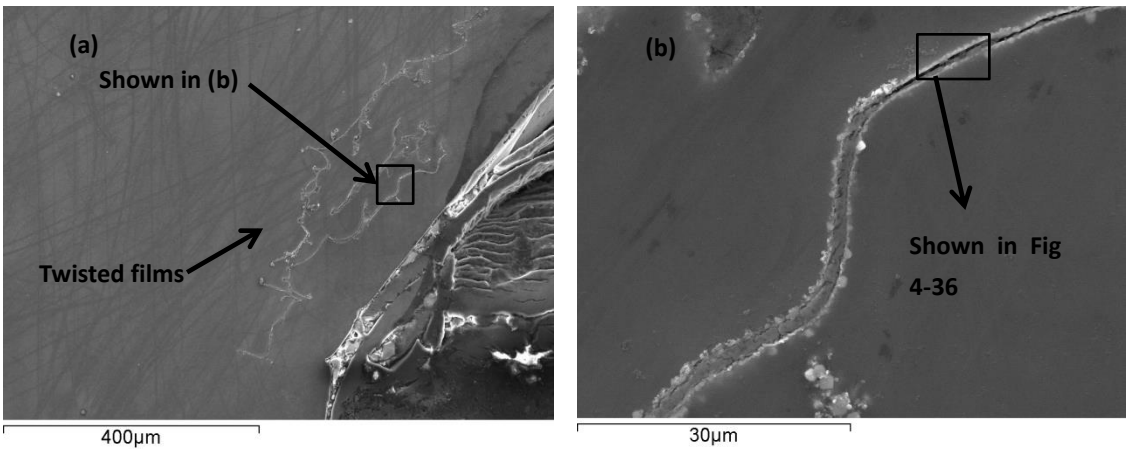

Fig 4-35 (a) twisted films found in a Y sample formed in 0.5%SF_6/CO_2. (b) A closer observation of the area denoted in (a), indicating the doubled nature of the twisted film.

Fig 4-35(a) shows a double oxide film defect contained in a Mg-Y alloy ingot produced under a cover gas of 0.5%SF_6/CO_2. The defect presented an appearance

similar to contorted wires. A closer observation (Fig 4-35 (b)) revealed the doubled nature of the linear films.

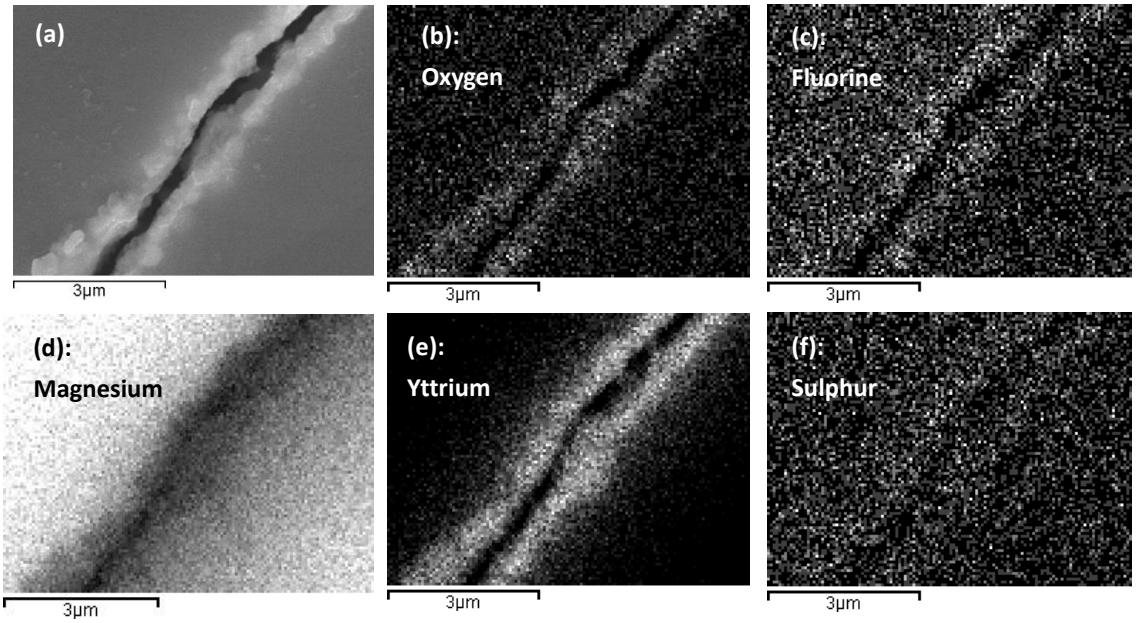

Fig 4-36 (a)SEM image corresponding to the area pointed out in Fig 4-35(b); (b ~ f) element map corresponding to (a): (b) oxygen, (c) fluoine; (d) magnesium; (e) yttrium, (f) sulphur.

The element content of the linear films, illustrated in Fig 4-36, was similar to the oxide films formed in 0.5%SF_6/air and shown in Fig 4-34. The oxide film had a single layer, containing a mixture of yttrium fluoride, yttrium oxide, magnesium fluoride and magnesium oxide. The magnesium content in the film was lower than the yttrium content, which was consistent with the EDS results of the double oxide film defect shown in Table 4-7. In addition, the existence of sulphur could not be clearly confirmed by the element mapping.

4.2.7 Summary.

The cross-section structure of the double oxide film defect, formed in different Mg-alloys and atmospheres, were shown in this section. The oxide films formed in commercial purity Mg alloy had a single or double layer structure composed of MgF_2 and MgO.

The films formed in AZ91 alloy contained magnesium, oxygen, fluorine, and aluminium. The existence of aluminium in the oxide film has not been reported in the previous publications [58, 59].

The films formed in Mg-Y alloy were enriched with yttrium, which was consistent with previous results shown Table 4-6 and Table 4-7 (i.e. the double oxide film defect on the fracture surface of Mg-Y castings, section 4.1.5 and 4.1.6).

4.3 The protective film growing on a Mg-alloy melt surface under different cover gases

4.3.1 Commercial purity Mg melt in SF_6/air

Fig 4-37~ Fig 4-42 show cross sections of the protective film formed on a commercial purity Mg melt surface in an atmosphere of 0.5%SF_6/air. The samples were held at 700 ^{o}C for 30 ~ 5 min respectively.

According to Fig 4-37(a), it can be seen that the surface film held for 30 min consisted of two layers. The corresponding EDS spectrum (Fig 4-37 (b ~ f)) revealed that the inner layer (i.e. the layer closer to the Mg substrate) was composed of MgF_2 and MgO, and the outer layer was enriched with sulphur, which may have occurred as MgS or $MgSO_4$ in the protective film.

Based on Fig 4-38 ~ Fig 4-40, the surface films held for 25 min ~ 15 min also had a double-layer structure with the same compositions of the inner and the outer layers.

Fig 4-41 and Fig 4-42 reveal a similar doubled-layer structure of the surface films held for 5 ~ 10 min. However, in these two films, the thickness of the outer S-enriched layers was much smaller in contrast to the films held for 15 min ~ 30 min (Outer layer thickness: 2.73 um for 30-min film, 3.94 um for 25-min film, 3.11 um for 20-min film,1.91 um for 15-min film, 0.54 um for 10-min film, 0.48 um for 5-min film) .

According to this comparison of the structure of the films held for 30 min ~ 5 min, it can be suggested that fluorine in the protective gas was preferentially consumed, forming the inner layer, while sulphur accumulated in the cover gas. When the fluorine was nearly depleted, the accumulated sulphur subsequently reacted with the Mg melt, forming the S-enriched layer. Furthermore, the growth of the outer layer indicated that the Mg melt was able to penetrate the surface film. A Mg-alloy melt penetration phenomenon was also reported in a previous published nodular growth process during Mg-alloy ignition [127].

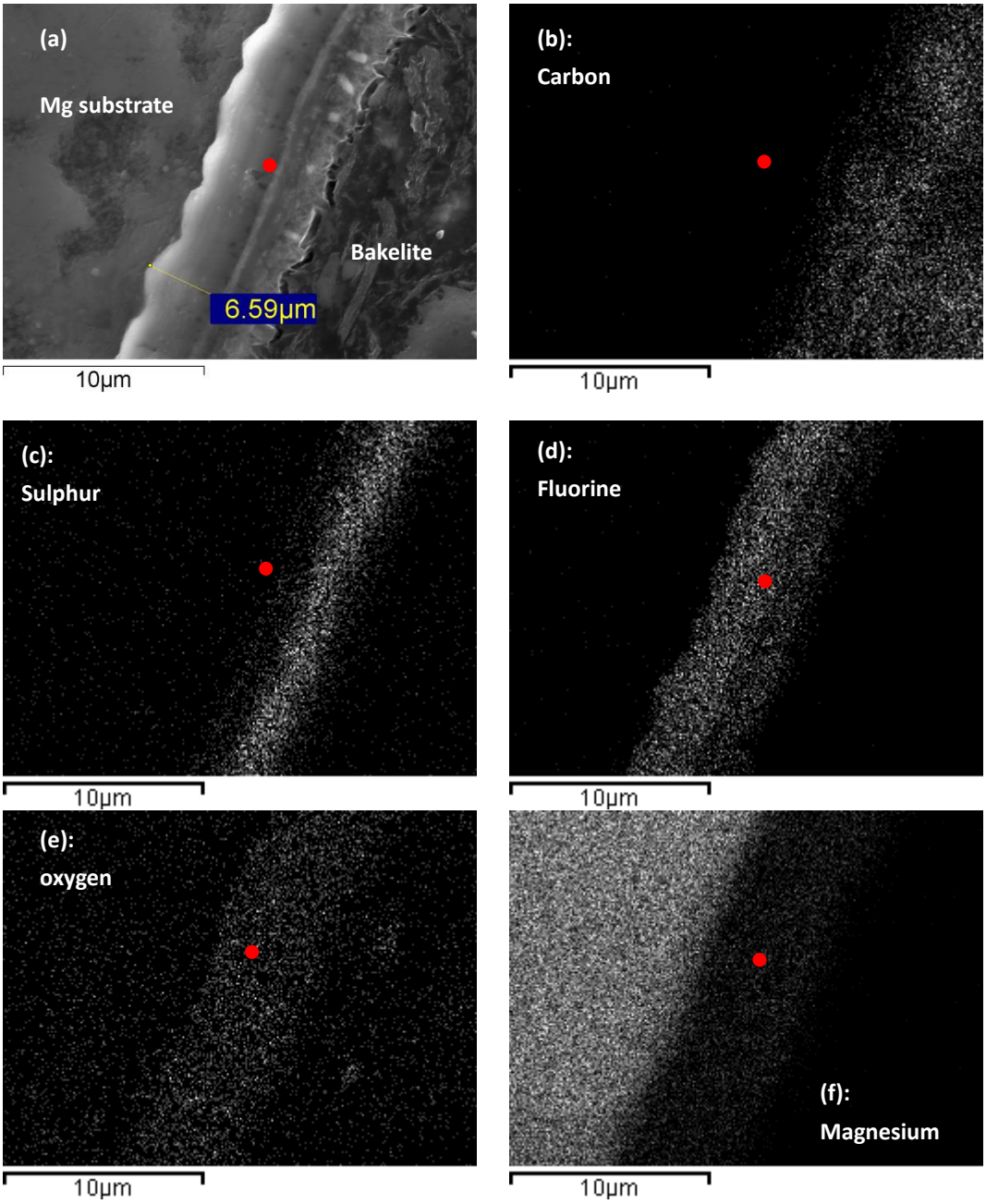

Fig 4-37 (a) a surface film formed in Mg + 0.5%SF_6/air, held at 700 ^{o}C for 30 min (b ~ f) element map corresponding to (a): (b) carbon, (c) sulphur; (d) fluorine; (e) oxygen, (f) magnesium. The red point in (a) ~ (f) denotes the location of the boundary between the two layers.

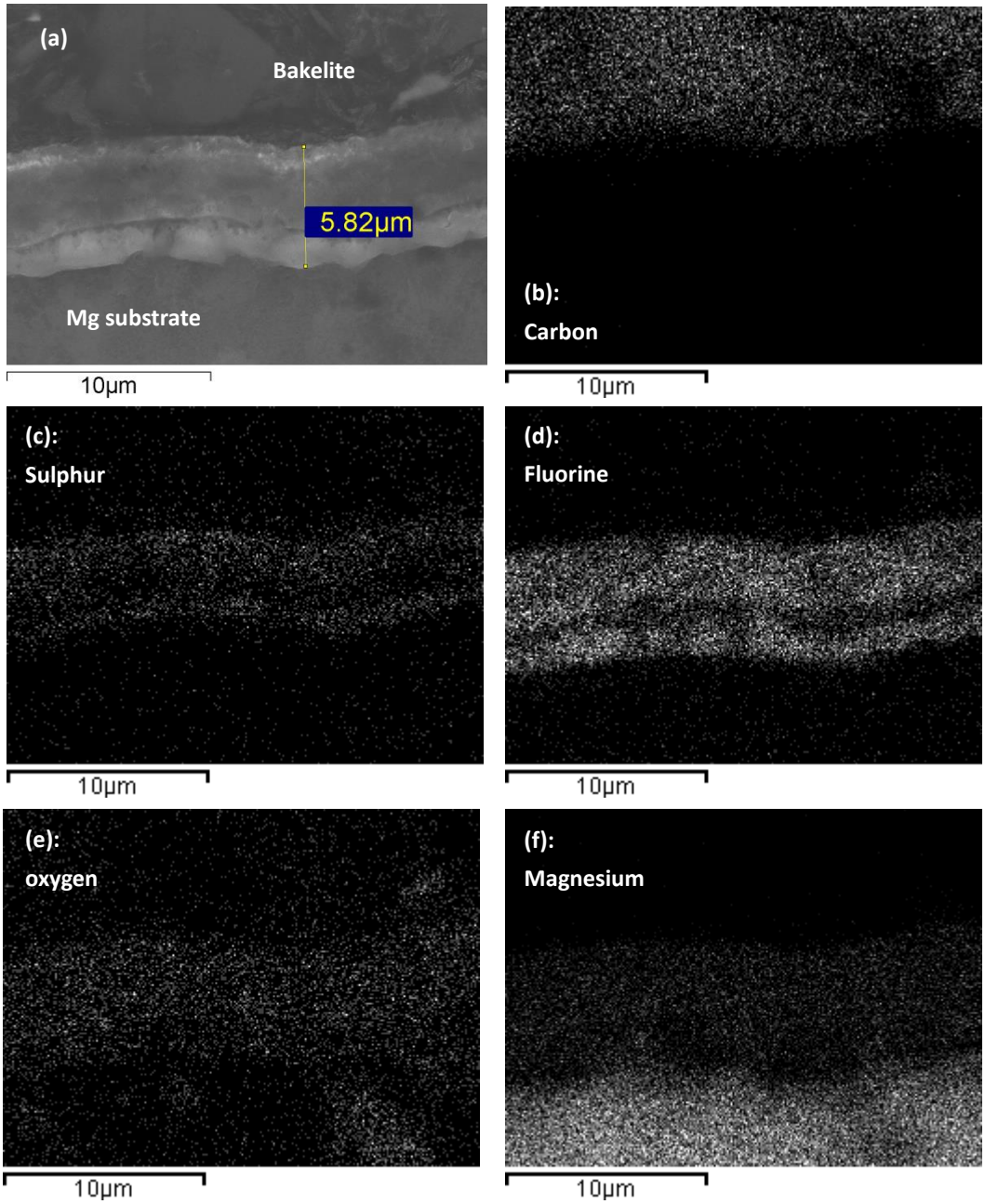

Fig 4-38 (a) a surface film formed in Mg + 0.5%SF_6/air, held at 700 ^{o}C for 25 min (b ~ f) element map corresponding to (a): (b) carbon, (c) sulphur; (d) fluorine; (e) oxygen, (f) magnesium.

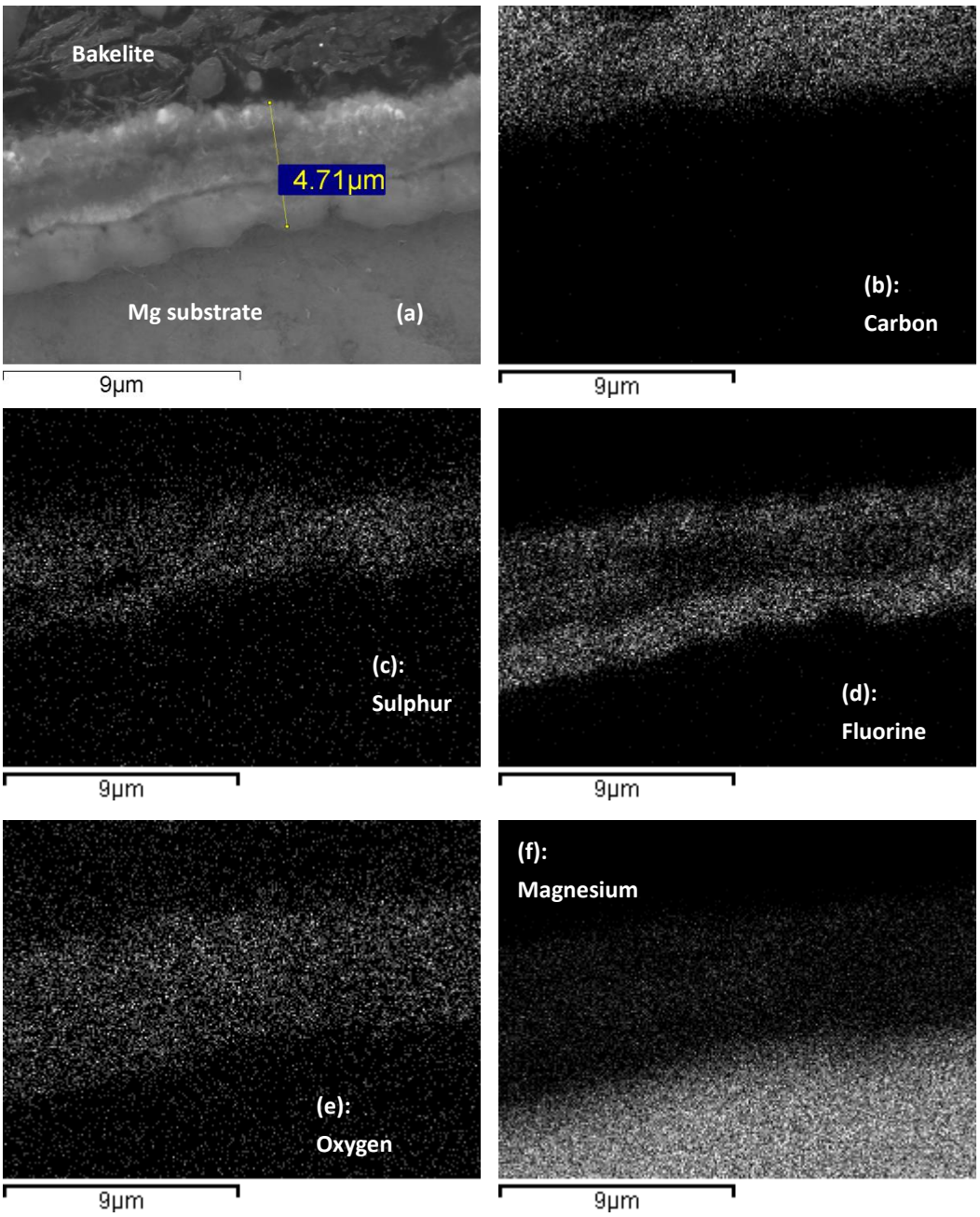

Fig 4-39 (a) a surface film formed in Mg + 0.5%SF_6/air, held at 700 ^{o}C for 20 min (b ~ f) element map corresponding to (a): (b) carbon, (c) sulphur; (d) fluorine; (e) oxygen, (f) magnesium.

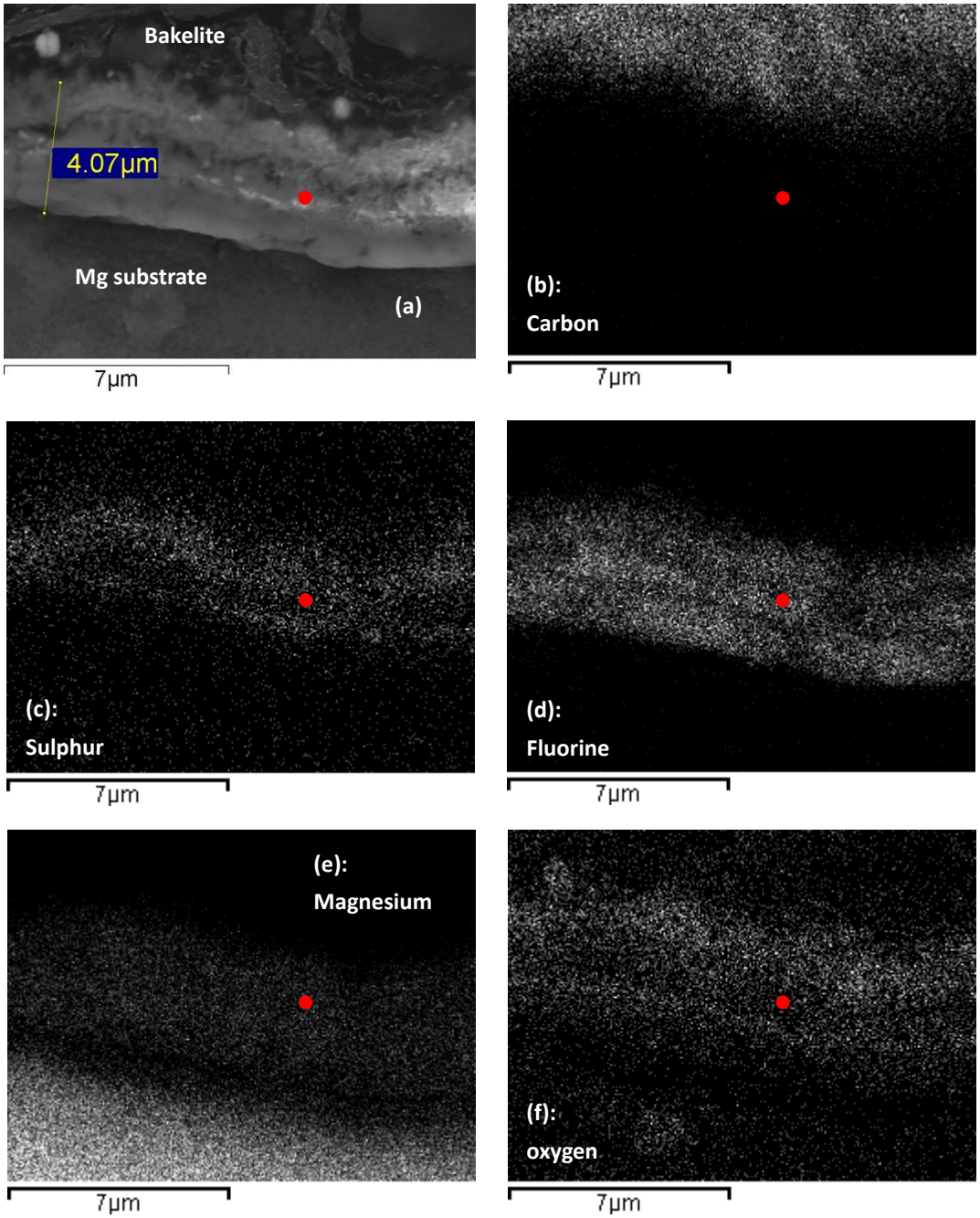

Fig 4-40 (a) a surface film formed in Mg + 0.5%SF_6/air, held at 700 ^{o}C for 15 min (b ~ f) element map corresponding to (a): (b) carbon, (c) sulphur; (d) fluorine; (e) magnesium, (f) oxygen. The red point in (a ~ f) denotes the location of the boundary between two layers.

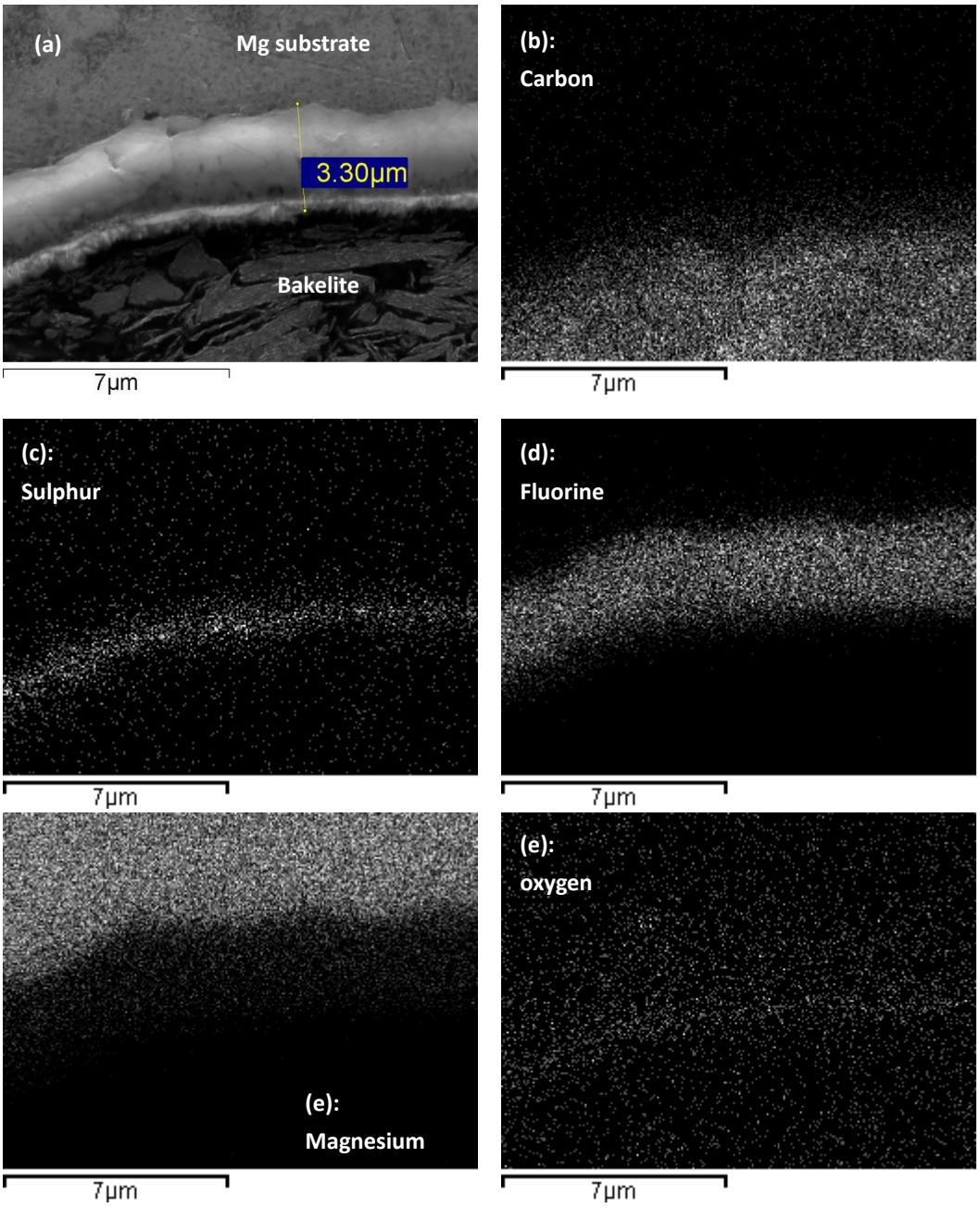

Fig 4-41 (a) a surface film formed in Mg + 0.5%SF_6/air, held at 700 ^{o}C for 10 min (b ~ f) element map corresponding to (a): (b) carbon, (c) sulphur; (d) fluorine; (e) magnesium, (f) oxygen.

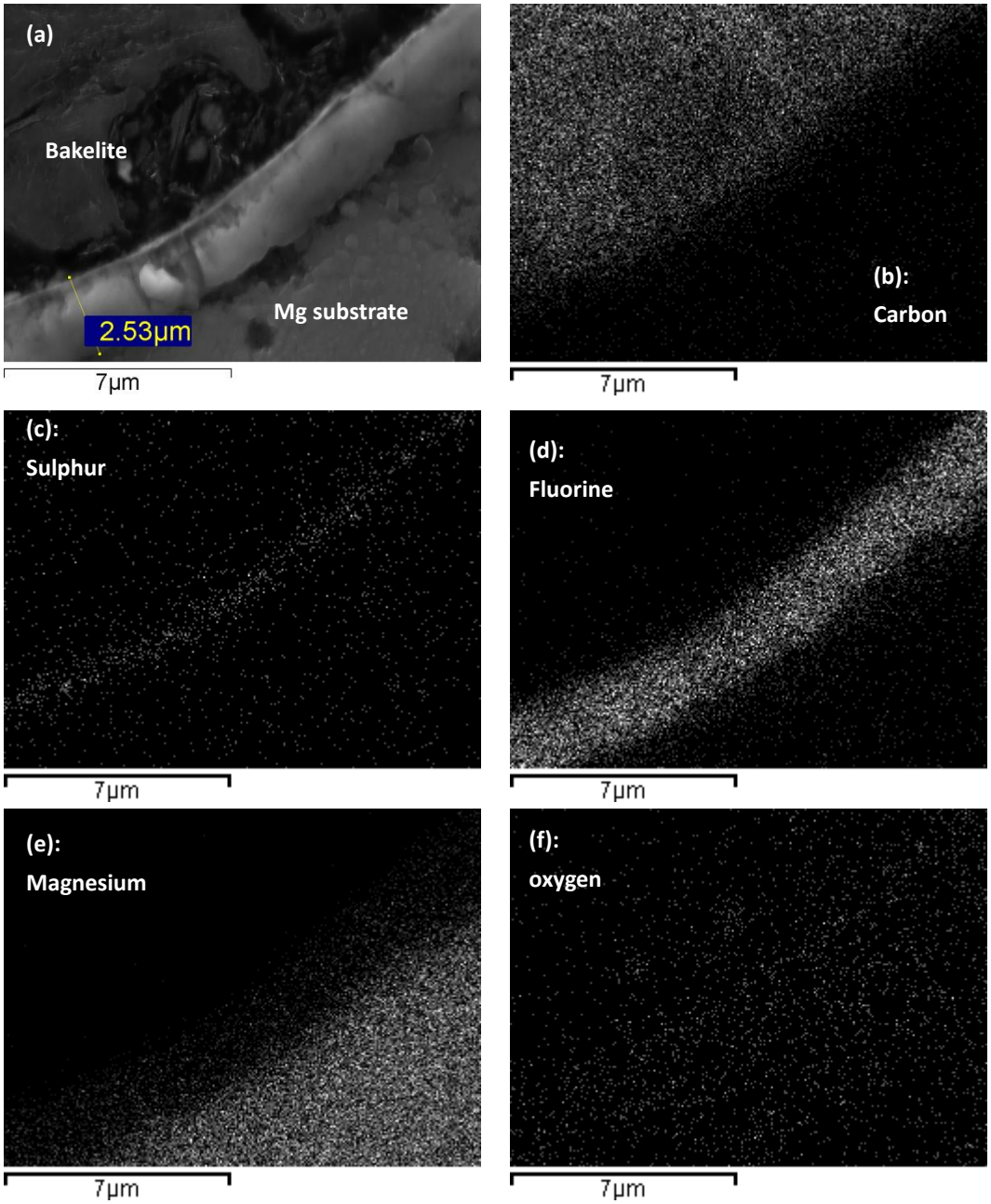

Fig 4-42 (a) a surface film formed in Mg + 0.5%SF_6/air, held at 700 ^{o}C for 5 min (b ~ f) element map corresponding to (a): (b) carbon, (c) sulphur; (d) fluorine; (e) oxygen, (f) magnesium.

4.3.2 Commercial purity Mg melt in SF_6/CO_2

Fig 4-43 ~ Fig 4-48 show cross sections of the protective films formed on a commercial purity Mg melt surface in an atmosphere of 0.5%SF_6/CO_2.

It can be seen that all the films had a compact single layer, which was different from the double-layer Mg films formed in 0.5%SF_6/air (Fig 4-37~ Fig 4-42).

The corresponding element maps show that sulphur was not detected in any of these single-layer films, suggesting the sulphur in the cover gas did not begin to react with the Mg melt at a holding time of less than 30 min. Moreover, the existence of oxygen was confirmed in the surface films held for 30 min ~ 20 min (Fig 4-43 (e), Fig 4-44(e) and Fig 4-45(e)), but could not be clearly recognized in the surface films held for 15 min ~5min (Fig 4-46(e), Fig 4-47(e) and Fig 4-48(e)), suggesting that the Mg melt may mainly react with fluorides in the cover gas at the early stage of the reaction process.

Fig 4-47(b) reveals carbon concentrations, which may have been Mg carbide, inside the surface film, indicating that carbon could be produced during the formation process of the protective film, following the equations: $Mg + CO_2 = MgO + CO$, $\triangle G(700^oC) = -298.69$ kJ; $CO + Mg = MgO + C$, $\triangle G(700^oC) = -298.67$ kJ. This finding further support the previous EDS results shown in Table 4-7, which revealed a higher carbon content in the oxide film area.

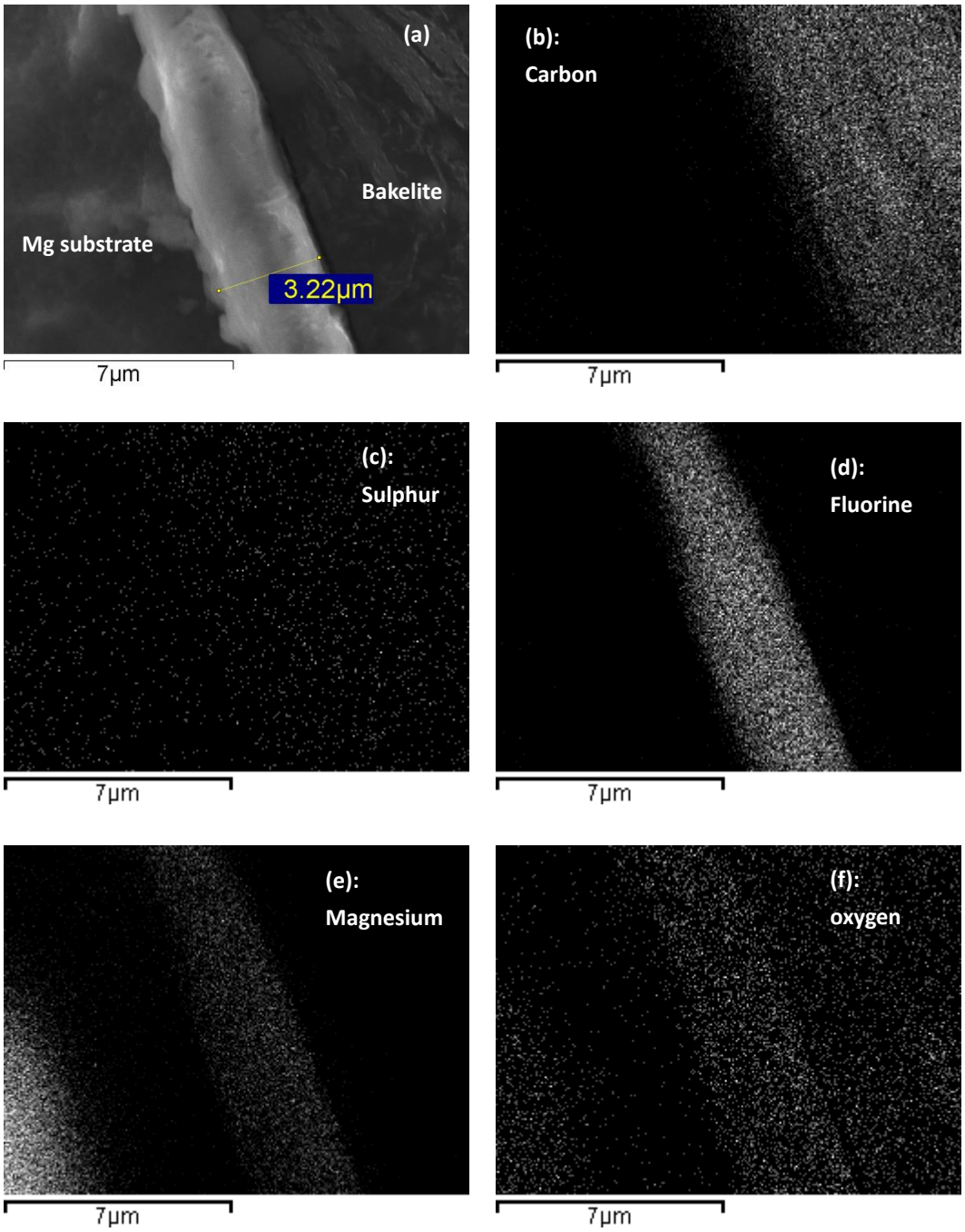

Fig 4-43 (a) a surface film formed in Mg + 0.5%SF_6/CO_2, held at 700 ^{o}C for 30 min (b ~ f) element map corresponding to (a): (b) carbon, (c) sulphur; (d) fluorine; (e) magnesium, (f) oxygen.

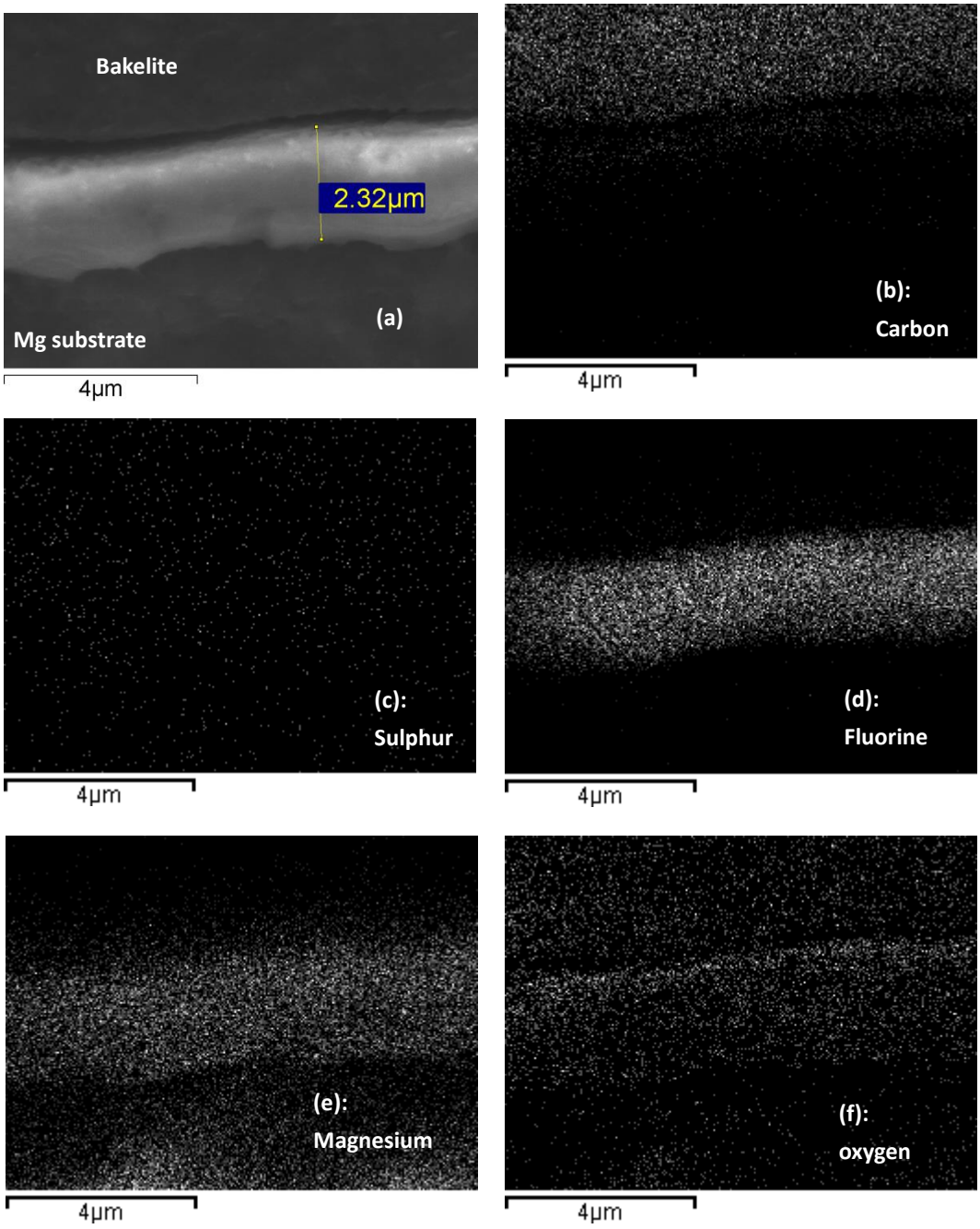

Fig 4-44 (a) a surface film formed in Mg + 0.5%SF_6/CO_2, held at 700 ^{o}C for 25 min (b ~ f) element map corresponding to (a): (b) carbon, (c) sulphur; (d) fluorine; (e) magnesium, (f) oxygen.

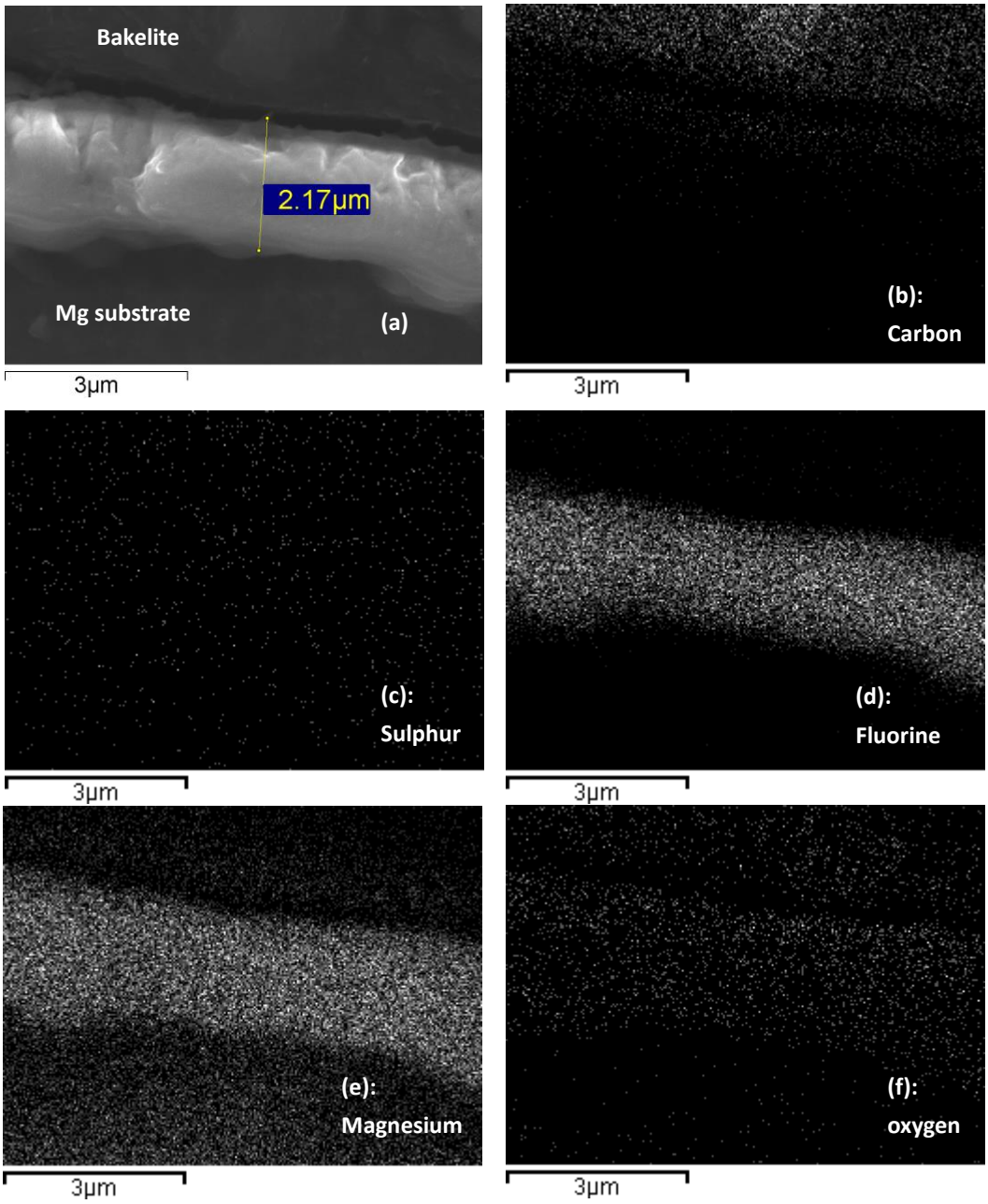

Fig 4-45 (a) a surface film formed in Mg + 0.5%SF_6/CO_2, held at 700 ^{o}C for 20 min (b ~ f) element map corresponding to (a): (b) carbon, (c) sulphur; (d) fluorine; (e) magnesium, (f) oxygen.

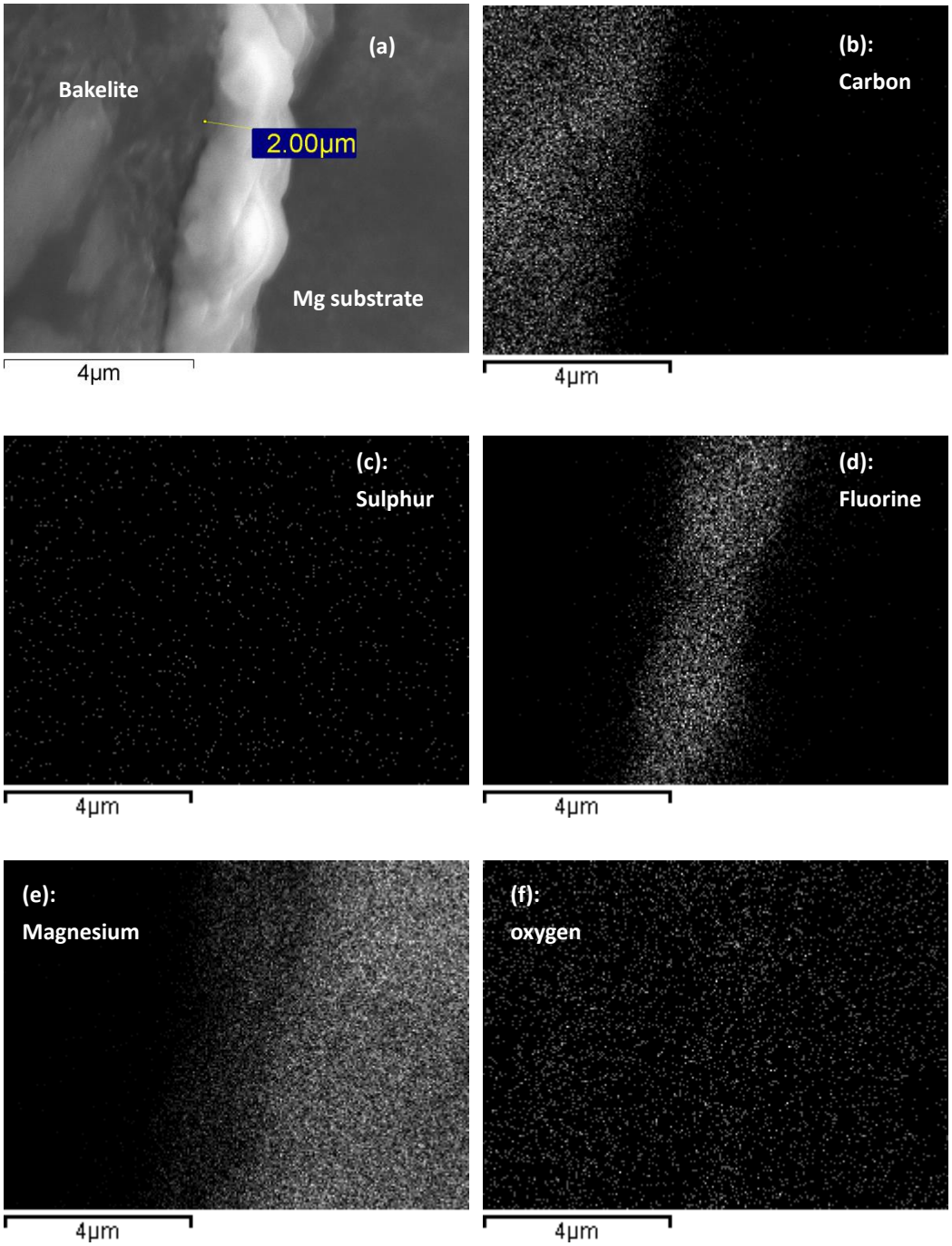

Fig 4-46 (a) a surface film formed in Mg + 0.5%SF_6/CO_2, held at 700 ^{o}C for 15 min (b ~ f) element map corresponding to (a): (b) carbon, (c) sulphur; (d) fluorine; (e) magnesium, (f) oxygen.

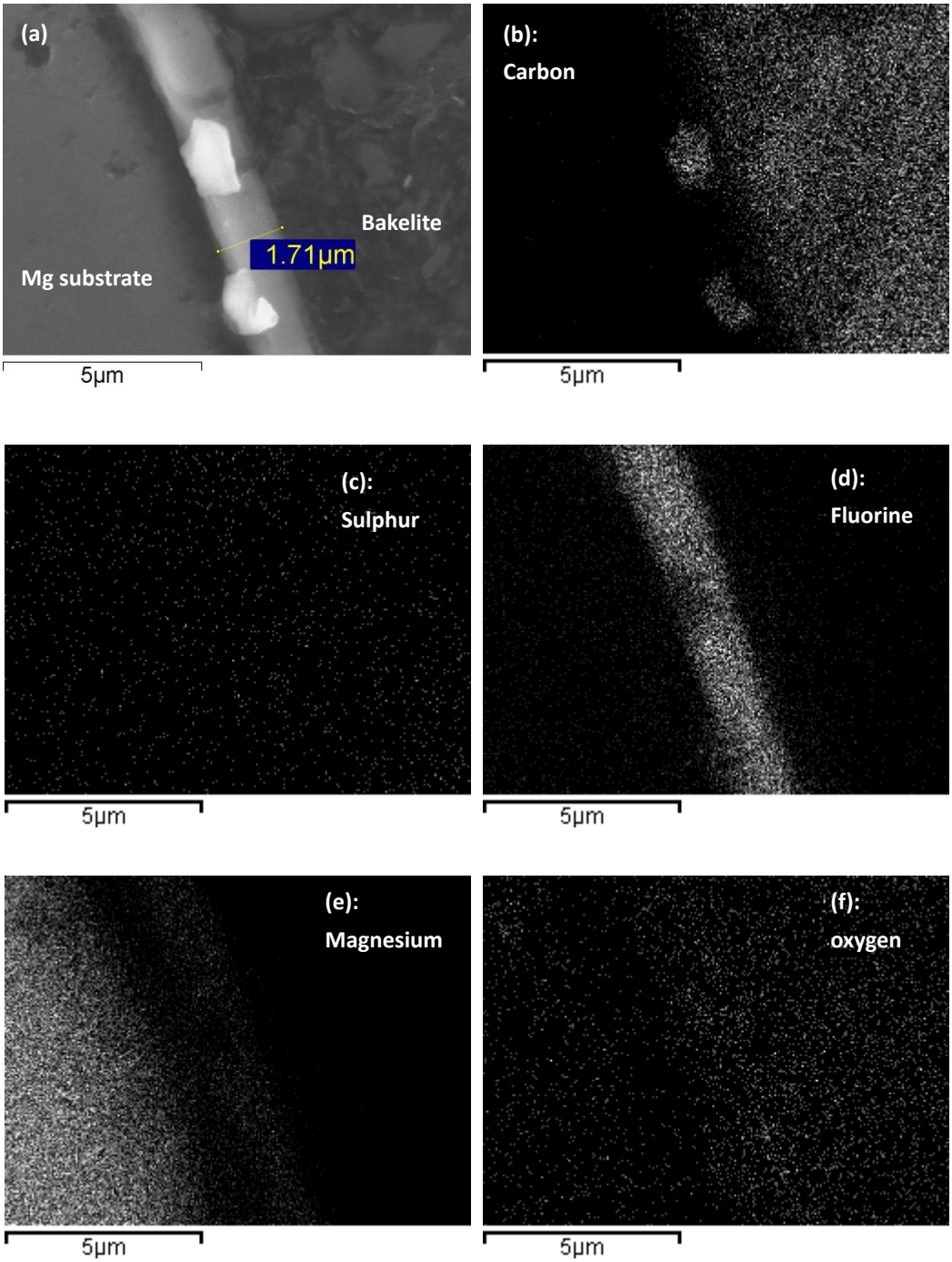

Fig 4-47 (a) a surface film formed in Mg + 0.5%SF_6/CO_2, held at 700 ^{o}C for 10 min (b ~ f) element map corresponding to (a): (b) carbon, (c) sulphur; (d) fluorine; (e) magnesium, (f) oxygen.

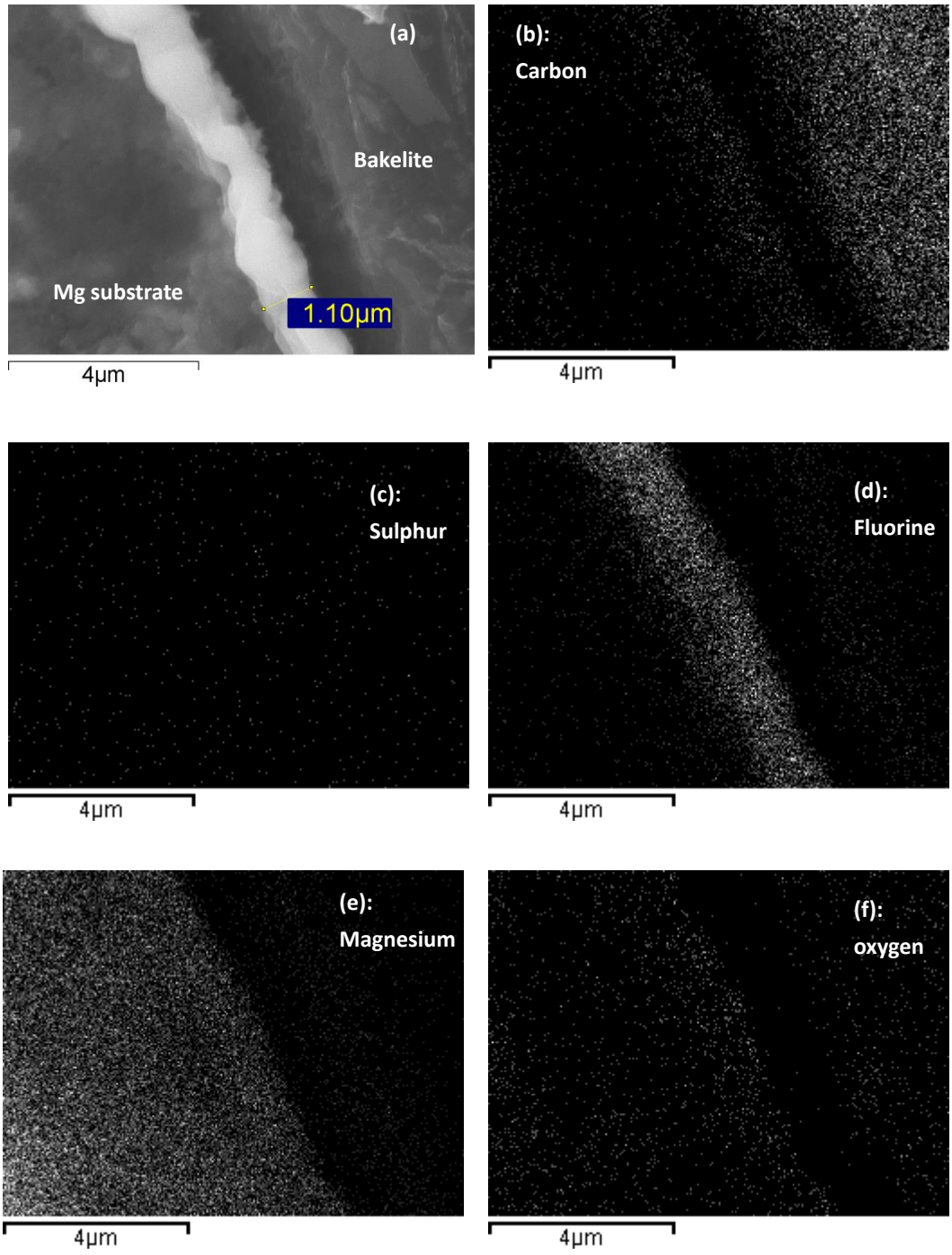

Fig 4-48 (a) a surface film formed in Mg + 0.5%SF_6/CO_2, held at 700 ^{o}C for 5 min (b ~ f) element map corresponding to (a): (b) carbon, (c) sulphur; (d) fluorine; (e) magnesium, (f) oxygen.

4.3.3 AZ91 melt in SF_6/air

The cross sections of the surface films, grown on an AZ91 melt surface in an atmosphere of 0.5%SF_6/air, are shown in Fig 4-49 ~ Fig 4-54.

Fig 4-49 shows the surface film held for 30 min. Two layers, having approximately the same thickness, can be seen in this film: an inner compact layer composed of MgF_2 and MgO, and an outer layer enriched with sulphur. Fluorine was not homogenously distributed in the outer layer, but existed as MgF_2 grains, embedded into a matrix composed of MgO and $MgSO_4$ or MgS. Aluminium and zinc were not found in the surface film, but there was a Mg-Al phase attached to the underside of the surface film.

The 25-min film, shown in Fig 4-50, had the similar double-layer structure. The components of the two layers were the same as the layers of the 30-min film, but fluorine was uniformly distributed in the outer layer of the 25-min film, rather than existing as MgF_2 grains. In addition, the outer layer was thinner compared with the inner layer. An Al-enriched phase could be also seen under the surface film.

The structure of the films held for 20 min ~ 10 min (Fig 4-51 ~ Fig 4-53) was the same as in the 25-min film. All the films had an outer S-rich layer and an inner layer composed of MgF_2 and MgO, but the thickness of the outer layer decreased with reduction in holding time.

The film held for 5 min (Fig 4-54) had a different structure. There was only one single layer consisting of MgF_2 and MgO, in this surface film. Sulphur, aluminium, and zinc could not be seen in the film based on the EDS element map, but there was a Mg-Al phase under the film.

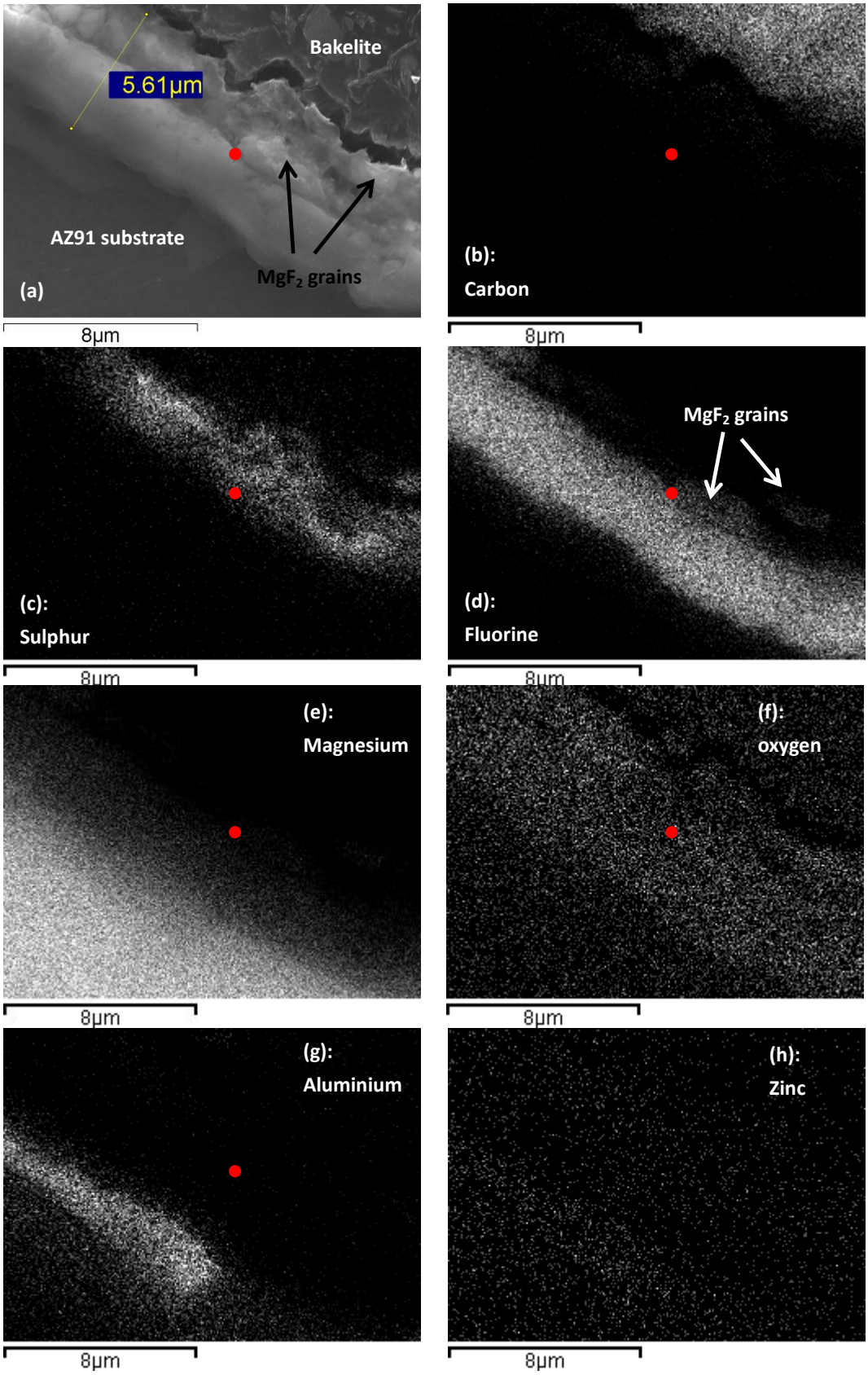

Fig 4-49 (a) a surface film formed in AZ91 + 0.5%SF_6/air, held at 700 ^{o}C for 30 min; Element map (b) C, (c) S; (d) F; (e) Mg, (f) O, (g) Al, (h) Zn. The red point in (a ~ h) denotes the location of the boundary between two layers in (a) ~ (f).

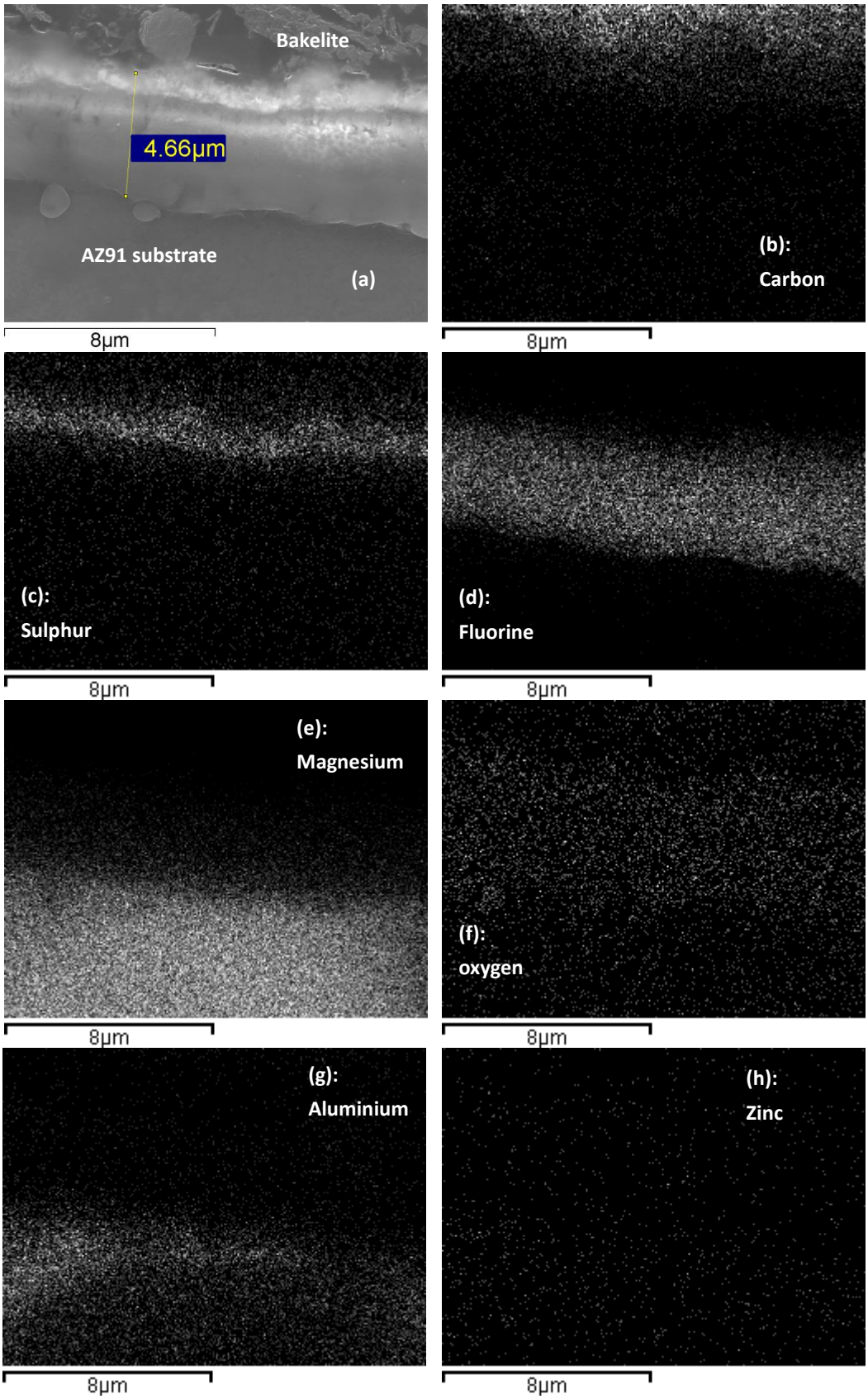

Fig 4-50 (a) a surface film formed in AZ91 + 0.5%SF_6/air, held at 700 ^{o}C for 25 min (b ~ f) element map corresponding to (a): (b) C, (c) S; (d) F; (e) Mg, (f) O, (g) Al, (h) Zn.

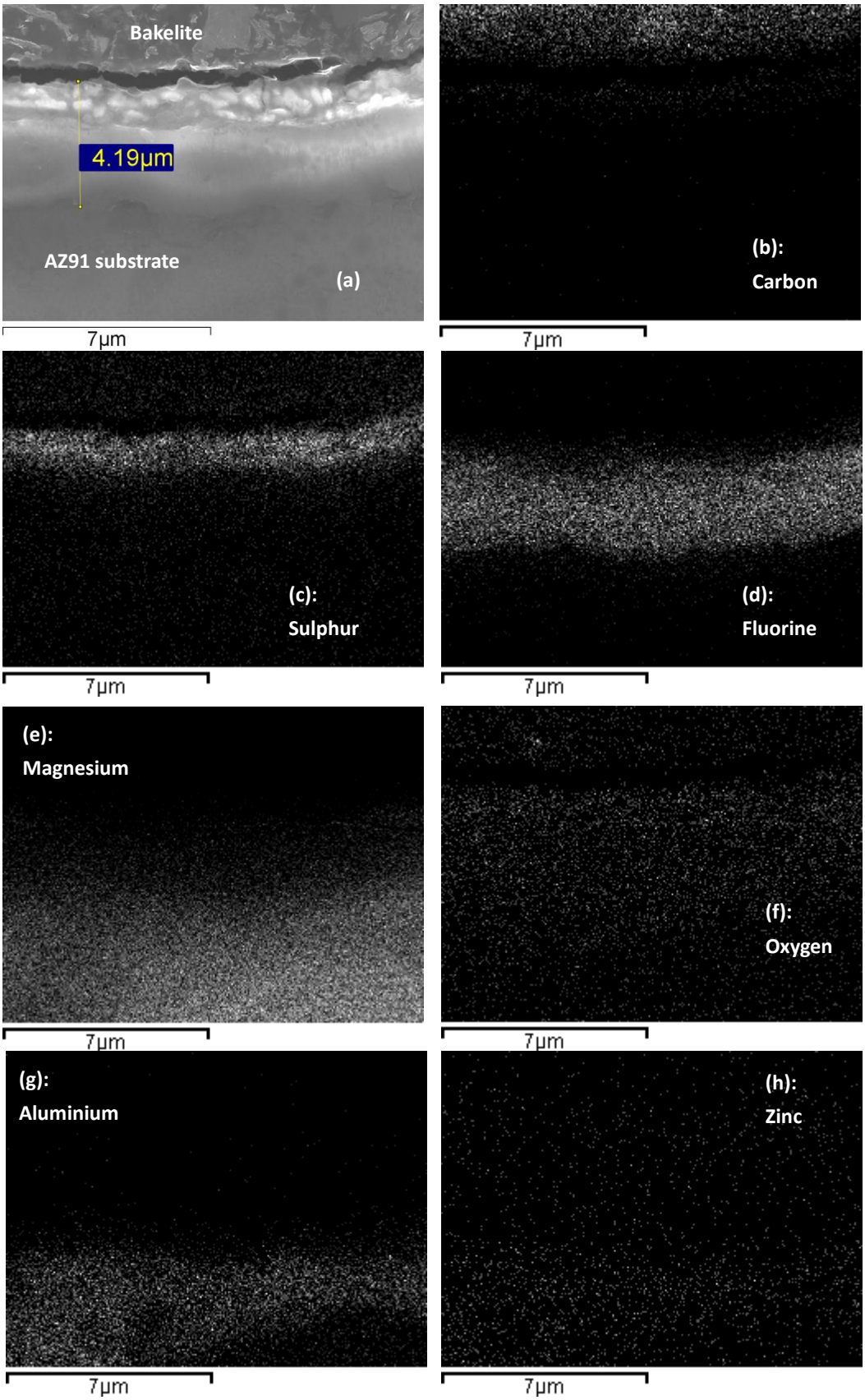

Fig 4-51 (a) a surface film formed in AZ91 + 0.5%SF6/Air, held at 700 ^{o}C for 20 min (b ~ f) element map corresponding to (a): (b) C, (c) S; (d) F; (e) Mg, (f) O, (g) Al, (h) Zn.

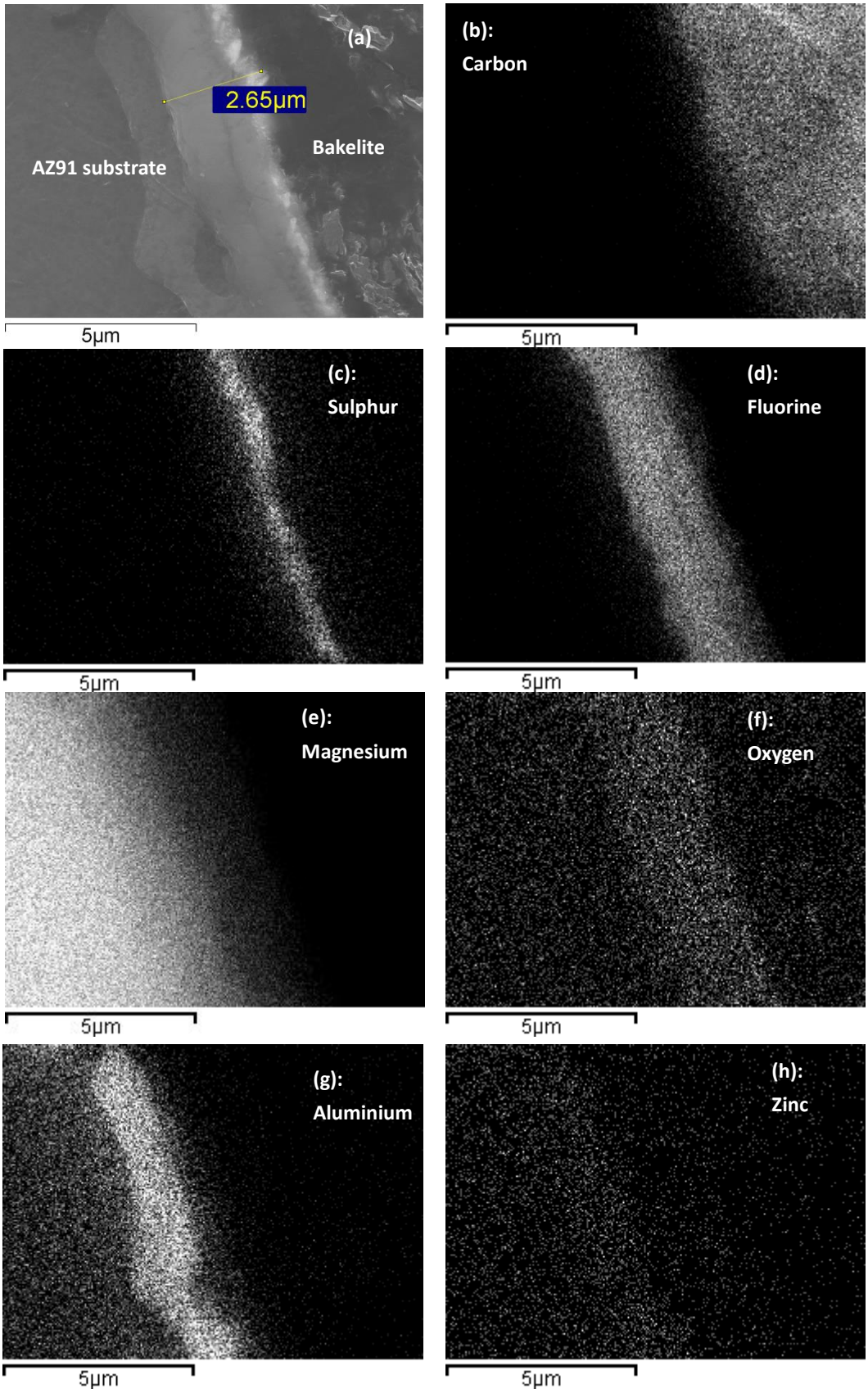

Fig 4-52 (a) a surface film formed in AZ91 + 0.5%SF_6/air, held at 700 ^{o}C for 15 min (b ~ f) element map corresponding to (a): (b) C, (c) S; (d) F; (e) Mg, (f) O, (g) Al, (h) Zn.

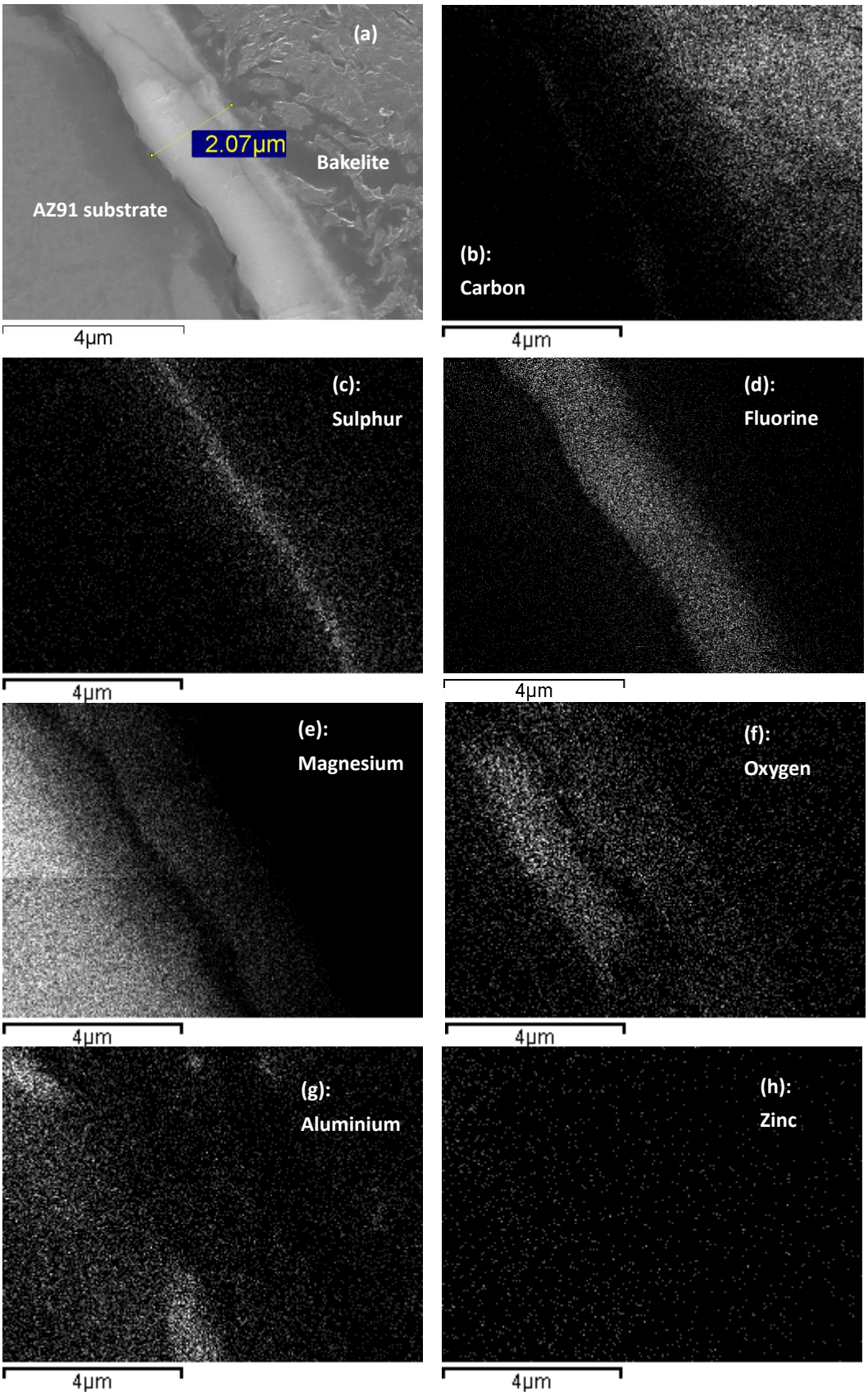

Fig 4-53 (a) a surface film formed in AZ91 + 0.5%SF_6/air, held at 700 ^{o}C for 10 min (b ~ f) element map corresponding to (a): (b) C, (c) S; (d) F; (e) Mg, (f) O, (g) Al, (h) Zn.

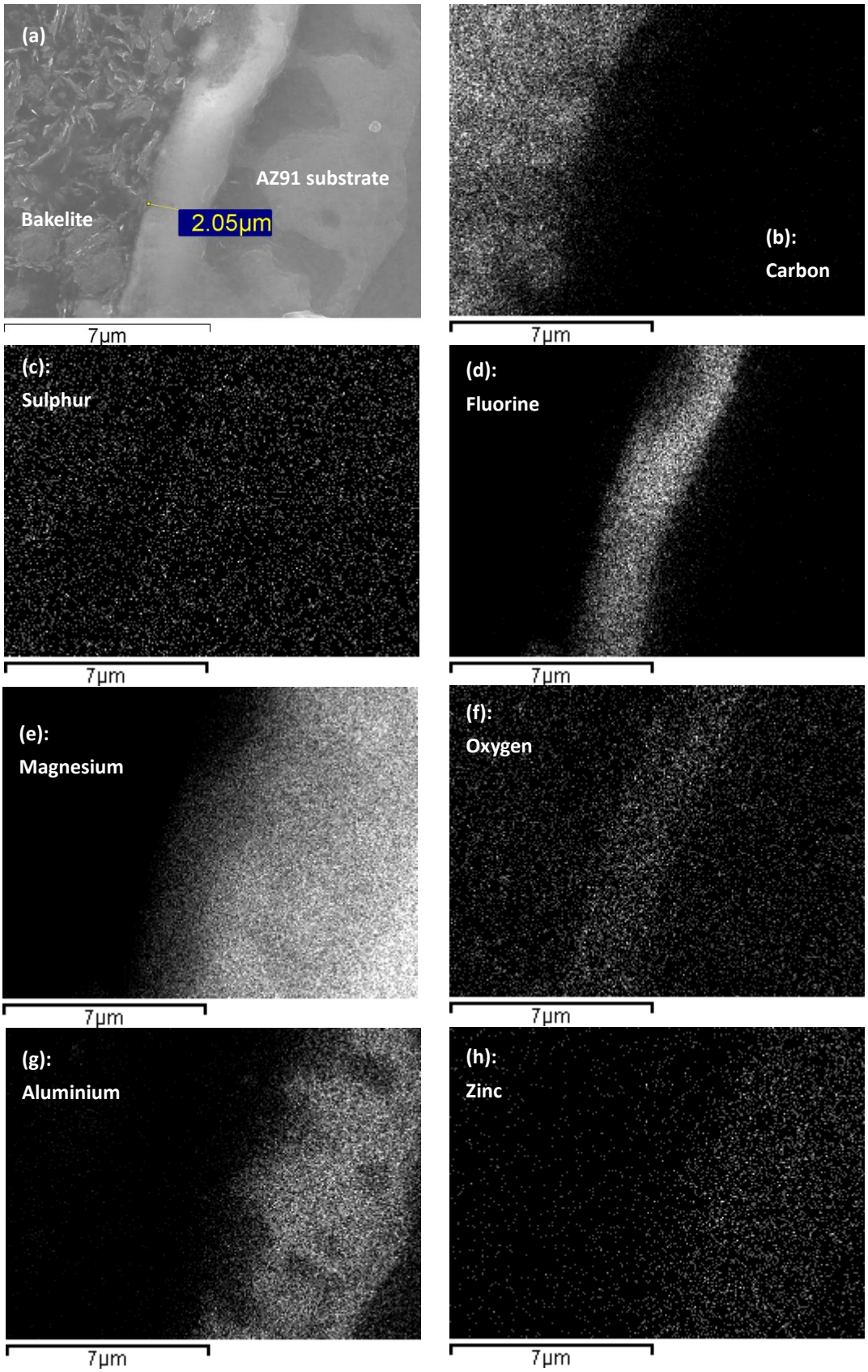

Fig 4-54 (a) a surface film formed in AZ91 + 0.5%SF_6/air, held at 700 ^{o}C for 5 min. Element map corresponding to (a): (b) C, (c) S; (d) F; (e) Mg, (f) O, (g) Al, (h) Zn.

4.3.4 AZ91 melt in SF_6/CO_2

The cross sections of the surface films, grown on an AZ91 melt surface under a cover gas of 0.5%SF_6/CO_2, are shown in Fig 4-55 ~ Fig 4-60.

Fig 4-55 and Fig 4-56 reveal a double-layer structure of the surface films held for 30 and 25 min. The inner layer was of a compact and uniform appearance, and the EDS results indicated that this inner layer was mainly composed of MgF_2. However, the outer layer consisted of MgF_2 grains and MgO. Sulphur was not detected in this film, which was different from the surface film formed in AZ91 +0.5%SF_6/air,

As shown in Fig 4-57, the 20-min film presented a mixed structure: a section had a similar double-layer structure to the 30-min film, while the other part had only a single layer composed of a uniform mixture of MgF_2 and MgO.

All the surface films held for 15 min ~ 5 min (Fig 4-58 ~ Fig 4-60) presented a single layer structure, mainly consisting of MgF_2. The existence of MgO could not be clearly confirmed in these films. Compared with the clear detection of oxygen in the 20 ~ 30 min films, it can be suggested that fluorides in the cover gas would be preferentially consumed at the early stage of the film growth process.

As in the films shown in Fig 4-49 ~ Fig 4-54, aluminium and zinc were not detected in all the films formed on an AZ91 melt surface under a cover gas of 0.5%SF_6/CO_2. This

was inconsistent with the results shown in Fig 4-28 ~ Fig 4-32, which indicated Al in the oxide films of the double oxide film defects formed in AZ91 alloy. This might be due to an extension of the holding time of the oxide film which could lead to the following reaction:

(1) $3Mg + Al_2O_3 = 3MgO + 2Al$, $\triangle G(700^oC) = -119.82$ kJ,

(2) $Mg + MgAl_2O_4 = MgO + Al$, $\triangle G(700^oC) = -106.34$ kJ.

Thus no Al could be found in the surface films shown in Fig 4-49 ~ Fig 4-60, which were held at 700 ^oC for at least 5 min. By contrast the double oxide film defects, shown in sections 4.2.3 ~ 4.2.4 (Fig 4-28 ~ Fig 4-32), were not held in the melt for a long time, since the casting solidified in the sand mould in less than about 2 min. This could be the reason why Al was detected in these double oxide films. In addition, Wang and Xiong [75] also revealed that the aluminium concentration in the oxide film reduced with an increase of the sample holding time at 680^oC, when they used SO_2 to protect liquid AZ91D alloy.

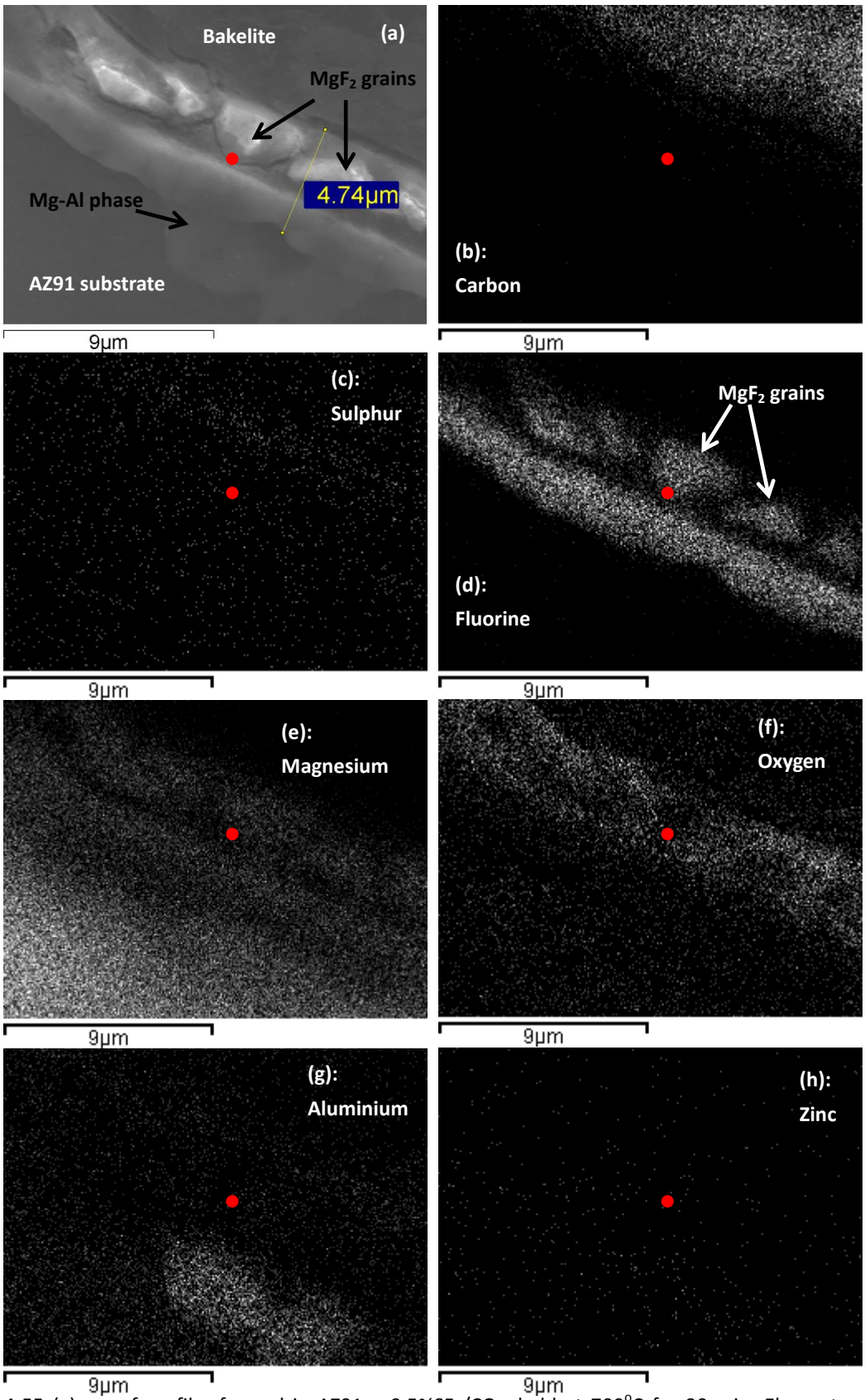

Fig 4-55 (a) a surface film formed in AZ91 + 0.5%SF_6/CO_2, held at 700°C for 30 min. Element map corresponding to (a): (b) C, (c) S; (d) F; (e) Mg, (f) O, (g) Al, (h) Zn. The red point in (a ~ h) denotes the location of the boundary between the two layers.

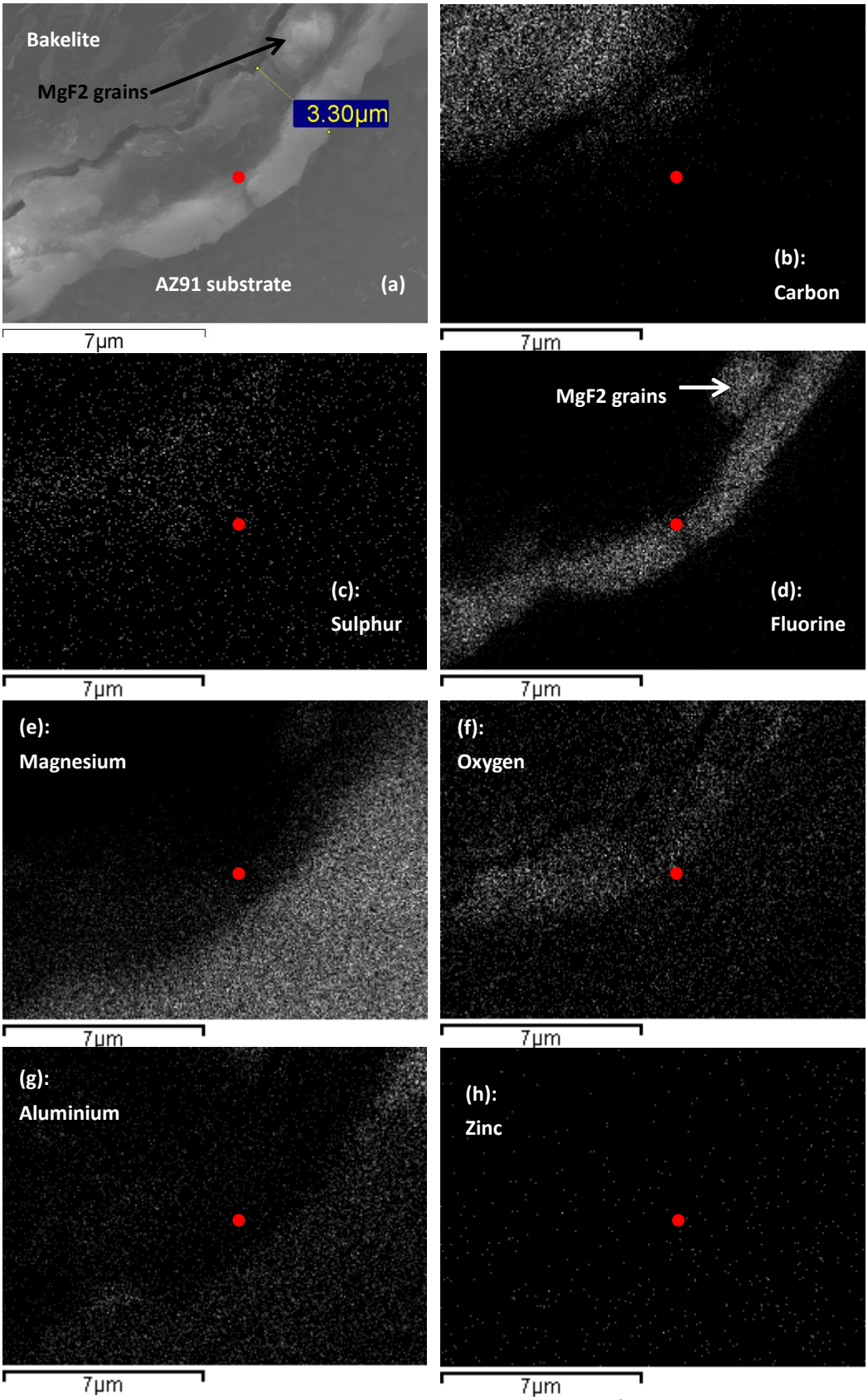

Fig 4-56 (a) a surface film formed in AZ91 + 0.5%SF_6/CO_2, held at 700°C for 25 min. Element map corresponding to (a): (b) C, (c) S; (d) F; (e) Mg, (f) O, (g) Al, (h) Zn. The red point in (a ~ h) denotes the location of the boundary between the two layers.

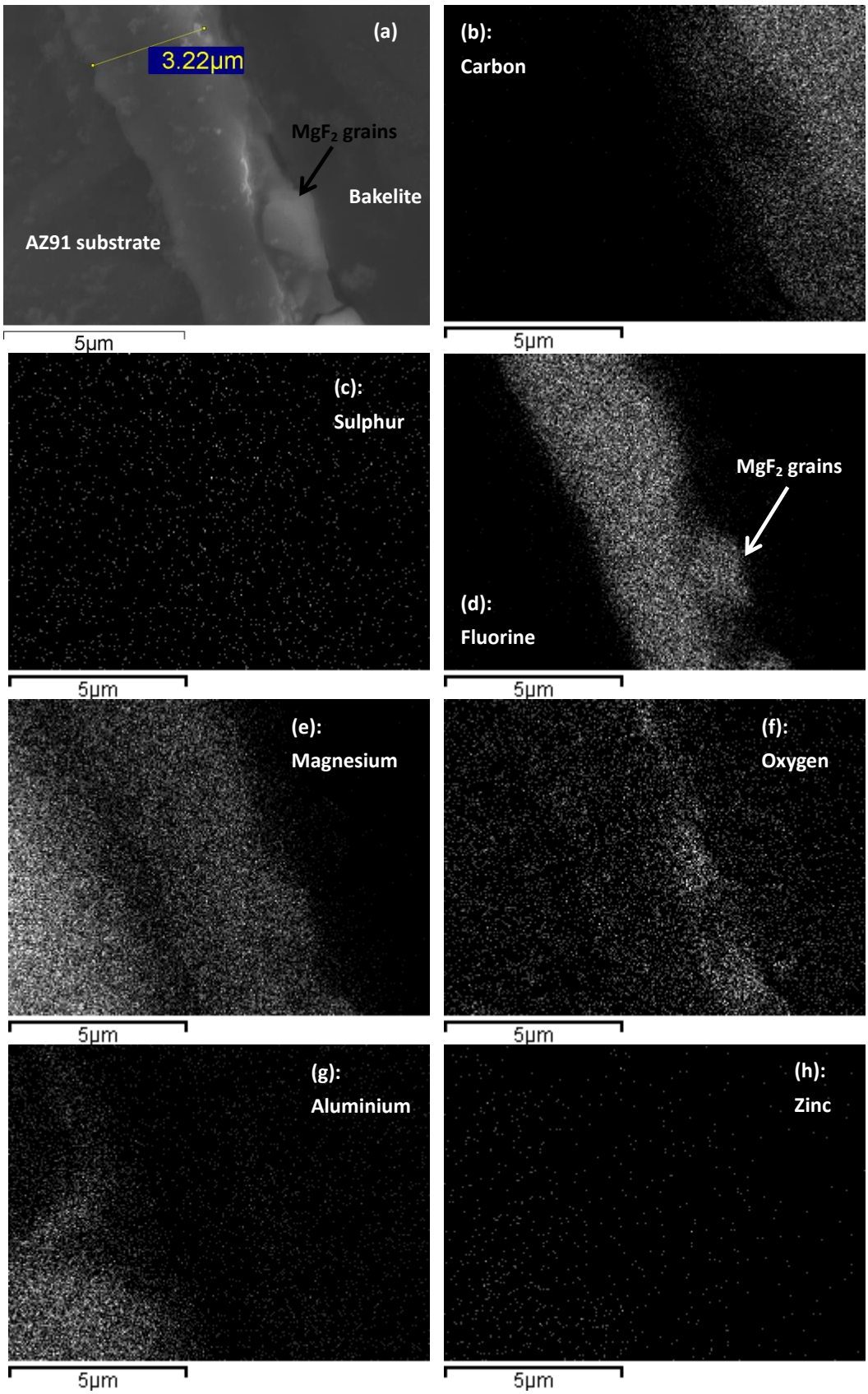

Fig 4-57 (a) a surface film formed in AZ91 + 0.5%SF_6/CO_2, held at 700°C for 20 min. Element map corresponding to (a): (b) C, (c) S; (d) F; (e) Mg, (f) O, (g) Al, (h) Zn.

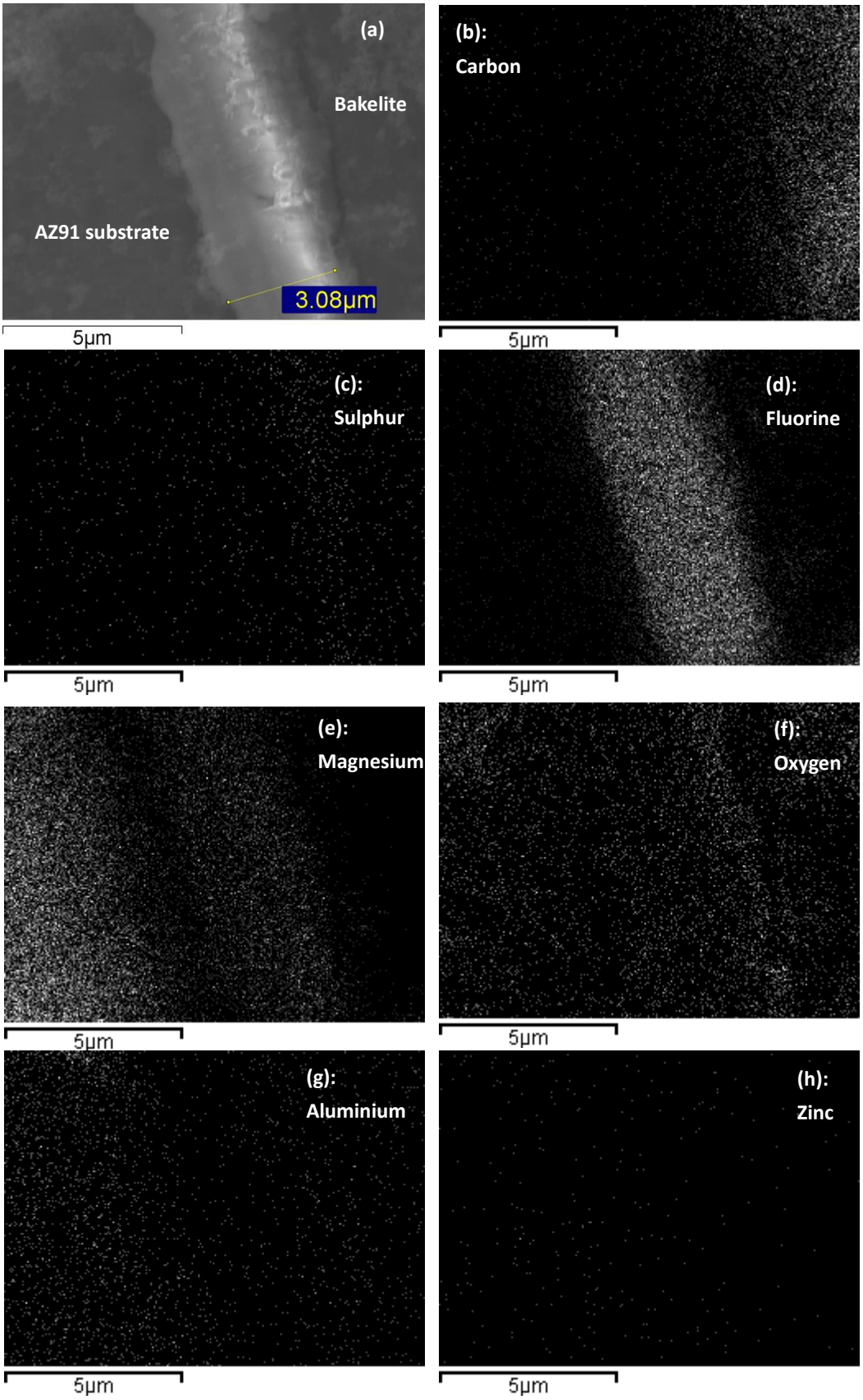

Fig 4-58 (a) a surface film formed in AZ91 + 0.5%SF_6/CO_2, held at 700^{o}C for 15 min. Element map corresponding to (a): (b) C, (c) S; (d) F; (e) Mg, (f) O, (g) Al, (h) Zn.

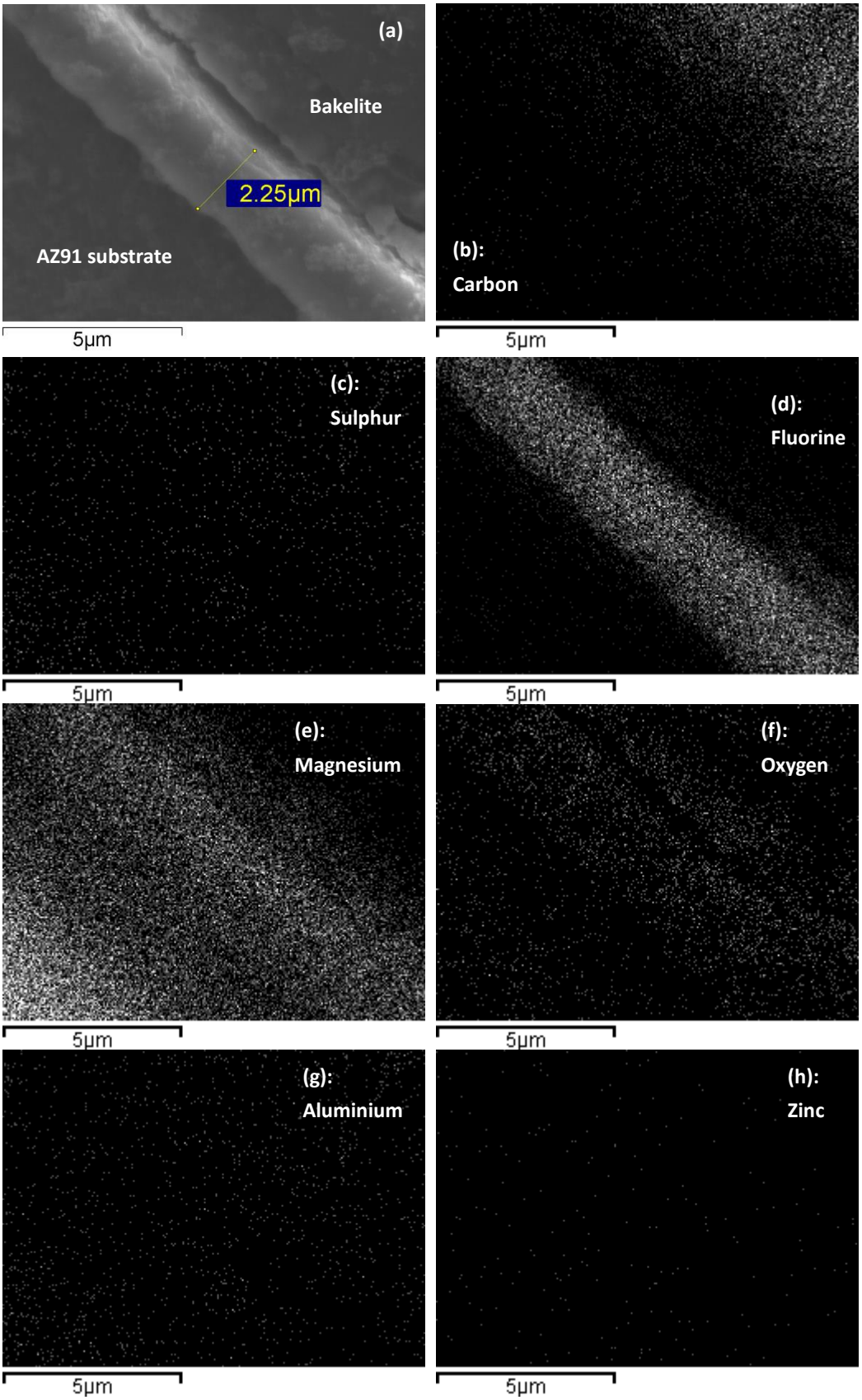

Fig 4-59 (a) a surface film formed in AZ91 + 0.5%SF_6/CO_2, held at 700°C for 10 min. Element map corresponding to (a): (b) C, (c) S; (d) F; (e) Mg, (f) O, (g) Al, (h) Zn.

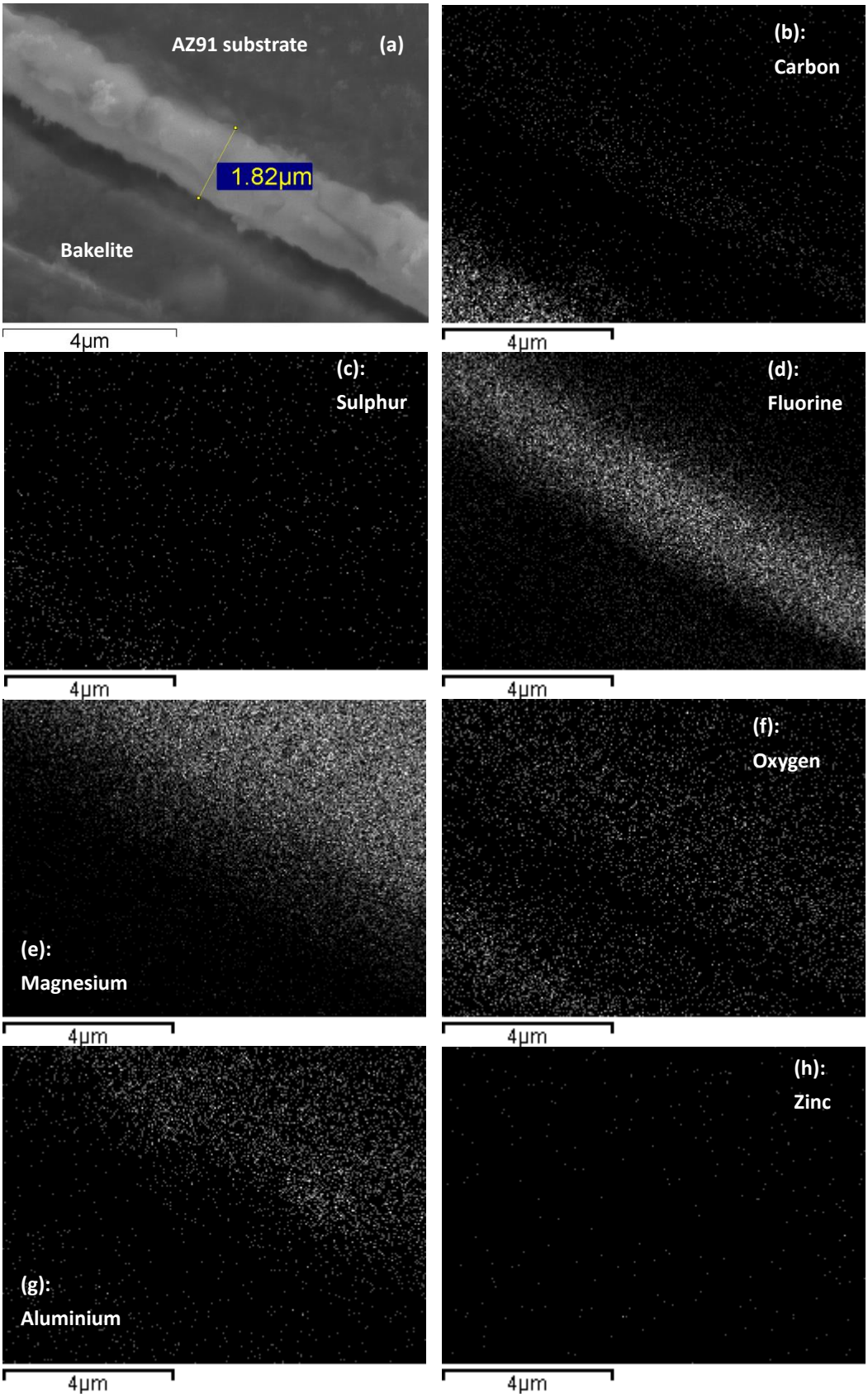

Fig 4-60 (a) a surface film formed in AZ91 + 0.5%SF_6/CO_2, held at 700°C for 5 min. Element map corresponding to (a): (b) C, (c) S; (d) F; (e) Mg, (f) O, (g) Al, (h) Zn.

4.3.5 Mg-Y melt in SF_6/air

Cross sections of the protective films formed on a Mg-Y melt surface under a cover gas of 0.5%SF_6/air, have been shown in Fig 4-61~ Fig 4-66.

Fig 4-61 shows the film held for 30 min and the corresponding EDS element map, indicating two layers to this film: an outer (thick) layer enriched with yttrium, and an inner (thin) layer having a relatively higher content of fluorine, oxygen and magnesium. Sulphur was mainly detected in the outer layer.

The 25-min and 20-min old films (Fig 4-62 and Fig 4-63) had a similar double-layer structure to the 30-min film, but the corresponding element map of the sulphur-enriched area did not show a clear boundary.

The 15-min film (Fig 4-64) presented a single-layer structure consisting of Y, Mg, O, and F. A few small F-enriched particles were found at the inner edge of the surface film. These particles might be the preliminary form of the inner layer shown Fig 4-61~ Fig 4-63. Sulphur could not be clearly recognized in this single-layer film.

The 10-min film and 5-min films also had a similar single-layer structure consisting of a mixture of yttrium, fluorine, oxygen, and magnesium, but the F-enriched particles shown in Fig 4-64(d) were not found. Sulphur concentrations were still seen in the 10-min film, but disappeared in the 5-min film.

The composition of all the films were consistent with the direct observation of a double oxide film defect on the fracture surface shown in section 4.1.5 (Fig 4-16 ~ Fig 4-17), which revealed the oxide film to mainly contain yttrium compounds, rather than Mg compounds. Thus the following equations could occur during the formation of the surface film:

(1) $Y + MgO = Y_2O_3 + Mg$;

(2) $Y + MgF_2 = YF_3 + Mg$.

In addition, the structures of these surface films indicated that a single-layer film consisting of MgF_2, MgO, YF_3 and Y_2O_3 would form first, during the film formation process. Then atomic fluorine and oxygen could penetrate through the preliminary single-layer film, forming the F-enriched inner layer or particles, as shown in Fig 4-61 and Fig 4-64. However, SO_2, which had a larger molecular size, might not be able to pass through the film, as quickly as the atomic F, and therefore the S-enriched area did not show a clear boundary as shown in Fig 4-62 ~ Fig 4-63.

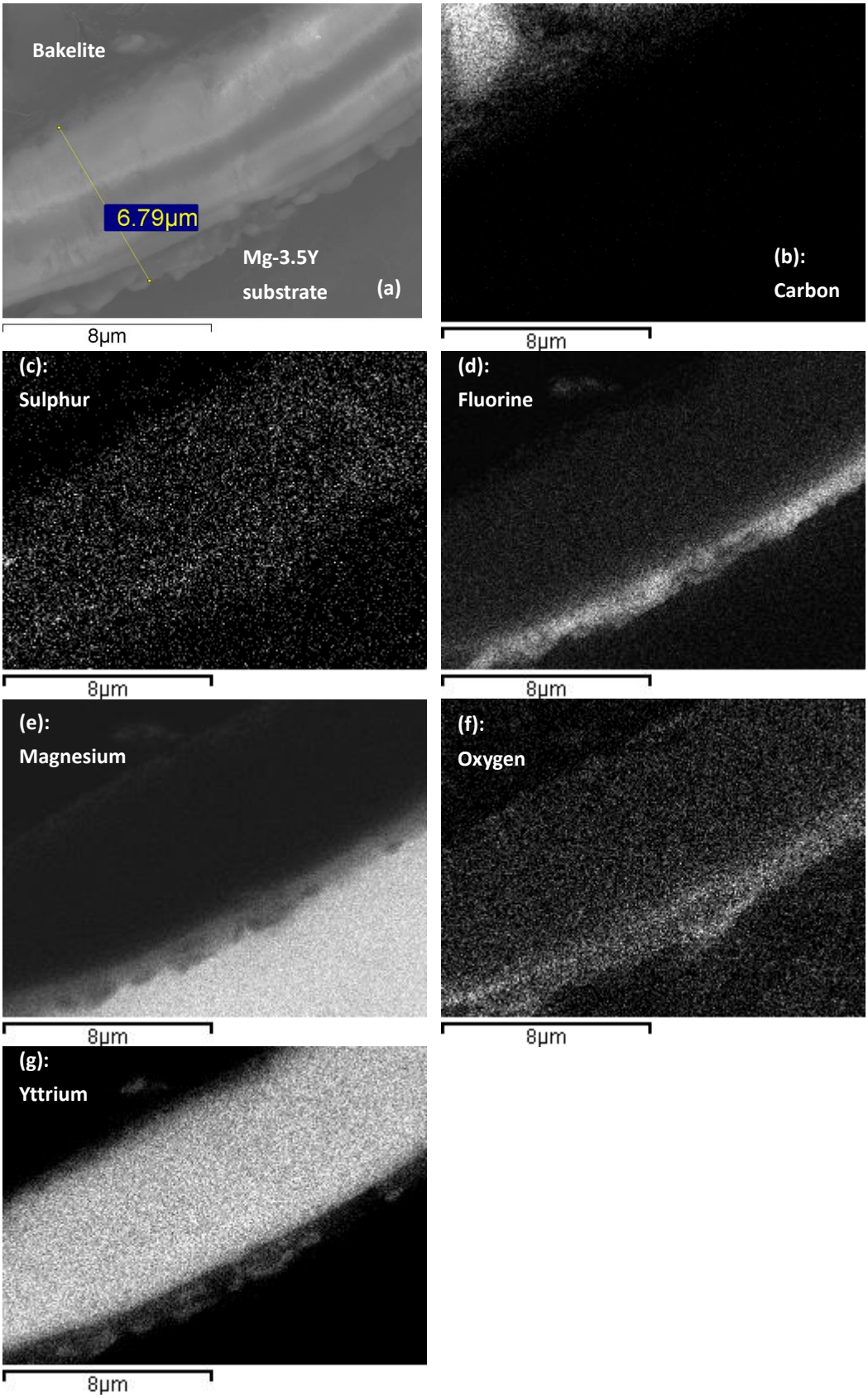

Fig 4-61 (a) a surface film formed in Mg-Y + 0.5%SF_6/air, held for 30 min. (b ~ g): the element map corresponding to (a): (b) C, (c) S; (d) F; (e) Mg, (f) O, (g) Y, the contrast of (d) and (e) was adjusted, to present the existence of magnesium and fluorine in the surface film.

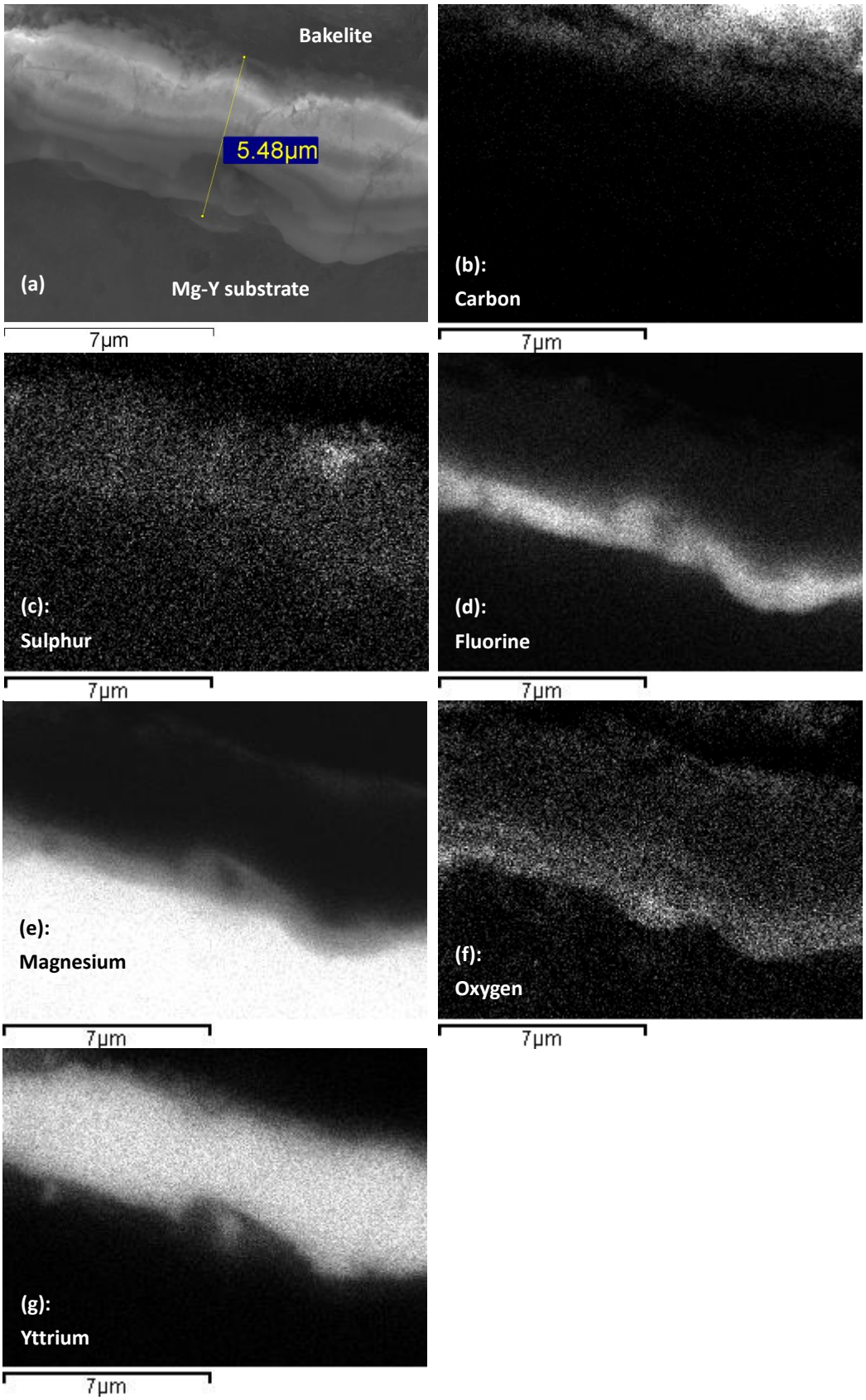

Fig 4-62 (a) a surface film formed in Mg-Y + 0.5%SF_6/air, held for 25 min. (b ~ g): the element map corresponding to (a): (b) C, (c) S; (d) F; (e) Mg, (f) O, (g) Y. The contrast of (d) and (e) was adjusted, to present the existence of magnesium and fluorine in the surface film.

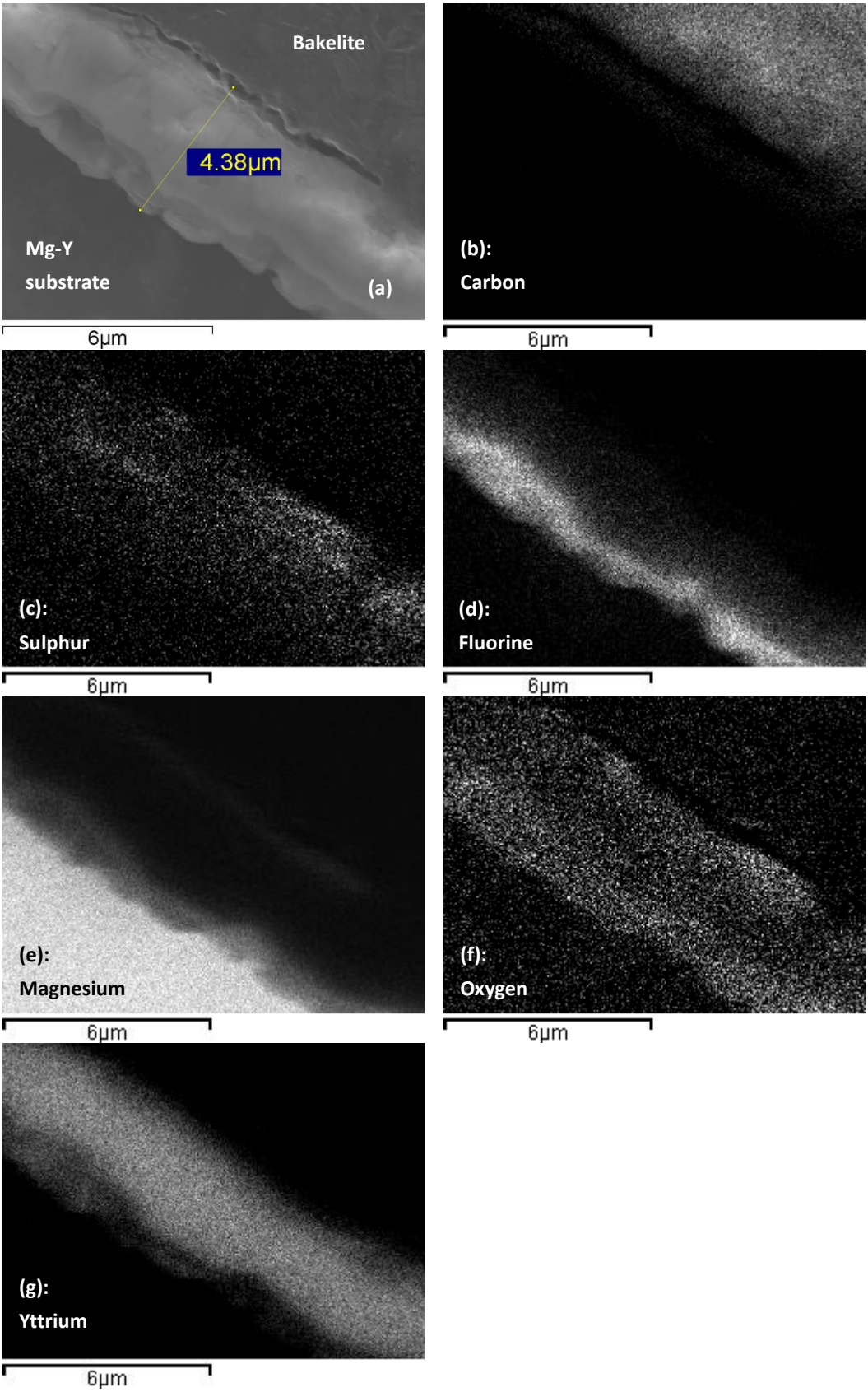

Fig 4-63 (a) a surface film formed in Mg-Y + 0.5%SF_6/air, held for 20 min. (b ~ g): the element map corresponding to (a): (b) C, (c) S; (d) F; (e) Mg, (f) O, (g) Y. The contrast of (d) & (e) was adjusted, to present the existence of magnesium and fluorine in the surface film.

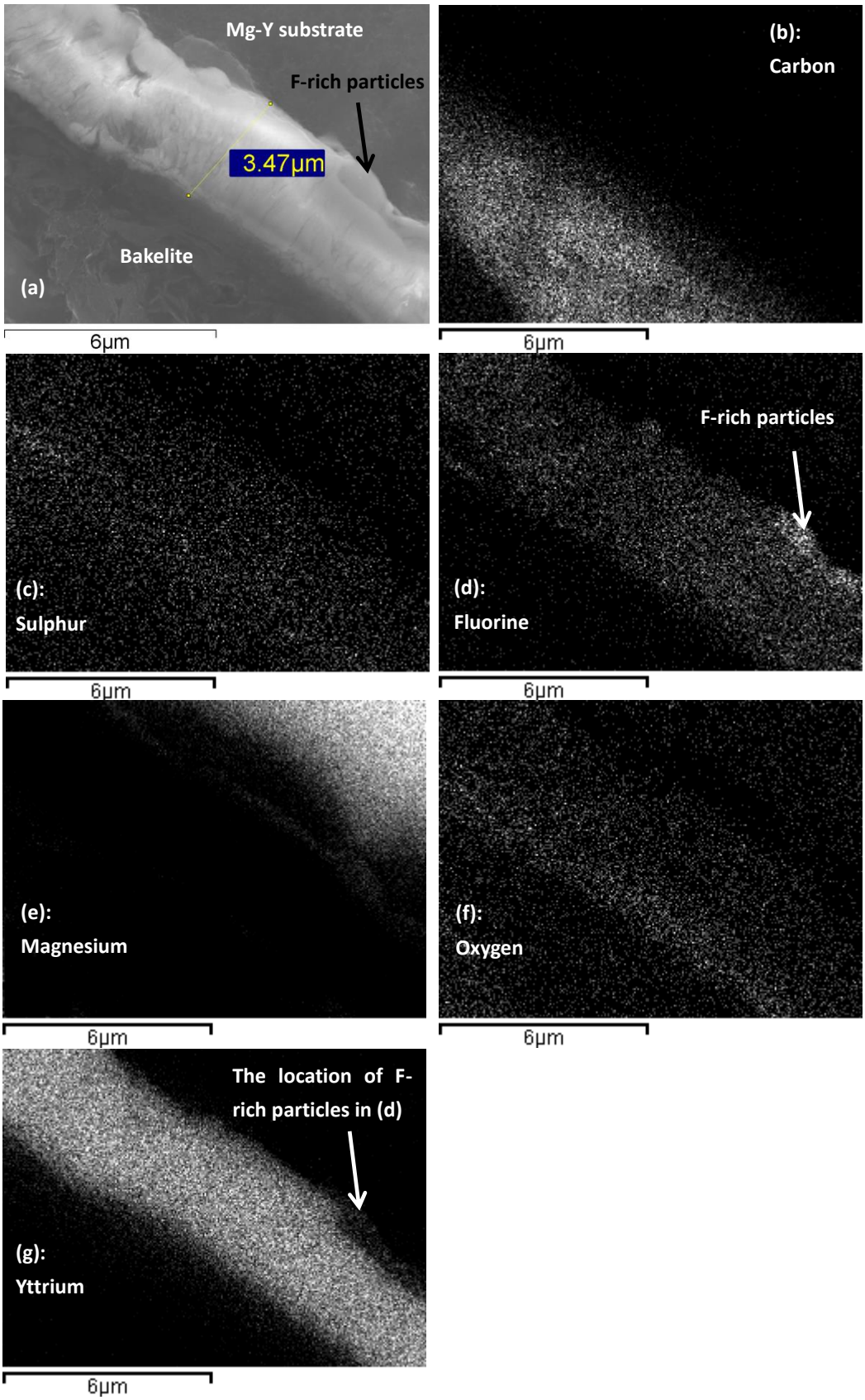

Fig 4-64 (a) a surface film formed in Mg-Y + 0.5%SF_6/air, held for 15 min. (b ~ g): the element map corresponding to (a): (b) C, (c) S; (d) F; (e) Mg, (f) O, (g) Y.

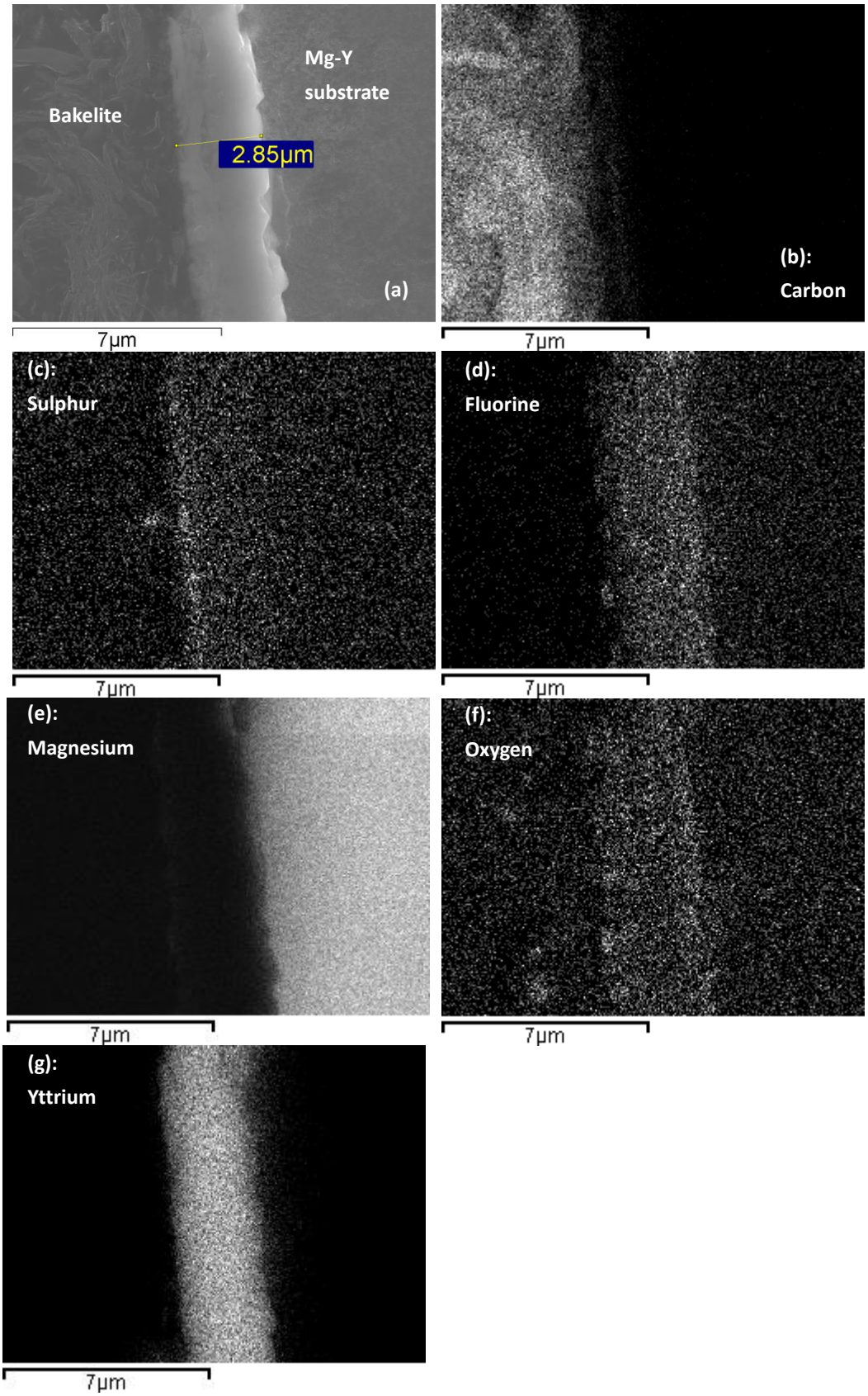

Fig 4-65 (a) a surface film formed in Mg-Y + 0.5%SF_6/air, held for 10 min. (b ~ g): the element map corresponding to (a): (b) C, (c) S; (d) F; (e) Mg, (f) O, (g) Y. The contrast of (d) was adjusted, to present the existence of magnesium.

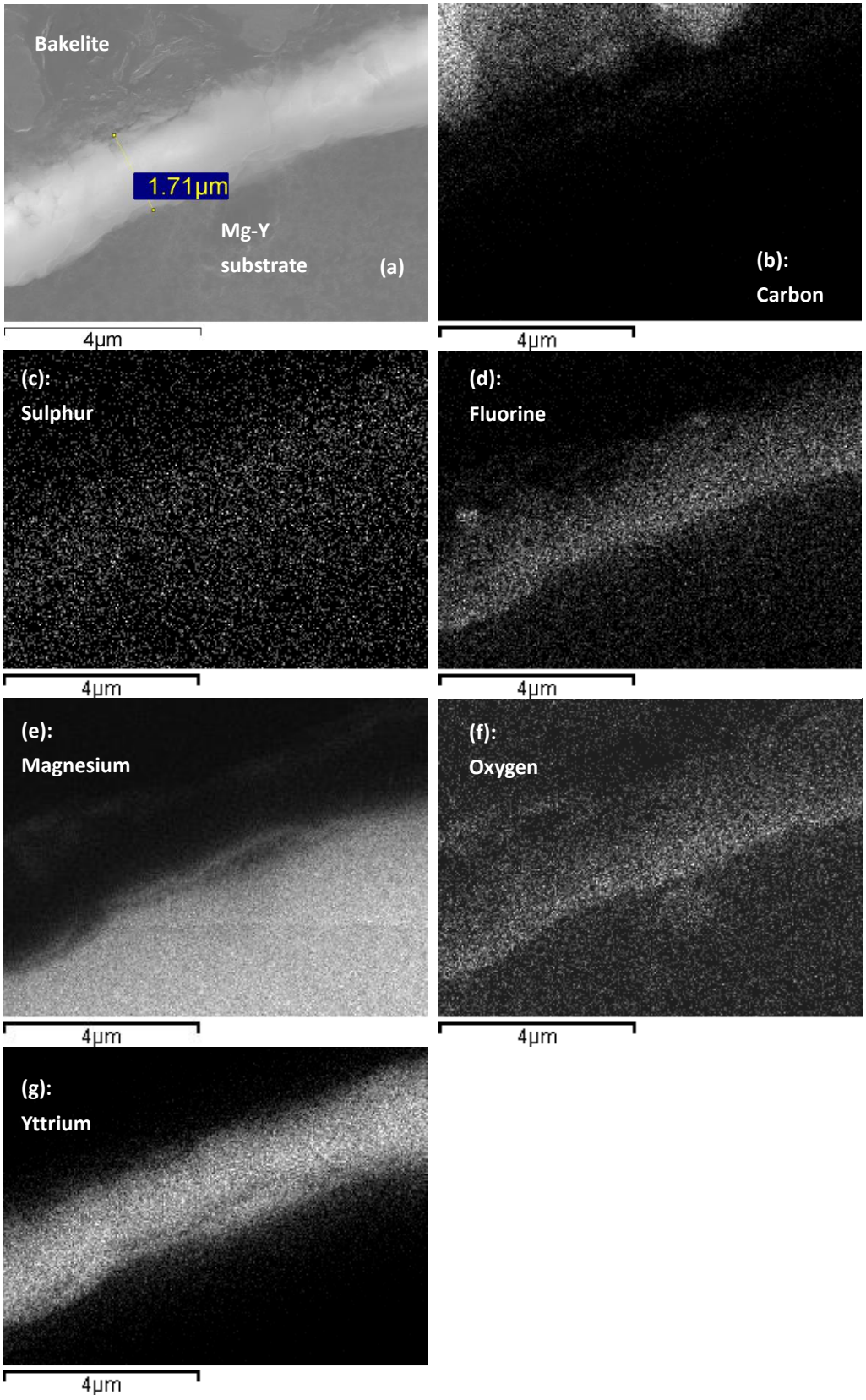

Fig 4-66 (a) a surface film formed in Mg-Y + 0.5%SF_6/air, held for 5 min. (b ~ g): the element map corresponding to (a): (b) C, (c) S; (d) F; (e) Mg, (f) O, (g) Y. The contrast of (d - f) was adjusted, to present the existence of magnesium and oxygen.

4.3.6 Mg-Y melt in SF_6/CO_2

Fig 4-67 ~ Fig 4-72 show cross sections of the protective films formed on a Mg-Y alloy melt surface in an atmosphere of 0.5%SF_6/CO_2. All the films showed a compact single-layer structure, rather than the double-layer structure shown in Fig 4-61. It can be seen that there were yttrium concentrations randomly distributed in the films, while fluorine was present with a uniform distribution. Oxygen was detected, which may have been in the form of MgO and Y_2O_3. Sulphur could not be found in all the films.

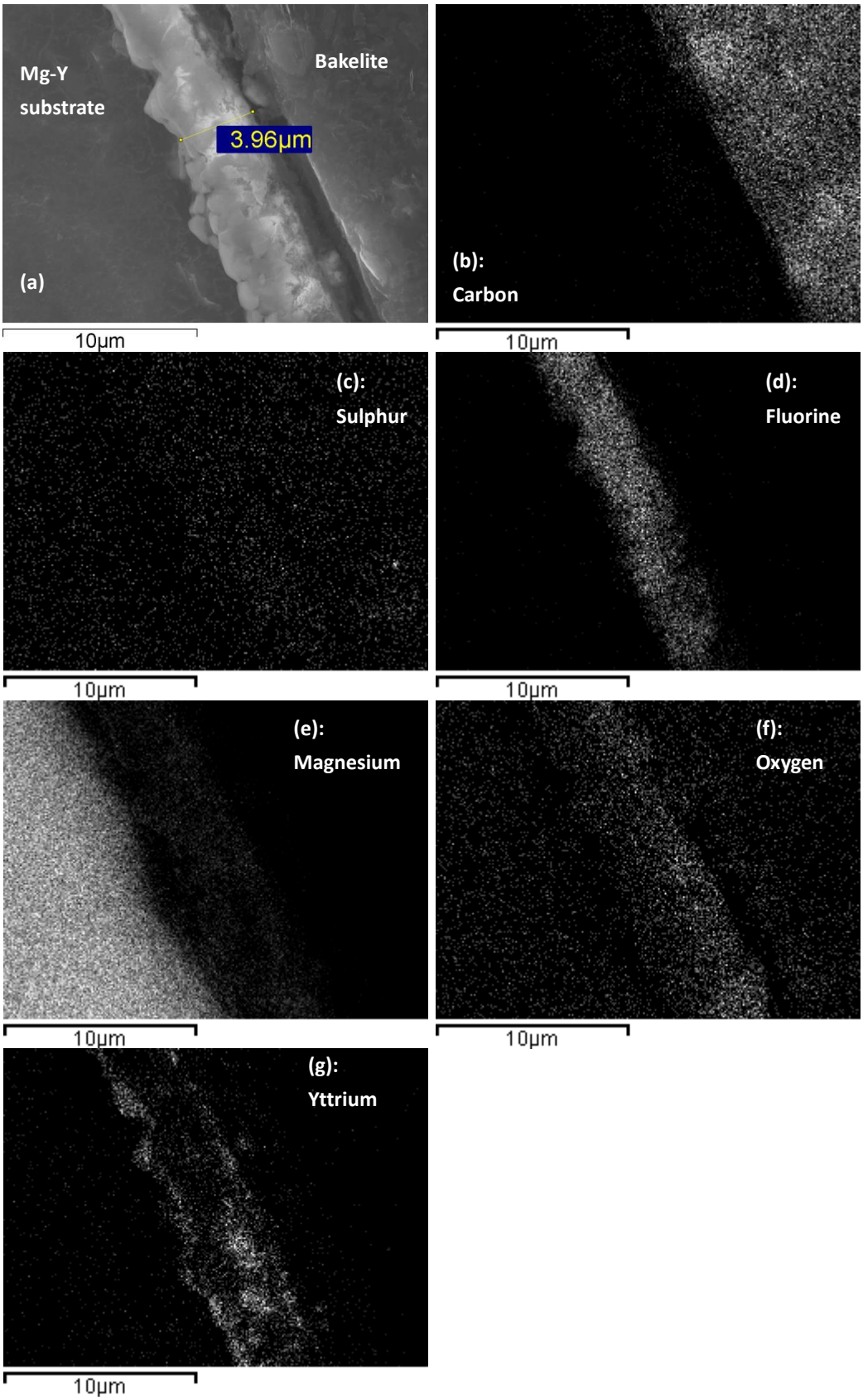

Fig 4-67 (a) a surface film formed in Mg-Y + 0.5%SF_6/CO_2, held at 700 ^{o}C for 30 min. (b ~ g): the element map corresponding to (a): (b) C, (c) S; (d) F; (e) Mg, (f) O, (g) Y.

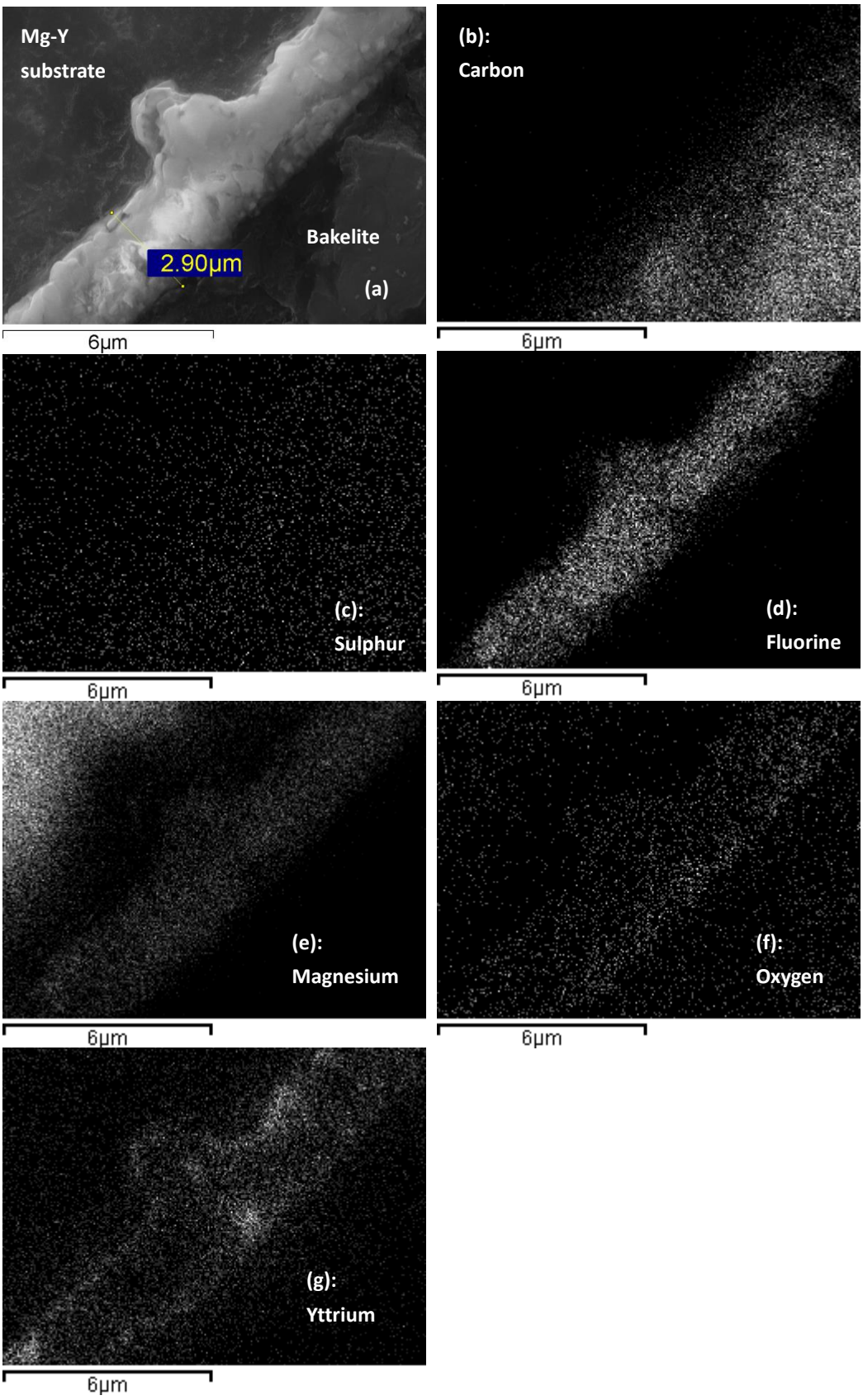

Fig 4-68 (a) a surface film formed in Mg-Y + 0.5%SF_6/CO_2, held at 700 ^{o}C for 25 min. (b ~ g): the element map corresponding to (a): (b) C, (c) S; (d) F; (e) Mg, (f) O, (g) Y.

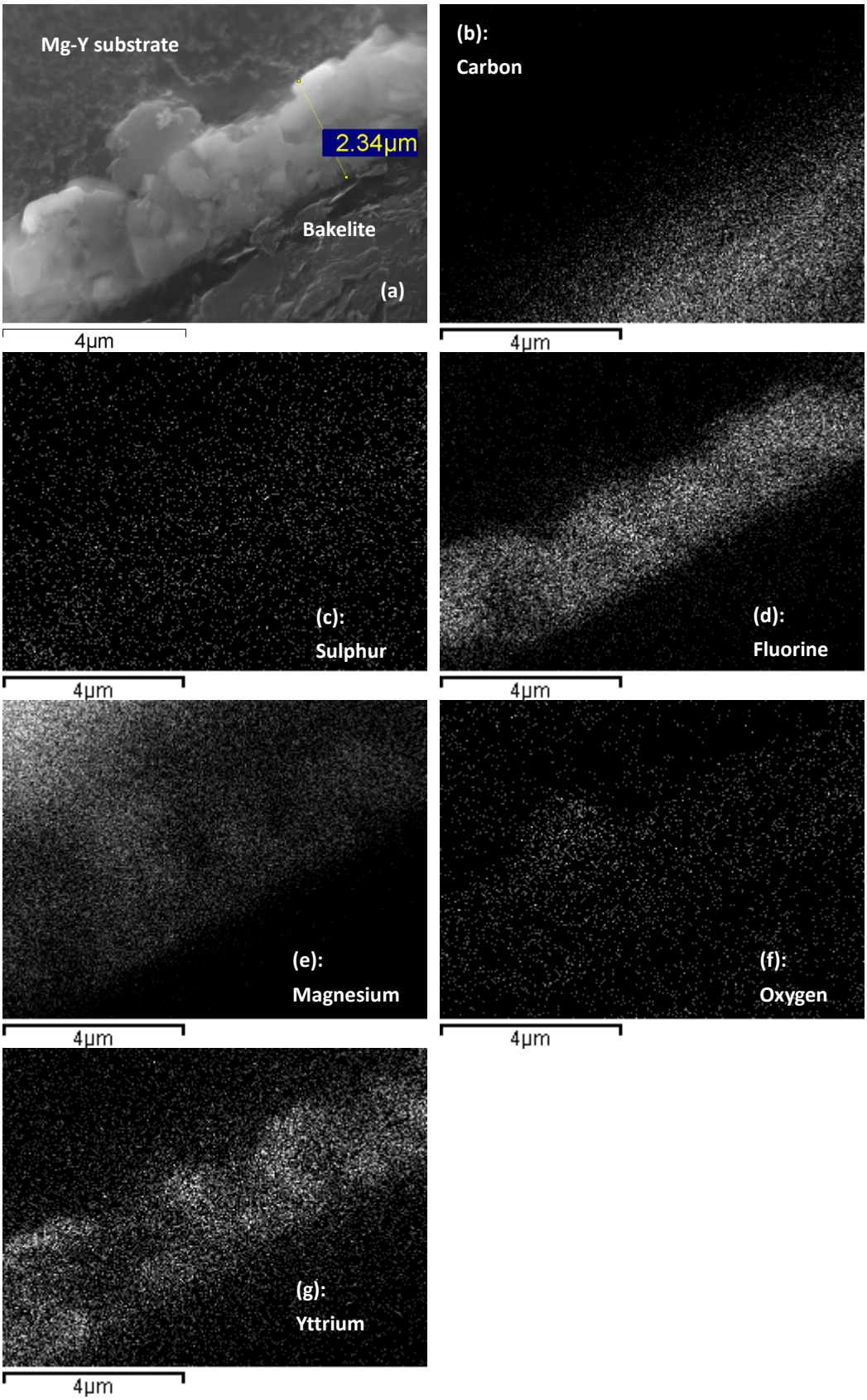

Fig 4-69 (a) a surface film formed in Mg-3.5Y + 0.5%SF_6/CO_2, held at 700 ^{o}C 20 min. (b ~ g): the element map corresponding to (a): (b) C, (c) S; (d) F; (e) Mg, (f) O, (g) Y.

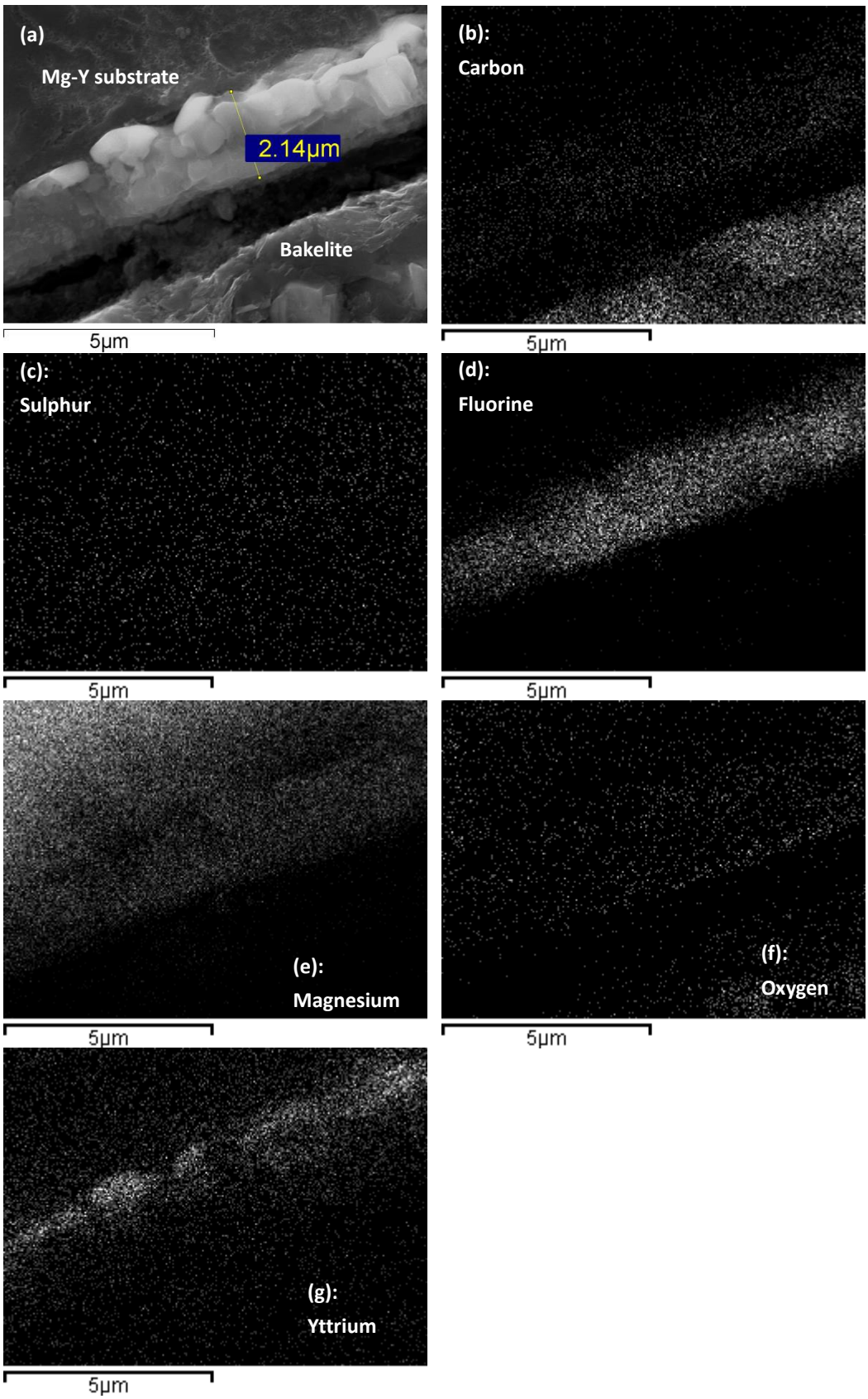

Fig 4-70 (a) a surface film formed in Mg-Y + 0.5%SF_6/CO_2, held at 700 ^{o}C for 15 min. (b ~ g): the element map corresponding to (a): (b) C, (c) S; (d) F; (e) Mg, (f) O, (g) Y.

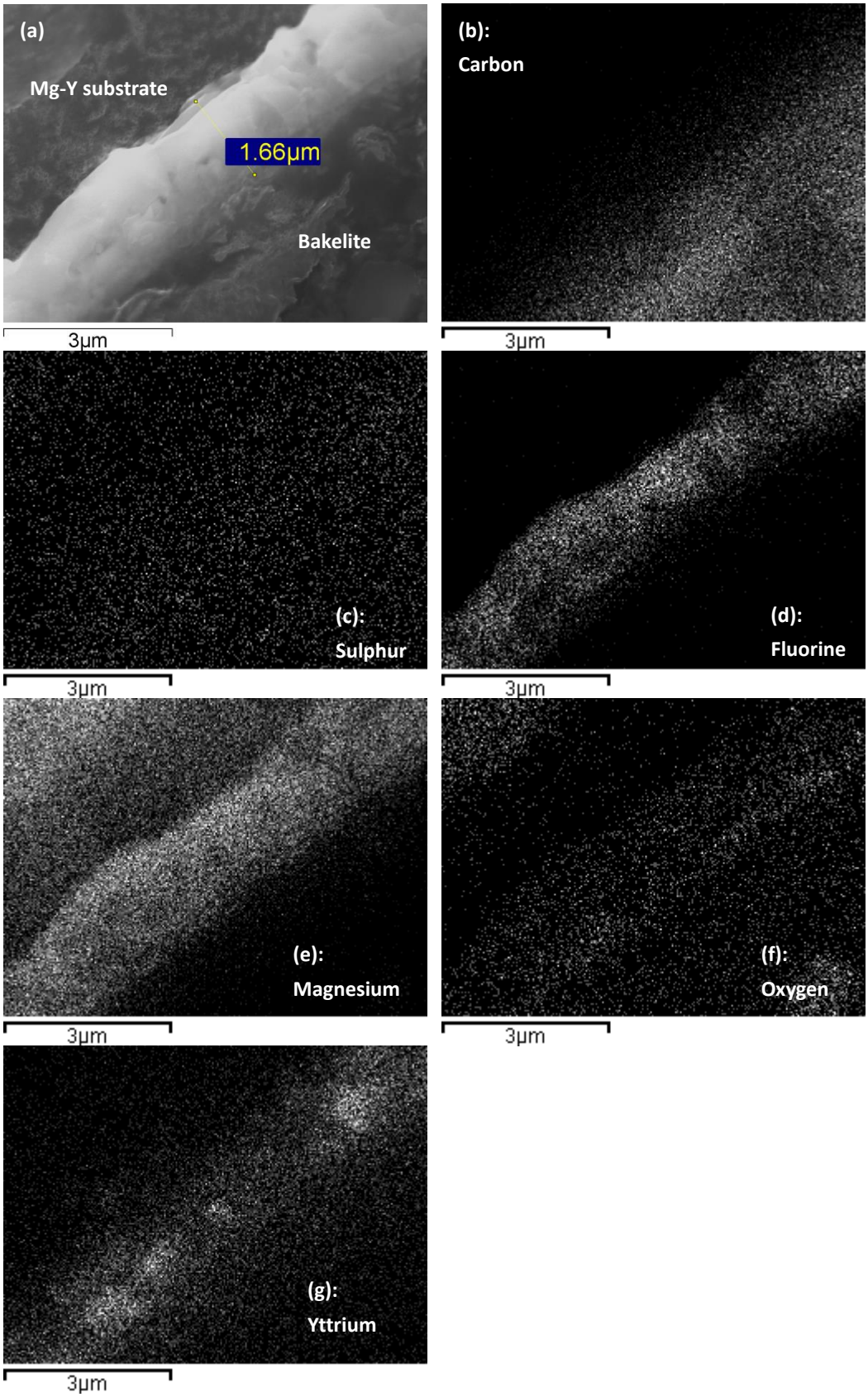

Fig 4-71 (a) a surface film formed in Mg-Y + 0.5%SF_6/CO_2, held at 700 ^{o}C for 10 min. (b ~ g): the element map corresponding to (a): (b) C, (c) S; (d) F; (e) Mg, (f) O, (g) Y.

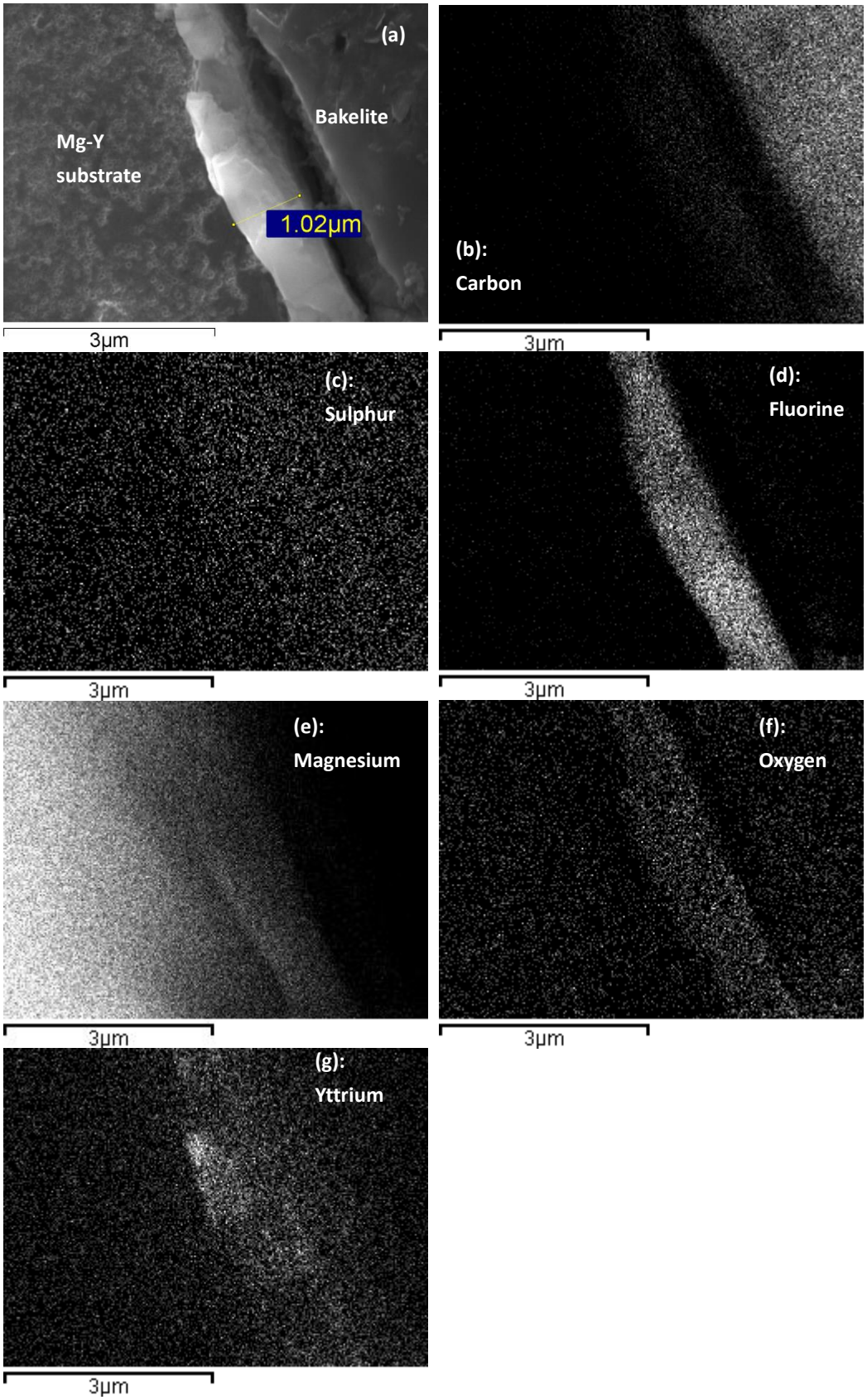

Fig 4-72 (a) a surface film formed in Mg-Y + 0.5%SF_6/CO_2, held at 700 ^{o}C for 5 min. (b ~ g): the element map corresponding to (a): (b) C, (c) S; (d) F; (e) Mg, (f) O, (g) Y.

4.3.7 The growth rates of the surface films formed in different alloys and atmospheres

Fig 4-73 summarizes the relationship between the holding time and the average thickness of the surface films shown in sections 4.3.1 ~ 4.3.6 (Fig 4-37 ~ Fig 4-72). All the films became thicker with increased holding time. This growth indicated that the protective surface films, which slow the rapid oxidation process of a Mg-alloy melt, could not completely isolate the melt from the surrounding atmosphere. The atoms in the cover gases and the melts, such as atomic F and Mg, could still penetrate through the surface films, reacting with each other and increasing the thickness of the films.

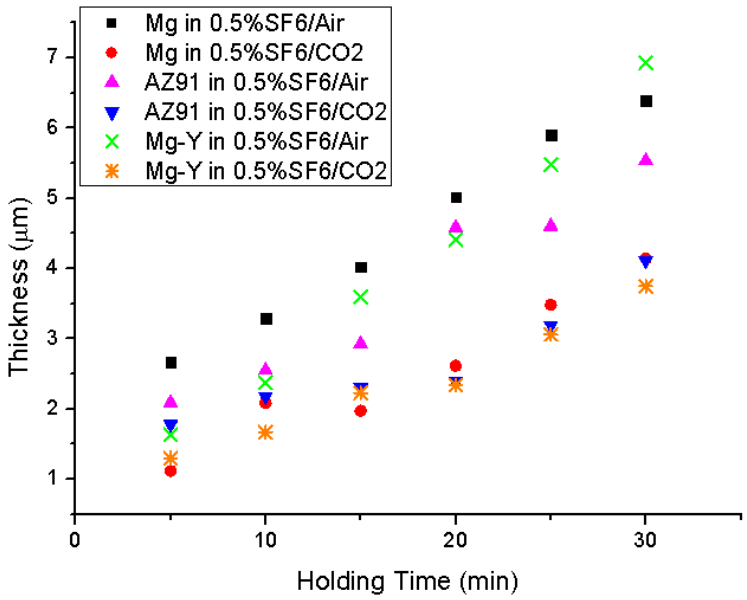

Fig 4-73 the average film thickness of the films shown in Fig 4-37~ Fig 4-72.

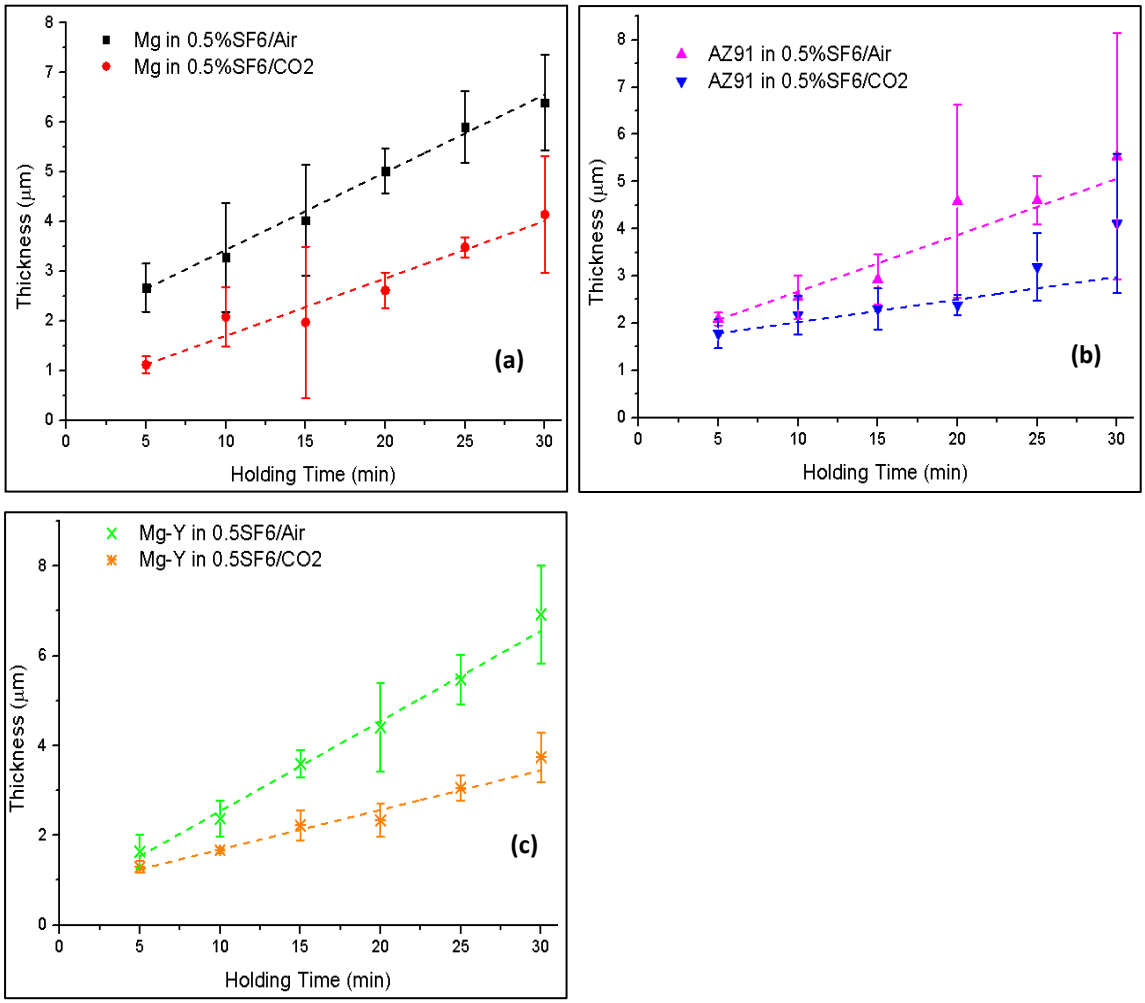

Fig 4-74 comparison of the growth rates in 0.5%SF_6/air and 0.5%SF_6/CO_2, (a) films growing on Mg melt surface; (b) films growing on AZ91 melt surface; (c) films growing on Mg-Y melt surface.

Fig 4-74 shows a comparison of the growth rates of the surface film formed in different cover gases (i.e. 0.5%SF_6/air & 0.5%SF_6/CO_2). The 95% confidence interval (95%CI) was computed via the following equation [107], under an assumption that the variation of the film thickness followed a Gaussian distribution:

$$\text{Eq. 4-1:} \qquad 95\%CI = \text{average thickness} \pm Z_{0.95} * SE$$

where $Z_{0.95}$ =1.96 was the 97.5% quantile of the standard Gaussian distribution, and

SE denoted the standard error. It can be seen that all the surface films formed in 0.5%SF_6/air grew faster than the films formed in 0.5%SF_6/CO_2, which is consistent with the results of Lee, et al. [85], who suggested that SF_6/CO_2 was more protective than SF_6/air for pure Mg melt, according to an ignition test. The different growth rates suggested that the consumption rate of the Mg-alloy melts in 0.5%SF_6/CO_2 was less than the rate in 0.5%SF_6/air.

Fig 4-74 indicated a linear relationship between the data points of the film thickness, but Lee et al. [85] suggested a parabolic rate of film growth when they studied Mg surface film growth under a cover gas containing less than 0.05% SF_6. The difference between Fig 4-74 and Lee's results may be due to the length of holding time. According to Lee's result [85], the surface film growth rate clearly decreased with increasing film thickness, when the holding time was longer than 2 hours. However, when the holding time was less than 1 hour, this growth rate reduction was not clear, and the data points of the film thickness were approximately linearly distributed. Therefore, the growth rate of the surface films shown in Fig 4-74 may clearly reduce when the holding time was extended to 2 hours, since the MgF_2 concentration would increase in the surface film and accordingly make the film more protective with increasing holding time.

4.3.8 Accumulation of sulphur in the cover gas.

Section 4.3.1, 4.3.3, 4.3.5 (Fig 4-37~ Fig 4-42, Fig 4-49 ~ Fig 4-54, Fig 4-61~ Fig 4-66)

indicated that sulphur may accumulate in the cover gas in the early stage of the surface film formation process. For a further investigation of this sulphur accumulation, a further experiment was carried out using the oxidation cell (its structure was shown in Fig 3-7). During the experiment, 100g commercial purity Mg was placed in the oxidation cell. Then, 90%SF_6/air was introduced into the cell at 0.4L/min. All the valves were opened during the whole process.

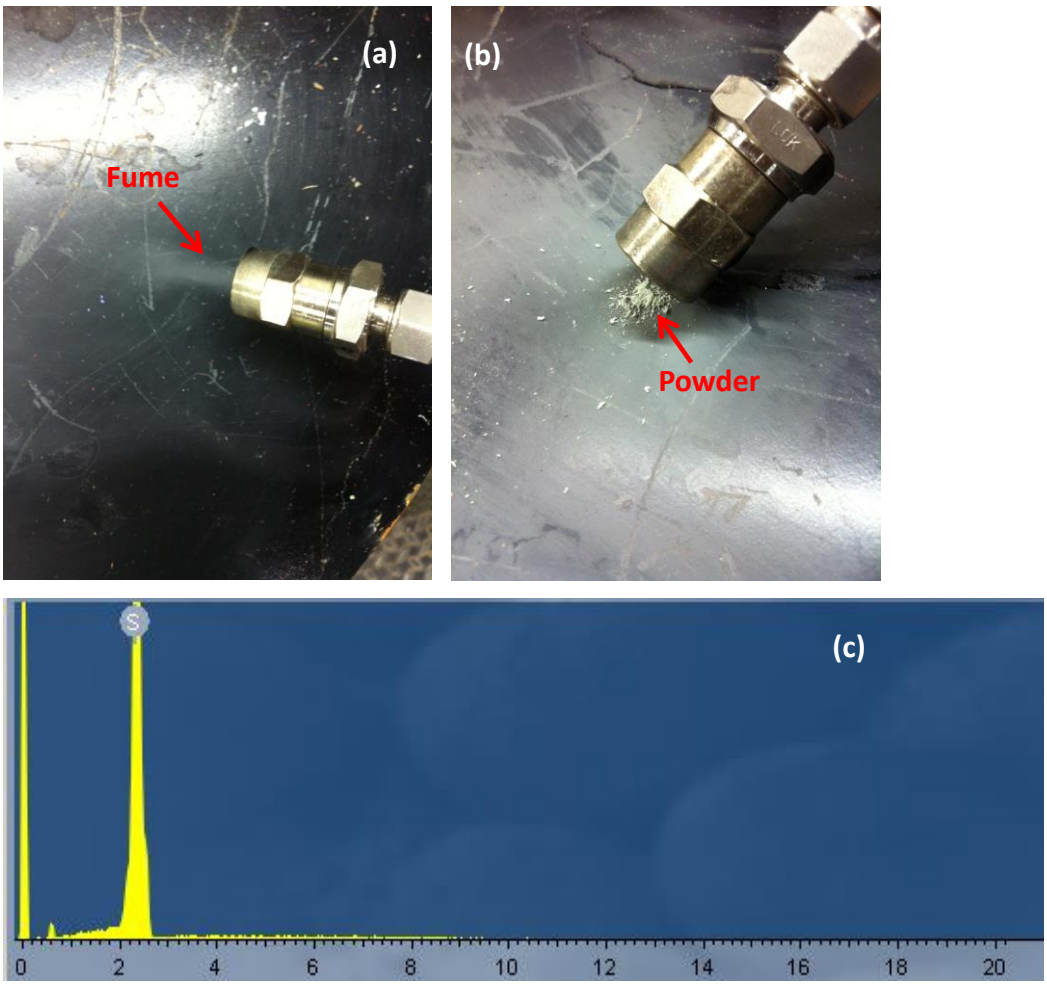

Fig 4-75 (a) a fume at the exit of the oxidation, (b) fume condensed to form powders, (c) EDS spectrum of the powder shown in (b).

As shown in Fig 4-75(a), a fume at the exit of the oxidation cell has been seen when

the oxidation cell was heated to over 500 ^{o}C. This fume subsequently condensed to form white powder (Fig 4-75(b)). EDS spectrum (Fig 4-75(c)) indicated that the powder was pure sulphur powder, demonstrating that sulphur gas was contained in the cover gas.

According to Wilkins [61], who suggested that SF_6 decomposed to provide sulphur gas at least 1700K (1426.5 ^{o}C), the detected sulphur in the cover gas may be formed due to following reaction:

$6Mg + 2SF_6 = 2MgF_2 + S_2(g)$ $\Delta G(700^{o}C) = -3996.092$ kJ.

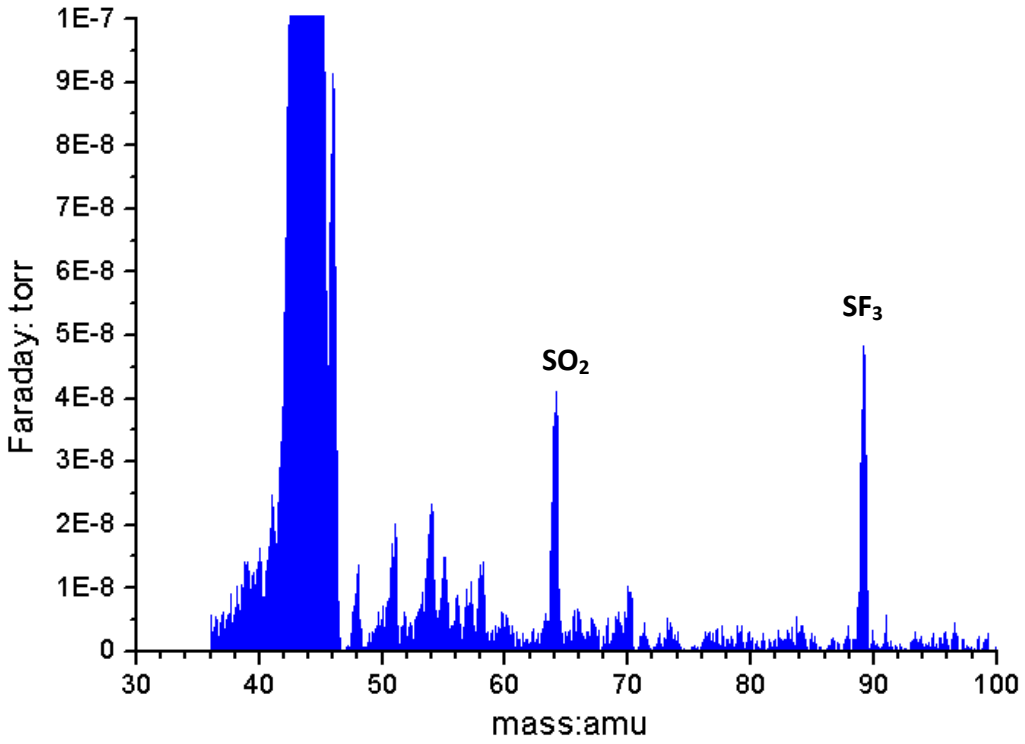

Fig 4-76 Spectrum of the cooled exhaust fumes from the oxidation cell.

Fig 4-76 shows the mass spectrum of the cooled exhaust fume from the oxidation

cell, indicating SO_2 contained in cover gas. SF_3 was also detected, demonstrating the thermal decomposition phenomenon of SF_6 suggested by [61, 128]. However, the existence of SF_4 and SF_5 can not be confirmed, since the spectrometer could not detect a gas, of which molecular mass is larger than 100.

Therefore, the detection of sulphur gas and SO_2 in the cover gas demonstrated that sulphur can accumulate in cover gas as sulphur gas or SO_2 during the surface film formation process.

4.3.9 Summary

Stages of the surface film formation process. As shown in section 4.3.1, 4.3.3, 4.3.5 (Fig 4-37~ Fig 4-42, Fig 4-49 ~ Fig 4-54, Fig 4-61~ Fig 4-66), in a cover gas of 0.5%SF_6/air, fluorine in the protective gas was preferentially consumed by the Mg-alloy melt, forming fluorides, while sulphur and oxygen accumulated in the cover gas (as shown in Fig 4-75 and Fig 4-76). Then, the sulphur and oxygen reacted with the Mg melt, forming the oxides, sulphides and sulphates in the surface film. Nitrogen was not found in all the films, but it may react with the Mg-alloy melt after a longer holding time (i.e. more than 30 min).

Therefore, a surface film formation process in 0.5%SF_6/air could be divided into the following three stages:

1. In the early stage, the Mg-alloy melt reacted with fluorides in the cover gas,

forming fluorides.

2. In the medium stage, sulphur and oxygen in the cover gas reacted with the melt, forming oxides, and sulphates or sulphides in the outer layer of the oxide film.

3. In the final stage, nitrogen reacted with the melt, forming nitrides.

Similarly, according to section 4.3.2, 4.3.4, 4.3.6 (Fig 4-43 ~ Fig 4-48, Fig 4-55 ~ Fig 4-60, Fig 4-67 ~ Fig 4-72), in a cover gas of 0.5%SF_6/CO_2, fluorine in the protective gas was preferentially consumed by the Mg-alloy melt, forming fluorides. Then, CO_2 subsequently reacted with the Mg melt, forming oxides and carbon. Sulphur was not detected in all the films formed in 0.5%SF_6/CO_2, but it may react with the Mg-alloy melt after a longer holding time (i.e. more than 30 min).

Therefore, a surface film formation process in 0.5%SF_6/ CO_2 could also be divided into the following 3 stages:

1. In the early stage, the Mg-alloy melt reacted with fluorides in the cover gas, forming fluorides.

2. In the medium stage, CO_2 in the cover gas reacted with the melt, forming oxides and carbon in the oxide film.

3. In the final stage, sulphur reacted with the melt, forming sulphides or sulphates.

Consumption rate of the cover gas. Fig 4-74 revealed a linear relationship between the oxide film thickness and the holding time. It also demonstrated that the thickness

of the surface films formed in 0.5%SF_6/CO_2 were relatively smaller than the films formed in 0.5%SF_6/air. Accordingly, a trapped gas of 0.5%SF_6/air contained in a double oxide film defect in a Mg-alloy melt can be consumed faster than a trapped gas of 0.5SF_6/CO_2.

Penetration of Mg-alloy melt. Fig 4-54 showed a double-layer structure of the surface film held for 30 min: an outer layer enriched with sulphur and an inner layer composed of MgF_2. However, the corresponding 5-min film (Fig 4-49) had only a single layer composed of MgF_2. Thus, it can be suggested that during the formation process of the 30-min film, AZ91 alloy melt has passed through the preliminary surface film composed of MgF_2, reacting with sulphur in the cover gas and forming the outer S-enriched layer. In conjunction with Fig 4-42 and Fig 4-66, this Mg-alloy melt penetration also occurred in the surface films formed in commercial purity Mg and Mg-Y alloys.

4.4 Thermodynamic calculations

HSC software from Outokumpu, HSC Chemistry for Windows (http://www.hsc-chemistry.net/), was used to carry out thermodynamic calculations, to explore the reactions that might occur to cover gas and oxide films as the cover gas reacted with the Mg-alloy melt. The calculations can suggest which products are most likely to form in the reaction process between a small amount of cover gas (i.e. amount of a trapped bubble) and a Mg-alloy melt.

In all the calculations, the pressure was set to 1 atm, and the temperature to 700 ^{o}C. The amount of the cover gas was assumed to be 7e-7 kg, which was approximately 0.35 cm^3 (3.12e-8 kmol) for 0.5%SF_6/CO_2, and 0.57 cm^3 (3.14e-8 kmol) for 0.5%SF_6/air. The amount of the Mg-alloy melt in contact with the trapped gas was assumed to be sufficient to complete all reactions. The decomposition products of SF_6 were SF_5, SF_4, SF_3, SF_2, F_2, S(g), S_2(g) and F(g) [50, 61, 63, 129].

The calculation results have been shown in Fig 4-77 ~ Fig 4-82. In these figures, the reactants and products less than 1e-15 kmol, were not shown, since 1e-15 kmol was too small (5 orders of magnitude less) compared with the amount of SF_6 (≈ 1.57e-10 kmol) and they may not affect the process in a practical way.

4.4.1 Commercial purity Mg in SF_6/air.

Fig 4-77 shows the result of a thermodynamic calculation of the reactions between a

pure Mg melt and a trapped gas of 0.5SF_6%/air. It can be seen that the whole reaction process could be divided into the following 3 stages:

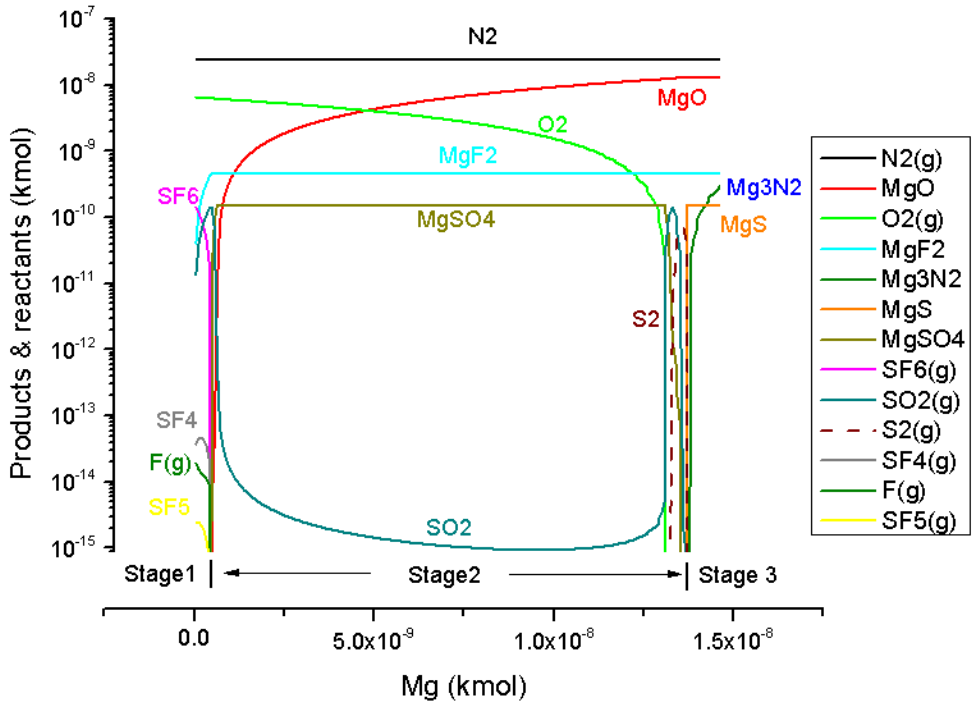

Fig 4-77 an equilibrium diagram for the reaction between 7e-7 kg 0.5%SF_6/air and a sufficient amount of commercial purity Mg alloy. The X axis denotes the amount of Mg alloy melt having reacted with the cover gas, and the vertical Y-axis denotes the amounts of the reactants and products.

In stage 1, fluorides in the entrained gas are preferentially consumed, producing MgF_2. Meanwhile, sulphur reacts with oxygen and accumulates as SO_2 in the residual gas.

In stage 2, all fluorides in the tapped gas have been depleted, SO_2 and O_2 react with Mg, forming $MgSO_4$ and MgO. Then, oxygen in the trapped gas has been consumed, while $MgSO_4$ decomposes to provide SO_2. The SO_2 subsequently reacts with liquid

Mg, forming MgO and provides further S_2(g), which reacts with the Mg melt, producing MgS.

In stage 3, the residual gas only contains nitrogen, and it subsequently reacts with Mg, forming Mg_3N_2.

These 3 stages, suggested by the thermodynamic calculation, were consistent with the three stages of the surface film growth process (i.e. the early, medium, and final stages suggested in section 4.3.9): the oxide film contained MgF_2 only in the early stage (stage 1), further contained sulphur in the medium stage (stage 2), and contained nitrides in the final (stage 3). The accumulation of sulphur in stage 1 was also demonstrated in Fig 4-76.

Therefore, the thermodynamic calculation can theoretically explain the surface film growth process shown in SF_6/air, and it can be suggested that the films shown in Fig 4-37~ Fig 4-42 correspond to stage 2 (medium stage) of the reaction process.

4.4.2 Commercial purity Mg in SF_6/CO_2.

Fig 4-78 shows the result of a thermodynamic calculation of the reactions between pure Mg and 0.5%SF_6/CO_2. The whole process could be divided into the following 3 stages:

In stage 1, SF_6 and its decomposition products are preferentially depleted, forming MgF_2. Sulphur accumulates in the residual gas as $S_2(g)$, and can react with CO_2, producing CO and SO_2.

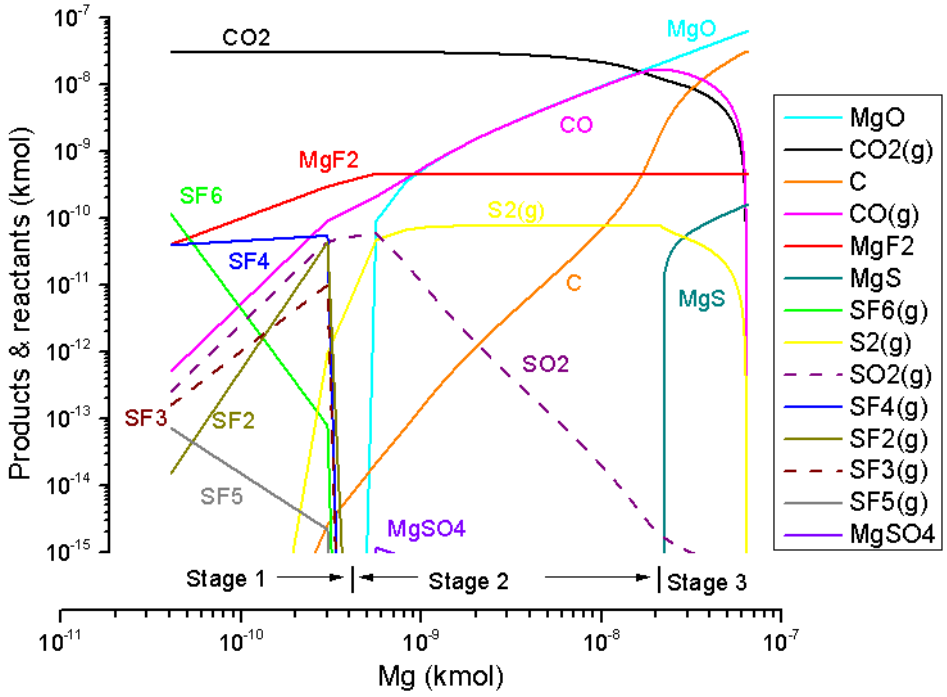

Fig 4-78 an equilibrium diagram for the reaction between 7e-7 kg 0.5%SF_6/CO_2 and a sufficient amount of commercial pure Mg alloy. The X axis denotes the amount of Mg alloy melt in contact with the entrained gas, and the vertical Y-axis denotes the amounts of the reactants and products.

In stage 2, when the fluorides have been consumed, CO_2 reacts with liquid Mg, forming CO and MgO. CO reacts further with Mg producing MgO and C. During the solidification process, (when the temperature is lower than 650 ^{o}C), carbon can combine with Mg forming MgC_2 and Mg_2C_3 [83]. This might be the reason why there were some carbon concentrations found inside the surface film shown in Fig 4-47.

At this stage, $MgSO_4$ can be theoretically produced, but its amount is quite small (1e-15 kmol of $MgSO_4$ in contrast to 4e-10 kmol of MgF_2), so that $MgSO_4$ might not be detected in the practical process. The reaction between SO_2 and Mg mainly follows the equation of $SO_2 + Mg = MgO + S_2(g)$, explaining why sulphur was not found in the surface film shown in Fig 4-43 ~ Fig 4-48 (see section 4.5.2).

In stage 3, $S_2(g)$ starts to react with liquid Mg, forming MgS. The residual gas always contains CO_2, CO and $S_2(g)$, until all the gases are consumed.

These 3 stages, suggested by the thermodynamic calculation, were also consistent with the three stages of the corresponding surface film growth process (i.e. the early, medium, and final stages suggested in section 4.3.9): the oxide film contained MgF_2 only in the early stage (stage 1), further contained MgO and C in the medium stage (stage 2), and further contained sulphur in the final stage (stage 3). The formation of magnesium carbides (see Fig 4-47) was also explained in the thermodynamic calculation.

Therefore, the thermodynamic calculation can theoretically explain the surface film growth process occured in SF_6/CO_2. It can be suggested that the films held for 30 ~ 20 min shown in section 4.5.2 (Fig 4-43 ~ Fig 4-45) correspond to stage 2 (medium stage) of the reaction process. The 15 ~ 5 min films (Fig 4-46 ~ Fig 4-48) may correspond to stage 1 (early stage).

4.4.3 AZ91 in SF_6/air.

Fig 4-79 shows the equilibrium diagram of the thermodynamic calculation of the reaction between the AZ91 alloy and 0.5%SF_6/air. 3 stages are contained in the whole reaction process:

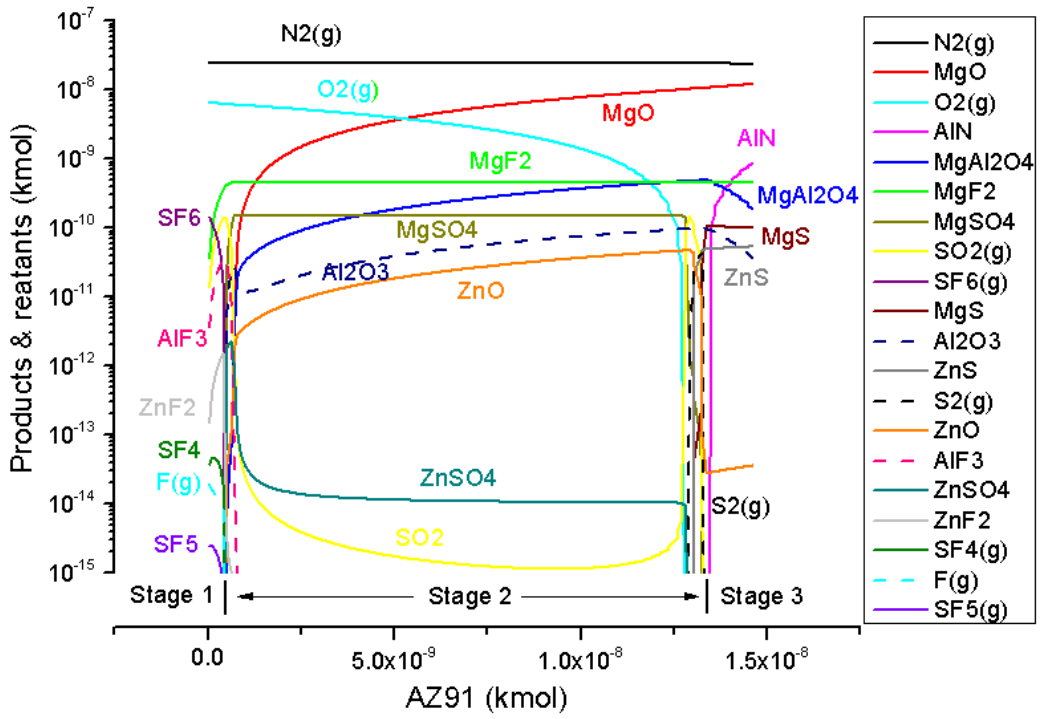

Fig 4-79 An equilibrium diagram for the reaction between 7e-7 kg 0.5%SF_6/air and a sufficient amount of AZ91 alloy. The X axis is the amount of AZ91 alloy melt having reacted with the entrained gas, and the vertical Y-axis is the amount of the reactants and products.

In stage 1, the AZ91 melt preferentially reacts with SF_6 and its decomposition products, theoretically producing MgF_2, AlF_3, and ZnF_2. However, the amount of ZnF_2 may be too small to be detected practically (1.25e-12 kmol of ZnF_2 compared with 3e-10 kmol of MgF_2). As in the reaction with pure Mg, sulphur accumulates in the

residual gas as SO_2.

In stage 2, after liquid AZ91 depletes all the fluorides in the trapped gas, the amount of AlF_3 and ZnF_2 quickly reduce due to the following equations:

$1.5Mg + AlF_3 = 1.5MgF_2 + Al$, $\triangle G(700^oC) = -175.64$ kJ;

$Mg + ZnF_2 = MgF_2 + Zn$, $\triangle G(700^oC) = -354.47$ kJ;

$O_2(g)$ and SO_2 react with the AZ91 melt, forming MgO, Al_2O_3, $MgAl_2O_4$, ZnO, $ZnSO_4$ and $MgSO_4$. However, the amount of ZnO and $ZnSO_4$ might be also too small to be found practically by EDS spectrum (9.5e-12 kmol of ZnO ,1.38e-14 kmol of ZnSO4, in contrast to 4.68e-10 kmol of MgF_2, when the amount of AZ91 on the X-axis is 2.5e-9 kmol).

The amount of $MgAl_2O_4$ and Al_2O_3 in the oxide film is suggested to be large according to Fig 4-79, which was consistent with the oxide films shown in section 4.2.3 (Fig 4-28 ~ Fig 4-30). However, the existence of aluminium could not be recognized in the surface films shown in section 4.3.3 (Fig 4-49 ~ Fig 4-54). The absence of Al might be due to the effect of the surface film on the reaction process, which could not be simulated using the HSC software.

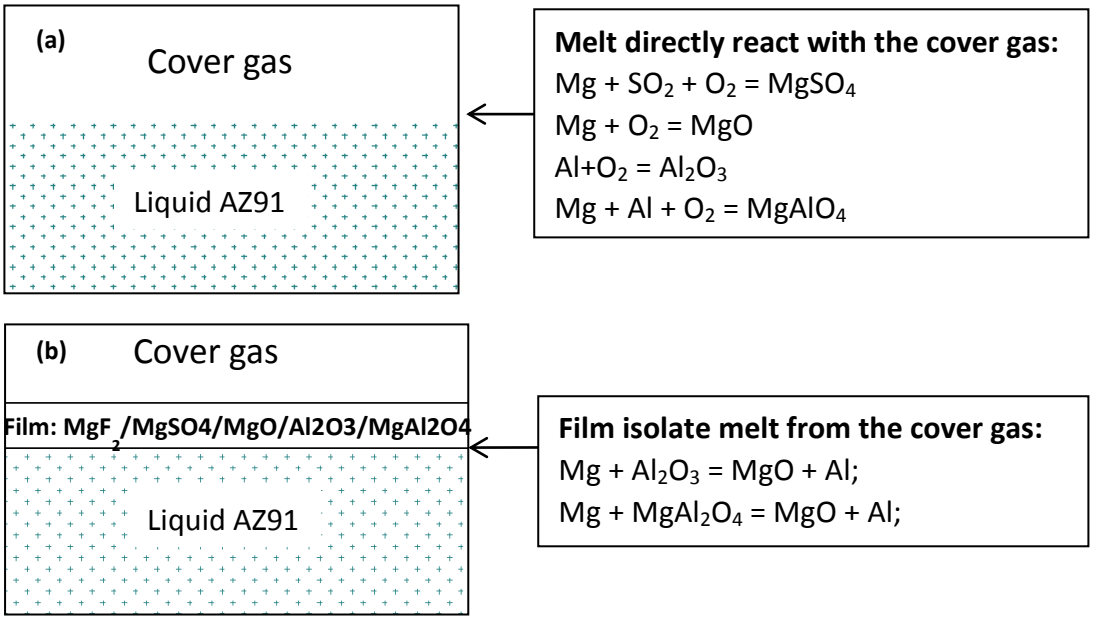

Fig 4-80 Reaction process between AZ91 melt and a cover gas of SF_6: (a) reactions not affected by a surface film; (b) reactions affected by a surface film.

As shown in (a), if the AZ91 alloy melt directly contacts with a sufficient amount of cover gas, the reaction process would occur according to the thermodynamic prediction. However, in the real process (Fig 4-80(b)), a preliminary surface film formed in stage 1 could isolate the melt from the cover gas. Thus the AZ91 melt would not contact with a sufficient amount of the cover gas, causing the melt to react with the surface film, due to the following equations:

$3Mg + Al_2O_3 = 3MgO + 2Al$, $\triangle G(700^oC) = -119.82$ kJ;

$Mg + MgAl_2O_4 = MgO + Al$, $\triangle G(700^oC) = -106.34$ kJ.

Therefore, if the surface film was not held at a high temperature for a long time, such as the oxide film shown in section 4.2.3 (Fig 4-28 ~ Fig 4-30), Al could be

detected in the films, since the Al_2O_3 and $MgAl_2O_4$ have not been completely depleted by the AZ91 melt; Otherwise, Al_2O_3 and $MgAl_2O_4$ in the surface film would be consumed by the melt, and no Al could be detected in the oxide film as shown in Fig 4-49 ~ Fig 4-54 (section 4.3.3).

In Stage 3, nitrogen reacts with the AZ91 melt, forming AlN until all the reactions are completed.

4.4.4 AZ91 in SF_6/CO_2.

The equilibrium diagram of the thermodynamic calculation of the reaction between AZ91 alloy and 0.5%SF_6/CO_2 (Fig 4-81) indicated that the reaction process could be divided into the following 3 stages:

In stage 1, SF_6 and its decomposition products were consumed by the AZ91 melt, forming MgF_2, AlF_3, and ZnF_2. As in the reaction of AZ91 in 0.5%SF_6/air, the amount of ZnF_2 was too small to be detected in practically (1.51e-13 kmol of ZnF_2 compared with 2.67e-10 kmol of MgF_2). Sulphur accumulated in the residual trapped gas as S_2(g) and a portion of the S_2(g) reacted with CO_2, forming SO_2 and CO

In stage 2, AlF_3 and ZnF_2 reacted with the Mg in the AZ91 melt, forming MgF_2, Al and Zn. Then, SO_2 began to be consumed, producing S_2(g) and oxides in the surface film.

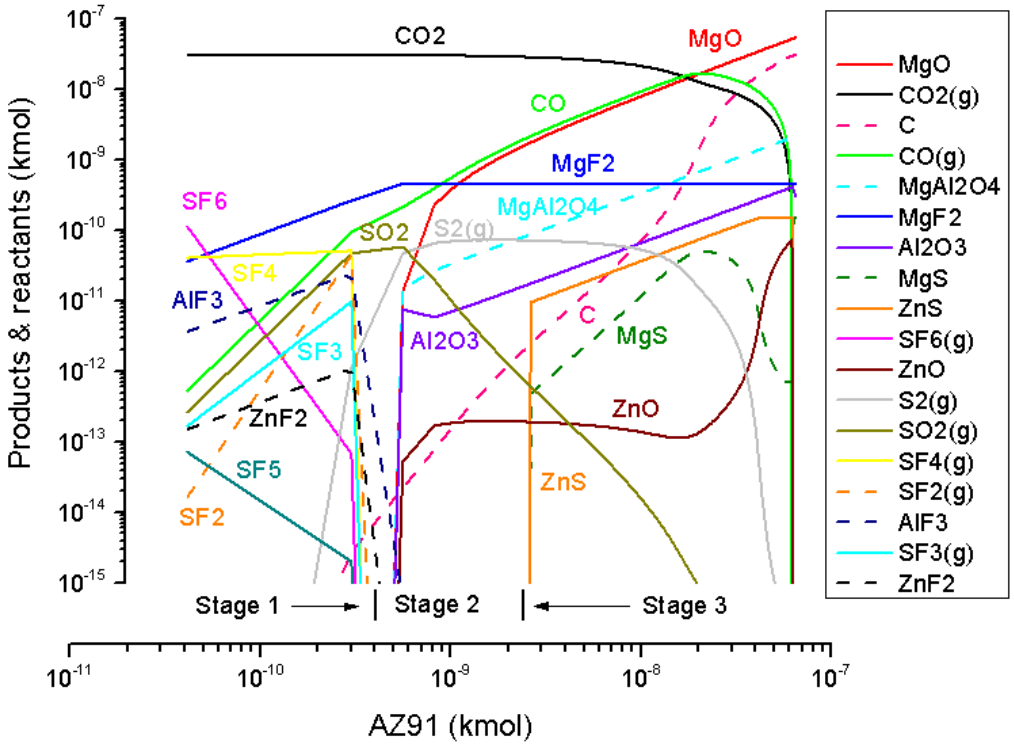

Fig 4-81 an equilibrium diagram for the reaction between 7e-7 kg 0.5%SF_6/CO_2 and a sufficient amount of AZ91 alloy. The X axis denotes the amount of Mg alloy melt having reacted with the entrained gas, and the vertical Y-axis denotes the amounts of the reactants and products.

Meanwhile, the CO_2 directly reacted with the AZ91 melt, forming CO, MgO, ZnO and Al_2O_3. The CO could react further with the AZ91 melt, producing C. The ZnO may not be able to be detected in practice, due to its small amount (1e-13 kmol of ZnO, compared with 1e-9 kmol MgO). The Al_2O_3 can be further combined with MgO, forming $MgAl_2O_4$. Due to the same effect of the surface film discussed in section 4.4.3 (see Fig 4-80), Al_2O_3 and $MgAl_2O_4$ in the surface films can react with Mg in the melt. Thus, aluminium was not detected in the surface films as shown in Fig 4-55 ~ Fig 4-60.

In stage 3, the AZ91 melt began to consume S_2(g) in the residual gas, forming ZnS and MgS. These reactions did not occur until the last stage of the whole process, which may explain why there was no S found in the surface film shown in section 4.3.4 (Fig 4-55 ~ Fig 4-60).

4.4.5 Mg-Y alloy in SF_6/air.

Fig 4-82 reveals that the reaction process of Mg-Y alloy in 0.5%SF6/air was similar to the reaction between pure Mg and 0.5%SF_6/air (Fig 4-77). It can also be divided into 3 stages:

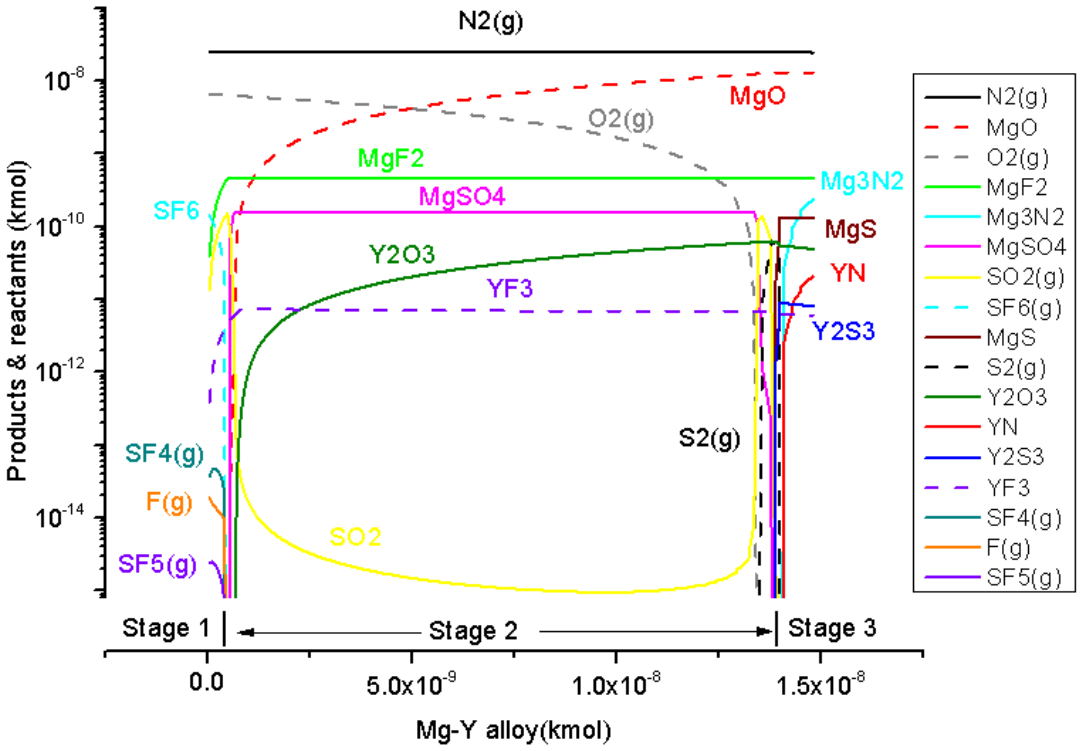

Fig 4-82 an equilibrium diagram for the reaction between 7e-7 kg 0.5%SF_6/air and a sufficient amount of Mg-Y alloy. The X axis is the amount of Mg-Y alloy melt having reacted with the entrained gas, and the vertical Y-axis denotes the amounts of the reactants and products.

In stage 1, fluorides in the entrained gas would be preferentially consumed, producing MgF_2 and YF_3. Simultaneously, sulphur reacted with oxygen and accumulated as SO_2 in the residual gas.

In stage 2, all fluorides in the trapped gas have been depleted. SO_2 and O_2 reacted with the Mg-Y melt, forming MgO, $MgSO_4$ and Y_2O_3. It was reported that $Y_2(SO_4)_3$ would decompose at 700 ^oC [130], thus $Y_2(SO_4)_3$ was assumed not to occur in the process.

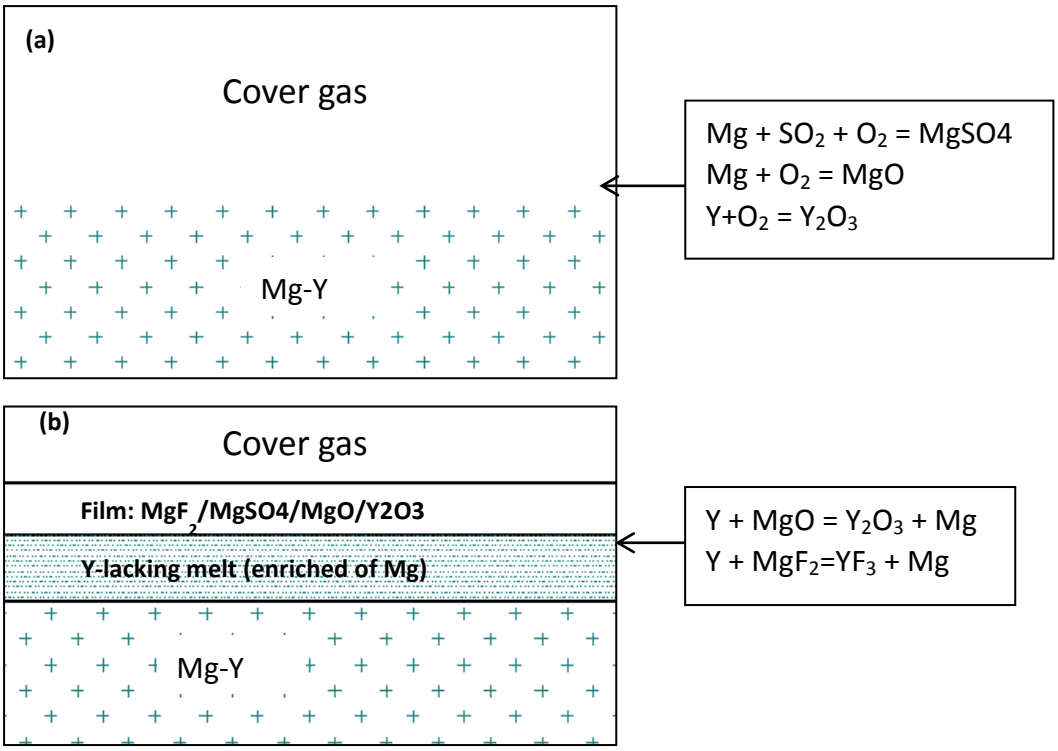

Fig 4-83 Reaction process between Mg-Y melt and a cover gas of SF_6: (a) reactions not affected by a surface film; (b) reactions affected by a surface film.

In addition, the existence of a surface film can also affect the reactions in this stage, which could not be simulated by the HSC software. As shown in Fig 4-83(a), if the Mg-Y melt could directly contact with a sufficient amount of cover gas, the reactions process would occur according to the thermochemical prediction. However, in the real process, a preliminary surface film formed in stage 1 could separate the melt and cover gas, as shown in Fig 4-83 (b). Thus the Mg-Y melt would not contact with a sufficient amount of the gas, causing yttrium react with the surface film due to the following equations:

$2Y + 3MgO = Y_2O_3 + 3Mg$, $\triangle G(700^oC)$ =-131.40 kJ;

$Y + 1.5MgF_2 = YF_3 + 1.5Mg$, $\triangle G(700^oC)$ = -53.18 kJ.

Therefore, a layer lacking in yttrium, and enriched with Mg, could form in the melt. This Y-lacking layer could further react with the atoms of fluorine and oxygen, which penetrated through the surface film, forming the inner Mg-enriched layer in the final surface film, as shown in Fig 4-61~ Fig 4-63.

Then, oxygen in the trapped gas m consumed, and $MgSO_4$ decomposes to provide SO_2. The SO_2 subsequently reacts with the Mg-Y melt, forming Y_2O_3, MgO and S_2(g). The S_2(g) further reacts with the melt, producing MgS and Y_2S_3.

In stage 3, the residual gas contains nitrogen only, which may react with Mg-Y melt, forming Mg_3N_2 and YN.

4.4.6 Mg-Y alloy in SF_6/CO_2.

Fig 4-84 indicates 3 stages, contained in the reaction process of Mg-Y alloy with a 0.5%SF_6/CO_2 cover gas.

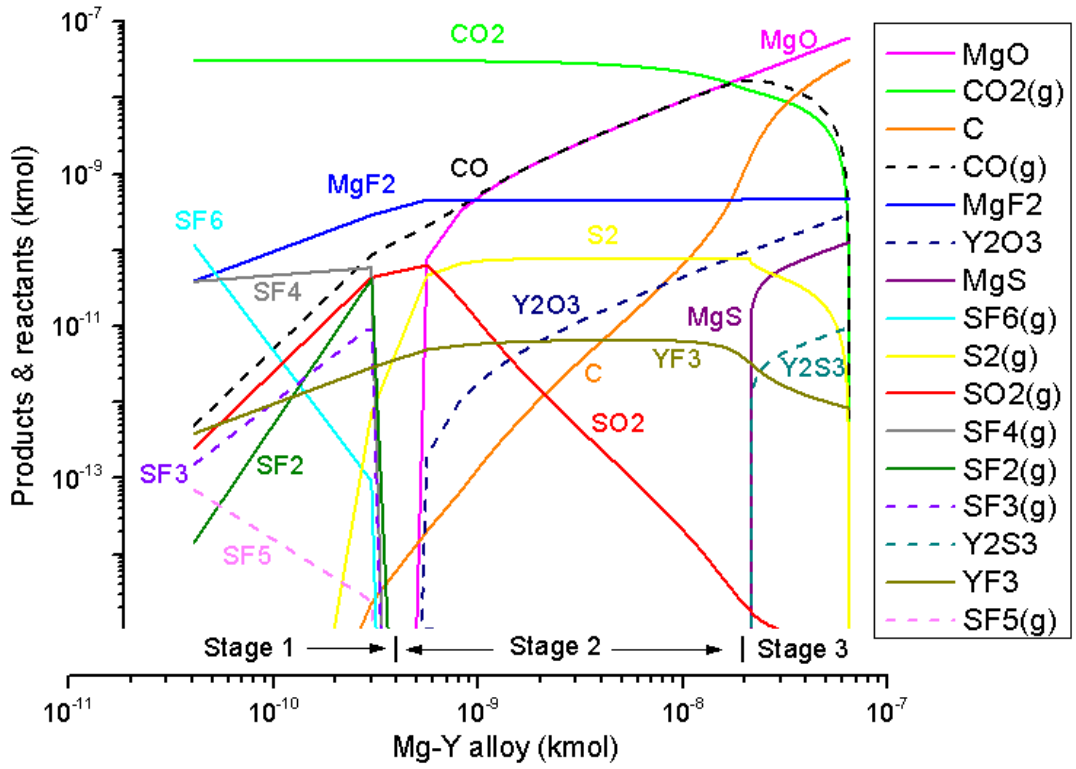

Fig 4-84, an equilibrium diagram for the reaction between 7e-7 kg 0.5%SF_6/CO_2 and a sufficient amount of Mg-Y alloy. The X axis was the amount of Mg-Y alloy melt having reacted with the entrained gas, and the vertical Y-axis was the amounts of the reactants and products.

In stage 1, MgF_2 and YF_3 are preferentially produced due to reaction between molten Mg-Y alloy and fluorides. Sulphur accumulates in the residual gas as $S_2(g)$ and a portion of $S_2(g)$ react with CO_2, forming SO_2 and CO.

In stage 2, the SO_2 may react with Mg-Y, producing $S_2(g)$, Y_2O_3 and MgO. The CO_2 starts to directly react with the Mg-Y liquid, forming CO, MgO, and Y_2O_3. The CO

could further react with the melt to produce carbon. Due to the same effect of the preliminary surface film discussed in section 4.4.5 (see Fig 4-83), the film formed in stage 1 may react with the melt, increasing the Y-content of the final films.

However, the Mg-Y films formed with 0.5%SF_6/CO_2 (Fig 4-67 ~ Fig 4-72) did not contained a MgF_2-enriched inner layer, as did the 0.5%SF_6/air films shown in section 4.3.6 (Fig 4-61~ Fig 4-63). This may be due to the reactions of Mg-Y in 0.5%SF_6/CO_2 occurring more slowly than the reactions between Mg-Y and 0.5%SF_6/air (see Fig 4-74(c)), causing the Y-lacking layer (see Fig 4-83) not to form.

In stage 3, the Mg-Y melt begins to consume S_2(g) in the residual gas, forming Y_2S_3 and MgS. These reactions are not carried out until this last stage of the whole process, which may be the reason for the absence of sulphur in the surface film shown in section 4.3.6 (Fig 4-67 ~ Fig 4-72).

4.4.7 Summary

It was clear that the stages suggested by the thermodynamic calculation (i.e. stage 1 ~ 3 in Fig 4-77 ~ Fig 4-82), were consistent with the three stages of the corresponding surface film growth process (i.e. the early, medium, and final stages suggested in section 4.3.9): in a cover gas of SF_6/air, the oxide film contained MgF_2 only in the early stage (stage 1), further contained sulphur in the medium stage (stage 2), and contained nitrides in the final (stage 3); in a cover gas of SF_6/CO_2, the

oxide film contained MgF_2 only in the early stage (stage 1), further contained MgO and C in the medium stage (stage 2), and further contained sulphur in the final stage (stage 3).

The other phenomenon occurred in the surface film growth process, such as the formation of magnesium carbides (see Fig 4-47) and the accumulation of sulphur in the cover gas (see Fig 4-76), was also explained in the thermodynamic calculation.

Therefore, the thermodynamic calculations can theoretically explain the oxide film growth process. The calculation results can be accordingly used to explain the mechanism of the oxide film growth occurring in the evolution process of a double oxide film defect.

4.5 Monte Carlo simulation

The Maximum Likelihood (ML) method and the Linear Least Squares (LLS) method have been widely used to estimate Weibull parameters for reliability of brittle and metal materials [102, 107]. . In the last 30 years, many researchers focused on the bias of Weibull modulus estimation [99, 102, 107, 131, 132], and some improvements have been achieved, especially in the case of the LLS method [99, 100, 102]. However, there is a shortcoming in these methods for a special type of data, where the lower tail deviates dramatically from the well-known linear fit in a classic LLS Weibull analysis. This deviation can be commonly found from the measured

properties of materials [133], and previous applications of the LLS method on this kind of dataset present an unreliable linear regression, such as [23, 34, 36, 111, 134, 135]. This deviation was previously thought to be due to an underlying 3-p or mixed Weibull distribution [136, 137], but the work reported in this section demonstrates that this deviation can be also caused by the linear transformation of the Weibull function, occurring in the traditional LLS method. Accordingly, it may not be appropriate to carry out a Weibull analysis according to the linearized Weibull function. Thus a Non-linear Least Square method (Non-LS), which has been rarely used in the field of materials and metallurgy, has been utilized to estimate the Weibull modulus of castings. Comprehensive Monte Carlo simulations were carried out to explore the reliability of parameter estimation by the Non-LS, the LLS, and the ML methods.

4.5.1 Deviation in the linearized Weibull plot

In practise, some data points of the measured properties seriously deviate from the linear behaviour in the traditional LLS method for Weibull estimation, resulting in a bad fit in the linear regression model. A good example was that of Griffiths and Lai's data of the measured UTS of a commercial purity Mg casting ("Top-filled results" in their paper) [23], as shown in Fig 4-85(a). It was obvious that the data points were not randomly scattered along the fitted straight line in this linear regression (see Fig 4-85(b)), and the corresponding R^2 value was only 79.1%, both of which suggested that it was a bad linear fit. These outliers would exert much influence on the

regression line, making the Weibull modulus dramatically deviate from its true value. This type of behaviour, (i.e. data deviation in the lower tail), in the plot of linearized Weibull function (such as Fig 4-85(a)) was widely occurred and resulted in estimation bias in various degrees, of which examples can be found in [23, 34, 36, 111, 134, 135].

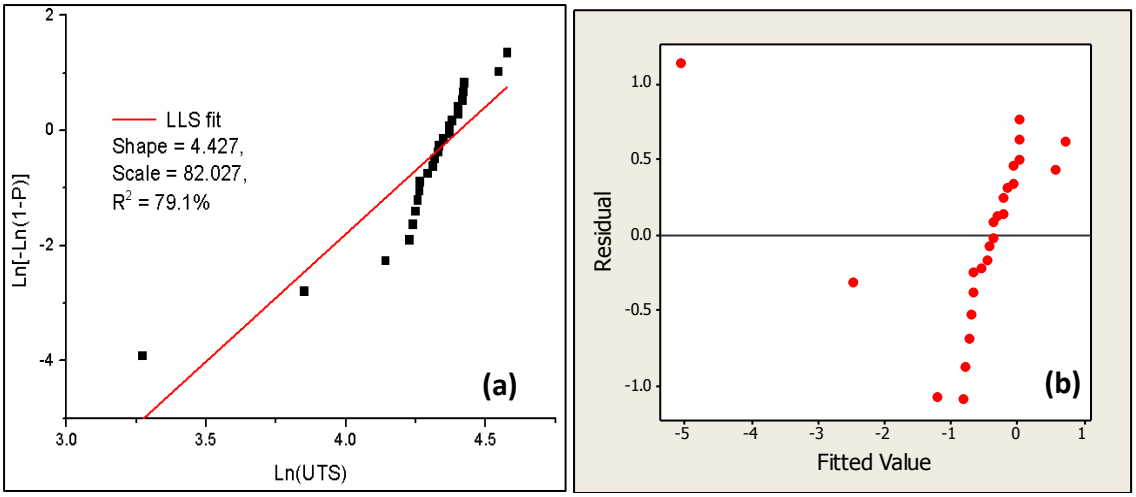

Fig 4-85, (a) Weibull estimation using the LLS method published in [23] (the "Top-filled" results); (b) residual plot corresponding to the linear regression in (a);

When this deviation occurs, a traditional solution is to firstly eliminate a few data points before the next step of the Weibull modulus analysis [96], because the data points in the lower tail were considered to be caused by gross pores. Nevertheless, the Weibull modulus obtained after such elimination would also neglect the effect of pores on the quality of the castings, and could not reflect the reproducibility of the whole set of castings.

Currently, there are two popular explanations for this deviation, based on a plot of

the linearized Weibull CDF (such as Fig 4-85(a)). Tiryakioglu and Campbell [136] thought the dataset might follow a 3-p Weibull function (Eq.2-3), and the deviation could be due to the threshold value of x_u (see x_u in Eq. 2-3). Another view was that the occurrence of the deviated data points was due to an underlying mixture of Weibull distributions [137, 138].

However, the re-analysis of Griffiths' data (Fig 4-86) indicated another underlying reason that this deviation can be caused by the linear transformation of the Weibull function.

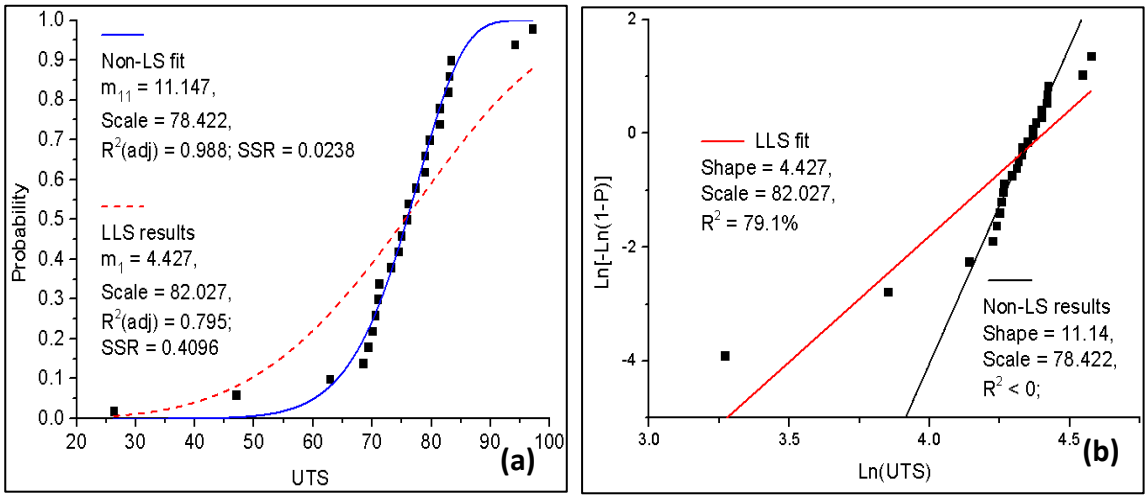

Fig 4-86 (a) the Weibull estimation of Griffiths' data shown in Figure 1, using the Non-LS method (Pest,i = (i-0.5)/N), and the LLS method (Pest,i = (i-0.5)/N). (b) the results of the two methods plotted in the plot of the linearized Weibull function.

As shown in Fig 4-86(a), the Griffiths' data shown in Fig 4-85(a) (i.e. UTS of a commercial pure Mg casting produced in a top-filled system) was re-analysed using the Non-LS method ($P_{est,i}$ = (i-0.5)/N). To compare the fitting performance, the Weibull function with the parameters obtained via the LLS method (i.e. $P_{est,i}$ = (i-

0.5)/N, originally used in Griffiths' paper [23]) was also plotted in Fig 4-86(a). Residual Sum of Squares (SSR) was used to evaluate the goodness-of-fit instead of R^2 in this non-linear model. The adjusted R^2 values were still listed.

According to Fig 4-86(a), it can be seen that the data points showed a good fit to the Non-linear regression curve (SSR = 0.0238), which is much better than the curve plotted according to the LLS estimation results (the Weibull parameters are shown in Fig 4-85(a), SSR = 0.4096). There was a significant difference between the Weibull modulus estimated by the two methods (m_{11} = 11.147 and m_1 = 4.427). Therefore, we cannot simply reject the Weibull behaviour of this dataset according to Tiryakioglu's equation (Eq. 2-25), which was based on the linearized Weibull plot (Fig 4-85(a)).

In addition, when the Non-LS estimation result was plotted in the linearized Weibull plot (i.e. black line in Fig 4-86(b)), the data points showed an extreme bad fit to the linearized line (R^2 <0), which was even much worse than the LLS estimation results (R^2 = 79.1%). The contradictory conclusions of Fig 4-86(a) and Fig 4-86(b), suggest the following question: "Is it appropriate to determine the Weibull behaviour of datasets according to the non-linear Weibull plot (such as Fig 4-86(a)), or the traditional linearized Weibull plot (such as Fig 4-86(b))?"

This different level of the goodness-of-fit may be due to a shortcoming of the

linearized Weibull function, as discussed in section 4.5.2.

4.5.2 A shortcoming of the linearized form of the Weibull function

It should be noted that the cumulative probability in the Weibull estimation using the least squares method, is set to a specific value (denoted by $P_{est,i}$ for the ith datum point) with the same weight for each datum point, according to the estimator defined in Eq. 2-6. However, in a practical process, the true cumulative probability, referred to as $P_{true,i}$, is of course not necessarily equal to the estimated cumulative probability ($P_{est,i}$). Bergman [139] also pointed out that it was erroneous to assume the same weight for each datum point by Eq. 2-6. Thus there is usually a difference between $P_{true,i}$ and $P_{est,i}$, making the estimated Weibull moduli biased.

Let $DY_{non\text{-}linear,\,i}$ indicate the difference between the true and estimated values on Y-axis for the ith datum point in the plot of the original Weibull CDF. It can be calculated by the following equation:

$$\text{Eq. 4-2:} \qquad DY_{non\text{-}linear,i} = |P_{true,i} - P_{est,i}|$$

Similarly, let $DY_{linear,\,i}$ indicate this difference on the Y-axis in the plot of the linearized Weibull function (such as Eq.2-5). It can be calculated by the following equation:

$$\text{Eq. 4-3:} \qquad DY_{linear,i} = |\ \mathrm{Ln}[-\mathrm{Ln}(1- P_{true,i})] - \mathrm{Ln}\left[-\mathrm{Ln}\left(1- P_{est,i}\right)\right]|$$

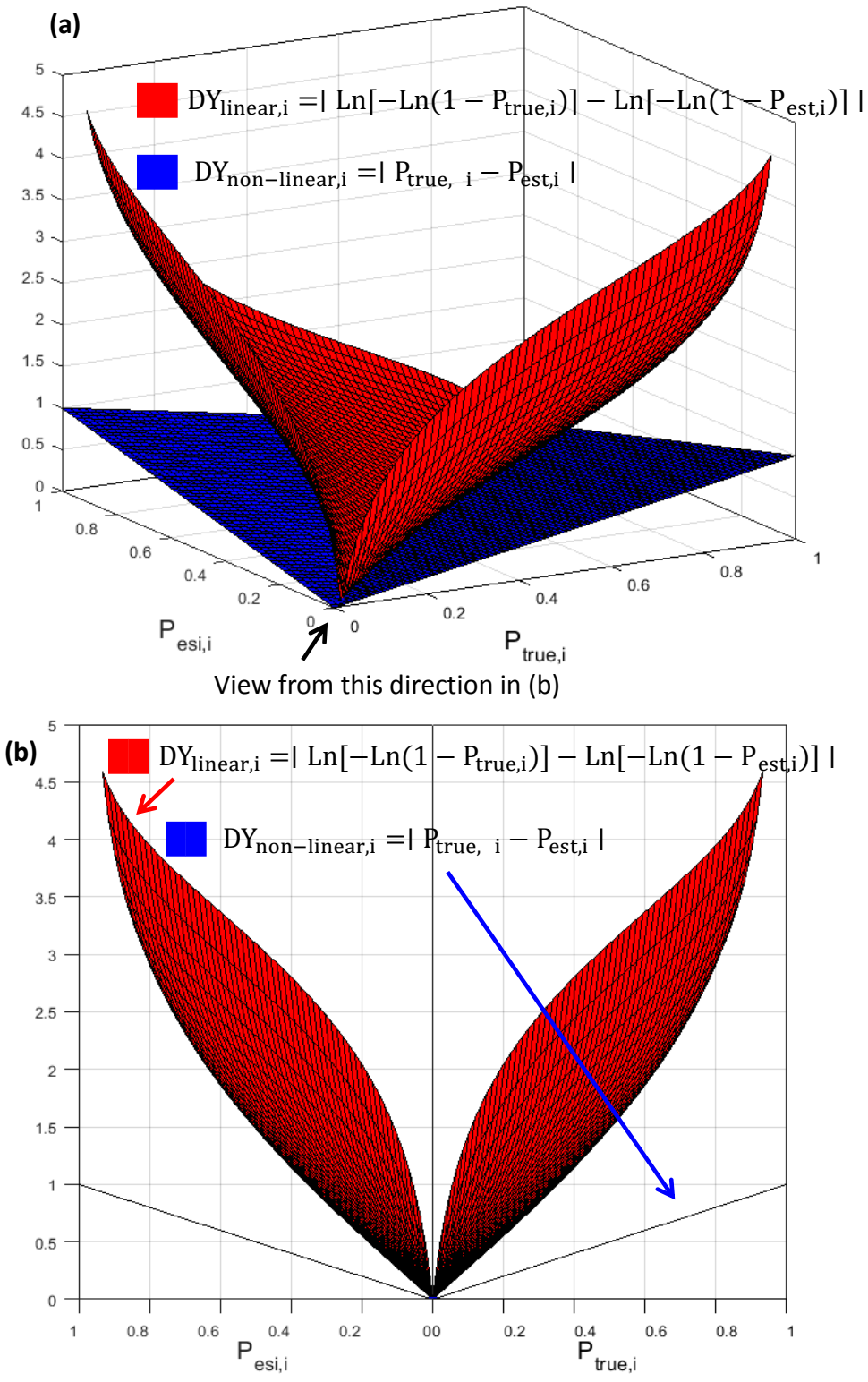

Fig 4-87, (a) a 3-D plot based on the functions of $DY_{linear,i}$ and $DY_{non\text{-}linear,i}$; (b) View from another direction of (a), indicating that $DY_{linear,i}$ is always be larger than $DY_{non\text{-}linear,i}$.

No matter how much $P_{true,i}$ and $P_{est,i}$ are, linear transformation can always numerically enlarge the difference between the true and estimated values on the Y axis. In other words, $DY_{linear,i}$ is always be larger than $DY_{non\text{-}linear,i}$, especially when $P_{est,i}$ significantly deviates from $P_{true,i}$, as shown in Fig 4-87. Such an increase, in the deviation from the estimated value to the true value on the Y axis, causes a lager distance between the estimated and true positions of the data points in the linearized Weibull function plot, compared with that in the original Weibull CDF plot. Since the regression algorithms (no matter whether linear or Non-linear) produced the results according to residuals (i.e. the smallest Sum of Residual Square), which is only related to the Y-coordinate, the enlargement accordingly may result in more bias of the estimated Weibull moduli.

Furthermore, it should be noted that $DY_{linear,i}$ and $DY_{non\text{-}linear,i}$ are only determined by $P_{true,i}$ and $P_{est,i}$,thus the enlargement due to the linear transformation also exists in the linearized form of the 3-p Weibull function.

This enlargement level can be further described via the following enlargement factor (EF):

Eq. 4-4: $$\text{Enlargement factor: } EF = \frac{DY_{non-linear,i}}{DY_{linear,i}}$$

A 3-D plot of this equation is shown in Fig 4-88. It can be seen that the EF value would be significantly small, even close to 0, when $P_{true,i}$ approaches to 0 or 1. This means that the $DY_{non\text{-}linear,i}$ would be dramatically enlarged at these positions. This is

the underlying reason why it was normally reported a deviation in the lower and upper tails of a dataset in a traditional Weibull estimation using the LLS method.

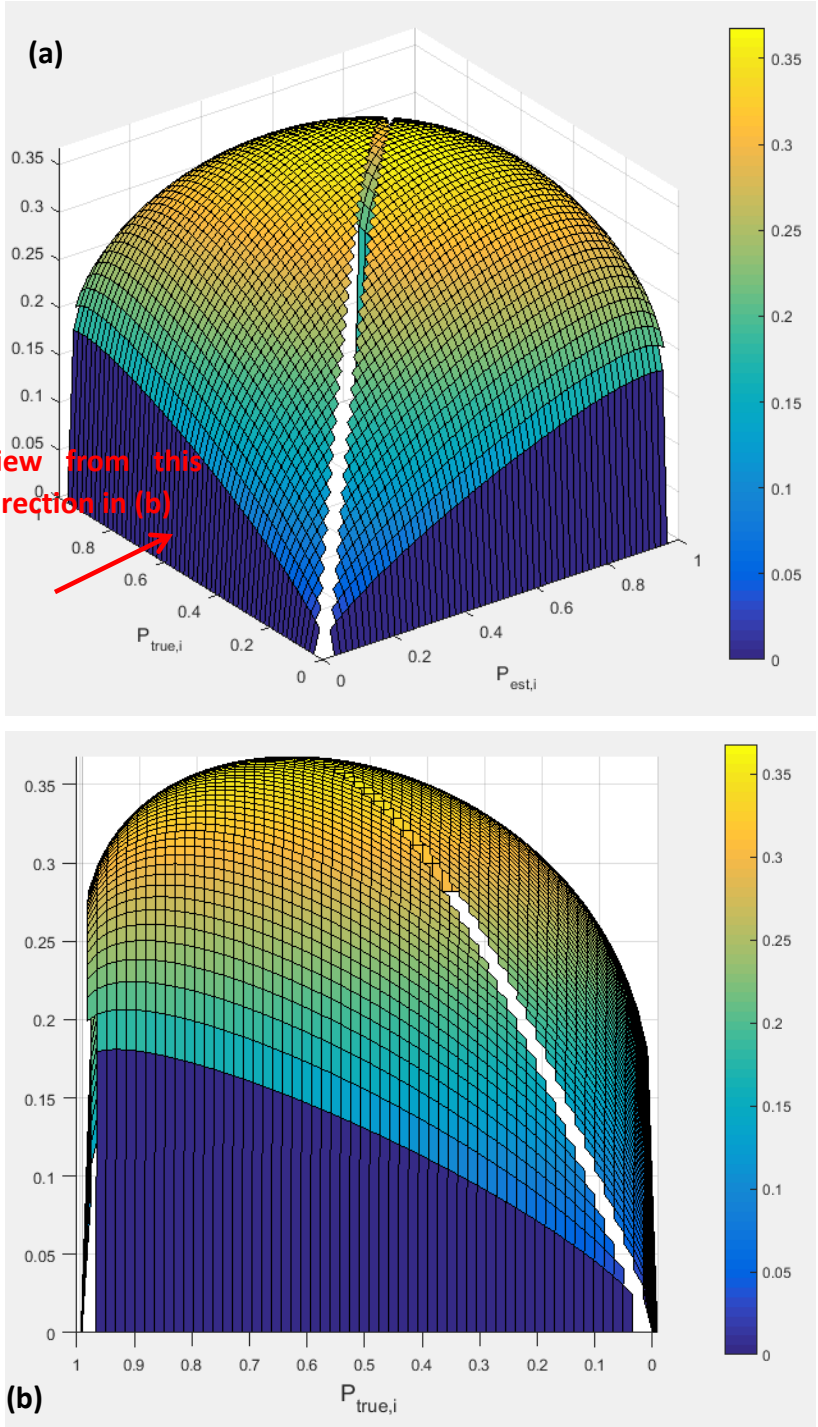

Fig 4-88 (a) the function of the enlargement level factor (EF). (b) View from another direction of (a), indicating the $D_{Ynon\text{-}linear,i}$ would be dramatically enlarged when $P_{ture,i}$ is close to 0 or 1.

Therefore, the extreme bad fit of the Non-LS result shown in Fig 4-86(b) may be due to the enlargement of the difference between the true and estimated probabilities. It is consequently suggested use the least square method in the plot of the non-linear Weibull CDF, rather than its linearized form. This approach is the non-linear least square method (Non-LS).

4.5.3. Examples of the negative effect of the enlargement of $DY_{non\text{-}linear,i}$ on Weibull estimation

i	x	$P_{true,i}$	$P_{est,i} = (i-0.5)/N$	$DY_{linear,i}$	$DY_{non\text{-}linear,i}$
1	34.0085	0.001938	0.02	0.018062	2.34314
2	34.6850	0.002406	0.06	0.057594	3.24576
3	37.1551	0.005122	0.10	0.094878	3.02130
4	42.4875	0.022199	0.14	0.117801	1.90484
5	51.1540	0.158850	0.18	0.021150	0.13734
6	51.8391	0.181473	0.22	0.038527	0.21573
7	54.0502	0.271693	0.26	0.011693	0.05155
8	54.5408	0.295427	0.30	0.004573	0.01843
9	55.1336	0.325901	0.34	0.014099	0.05221
10	55.2120	0.330076	0.38	0.049924	0.17674
11	55.3406	0.336997	0.42	0.083003	0.28175
12	55.7049	0.357082	0.46	0.102918	0.33283
13	56.6743	0.413777	0.50	0.086223	0.26074
14	57.0168	0.434843	0.54	0.105157	0.30805
15	57.8910	0.490647	0.58	0.089353	0.25148
16	58.0565	0.501496	0.62	0.118504	0.32925
17	58.2651	0.515268	0.66	0.144732	0.39860
18	58.6562	0.541344	0.70	0.158656	0.43479
19	59.7578	0.615759	0.74	0.124241	0.34242
20	60.5805	0.671011	0.78	0.108989	0.30892
21	60.8124	0.686338	0.82	0.133662	0.39136
22	61.0008	0.698679	0.86	0.161321	0.49409
23	62.7504	0.805486	0.90	0.094514	0.34101
24	63.0698	0.822946	0.94	0.117054	0.48552
25	64.0881	0.873164	0.98	0.106836	0.63899

Table 4-8 data (referred to as x) generated from a Weibull function with shape = 11, scale =60.

For a further illustration of Fig 4-87 and Fig 4-88, an example has been given in Table 4-8. This dataset was generated from a 2-p Weibull distribution with shape = 11 and scale= 60, which was close to the Non-LS estimation result of Griffiths' data [23]. The raw data were sorted in ascending order as detailed in the second column of Table 4-8. The true cumulative probabilities ($P_{true,i}$) were directly calculated from the Weibull function and listed in the third column. The estimated cumulative probability was computed according to $P_{est,i}$ = (i-0.5)/N (Eq. 2-7), and shown in the 4th column. $DY_{linear,i}$ and $DY_{non\text{-}linear,i}$ were listed in the 5th and 6th columns respectively.

Fig 4-89 (a-b) shows the corresponding Weibull estimation results using the Non-LS and the LLS methods. The black points indicate $P_{true,i}$, while the red points denote $P_{est,i}$. It can be seen that the deviation from the estimated value to the true value on the Y-axis is obviously larger in the plot of the linearized Weibull function ($DY_{linear,i}$ in Fig 4-89(b)), than in the plot of the original non-linear Weibull CDF ($DY_{non\text{-}linear,i}$ in Fig 4-89(a)), especially when $P_{true,i}$ is small. A deviation similar to that shown in Fig-4-83 (i.e. Griffiths and Lai's data) consequently occurred in the lower tail as shown in Fig 4-87(b).

Fig 4-89(c) shows the change of the enlargement factor (EF) along with $P_{true,i}$, revealing that the enlargement of $DY_{non\text{-}linear,i}$ is more dramatic when $P_{true,i}$ is close to 0 and 1, which is consistent with Fig 4-88.

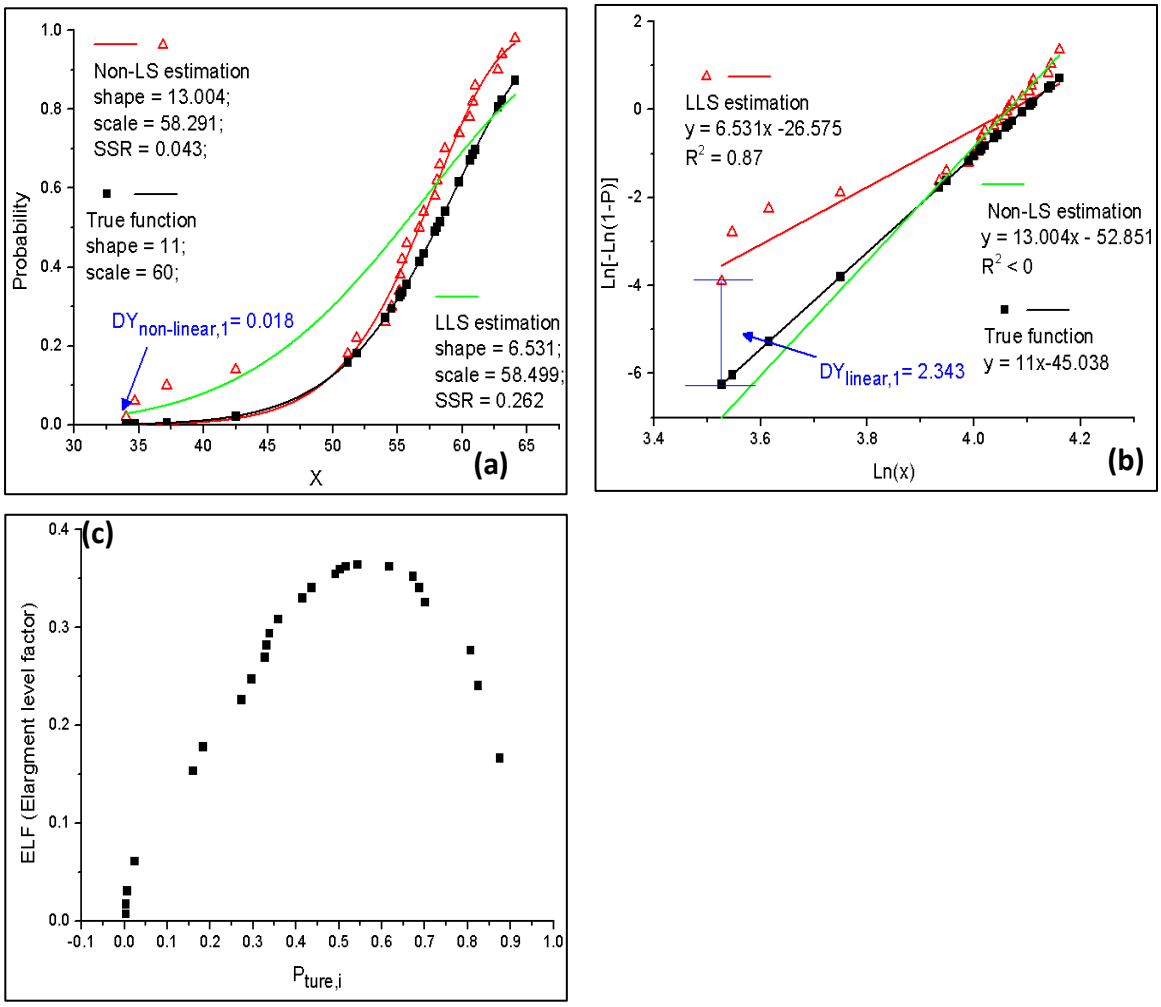

Fig 4-89, (a-b) Weibull estimation using (a) the Non-LS and (b) the LLS method, corresponding to the data listed in Table 4-8. The black points indicate $P_{true,i}$, while the red points denote $P_{est,i}$. (c) the change of ELF along with $P_{ture,i}$.

Accordingly, the performance of the Weibull moduli estimation was poorer in the LLS method than in the Non-LS method, which can explain the different levels of the goodness-of-fit of the regression lines and curves shown in Fig 4-86.

4.5.4 Simulation Procedure.

To further illustrate the discussion in section 4.5.2, Monte Carlo simulations were

performed using R Version 3.3.0 (https://www.r-project.org). As shown in Fig 4-90, three different procedures were used to investigate the bias of the estimated Weibull modulus.

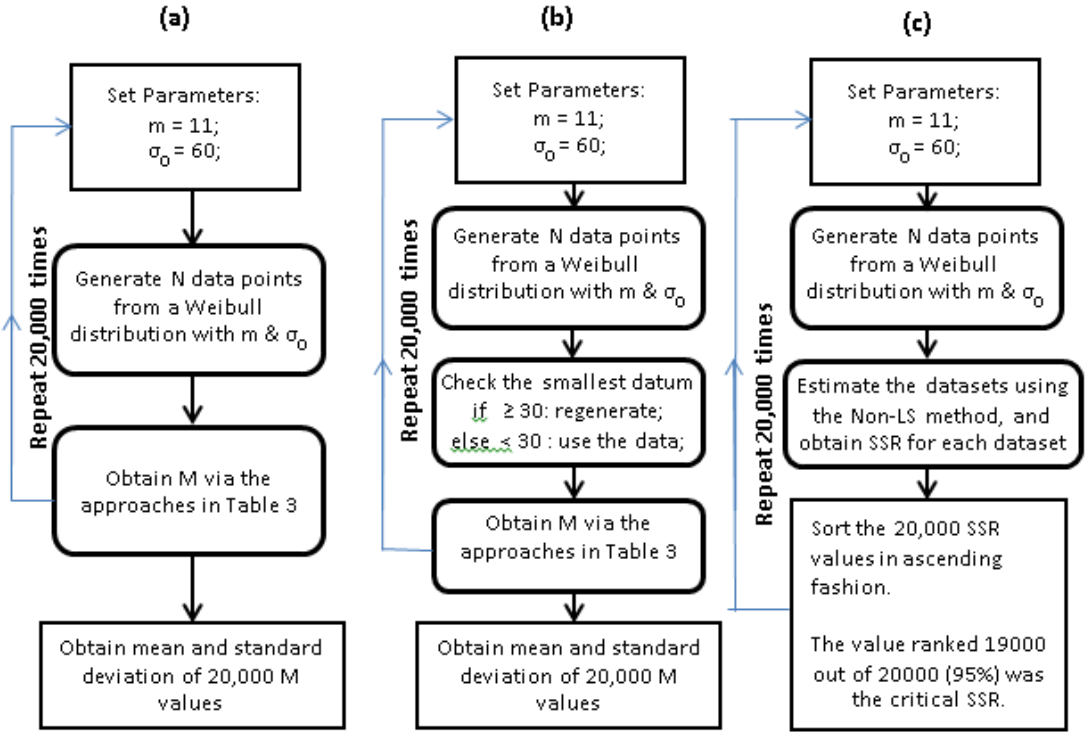

Fig 4-90 flowcharts summarizing the simulation procedures (a) direct comparison of the three estimation methods; (b) To study the effect of the enlargement of $DY_{non\text{-}linear,i}$, and using the data with the smallest datum point <30. (c) Calculation of critical SSR.

For direct comparison of the three estimation methods (Fig 4-90(a)), random data points of sample size N was firstly generated from a 2-p Weibull function (Eq. 2-4) with shape parameter =11 (referred to as m_{true}) and scale parameter = 60 (referred to as $\sigma_{0,true}$). Using the generated data, different approaches, listed in Table 4-9, were used to evaluate the Weibull modulus (written as m_{est}).

Estimators \ Methods	LLS	Non-LS	ML
Eq. 2-7	Approach 1	Approach 11	Approach 21
Eq. 2-8	Approach 2	Approach 12	
Eq. 2-9	Approach 3	Approach 13	
Eq. 2-10	Approach 4	Approach 14	
Eq. 2-11	Approach 5	Approach 15	
Eq. 2-12	Approach 6	Approach 16	
Eq. 2-13	Approach 7	Approach 17	
Eq. 2-14	Approach 8	Approach 18	
Eq. 2-15	Approach 9	Approach 19	
Eq. 2-16	Approach 10	Approach 20	

Table 4-9,the number of approaches corresponding to different estimators together with LLS and Non-LS methods.

The bias of the estimated Weibull modulus (m_{est}) was defined by the following equation [99, 101, 102],

$$\text{Eq. 4-5:} \quad M = m_{est} / m_{true}$$

M = 1 means the used approach is unbiased. In addition, since the estimated parameters are normalized by the true parameters, the setting of the scale and shape parameters are inconsequential [102, 113].The process was repeated for 20,000 times to obtain 20,000 M values. The bias level of different approaches was evaluated by the mean of the 20,000 M values, written as M_{mean}.

To study the effect of the dramatic enlargement of $DY_{non\text{-}linear,i}$ on Weibull moduli estimation (Fig 4-90(b)), the program checked whether the smallest datum of the

random generated dataset was < 30, thus making the data used for the simulation contain at least one datum point smaller than 30. This setting ensured a small value of the true probability of the first datum point ($P_{ture,1}$), thus the corresponding difference between the true and estimated values on the Y-axis ($DY_{non\text{-}linear,\ 1}$) would be dramatically enlarged in the linearized Weibull function plot, according to Fig 4-87 and Fig 4-88 (when $P_{ture,1}$ is close to 0).

Based on the linearized Weibull plot, Tiryakioglu et al. [113] developed an equation of critical R^2 (i.e. Eq. 2-25) to determine the Weibull behaviour of datasets. Similarly, based on the non-linear Weibull plot, the critical sum of residual squares (referred to as SSRC) could also be calculated using a Monte Carlo simulation as the procedures shown Fig 4-90(c). The SSRC obtained would be larger than the sum of residual squares (SSR) value of 95% datasets (i.e. 19,000 out of 20,000).

4.5.5 Results: direct comparison of the estimation approaches

Fig 4-91 illustrates the results of the simulations shown in Fig 4-90(a). In general, the estimated Weibull modulus became closer to m_{true} with increase in sample size N. Fig 4-91(a) summarized the M_{mean} obtained by the LLS and the ML methods (i.e. Approach 1 – 10 & 21 in Table 4-9). It can be seen that Approach 1 and 9 was relatively less biased for N ≥ 25, and Approach 5 was the least biased approach when the sample size N was < 25. This observation was consistent with the results of [99, 102]. Fig 4-91 (b) shows a summary of M_{mean} achieved by the Non-LS method (i.e.

Approach 11 – 20 in Table 4-9). It was obvious that Approach 12, which was the worst estimator for the LLS method (Approach 2 in Table 4-9), was less biased than the other estimators using the Non-LS method, especially when the sample size was smaller than 30.

For a further comparison, Approach 1, 5, 9 and 12 were put together as shown in Fig 4-92. For $15 \leq N < 35$ and $90 \leq N$, it was clear that Approach 12 resulted in the least bias for all the sample sizes. For $35 \leq N < 90$, Approach 1 and 12 were better than the other approaches. Fig 4-93 shows the Standard Error (SE) of M, revealing a negligible difference between the SE values of the approaches.

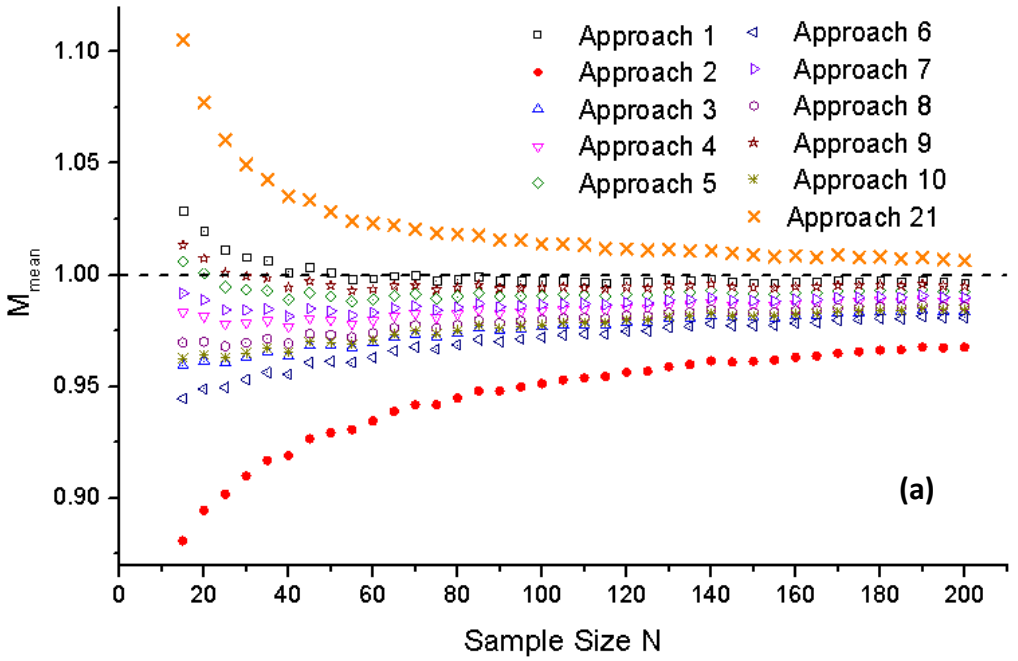

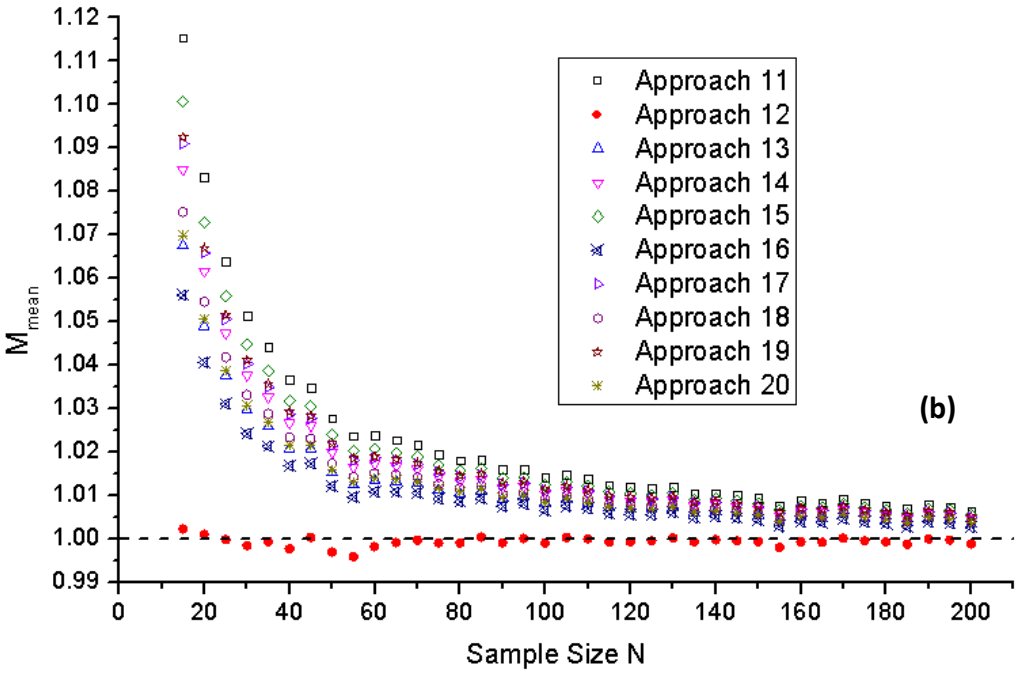

Fig 4-91 M_{mean} values obtained via (a) Approach 1 ~ 10 & 21 in Table 4-9 ; (b) Approach 11 ~ 20, for a direct comparison of the three estimation methods.

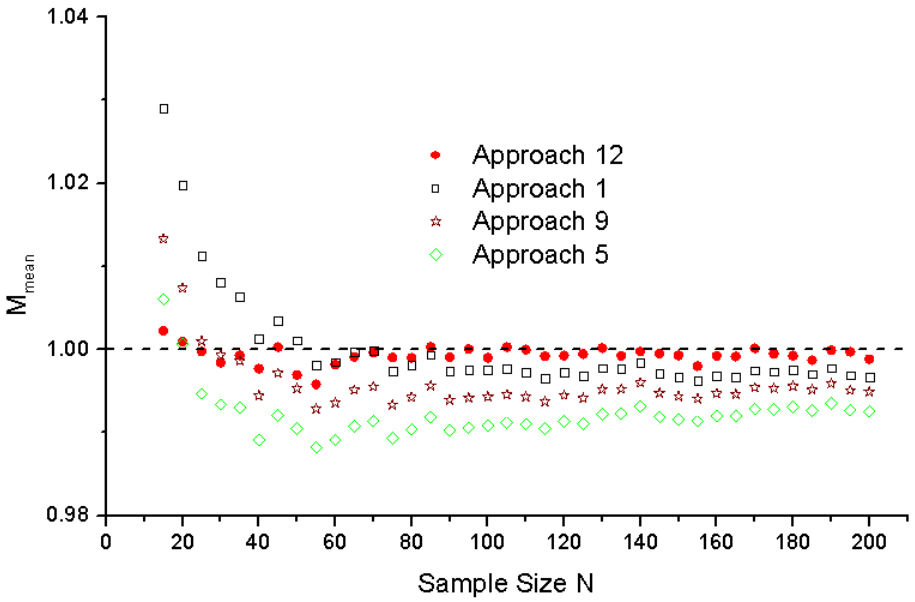

Fig 4-92 a further comparison of Approach 1, 5, 9, and 12 shown in Fig 4-91.

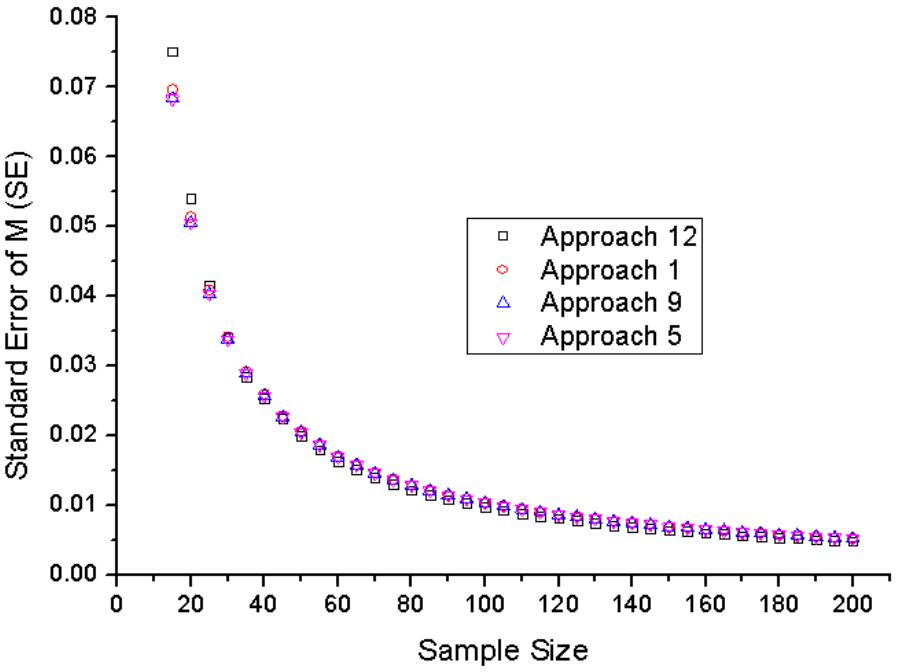

Fig 4-93, standard Error (SE) of the approaches shown in Fig 4-92.

4.5.6 Results: effect of a dramatic enlargement of $DY_{non\text{-}linear,i}$

Fig 4-94 shows the M_{mean} achieved from the datasets containing at least one datum point < 30. As can be seen from Fig 4-94(a), the LLS method (i.e. Approach 1 ~ 10 in Table 4-9) was seriously biased when dealing with this type of data. For 15≤ N ≤ 40,

which was the common sample size for obtaining the Weibull modulus of castings in the previous publications [23, 30, 33, 140], the M_{mean} values were no more than 0.7, presenting a significant bias of the estimated Weibull modulus. In addition, even with a large sample size, such as N = 120, the M_{mean} values of Approach 1 ~ 10 still did not exceed 0.85. Thus it can be suggested that the LLS method is not suitable for estimating the Weibull modulus, when $P_{est.i}$ dramatically deviated from $P_{ture,i}$ in the lower tail. This may be the reason why the data points shown in Fig 4-85 deviated from the linear fit.

By contrast, according to Fig 4-94 (b), the Non-LS method (i.e. Approach 11 ~ 20 in Table 4-9) was significantly less biased. Even the worst approach (Approach 12) of the Non-LS method could cause a smaller bias (M_{mean} > 0.87, at N =15) than any approaches using the LLS method (M_{mean} < 0.85, at N = 120). In addition, Approach 11 was associated with the least biased estimates among all the approaches using the Non-LS methods (Approach 11 ~ 20), especially when the sample size was smaller than 30.

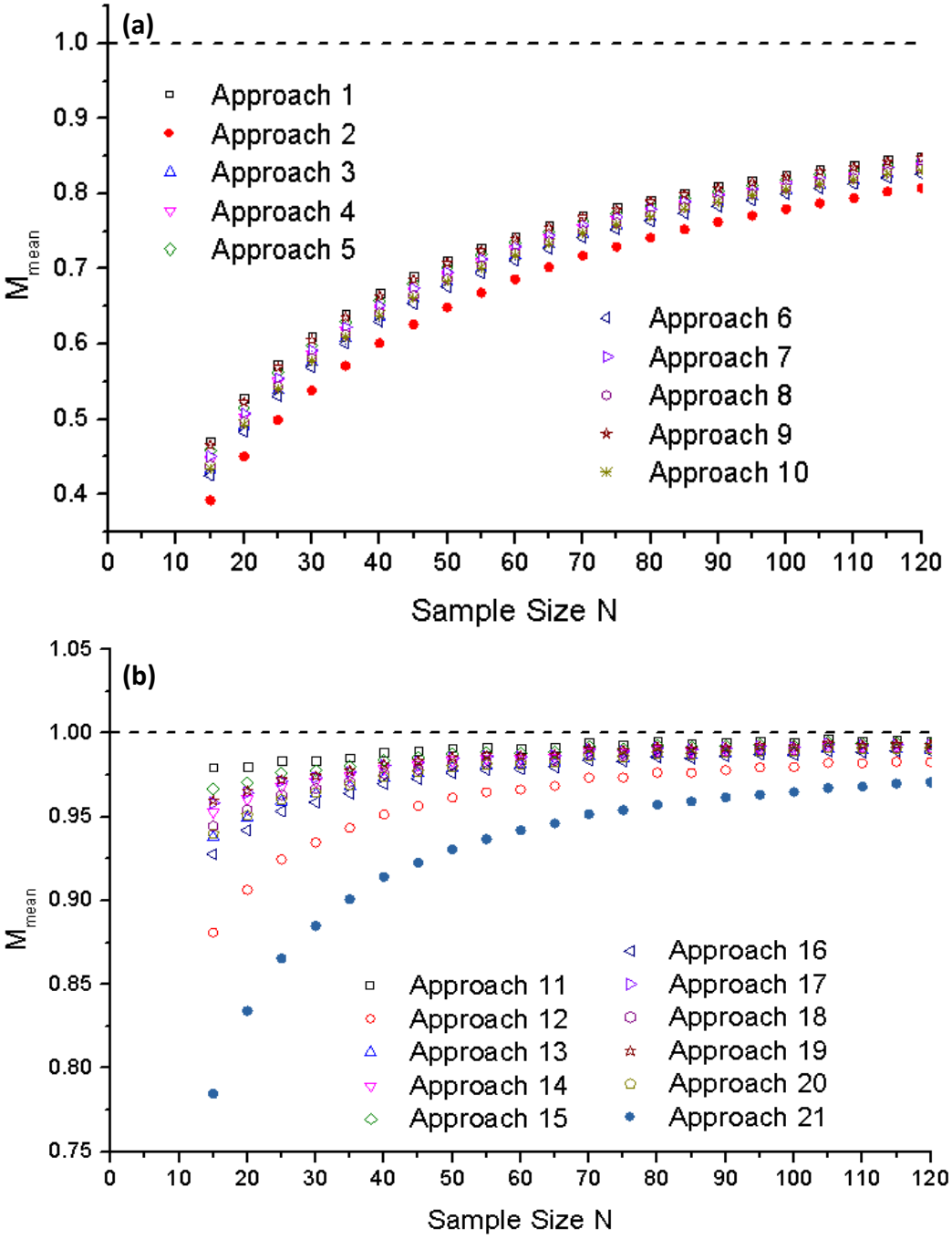

Fig 4-94. M_{mean} of Approach (a) 1 ~ 10, (b) 11 ~ 21 in Table 4-9 applied on the dataset containing at least one datum < 30.

Moreover, it should be noted that Approach 12, which was unbiased in Fig 4-91(b), became the most seriously biased estimator among the approaches of the Non-LS method, indicating that the bias of the approaches could be different depending on

the level of the enlargement of $DY_{non\text{-}linear,i}$.

The M_{mean} obtained via the ML method (Approach 21) was also shown in Fig 4-94 (b), but it was clear that Approach 21 was more biased for all the sample sizes examined, in contrast to the Non-LS method.

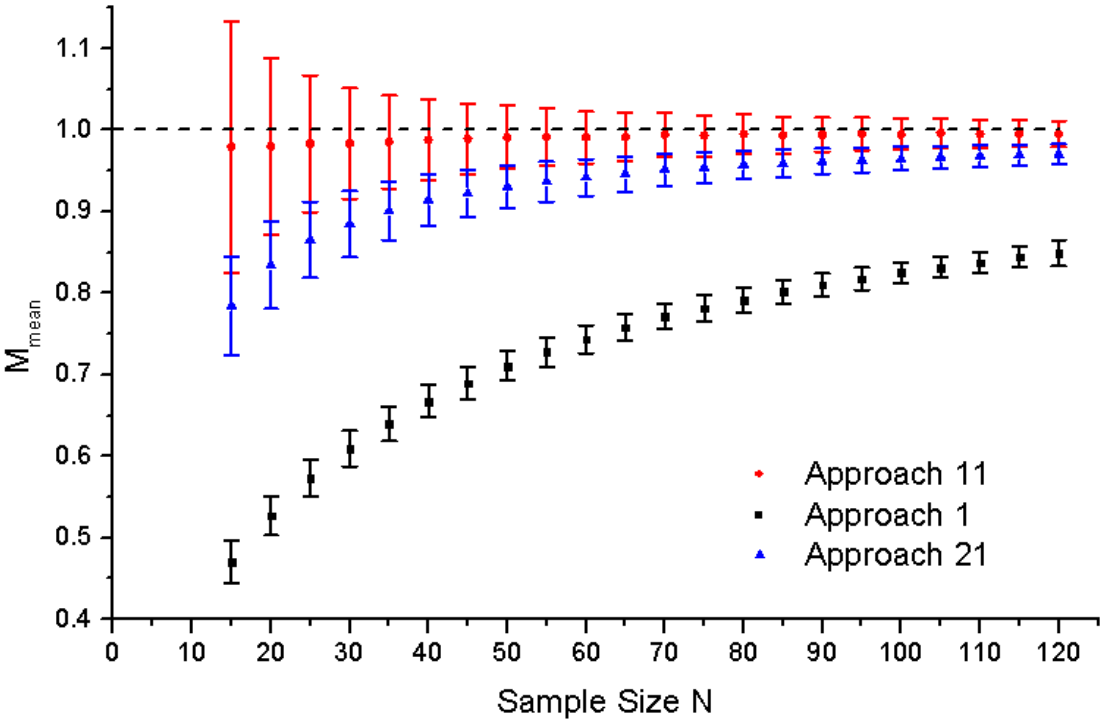

Fig 4-95 95%CI of Approach 1, 11, 21, applied on dataset containing at least one datum < 30.

The 95%CI (confidence interval) of Approach 1, 11, and 21 was computed with the assumption that the M values followed a standard normal distribution, as shown in Fig 4-95.

Therefore, the Non-LS method was relatively reliable, when the estimated probability ($P_{est.i}$) deviated dramatically from true probability ($P_{ture,i}$) in the lower tail, and

Approach 11 was recommended to be the default to estimate the Weibull modulus for this type of data.

4.5.7 Results: critical sum of residual squares (SSRC).

N	SSRC	$SSRC_{mean}$
15	0.0756771	5.0451E-03
20	0.0784904	3.9245E-03
25	0.0797666	3.1907E-03
30	0.0802094	2.6736E-03
35	0.0818855	2.3396E-03
40	0.0816979	2.0424E-03
45	0.0832347	1.8497E-03
50	0.0826510	1.6530E-03
55	0.0837245	1.5223E-03
60	0.0829798	1.3830E-03
65	0.0834890	1.2844E-03
70	0.0831899	1.1884E-03
75	0.0844495	1.1260E-03
80	0.0846093	1.0576E-03
85	0.0842047	9.9064E-04
90	0.0849502	9.4389E-04
95	0.0840484	8.8472E-04
100	0.0846551	8.4655E-04
105	0.0833319	7.9364E-04
110	0.0842549	7.6595E-04
115	0.0845723	7.3541E-04
120	0.0838167	6.9847E-04

Table 4-10, the SSRC values, the used estimator is P = (i-0.5)/N.

Table 4-10 shows the SSRC values for different sample sizes. The estimator used is P = (i-0.5)/N (i.e. Eq. 2-7). As previously referred to, 95% Weibull datasets (19,000 out of 20,000) in the simulation had a smaller SSR than SSRC. Applying this criterion to the Non-LS estimation result shown in Fig 4-86 (N =25), it can be suggested that Griffiths' data (Fig 4-85) follows a 2-p Weibull distribution.

However, it should be noted that this suggestion was quite different using Tiryakioglu's equation (i.e. Eq. 2-25), which suggested Griffiths' data (Fig 4-85) followed a 3-p/mixed Weibull distribution. According to the discussion shown in section 4.5.2, Tiryakioglu's equation may falsely interpret the distribution of Griffiths' data to be a 3-p/mixed Weibull distribution when it is actually 2-p, due to the shortcomings of the linearized Weibull function.

In addition, since the SSR value is affected by the sample size N, SSRC values of the samples that having different sizes could not be directly compared with each other. Therefore the mean sum of residual squares ($SSRC_{mean}$) can be further used to evaluate the goodness-of-fit of the non-linear regression results, as shown in the third column of Table 4-10 and the following equation:

$$\text{Eq. 4-6:} \qquad SSRC_{mean} = SSRC / N$$

The best fit curve of $SSRC_{mean}$ was computed as shown in Fig 4-96, which followed the formula below:

$$\text{Eq. 4-7:} \qquad SSRC_{mean} = 0.06463 * N^{-0.93778}$$

Therefore the author recommends to use Eq. 4-7 instead of Tiryakioglu's equation (Eq. 2-25) to determine the Weibull behaviour of datasets.

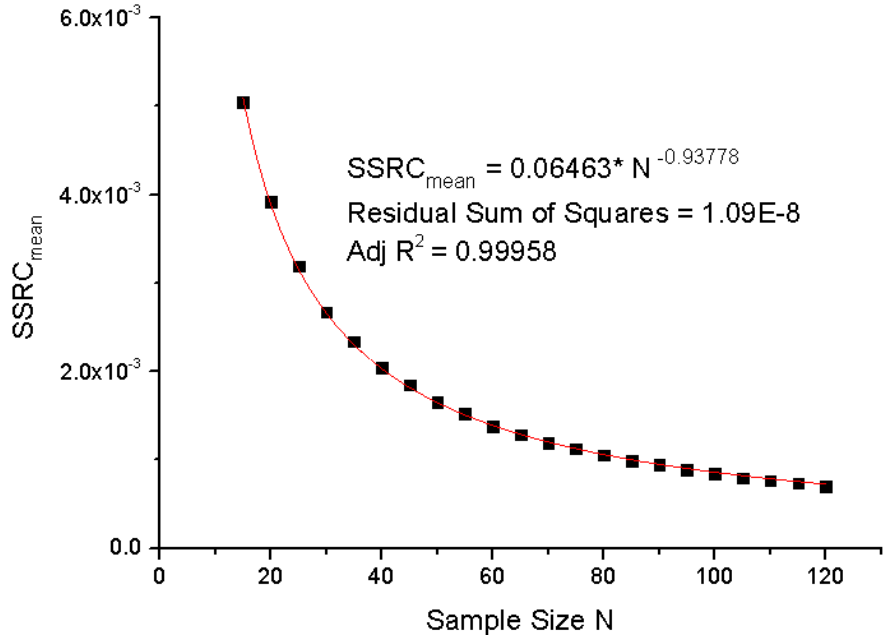

Fig 4-96 the $SSRC_{mean}$ for different sample size.

4.5.8 Summary

Fig 4-87 demonstrated that the difference between the estimated and true cumulative probabilities of data points ($DY_{non\text{-}linear,i}$) would be significantly enlarged due to the linear transformation of the Weibull function. Fig 4-88 revealed that this enlargement level was not uniform: the enlargement could be more dramatic in the lower and upper tails (i.e. when $P_{true,i}$ is close to 0 or 1).

The data examples (Fig 4-86 & Fig 4-89) further indicated that this non-uniform enlargement of $DY_{non\text{-}linear,i}$ can affect the judgement of the Weibull behaviour of datasets. According to the re-analysis of Griffiths' data (Fig 4-86) and the corresponding critical SSRC values (Table 4-10), it is not necessarily correct to reject

the Weibull behaviour of this dataset, according to the goodness-of-fit of the linear regression line, such as the popular method using R^2 value, suggested by [110, 113] (Eq. 2-25). It should be noted that if a significant enlargement of $DY_{non\text{-}linear,i}$ occurred in the lower tail (i.e. the first few data points), even a dataset generated from a Weibull distribution would probably achieve a bad fit to the linear regression line, as shown in Fig 4-89(b).

Therefore, the non-uniform enlargement of $DY_{non\text{-}linear,i}$ is an underlying reason for the deviation of the data points widely reported in previous publications[23, 34, 36, 111, 134, 135]. Although previous researchers suggested that this deviation could be due to an underlying 3-p or mixed Weibull distribution [136-138], more analysis is still required to distinguish the actual reason.

The results of the Monte Carlo simulations (section 4.5.5 ~ 4.5.6) demonstrated that the non-uniform enlargement of $DY_{non\text{-}linear,i}$ resulted in a greater bias in the Weibull modulus estimation. For a common set of data such as was shown in Fig 4-91, where the difference between $DY_{linear,i}$ and $DY_{non\text{-}linear,i}$ is not necessarily large, the Non-LS method is slightly less biased than the LLS method. However, when high enlargement of $DY_{non\text{-}linear,i}$ occurs in the lower tail (Fig 4-94), the Non-LS method has a considerable merit over the LLS method.

It is therefore recommended that the plot of the original non-linear Weibull CDF and

the Non-LS method, which avoids the linear transformation, should be used for the Weibull analysis of material properties.

4.6 Application of the Monte Carlo simulation: Weibull modulus estimation of Mg-alloy castings.

The Monte Carlo simulations indicated that the bias of estimators could be different depending on the data types (i.e. Approach 12 was the best estimator in Fig 4-91(b), but Approach 11 resulted in the least bias in Fig 4-94(b)). In a practical case, since the $P_{true,i}$ is unknown, we are not able to determine the data type according to $DY_{linear,i}$ and $DY_{non\text{-}linear,\ i}$, so that it requires more work to investigate how to choose the best estimator.

However, for the analysis of Mg-alloy castings, it may not be required to consider the effect of data type, since the difference between Approach 11 and 12 is small for a Mg-alloy when N = 40. As can be seen from Fig 4-91(b), for a sample size of N = 40, there is a difference of 5% m_{true} between the estimated values of Approach 11 and 12. In addition, for top-filled Mg-alloy castings, the m_{true} may range from 4 to 20, which means that the difference between the estimated Weibull modulus for Approach 11 and 12 may be less than 1.

Accordingly, in this section, the reproducibility of castings was determined by the estimated results of Approach 11. Approach 1 and 12 were also applied as a

comparison.

Table 4-11 ~ Table 4-13 summarize the raw data for UTS and %Elongation for Mg-alloy castings, sorted in an ascending fashion. The castings were produced according to the process described in section 3.1.4. These tables also summarize whether the double oxide film defects on the fracture surface can be seen by naked eye.

Test bar No.	Mg, 0.5%SF_6+Air			Mg, 0.5%SF_6+CO_2		
	UTS (MPa)	El (%)	Defects visible to the naked eye ?	UTS (MPa)	El(%)	Defects visible to the naked eye ?
1	45.51	2.61	N	52.29	2.46	N
2	55.15	2.76	N	53.61	3.26	N
3	55.29	2.86	Y	54.57	3.42	N
4	58.97	2.96	N	58.46	3.46	N
5	59.14	2.98	N	59.31	3.57	N
6	59.24	3.01	N	62.59	3.68	N
7	59.84	3.18	N	63.56	3.86	N
8	61.08	3.22	Y	63.86	3.93	N
9	61.15	3.36	Y	64.82	4.09	N
10	61.35	3.43	N	66.20	4.21	N
11	63.65	3.47	N	66.67	4.28	N
12	63.72	3.57	N	67.02	4.39	Y
13	64.01	3.57	N	67.66	4.40	N
14	64.06	3.71	N	67.76	4.46	N
15	64.15	3.77	N	68.09	4.52	N
16	64.31	3.79	N	68.67	4.56	N
17	64.69	3.81	N	69.38	4.61	N
18	64.83	3.84	Y	69.49	4.72	N
19	67.52	4.02	Y	69.89	4.81	N
20	68.84	4.03	Y	69.94	4.86	N
21	70.27	4.11	Y	70.18	5.03	N
22	70.92	4.12	N	70.36	5.27	N
23	71.44	4.12	Y	70.58	5.28	Y
24	71.63	4.16	Y	72.00	5.38	N
25	71.90	4.32	N	72.79	5.47	N
26	72.58	4.36	N	72.99	5.60	Y
27	73.21	4.41	N	73.28	5.62	N
28	73.33	4.48	N	74.56	5.66	N
29	73.41	4.51	N	74.96	5.66	N
30	74.34	4.54	Y	75.21	5.70	N
31	75.28	4.56	N	75.50	5.74	N
32	75.63	4.58	Y	75.62	5.76	N
33	76.61	4.68	Y	75.98	5.93	N
34	77.21	4.69	Y	76.63	6.00	N
35	79.70	4.75	N	76.70	6.01	N
36	81.04	4.78	N	78.33	6.48	N
37	81.42	4.86	N	78.73	6.95	N
38	81.76	4.89	N	79.60	7.14	N
39	82.21	5.39	Y	80.34	7.31	N
40	84.62	5.92	Y	82.17	8.88	N

Table 4-11 raw data of UTS and elongation of Mg castings.

Test bar No.	AZ91, 0.5%SF_6+Air			AZ91, 0.5%SF_6+CO_2		
	UTS (MPa)	El (%)	Defects visible to the naked eye ?	UTS (MPa)	El(%)	Defects visible to the naked eye ?
1	102.56	0.79	Y	82.12	0.34	Y
2	113.87	1.21	Y	83.23	0.37	Y
3	118.50	1.24	Y	84.86	0.45	Y
4	119.77	1.29	Y	85.04	0.56	Y
5	120.34	1.32	N	90.10	0.67	Y
6	121.05	1.33	N	94.03	0.67	Y
7	121.70	1.35	N	99.51	0.76	N
8	122.25	1.36	N	110.82	0.95	N
9	123.66	1.39	N	112.59	0.97	Y
10	123.82	1.40	N	115.79	1.03	Y
11	124.27	1.42	N	117.32	1.04	Y
12	124.32	1.43	Y	119.10	1.06	N
13	124.82	1.44	N	119.15	1.13	Y
14	124.83	1.49	N	119.25	1.21	N
15	125.05	1.49	N	120.35	1.22	N
16	125.34	1.49	N	120.99	1.23	Y
17	125.47	1.50	Y	121.98	1.23	Y
18	126.05	1.53	N	122.22	1.23	Y
19	126.37	1.57	N	123.92	1.24	N
20	126.41	1.58	N	123.99	1.26	Y
21	128.61	1.58	N	124.77	1.26	Y
22	128.64	1.61	N	125.62	1.32	N
23	128.80	1.63	N	125.64	1.32	Y
24	129.25	1.63	N	127.49	1.39	N
25	129.91	1.70	N	128.19	1.43	N
26	130.58	1.72	Y	129.33	1.49	Y
27	130.65	1.72	N	130.35	1.53	N
28	131.00	1.75	N	130.86	1.55	Y
29	132.39	1.79	N	132.16	1.62	N
30	132.54	1.82	N	132.72	1.65	N
31	133.82	1.84	N	133.41	1.71	N
32	134.09	1.98	N	133.78	1.82	N
33	134.59	1.98	Y	135.73	1.92	N
34	134.70	1.99	N	136.49	1.92	N
35	136.00	2.17	Y	136.93	1.93	N
36	140.42	2.32	N	137.54	2.00	N
37	142.20	2.32	N	140.12	2.05	N
38	146.01	2.36	N	141.88	2.09	Y
39	146.88	2.56	N			
40	153.24	2.90	N			

Table 4-12 raw data of UTS and elongation of AZ91 castings.

Test bar No.	Mg-Y, 0.5%SF_6+Air			Mg-Y, 0.5%SF_6+CO_2		
	UTS (MPa)	El (%)	Defects visible to the naked eye ?	UTS (MPa)	El(%)	Defects visible to the naked eye ?
1	100.72	0.98	Y	82.90	0.39	Y
2	102.49	1.93	Y	84.80	0.55	Y
3	107.81	2.51	Y	86.01	0.90	Y
4	115.59	2.81	Y	98.28	1.04	Y
5	116.07	2.88	Y	102.93	1.22	Y
6	116.56	3.03	Y	104.55	1.44	Y
7	116.56	3.07	Y	108.32	1.67	Y
8	117.51	3.09	Y	112.00	1.78	Y
9	118.41	3.22	Y	113.92	1.83	Y
10	120.72	3.33	Y	116.87	2.03	Y
11	120.72	3.36	Y	118.07	2.42	Y
12	121.05	3.69	Y	120.36	2.52	Y
13	122.07	3.81	Y	120.55	2.57	Y
14	124.57	3.85	Y	120.67	2.63	Y
15	124.60	3.89	Y	120.92	2.66	Y
16	124.74	3.95	Y	122.17	2.73	N
17	124.90	3.95	Y	122.20	2.77	Y
18	124.98	4.10	Y	122.73	2.87	N
19	125.04	4.25	Y	122.97	2.90	Y
20	126.19	4.26	Y	123.78	2.98	Y
21	126.94	4.44	Y	124.04	3.00	Y
22	127.58	4.44	Y	124.07	3.00	Y
23	127.67	4.54	Y	124.46	3.00	Y
24	128.35	4.74	Y	124.81	3.06	Y
25	128.73	4.78	Y	125.32	3.12	Y
26	129.32	4.82	Y	125.44	3.17	Y
27	129.42	4.86	Y	126.10	3.21	Y
28	129.46	4.87	Y	126.30	3.25	Y
29	129.62	4.87	N	126.63	3.29	Y
30	129.92	5.03	Y	127.48	3.31	Y
31	129.92	5.05	Y	128.27	3.34	Y
32	130.09	5.06	Y	128.62	3.35	Y
33	131.14	5.22	Y	128.90	3.58	Y
34	131.41	5.25	N	129.79	3.73	Y
35	131.51	5.26	Y	130.19	3.75	Y
36	131.83	5.26	N	130.36	3.79	Y
37	132.22	5.50	Y	130.57	3.87	Y
38	133.77	6.02	N	131.29	4.03	Y
39	135.03	6.08	Y	131.69	4.16	Y
40	136.47	6.15	N	133.04	4.25	Y

Table 4-13 raw data of UTS and Elongation of Mg-Y castings.

4.6.1 Commercial purity Mg alloy

Fig 4-97 shows the estimation of Weibull modulus for commercial purity Mg alloy castings, using the LLS method (Approach 1). It can be seen that all the data points approximately followed the linear regression line, and there was no significant deviation. All the R^2 values are larger than the critical R^2 (i.e. $(R_{0.05})^2$ = 0.9256, Tiryakioglu's equation, Eq. 2-25), indicating a good linear fit.

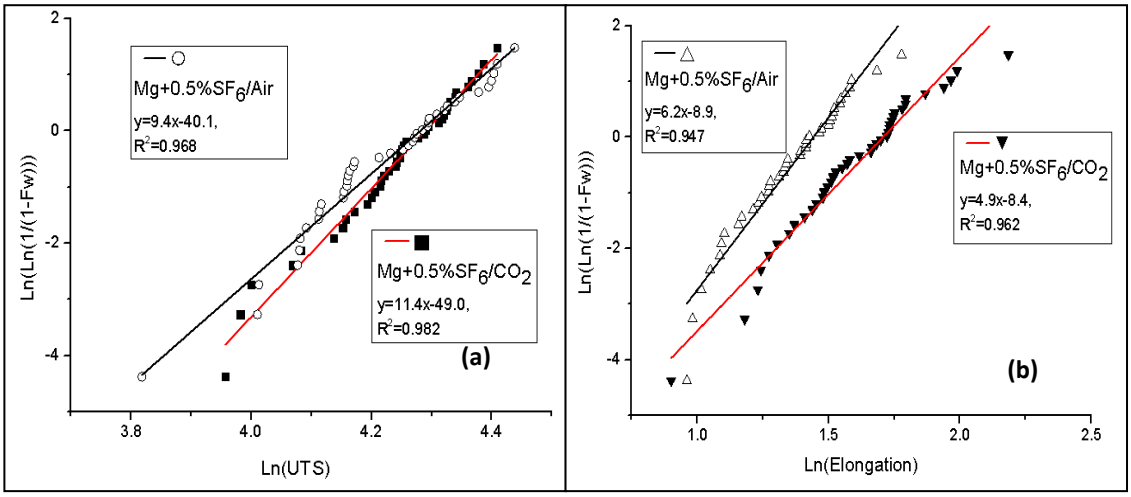

Fig 4-97, the Weibull modulus of (a) UTS, (b) Elongation, of commercial pure Mg castings, estimated via the LLS method (Approach 1).

Fig 4-98 shows the non-linear regressions obtained using Approach 12 (the green solid curve) and Approach 11 (the dashed-black curve). The Weibull function obtained by Approach 1 was also plotted on these figures (the red dashed curve). It can be seen that there was no significant difference between the Non-LS estimation result and the LLS estimation result. In addition, in Fig 4-98(b-c), the SSR of the LLS curves (Approach 1) were even smaller than the critical SSR values (i.e. SSRC = 0.0816979 shown in Table 4-10), revealing a good non-linear fit. In conjunction with

Fig 4-91, which indicated that the M_{mean} values of Approach 1 and 12 was close in the estimation of a common set of data, the datasets shown in Table 4-11 may be the common set of data, of which the enlargement of $DY_{non\text{-}linear,i}$ was not dramatic.

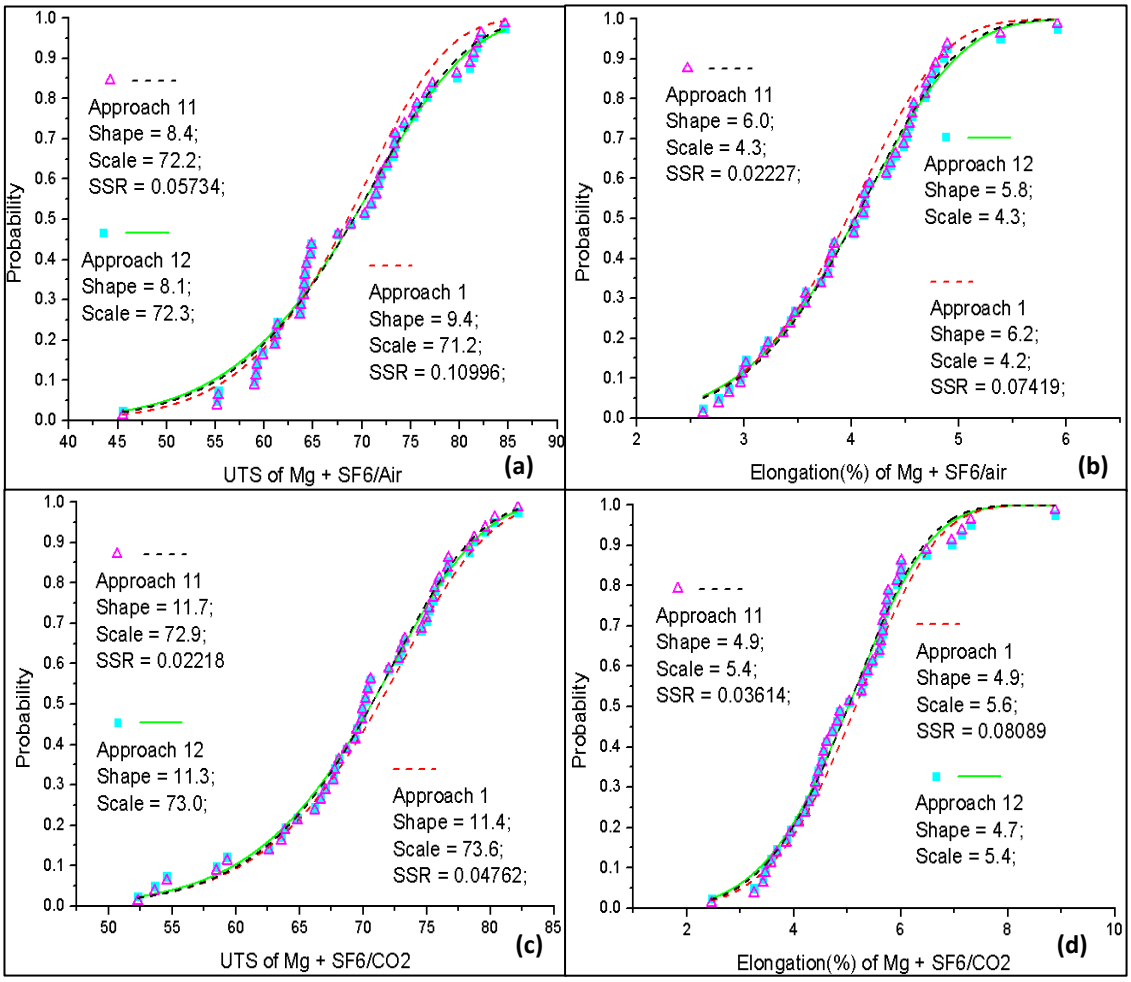

Fig 4-98, the Weibull modulus estimated via Non-LS method (Approach 11 & 12). (a) UTS of Mg casting produced in 0.5%SF_6/air; (b) Elongation of Mg casting produced in 0.5%SF_6/air; (c) UTS of Mg casting produced in 0.5%SF_6/CO_2; (d) Elongation of Mg casting produced in 0.5%SF_6/CO_2;

Therefore, the Weibull moduli of UTS for the Mg casting produced in SF_6/CO_2 (m=11.7) was higher than that of the casting produced in SF_6/air (m=8.1).

Meanwhile, the pure Mg casting produced in SF_6/CO_2 had a bit lower Weibull moduli of %Elongation (m=4.9) than that produced in SF_6/air (m=6). However, the differences between the Weibull moduli were not statistically significant, thus there was no obvious difference between the qualities of the commercial purity Mg castings produced with the different cover gases.

4.6.2 AZ91 alloy

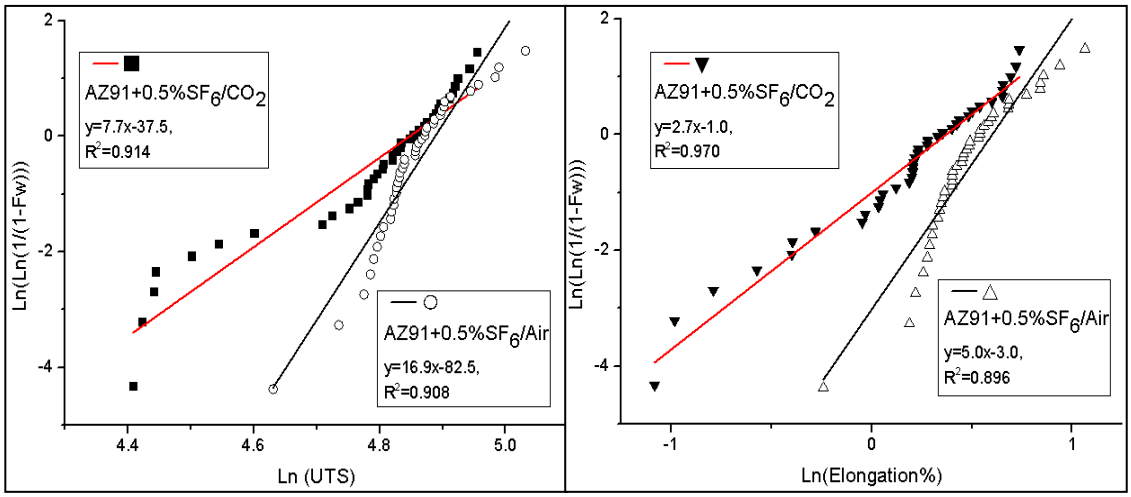

Fig 4-99 , the Weibull modulus of (a) UTS, (b) Elongation, of AZ91 castings, estimated via the LLS method (Approach 1).

Fig 4-99 shows the Weibull plots of the UTS and %Elongation of the AZ91 alloy castings, obtained by Approach 1. It can be seen that only one dataset (elongation of AZ91 + 0.5%SF_6/CO_2) was approximately linearly distributed, while the others deviated towards or away from the linear regression line. According to the critical R^2 ($(R_{0.05})^2$ = 0.9256) based on Tiryakioglu's equation (Eq. 2-25), the Weibullian behaviour of the UTS data and the %Elongation data of AZ91 + 0.5%SF_6/Air would be

rejected.

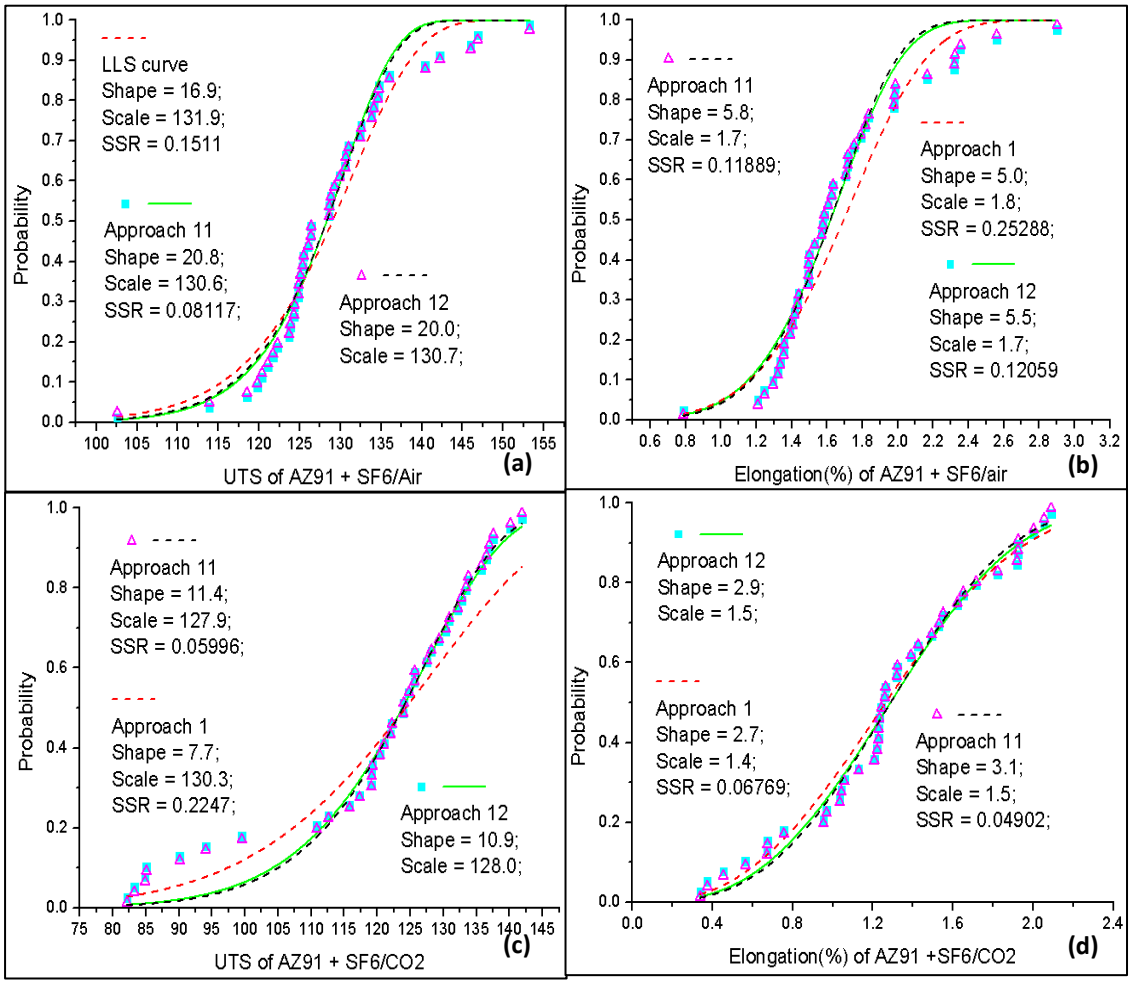

Fig 4-100, the Weibull modulus estimated via Non-LS method (Approach 11 & 12). (a) UTS of AZ91 casting produced in 0.5%SF_6/Air; (b) Elongation of AZ91 casting produced in 0.5%SF6/Air; (c) UTS of AZ91 casting produced in 0.5%SF_6/CO_2; (d) Elongation of AZ91 casting produced in 0.5%SF_6/CO_2;

Fig 4-100 shows the curves obtained using Approach 1, 11 and 12. As can be seen from Fig 4-100 (a and c), the red curve obtained using Approach 1 showed a clear difference compared with the curves from Approach 11 and 12. In addition, the curves obtained by Approach 11 had SSR values smaller than the critical SSR (SSRC = 0.0816979, Table 4-10), indicating the data following a 2-p Weibull distribution. Therefore, these datasets (i.e. UTS of AZ91 + 0.5%SF_6/air, and UTS of AZ91 +

0.5%SF_6/CO_2,) may be falsely interpreted to be 3-p/mixed distribution by Tiryakioglu's equation (Eq. 2-25) in Fig 4-99, when they are actually 2-p.

In Fig 4-100(b), the dataset (i.e. elongation of AZ91 + 0.5%SF_6/air) had a SSR larger than the critical SSR (SSRC = 0.0816979). Thus these data points may follow a 3-p/mixed Weibull distribution. In Fig 4-100(d), the red curve of Approach 1 showed a tiny difference to the curves of Approach 11 and 12.

Therefore, the UTS Weibull moduli of the AZ91 casting produced in SF_6/air was 20.8, while the casting produced in SF_6/CO_2 had a lower UTS Weibull moduli of 11.4, presenting a clear difference. The AZ91 casting protected by 0.5%SF_6/air accordingly had a better reproducibility than that produced in 0.5%SF_6/CO_2.

4.6.3 The Mg-Y alloy

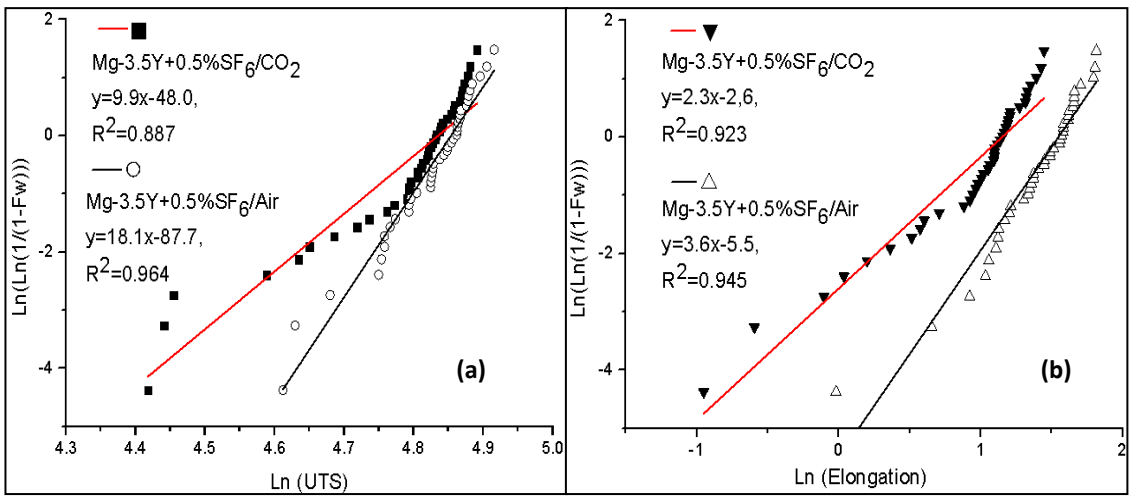

Fig 4-101, the Weibull modulus of (a) UTS, (b) Elongation, of Mg-Y castings, estimated via the LLS method (Approach 1).

The Weibull plots of Mg-Y castings, obtained using Approach 1, are illustrated in Fig 4-101. Both the UTS and %Elongation data points of the Mg-Y alloy + 0.5%SF_6/air were approximately linearly plotted, but the data points of the other casting (Mg-Y + 0.5%SF_6/CO_2) presented a bad linear fit. The Weibull behaviour of all the data of Mg-Y + 0.5%SF_6/CO_2 was rejected by Tiryakioglu's equation (Eq. 2-25, the critical R^2 ($(R_{0.05})^2$ = 0.9256,).

However, the Non-LS estimation (Fig 4-102) indicated that Tiryakioglu's equation falsely interrupted the data shown in Fig 4-101. As can be seen from Fig 4-102(c), there was a significant difference between the Non-LS estimation (Approach 11) and the LLS estimation (Approach 1). In addition, the SSR of the Approach 11 curve was small than the critical SSR (SSRC = 0.0816979), suggesting the data followed a 2-p Weibull distribution. In conjunction with Fig 4-94, the $DY_{non\text{-}linear,i}$ of the data points may be dramatically enlarged in the lower tail, due to the linearized transformation.

In Fig 4-102(d), the SSR was larger than SSRC, rejecting the Weibull behaviour of this dataset. Thus the Weibull modulus of this data was unknown.

Therefore, the UTS Weibull moduli of the Mg-Y casting produced in SF_6/CO_2 was 19.7, which was similar to the UTS Weibull moduli of the casting protected by SF_6/air (m=21.8). Accordingly, there was not a clear difference between the quality of the Mg-Y castings produced in SF_6/air and SF_6/CO_2.

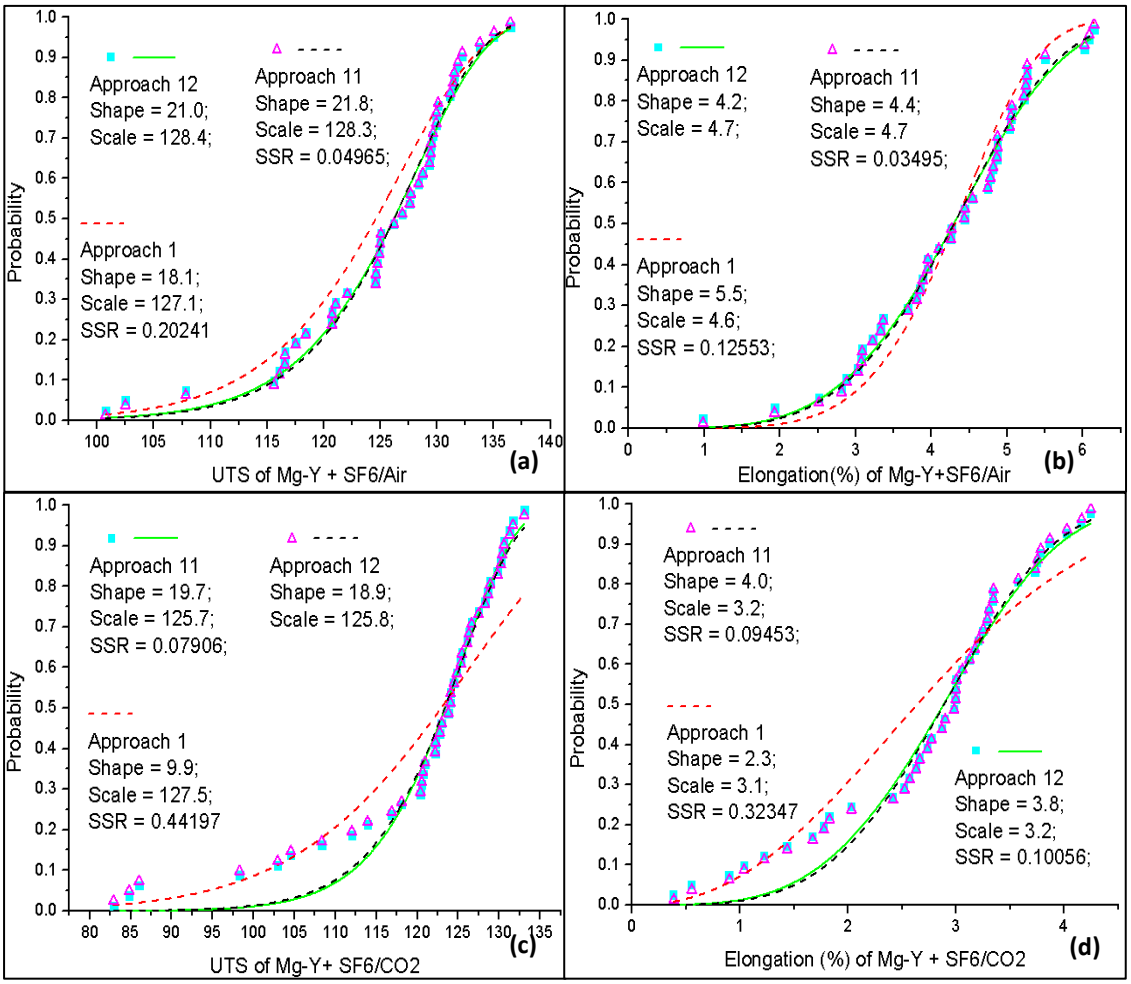

Fig 4-102 the Weibull modulus estimated via Non-LS method (Approach 11 & 12). (a) UTS of Mg-Y casting produced in 0.5%SF6/Air; (b) Elongation of Mg-Y casting produced in 0.5%SF6/air; (c) UTS of Mg-Y casting produced in 0.5%SF6/CO2; (d) Elongation of Mg-Y casting produced in 0.5%SF6/CO2;

4.6.4 Summary

The comparison between the Weibull modulus estimated by the LLS method and the Non-LS method supported that data points could be falsely interrupted due to linearized Weibull function and corresponding R^2 (such as AZ91 alloy casting produced in SF_6/air, Mg-Y alloy casting produced in SF_6/CO_2).

The estimated Weibull modulus of the Mg-alloy castings was summarized in Table 4-14. Two values of the Weibull modulus (i.e. %Elongation of AZ91 + SF_6/air, %Elongation of Mg-Y + SF_6/CO_2) were not listed, since the data points may follow a 3-p or mixed Weibull distribution. It can be seen that the Mg-Y and commercial purity Mg castings produced in SF_6/air did not have a statistical better quality than the corresponding castings produced in SF_6/CO_2. However, the UTS Weibull modulus of AZ91 alloy castings suggested that the casting produced in SF_6/air had a better quality than that produced in SF_6/CO_2.

Cover gas		Commercial purity Mg	AZ91	Mg-Y
SF_6/air	UTS	8.1	20.8	21.8
	%Elongation	6	N/A	4.7
SF_6/CO_2	UTS	11.7	11.4	19.7
	%Elongation	4.9	3.1	N/A

Table 4-14, summary the estimated Weibull modulus of Mg-alloy castings.

Previous researchers suggested that the deviation (for example, Fig 4-99(a)) could be due to the physical flaws (i.e. defects, porosity, segregation) contained in materials [133, 141], and the data points can be interrupted to follow an underlying 3-p or mixture Weibull distribution [136-138]. However, both the simulation results (section 4.5) and the practical experiment results (section 4.6) show that more analysis is still required to distinguish what is the actual reason of this deviation. Table 4-11 ~ Table 4-13 summarize whether the double oxide film defects on the fracture surface can be

seen by naked eyes, but a relationship between the defects distribution and the corresponding deviations can not be found in the linear Weibull estimation. In addition, the Non-LS estimation of the UTS data of AZ91 and Mg-Y alloys (Fig 4-99 ~ Fig 4-102) indicated that the deviation is due to the linearization of Weibull function.

Therefore, a deviation caused by the non-uniform enlargement of $DY_{non\text{-}linear,i}$ may have been falsely interrupted to be due to physical flaws in previous research.

4.7 Hydrogen contained in the trapped gas of double oxide film defects.

Fig 4-103 shows an X-rays image of a specimen sampled from a commercial purity Mg-alloy casting. A trapped bubble (denoted by the red arrow) was contained in this sample. The protective gas used in the casting process was 0.5%SF_6/air. This sample was subsequently placed into the pore gas analyser (see Fig 3-8) for an investigation of the components of the trapped gas.

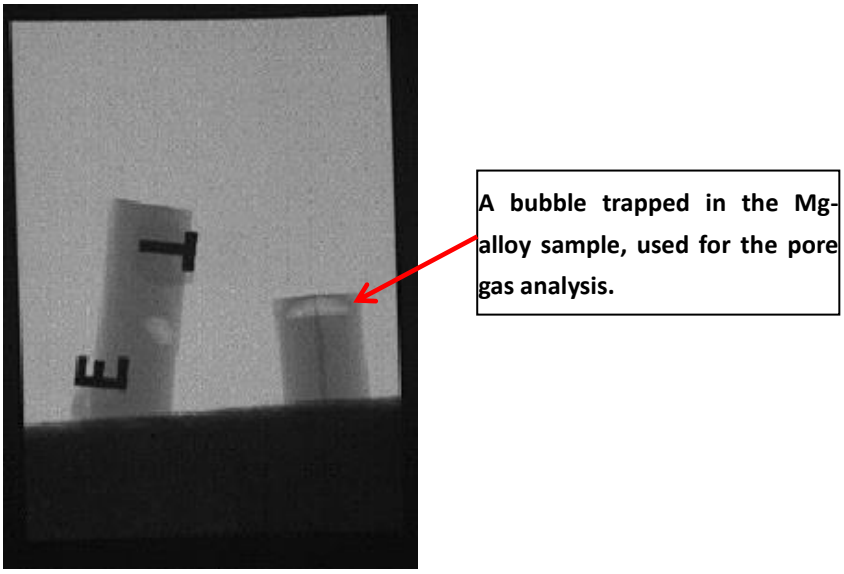

Fig 4-103 a trapped bubble sampled form a commercial purity casting. The diameter of the cylindrical sample is 10 mm

Fig 4-104 shows the mass spectrum result of the trapped bubble. It can be seen that hydrogen and nitrogen were released from the bubble, when the sample was cracked by the needle. The amount of hydrogen was much larger than the amount of nitrogen. Oxygen and decomposition products of SF_6 were not detected in trapped gas. They may have been depleted due to the reactions between the trapped gas and

the surrounding Mg-alloy melt.

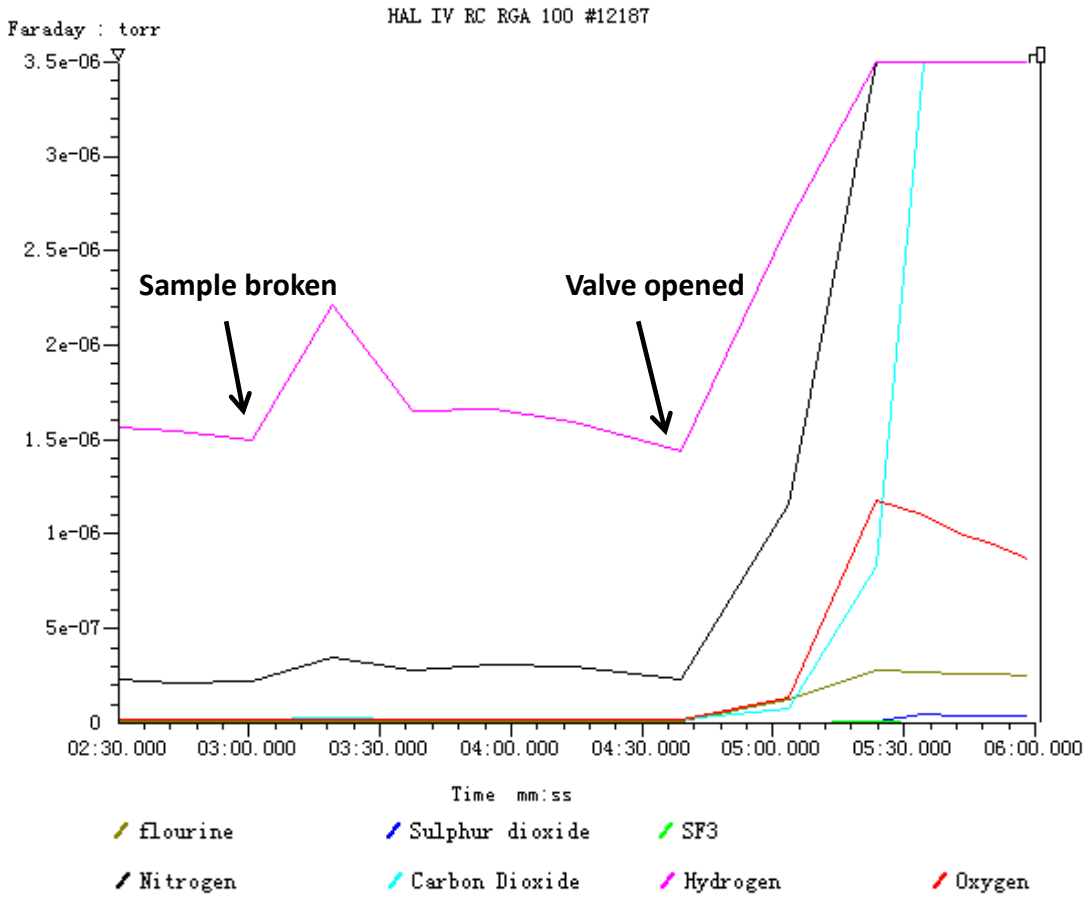

Fig 4-104 Mass spectrum of the trapped bubble shown in Fig 4-103.

The detection of hydrogen in the trapped bubble indicated that the hydrogen was able to diffuse from the Mg alloy melt into an entrained gas. This is a direct evidence of Campbell's conjecture [22] mentioned in section 2.5.1.

4.8 Deactivation of double oxide film defects.

Fig 4-105(a) shows strips sampled from the bottom part of a Mg-Y alloy ingot, produced in an atmosphere of 0.5%SF_6/CO_2. An oxides disposition layer could be

seen in this strip. As shown in Fig 4-105(b), a double oxide film defect was found in the oxides disposition layer. Fig 4-105(c) indicated a tube-like structure of this double oxide film defect.

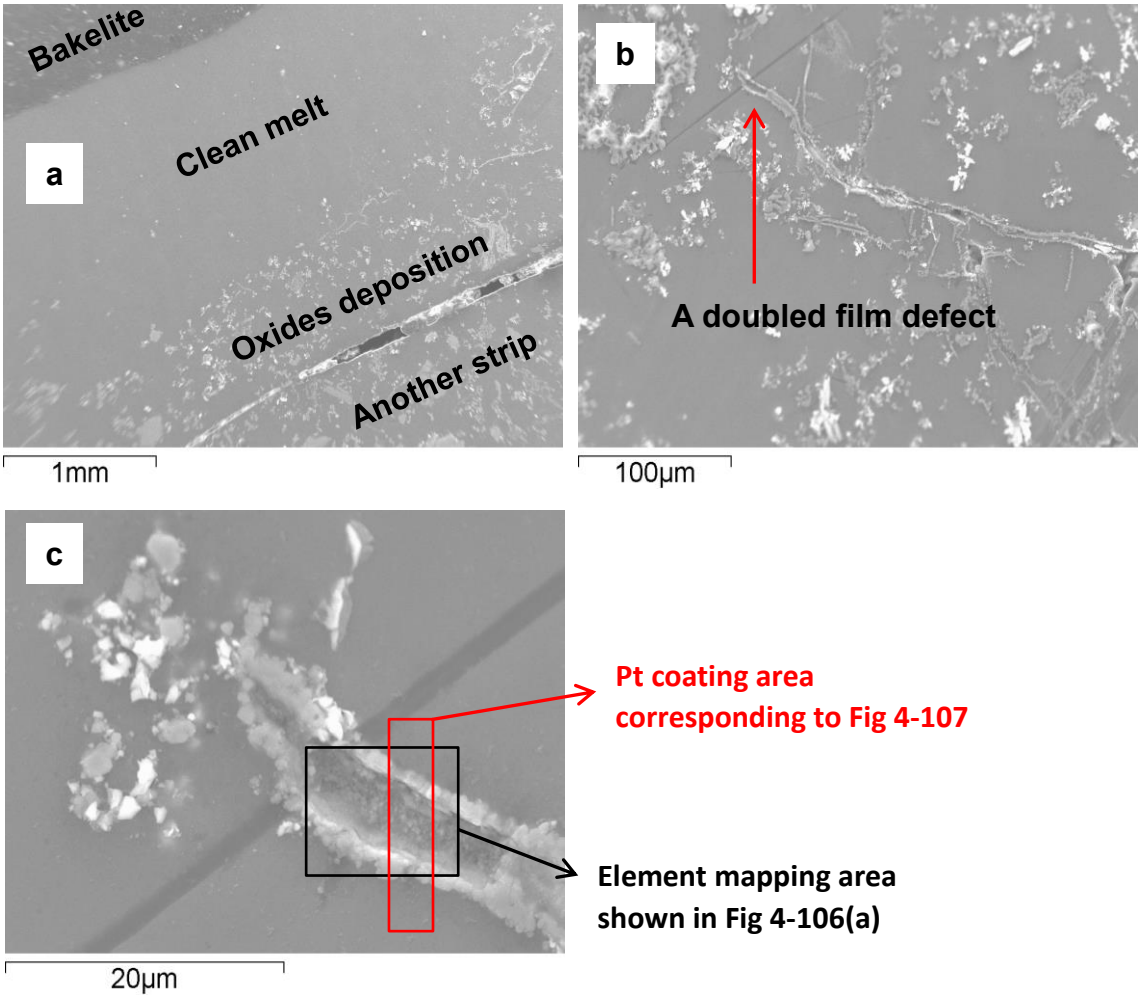

Fig 4-105 (a) a strip sampled from a Mg-Y casting, produced in 0.5%SF6/air. (b) a double oxide film defect contained in the oxides deposition layer shown in (a); (c) a further observation of double oxide film defect, the black rectangular denotes the element mapping area shown in Fig 4-106, and the red rectangular denotes the Pt coating area shown in Fig 4-107.

Fig 4-106 shows the element map of this double oxide defect. It can be that this

defect contained double outer layers enriched with fluorides, and its inner part was composed of oxides.

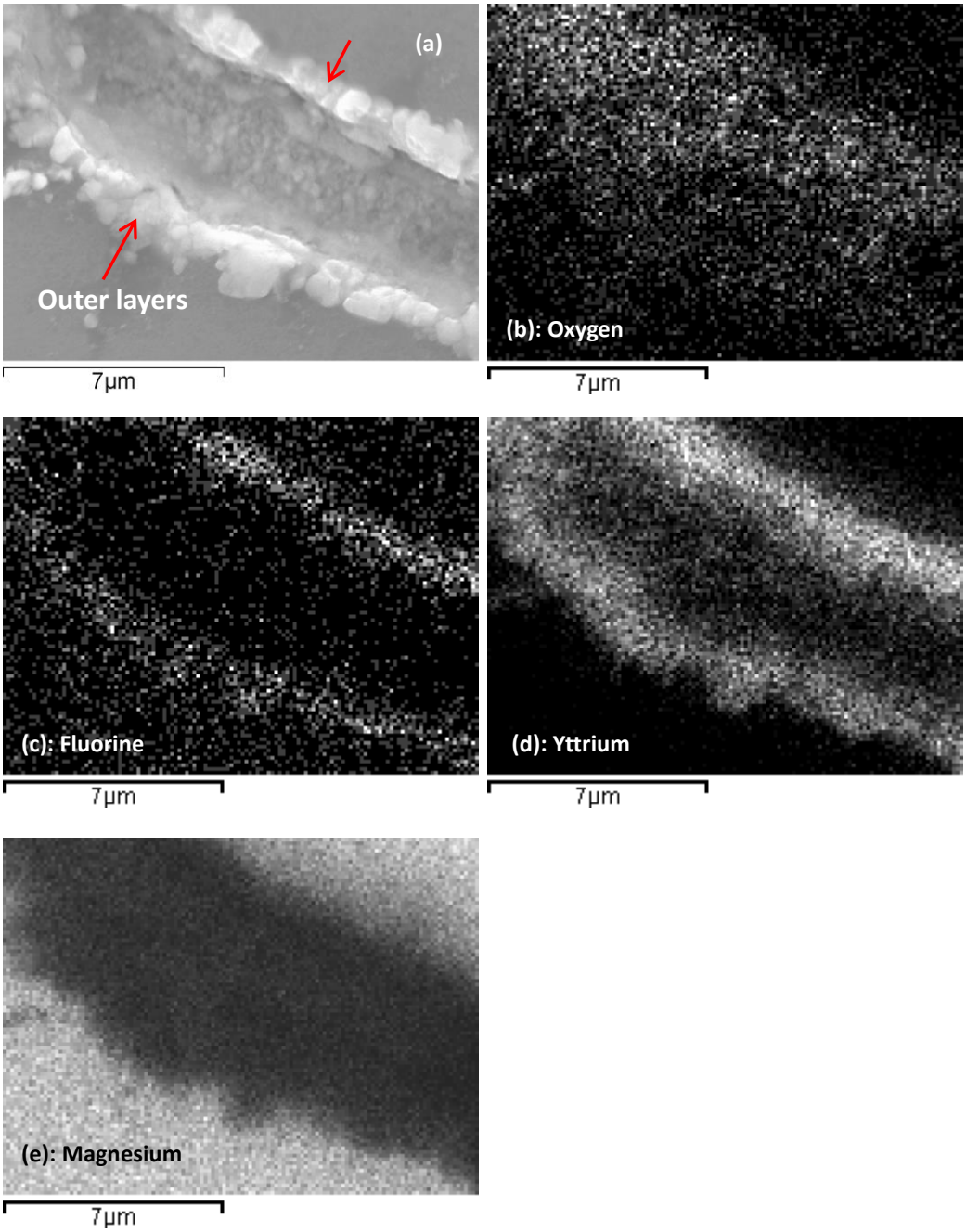

Fig 4-106 Element map of the double oxide film defect shown in Fig 4-105. (a) the area for element mapping, (b) oxygen, (c) fluorine, (d) yttrium, (e) magnesium. The contrast in (e) has been adjust to show the Mg element contained in the double oxide film defect.

A focus ion milling (FIB) process was subsequently carried out by Dr. Keyhum Kim, for exploring the cross section of this double oxide film defect. Fig 4-107 shows the defect after the ion beam milling. The area of the platinum coating corresponded to the area denoted by the red rectangular in Fig 4-105(c).

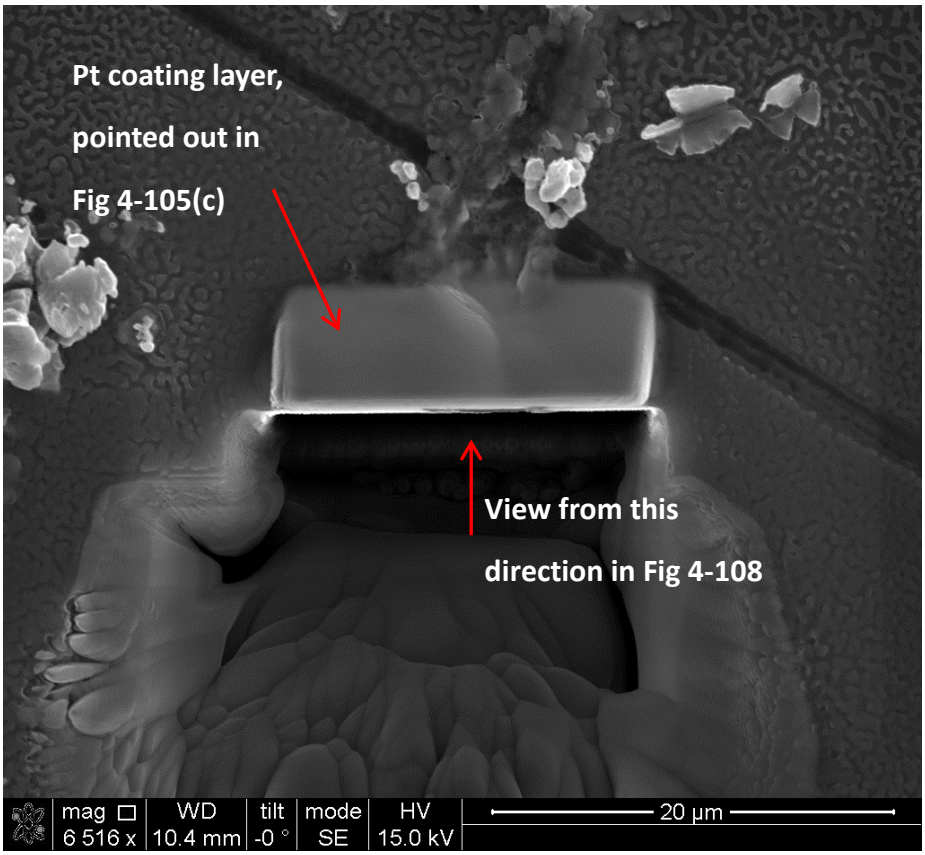

Fig 4-107 the double oxide film defect after ion beam milling.

Fig 4-108 shows the cross sections of the double oxide film defect, obtained by the FIB technique. It revealed that the defect had a sandwich-like structure, rather than a tube-like structure. The corresponding element map (Fig 4-109) revealed that the outer-layer of this sandwich-like structure was enriched with fluorides, and the inner

part might be composed of Y_2O_3 and MgO. The existence of sulphur could not be clearly confirmed in this element map, but there was a sulphur peak in the corresponding EDS spectrum (Fig 4-109(h)). A gap, which may be filled with the residual entrained gas, could be seen between the outer layer and the inner part composed of oxides.

Therefore, a sketch of this sandwich-like structure was produced as shown in Fig 4-110.

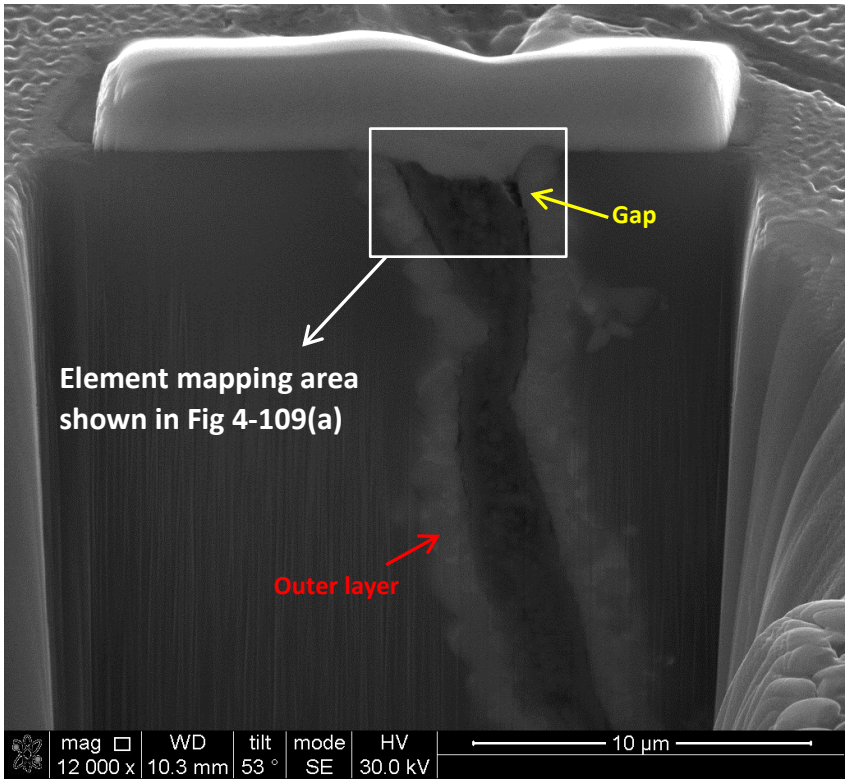

Fig 4-108 cross section of the double oxide film defect shown in Fig 4-105, obtained by FIB technique.

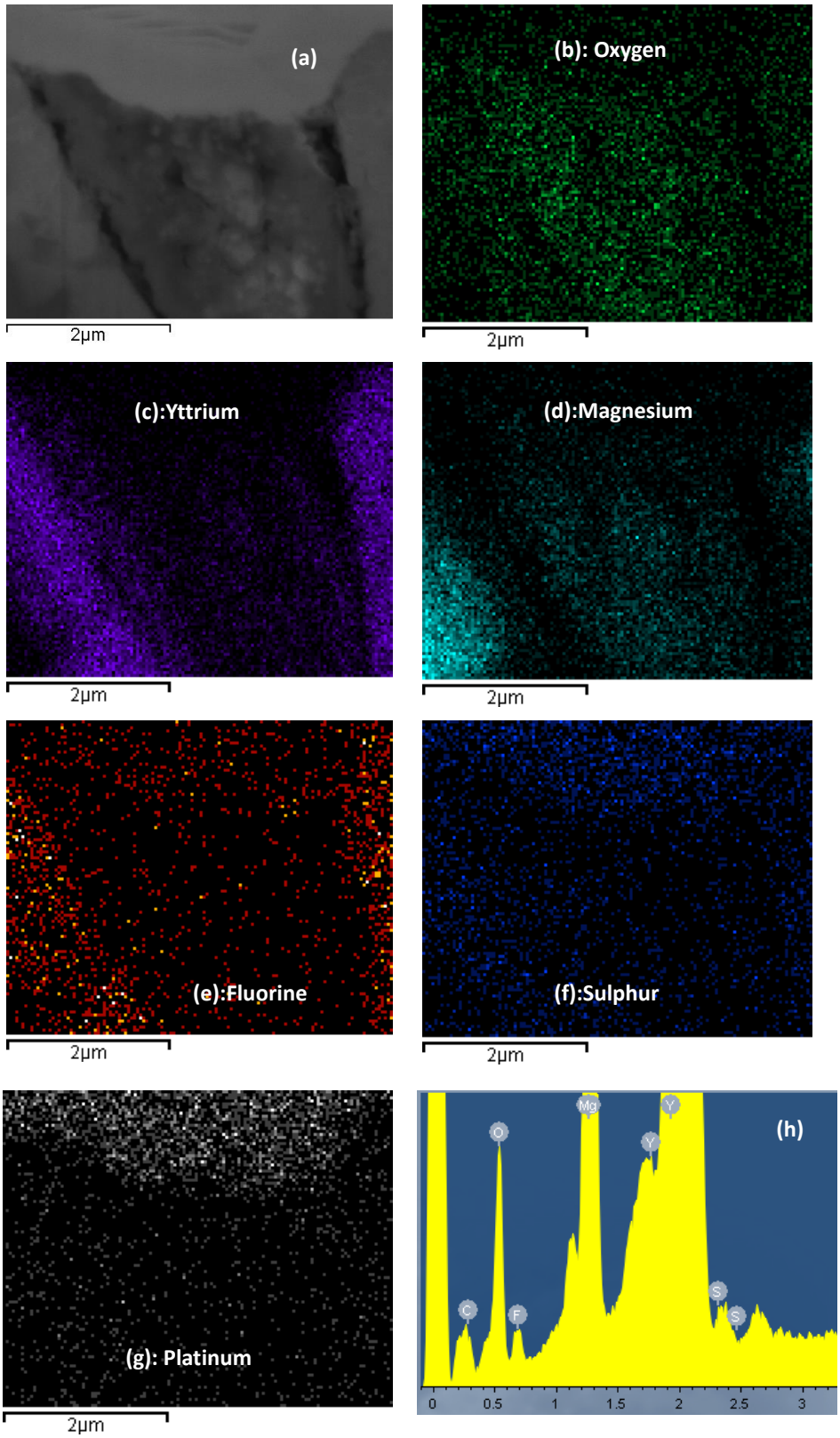

Fig 4-109 element map and EDS spectrum corresponding to the area pointed out in Fig 4-108.

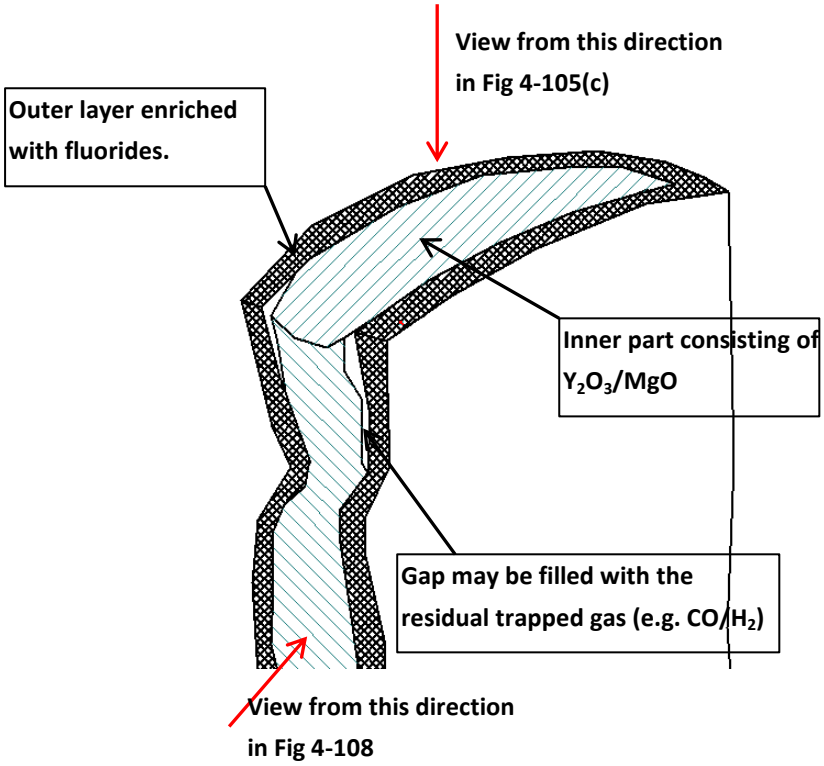

Fig 4-110 a sketch of the sandwich-like structure of the double oxide film defect.

This sandwich-like structure proposed that the oxide interfaces of double oxide film defects could grow together due to the reaction between the entrained gas and the surrounding Mg-alloy melt. Accordingly, the double oxide films may be able to be bonded together, deactivating the double oxide film defect.

5. Discussion

5.1 The Evolution of a double oxide film defect formed in Mg alloys

The reaction process between the cover gas and the Mg-alloy melt was described in section 4.4 from thermodynamic calculations. This theoretical calculation were consistent with the real experiment results (i.e. the oxide film growth process) shown in section 4.3. However, for a gas trapped in a practical casting, the evolution process can be more complicated than the surface growth process and the theoretical calculations, due to the following three reasons:

(1) *Hydrogen diffusion.* Raiszadeh and Griffiths [37], Yue et al.[42] showed that hydrogen can diffuse into a double oxide defect formed in an Al alloy casting. Fig 4-104 (section 4.7) indicated that this diffusion process also occurred in double oxide film defects formed in a Mg-alloy melt. However, hydrogen may not affect the reactions between the trapped gas and the Mg-alloy melt, due to the following reactions:

$2NH_3(g) = N_2(g) + 3H_2(g)$, $\triangle G(700\ ^oC) = -116.956$;

$Mg + H_2O = MgO + H_2(g)$, $\triangle G(700\ ^oC) = -348.812$ kJ;

(2) *Melt flow*. The surface film growth process (section 4.3) indicated that the cover gas could contact with and react with more liquid Mg-alloy melt with increased holding time. In conjunction with the thermodynamic calculations (section 4.4.), of which variables in X-axis is the amount of Mg-alloy having reacted with the cover gas,

it can be suggested that the evolution process of a double oxide defect is time-dependant in a still Mg-alloy melt.

However, in a practical casting process, the evolution of the double oxide film defect is not time-dependent. The films of double oxide film defects can be cracked due to the melt flow, resulting in a trapped gas in melt flow to be in contacted with more liquid Mg-alloy, compared with an entrained gas in a still melt. The reaction process was therefore accelerated due to the melt flow. Even in the same casting, different trapped gases would be in contact with different amount of fresh liquid Mg-alloy. Thus they would not be corresponding to the same stage of the reaction process (i.e. the stages suggested in section 4.3.9 and section 4.4). This is the reason why the double film defects, sampled from the same casting, contained different compositions in the oxide films, as shown in [142] (author's paper).

(3) *Oxides in the initial oxide film*. The surface film growth process (section 4.3) and the corresponding thermodynamic calculations (section 4.4) showed that the oxide film only contained MgF_2 in the early stage (i.e. stage 1 in the calculations), but it should be noted that the initial oxide film of a double oxide film defect may not necessarily contain MgF_2 only, due to the following two reasons:

Firstly, the surface film formation process occurring in the steel crucible was different with the thermodynamic calculations ((section 4.4) and surface film growth

process occurring in the oxidation cell (section 4.3), since the amount of SF_6 was sufficient in the steel crucible, but limited in the oxidation cell and the calculations. In addition, in the casting experiment reported in this thesis, it took approximately 15 mins to melt the Mg-alloy ingots in the steel crucible. Thus the initial protective film, covering the Mg-alloy melt surface in the crucible, was an old oxide film. Xiong and Wang's result [59] suggested this old oxide film consisted of MgF_2/MgO, but Nie et.al [60] found MgS in the oxide film after a holding time of 25 hours. Since the casting process reported here was completed in less than 30 min, it can be suggested that the oxide film contained fluorides and oxides, but no sulphates or sulphides.

Secondly, during the pouring process, the Mg-alloy melt flow, between the exit of the crucible and the pouring basin of the sand mould, was not protected by the cover gas, which can also result in the initial film of double oxide film defects to contain oxides.

Therefore, the evolution of the double oxide film defects formed in the three Mg alloy castings (i.e. commercial purity Mg, AZ91, Mg-Y) under two protective gases (SF_6/Air, SF_6/CO_2), can be suggested to be as described in the following sections.

5.1.1 Commercial purity Mg in SF_6/air.

Fig 5-1 illustrates the formation and evolution of a double oxide film defect formed in a commercial purity Mg casting cast with a protective gas of SF_6/air. In conjunction

with the results shown in section 4.1 ~ 4.4, the process can be described according to the following stages.

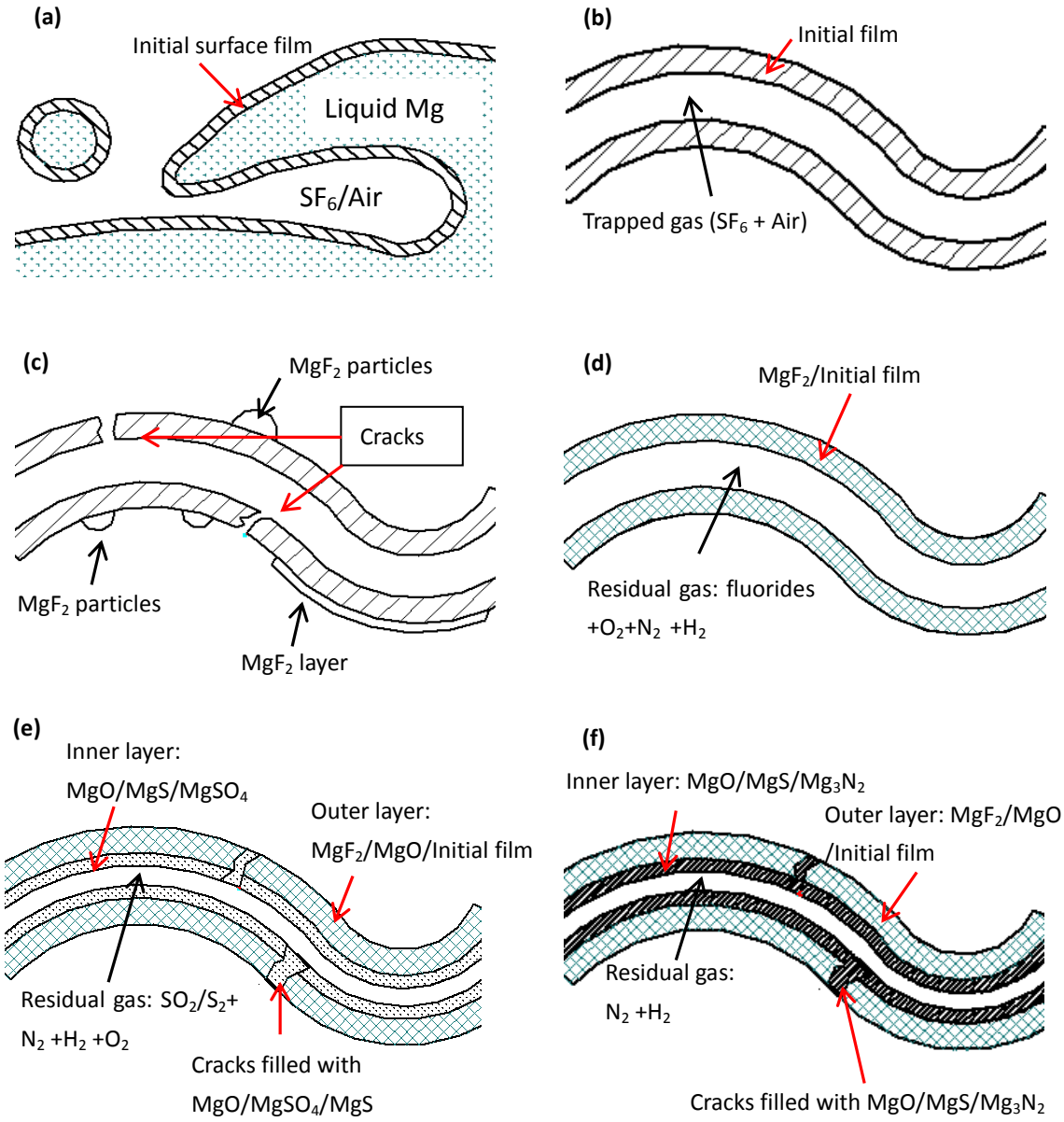

Fig 5-1, The formation and evolution process of a double oxide film defect formed in a pure Mg casting in an atmosphere of SF_6/air (a) entrainment of a surface film formation; (b) the newly-formed double oxide film defect; (c) cracks; (d ~ f) final entrainment defects.

In stage 1, Fig 5-1 (a), an oxide film has been formed on the melt surface due to reactions between the liquid Mg-alloy and the cover gas. As previously discussed, this initial surface film, formed in the steel crucible or during pouring process, would consist of MgF_2/MgO.

In stage 2, Fig 5-1(b), the newly-formed defect would be covered by the initial film. The entrained gas originally consists of SF_6 and air.

In stage 3, Fig 5-1 (c), the fluorine in the trapped gas can penetrate through the initial surface film, forming MgF_2 particles attached to the oxide film, as in the MgF_2 semi-circular features shown in Fig 4-22 and Fig 4-24. In addition, in conjunction with observations shown in Fig 4-26 and Fig 4-27, these particles may further form a MgF_2 layer.

Meanwhile, the initial surface film can be cracked due to melt movement, and fresh liquid Mg can come into contact with the interior atmosphere of the defect through the cracks, reacting with the trapped gas and forming new surface films. According to the surface film growth process suggested in section 4.3.9 and the thermodynamic calculation (section 4.4.1, Fig 4-77), the formation of new surface film can reduce the total fluorine content in the trapped gas, but the sulphur accumulates in the residual gas as SO_2 (as demonstrated in section 4.3.8, Fig 4-76).

Simultaneously, hydrogen can diffuse into the entrained gas, through the cracks and the permeable film.

Therefore in stage 4, three types of final entrainment defects may exist, as shown Fig 5-1(d) ~ (f), depending on the amount of liquid Mg that reacts with the trapped gas:

Firstly, Fig 5-1(d), if the amount of the liquid Mg, that comes into contact with the entrained gas, was not enough to consume the fluorides in the trapped gas, corresponding to stage 1 shown in Fig 4-77 (i.e. the early stage suggested in section 4.3.9), the surface film can contain MgF_2 and the compounds of the initial surface film (i.e. MgF_2/MgO), which is consistent with the components of the oxide film shown in Fig 4-2, Fig 4-3, and Fig 4-22 ~ Fig 4-24. The residual entrained gas contains SF_6, hydrogen, air and the decomposition products of SF_6.

Secondly, Fig 5-1 (e), if the liquid Mg, in contact with the entrained gas, consumed nearly all of the fluorides in the trapped gas, but did not deplete sulphur, corresponding to the stages 2 shown in Fig 4-77 (i.e. medium stage suggested in section 4.3.9), the final surface film can contain further $MgSO_4$ and MgS, which was consistent with the components of the surface films shown in Fig 4-37 ~ Fig 4-42. In addition, the film-cracking due to the melt flow can cause different film structures. As shown in Fig 5-1 (e), for the un-cracked film, an outer layer composed of $MgSO_4$/MgS/MgO may become attached to the initial MgF_2/MgO film, making a

double-layered structure like the surface film shown in Fig 4-37, but the cracked area is filled with a mixture of $MgSO_4$/MgS/MgO, presenting a single layer. The residual entrained gas therefore mainly contains sulphur dioxide/sulphur, air and hydrogen at this stage.

Finally, if all fluorides and sulphur in the entrained gas were consumed by the Mg melt, corresponding to stage 3 shown in Fig 4-77 (i.e. final stage suggested in section 4.3.9), the surface film may contain MgS/$MgSO_4$, MgO, MgF_2 and Mg_3N_2, as shown in Fig 5-1 (f). The residual entrained gas then only contains N_2 and H_2, which was consistent with the trapped gas shown in Fig 4-103. If the process continued further, making more liquid Mg come into contact with the entrained gas, N_2 can be depleted, so that the final entrained gas may only contain H_2.

5.1.2 Commercial purity Mg in SF_6/CO_2.

The evolution process of a double oxide film defect formed in pure Mg castings protected by SF_6/CO_2 was quite similar to the previous process described in section 5.1.1 for Mg and SF_6/air. The corresponding stages are illustrated in Fig 5-2.

In stage 1 ~ 2, Fig 5-2(a -b), a folded oxide film forms a double oxide film defect. The initial film, covering the original defect, can consist of MgF_2/MgO.

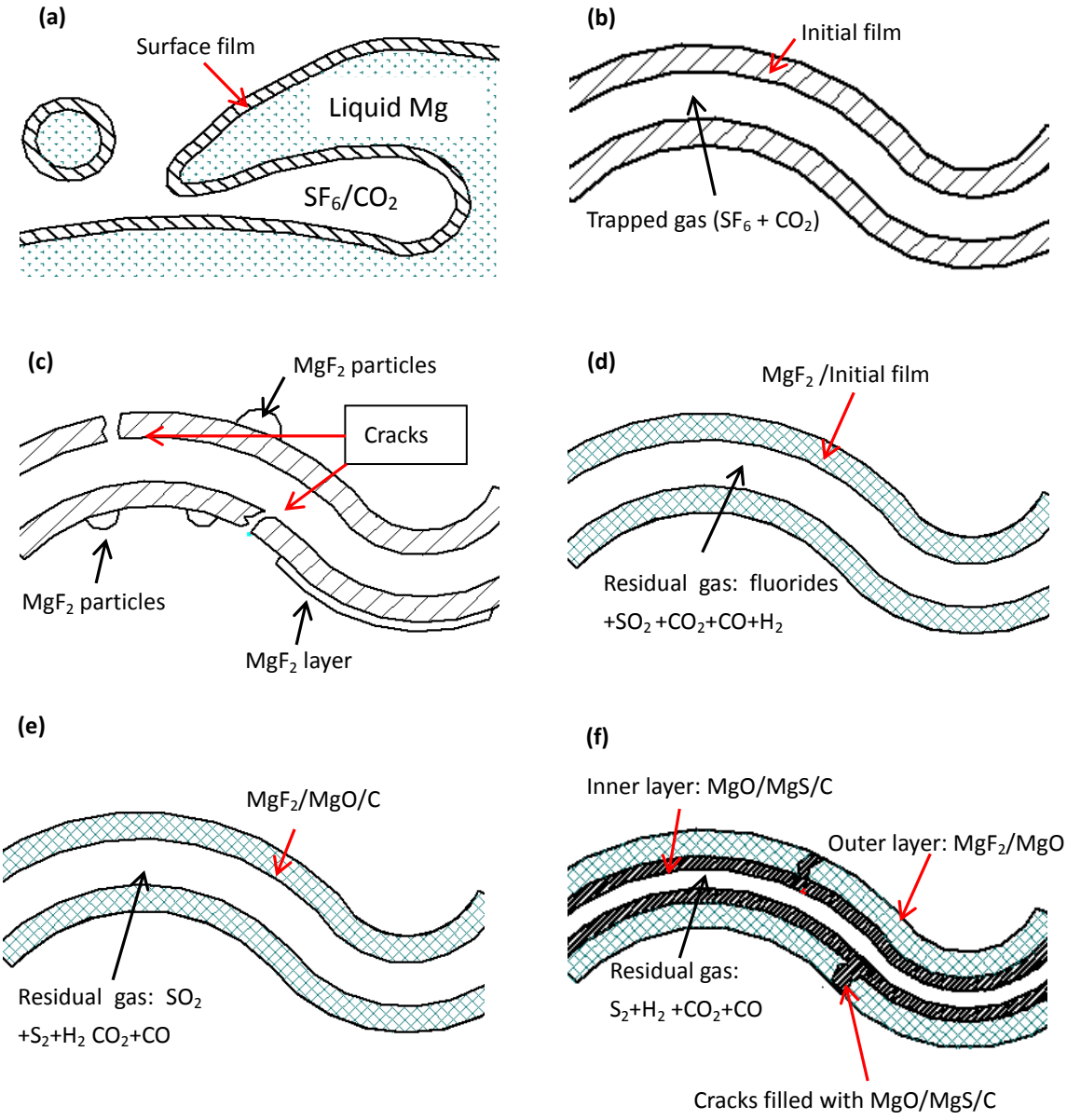

Fig 5-2. Formation and evolution process of a double oxide film defect formed a pure Mg casting in a atmosphere of SF_6/CO_2 (a) entrainment of a surface film formation; (b) the original double oxide film defect; (c) cracks; (d ~ f) final entrainment defects.

In stage 3, Fig 5-2 (c), the MgF_2 layers and particles, attached to the oxide film, are formed due to the fluorine penetration, which was consistent with the MgF_2 inner

layer shown in Fig 4-26, and the MgF_2 particles shown in Fig 4-27. Meanwhile, the cracking process due to melt flow accelerated the reaction process (Fig 4-78). Hydrogen simultaneously diffuses from the melt into the entrained gas.

Thus finally, in stage 4, there are also three types of final double oxide defects as shown Fig 5-2 (d) ~ (f).

Firstly, Fig 5-2(d), if fluorides in the trapped gas are not depleted by the molten Mg that come into contact with the entrained gas, corresponding to stage 1 shown in Fig 4-78(i.e. the early stage in section 4.3.9), the surface film contains MgF_2 and the compounds of the initial surface film (i.e. MgF_2/MgO), which is consistent with the components of the surface film shown in Fig 4-6, and Fig 4-26 ~ Fig 4-27. The residual entrained gas contains SF_6, hydrogen, CO_2, CO, SO_2 and the decomposition products of SF_6.

Secondly, Fig 5-2 (e), if the fluorides are depleted, corresponding to the stage 2 shown in Fig 4-78 (i.e. the medium stage in section 4.3.9), the final surface film can contain further MgO and C, which was consistent with the components of the surface films shown in Fig 4-47. The residual entrained gas therefore can contain sulphur dioxide/sulphur, CO_2, CO and hydrogen.

Finally, Fig 5-2 (f), if the reaction process occurs in stage 3 shown in Fig 4-78 ((i.e. the final stage in section 4.3.9), the surface film can contain further MgS and has multiple structures. The un-cracked area has an inner layer composed of MgS/MgO/C attached to the initial film, but the cracking area may be filled with a single layer of MgS/MgO/C.

5.1.3 AZ91+SF_6/air

As discussed in section 4.4.3, the oxide film can react with the AZ91 alloy melt, due to the following reactions:

$1.5Mg + AlF_3 = 1.5MgF_2 + Al$, $\triangle G(700^oC) = -175.64$ kJ;

$3Mg + Al_2O_3 = 3MgO + 2Al$, $\triangle G(700^oC) = -119.82$ kJ;

$Mg + MgAl_2O_4 = MgO + Al$, $\triangle G(700^oC) = -106.34$ kJ.

It should be noted that the reaction process, between the oxide film and the liquid Mg-alloy, may be time-dependant, since the melt flow can not affect these reactions, which was different with the reactions between the trapped gas and the Mg-alloy melt. Thus, an old AZ91 oxide film (held in the melt for at least 5 min) did not contain Al as shown in Fig 4-49 ~ Fig 4-55, but a young AZ91 oxide film (cooled down in less than 2 min) contained Al as the films shown in Fig 4-28 ~ Fig 4-30.

Therefore, the evolution process of double oxide film defects formed in an AZ91 alloy under a cover gas of SF_6/air can be suggested to have the following stages:

In stage 1 ~ 2, Fig 5-3 (a -b), a folded melt surface film forms a double oxide film defect. The initial film of this defect consists of MgF_2/MgO/ $MgAl_2O_4$/Al_2O_3/AlF_3, if the melt surface film is a young oxide film (held for less than 2 mins); or MgF_2/MgO, if the melt surface film is an old oxide film (held for more than 5 mins).

In stage 3, Fig 5-3 (c), MgF_2 layers or particles can be formed under the initial film, as with the MgF_2 layer shown in Fig 4-29. Meanwhile, the melt flow can crack the initial film, introducing fresh AZ91 melt into the defect, forming oxides and fluorides to fill the cracked area. Aluminium is contained in the newly formed area of the film, and it will not disappear due to the reaction between the melt and Al oxides, since the casting was solidified in a short time (less than 2 min) as previously mentioned. Hydrogen simultaneously diffuses from the melt into the entrained gas.

Thus finally, in stage 4, there are also three types of final double oxide defects as shown Fig 5-3 (d) ~ (f).

Firstly, if fluorides in the trapped gas are not depleted by the melt that come into contact with the entrained gas, corresponding to stage 1 shown in Fig 4-79 (i.e. the early stage suggested in section 4.3.9), the surface film should contain MgF_2/AlF_3 and the compounds of the initial surface film (MgF_2/MgO or MgF_2/MgO/ $MgAl_2O_4$/Al_2O_3/AlF_3), as shown in Fig 5-3 (d). It should be noted that AlF_3 may only

exist in the cracked area if the initial film is an old oxide film (i.e. containing MgF_2/MgO), since cracks are the only area that the trapped gas directly contact with fresh liquid AZ91. This may be the reason why aluminium is only contained in a section of the oxide film shown in Fig 4-29. In addition, if the initial surface film is a young oxide film (i.e. containing MgF_2/MgO/ $MgAl_2O_4$/Al_2O_3/AlF_3) Al would be detected in the whole area of the oxide film, as shown in Fig 4-30. The residual entrained gas contains H_2, O_2, N_2, SO_2 SF_6 and the decompositions of SF_6.

Secondly, if the fluorides are depleted, corresponding to stages 2 shown in Fig 4-79 (i.e. the medium stage suggested in section 4.3.9), the final surface film with their cracked and un-cracked areas has different structures as shown in Fig 5-3 (e). The cracked area is filled with a single layer composed of MgO/ $MgSO_4$/ MgS/ Al_2O_3/ $MgAl_2O_4$. However, the un-cracked area would have a doubled-layer structure similar with the films shown in Fig 4-49 ~ Fig 4-53 : an inner layer composed of MgO/$MgSO_4$/MgS, and an outer layer consisting of MgF_2/MgO + the compounds of the initial film. The residual entrained gas therefore should contain sulphur dioxide/sulphur, H_2, O_2, and N_2.

Finally, if the reaction process in the stage 3 shown in Fig 4-79 (i.e. the final stage suggested in section 4.3.9) occurs, the cracked area of the surface film may contain AlN, while the outer layer of the un-cracked area can contain MgS/$MgSO_4$, MgO, and AlN, as shown in Fig 5-3 (f). The residual entrained gas may then only contain N_2 and

H_2. If the process continues further, and more liquid Mg came into contact with the entrained gas, N_2 could be depleted, so that the final entrained gas may only contain H_2.

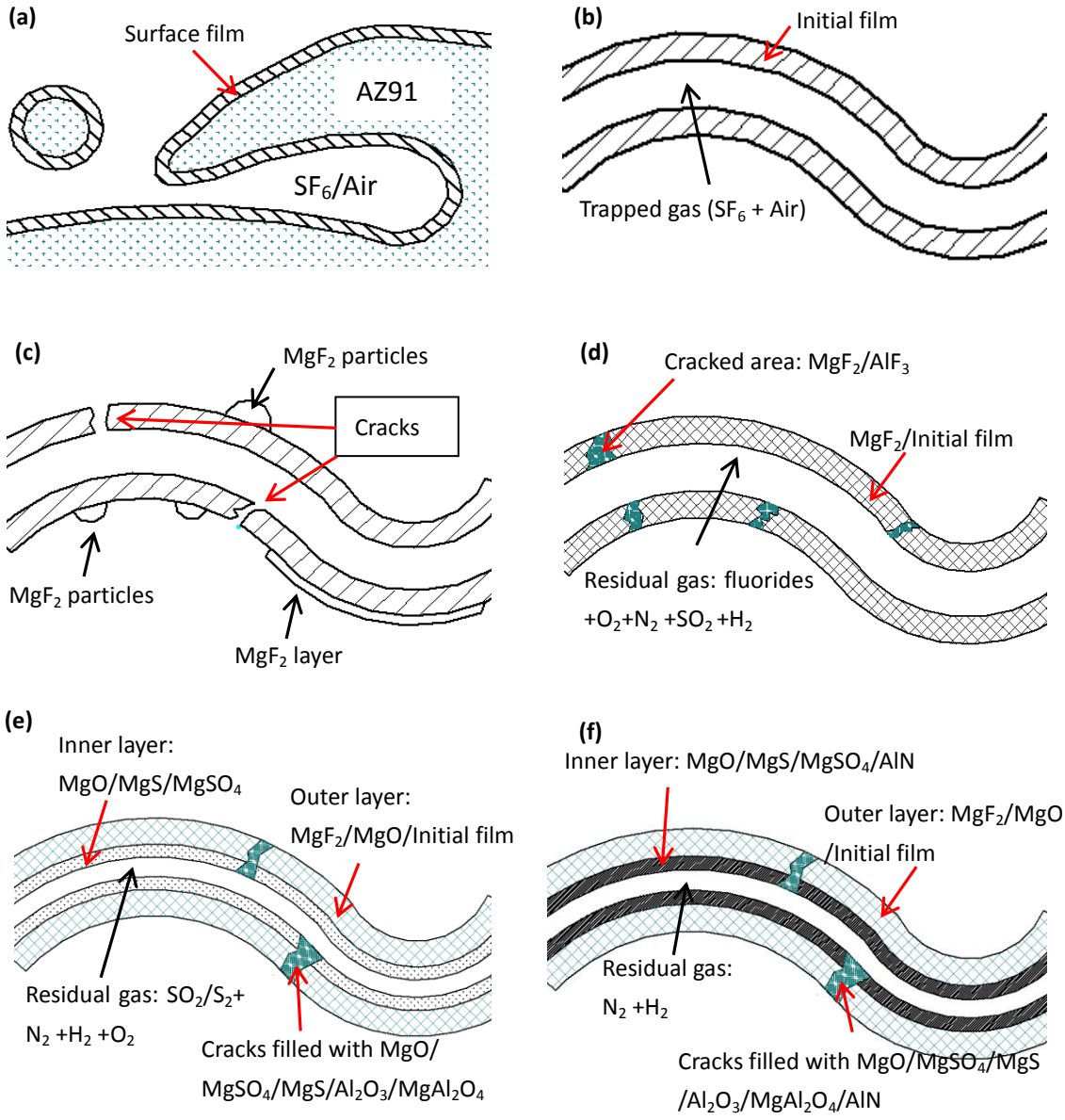

Fig 5-3. Formation and evolution process of a double oxide film defect formed an AZ91 casting in a atmosphere of SF_6/air (a) entrainment of a surface film formation; (b) the original double oxide film defect; (c) cracks caused by melt flow; (d ~ f) final entrainment defects.

5.1.4 AZ91+SF_6/CO_2

The evolution process of a double oxide film defect in AZ91 melt protected by SF_6/CO_2 is illustrated in Fig 5-4.

In stages 1 to 2, Fig 5-4 (a -b), a folded melt surface film forms a double oxide film defect. If the melt surface film is a young oxide film (solidified in less than 2 min), the initial film of this defect should consist of $MgF_2/AlF_3/MgO/Al_2O_3/MgAl_2O_4$; if the melt surface film is an old oxide film (held for more than 5 mins), the initial surface film may consist of MgF_2/MgO/C, as with the absence of aluminium in the films shown in Fig 4-55 to Fig 4-60. According to the surface film held for 30 min, shown in Fig 4-55, sulphur may not exist in the surface film.

In stage 3, Fig 5-4 (c), the MgF_2 layers and particles attached to the oxide film are formed, while the melt flow cracks the initial surface film. Hydrogen simultaneously diffuses from the melt into the entrained gas.

In stage 4, three types of final double oxide defects are shown Fig 5-2 (d) ~ (f).

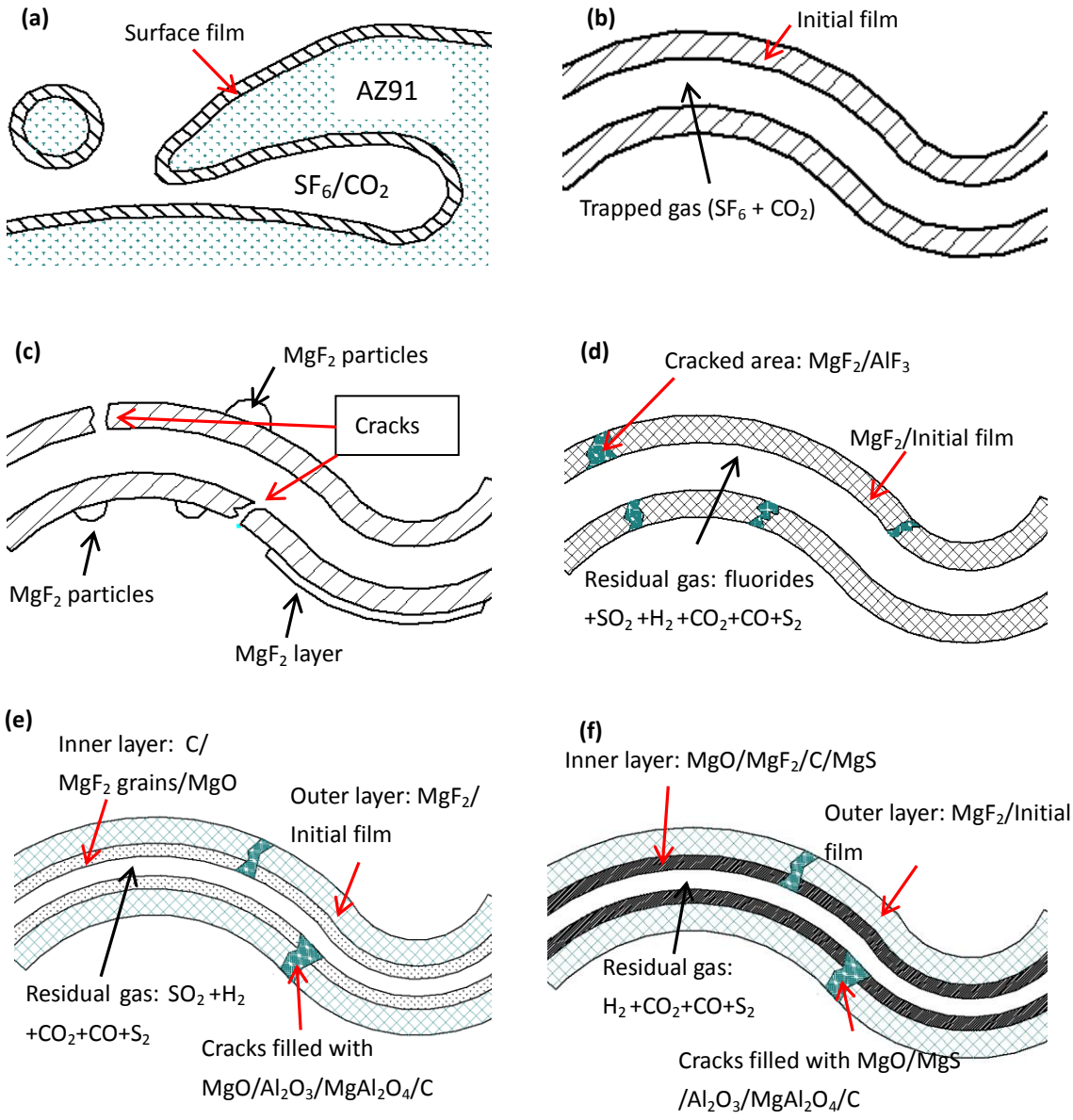

Fig 5-4.Formation and evolution process of a double oxide film defect formed in an AZ91 casting in a atmosphere of SF_6/CO_2 (a) entrainment of a surface film formation; (b) the original double oxide film defect; (c) cracks; (d ~ f) final entrainment defects.

Firstly, if fluorides in the trapped gas are not depleted by the AZ91 melt that comes into contact with the entrained gas, corresponding to stage 1 shown in Fig 4-81, (i.e.

the early stage suggested in section 4.3.9), the cracked and un-cracked areas of the final surface of would contain different components as shown in Fig 5-4 (d): the cracked area would be filled with MgF_2/AlF_3, but the un-cracked area would be a mixture of MgF_2 and the compounds of the initial film. If the initial film was an old oxide film composed of MgF_2/MgO/C, aluminium can only exist in a section of the oxide film (i.e. the cracked area), which is consistent with the film shown in Fig 4-32. If the initial film was a young film composed of MgF_2/AlF_3, aluminium can be found in all areas of the film. The residual entrained gas then contains hydrogen, CO_2, CO, SO_2, S_2(g), SF_6 and the decomposition products of SF_6.

Secondly, in Fig 5-4 (e), if the fluorides are depleted, corresponding to the stage 2 shown in Fig 4-81 (i.e. the medium stage suggested in section 4.3.9), the cracked area could be composed of a single layer of $MgO/MgAl_2O_4/Al_2O_3$/C. However, according to Fig 4-55 to Fig 4-57, the un-cracked area may have an inner layer composed of MgF_2 grains/MgO/C/. The residual entrained gas may therefore contain sulphur dioxide, sulphur, hydrogen, O_2, CO_2 and CO.

Finally, if the reaction process occurs in the stage 3 shown in Fig 4-81 (i.e. the final stage suggested in section 4.3.9), the inner layer contains further MgS as shown in Fig 5-4 (f), while the cracks may be filled with $MgO/MgS/Al_2O_3/MgAl_2O_4$/C. The residual gas may contain H_2 +CO_2+CO+S_2 until all the trapped gas is consumed.

5.1.5 Mg-Y alloy+SF_6/air

As discussed in section 4.4.5, a Y-free layer in the Mg-Y melt can cause the formation of a MgF_2-enriched inner layer in the protective surface film, as shown in Fig 4-61 to Fig 4-64. However, it should be noted that this Y-free layer can only exist in a still melt, and melt flow can continually introduce yttrium into the area surrounding an immersed double oxide films. Thus the MgF_2-enriched layer may not exist in a double oxide film defect formed in a Mg-Y melt, as shown in Fig 4-34 and Fig 4-36. Therefore, the evolution process of the defect formed in a Mg-Y alloy protected by SF_6/air can be described in the following stages.

In stage 1 ~ 2, Fig 5-5 (a -b), double oxide film defect may initially consists of MgF_2/YF_3/ MgO/Y_2O_3. In addition, Fig 4-61 to Fig 4-66 showed that sulphur appeared in the melt surface film after a holding time of 20 min, longer than the melting process (15 min) in the casting experiment. Thus the initial film of an original double oxide film defect may not contain sulphur.

In stage 3, Fig 5-5 (c), cracks that are caused by melt flow, accelerate the reactions of the entrained gas, and H can diffuse into the double oxide film defect. However, according to Fig 4-34 and Fig 4-36, the MgF_2/YF_3 particles or layers attached to the initial film may not form, since the main oxides in the film is Y_2O_3 (see Table 4-6 and Table 4-7), which has a P-B ratio of 1.13 > 1, making the film more protective than a MgO film (P-B ratio of MgO is 0.81).

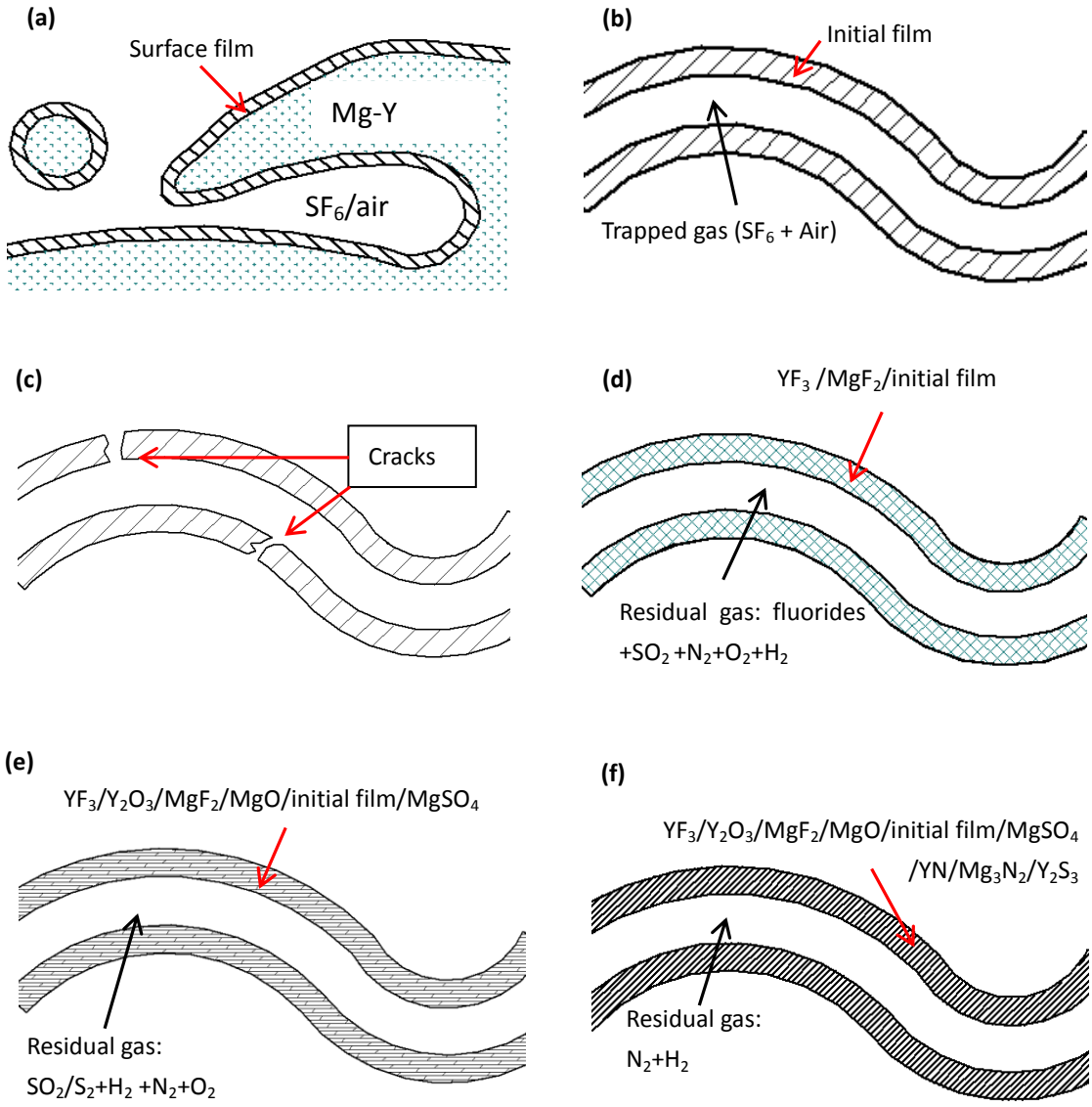

Fig 5-5. Formation and evolution process of a double oxide film defect formed a Mg-Y casting in a atmosphere of SF_6/air (a) entrainment of a surface film formation; (b) the original double oxide film defect; (c) cracks caused by melt flow; (d ~ f) final entrainment defects.

Thus finally, there are three types of final double oxide film defects as shown in Fig 5-5 (d) to (f).

Firstly, if fluorides in the trapped gas are not depleted, corresponding to stage 1 shown in Fig 4-82 (i.e. the early stage suggested in section 4.3.9), the surface film contains YF_3/MgF_2 and the compounds of the initial surface film, as shown in Fig 5-5 (d), which is consistent with the films shown in Fig 4-34. The residual entrained gas may then contain hydrogen, O_2, N_2, SO_2, SF_6 and decomposition products of SF_6.

Secondly, Fig 5-5 (e), if the fluorides are depleted, corresponding to stage 2 shown in Fig 4-82 (i.e. the medium stage suggested in section 4.3.9), the final surface film may contain MgS/$MgSO_4$, as with the film shown in Fig 4-17. According to Fig 4-61 ~ Fig 4-63, a separate layer enriched with sulphur may not exist, and the whole film can be a compact single layer.

Finally, if the reaction process occurs in the stage 3 shown in Fig 4-82 (i.e. the final stage suggested in section 4.3.9), the inner layer may contain Mg_3N_2, YN and Y_2S_3, as shown in Fig 5-5(e). The residual gas will be N_2+H_2 until all the trapped gas is consumed.

5.1.6 Mg-Y alloy+SF_6/CO_2

The evolution process of a double oxide film defect formed in Mg-Y castings

protected by SF_6/CO_2 can be described as in the following stages and illustrated in Fig 5-6.

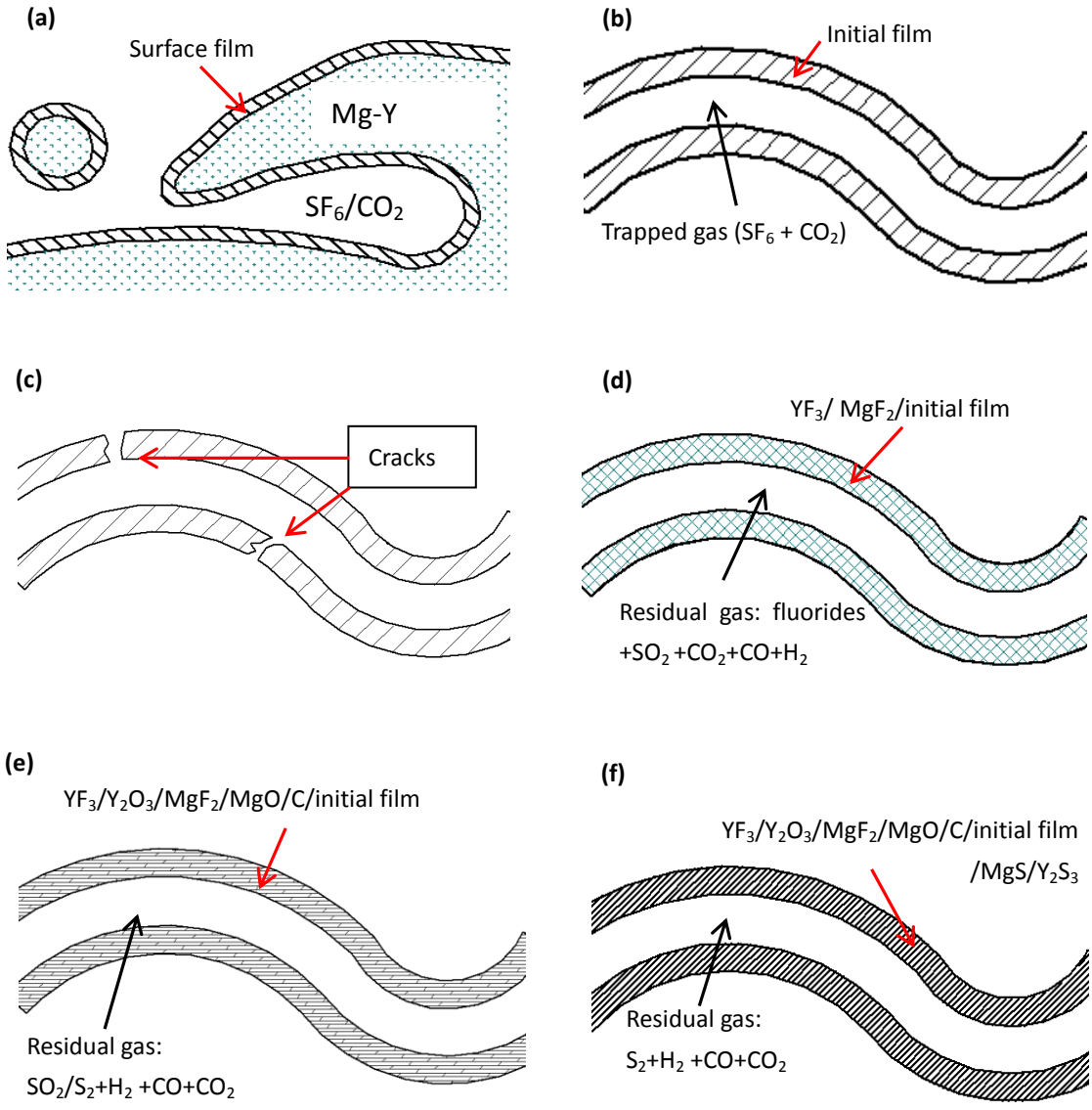

Fig 5-6. Formation and evolution process of a double oxide film defect formed a Mg-Y casting in a atmosphere of SF_6/CO_2 (a) entrainment of a surface film formation; (b) the original double oxide film defect; (c) cracks caused by melt flow; (d ~ f) final entrainment defects.

In stages 1 to 2, Fig 5-6 (a -b), a folded oxide film forms a double oxide film defect. The initial film may consist of $MgF_2/YF_3/MgO/Y_2O_3$, as with the film shown in Fig 4-67. The original trapped gas then contains SF_6 and CO_2.

In stage 3, Fig 5-6 (c), the entrained gas may react with liquid Mg-Y alloy, while hydrogen diffuses into the entrained gas.

In stage 4, three types of final double oxide defects can be formed as shown Fig 5-6 (d) to (f).

Firstly, if fluorides in the trapped gas are not depleted, corresponding to stage 1 shown in Fig 4-84 (i.e. the early stage suggested in section 4.3.9), the surface film may contain MgF_2/YF_3 and the compounds of the initial surface film, as shown in Fig 5-6 (d), which is consistent with the results shown in Fig 4-36. The residual entrained gas may contain SF_6, hydrogen, CO_2, CO, SO_2 and the decomposition products of SF_6.

Secondly, if the fluorides are depleted, corresponding to the stage 2 shown in Fig 4-84 (i.e. the medium stage suggested in section 4.3.9), the final surface film can may contain $MgO/Y_2O_3/C$ as shown in Fig 5-6 (e), which is consistent with the surface films shown in Fig 4-67 ~ Fig 4-72. The residual entrained gas may therefore contain sulphur dioxide/sulphur, CO_2, CO and hydrogen.

Finally, Fig 5-6 (f),if the reaction process in the stage 3 shown in Fig 4-84 (i.e. the final stage suggested in section 4.3.9) occurs, the surface film can contain MgS/Y_2S_3. The components of the entrained gas can then be $S_2+H_2+CO+CO_2$.

5.2 Deactivation of the double oxide film defect and the reproducibility of Mg casting properties.

The double oxide film defects on the fracture surfaces (see section 4.1,Fig 4-1 ~ Fig 4-21) suggested that double oxide film defects can exist containing a trapped gas within them, acting as a crack initiator, as do double oxide film defects in Al castings [22]. The corresponding evolution process and the thermodynamic calculation (see section 4.4, Fig 4-77 ~ Fig 4-84) further indicated that the entrained gas can be mostly consumed by the reaction with the molten Mg-alloys. Thus double oxide films in a liquid Mg-alloy may be more easily grow together, compared with that in an aluminium alloy melt, since a molten Al alloy can not efficiently consume nitrogen (78% volume of the initial trapped gas) in the entrained gas [80, 81].

The sandwich-like double oxide film defect (see Fig 4-108, section 4.8) showed that the oxide interfaces of double oxide film defects can grow together. The doubled films may be accordingly bonded with each other. As conjectured by Campbell [22], a bonded double oxide films is likely to confer an improvement in strength in contrast to a un-bonded double oxide films, thus increasing the quality of Mg alloy castings.

A comparison of the film growth rates (section 4.3.7, Fig 4-73 ~ Fig 4-74) revealed that the oxide films grew faster in 0.5%SF_6/air than in 0.5%SF_6/CO_2. In addition, all the oxide films formed in 0.5SF_6/CO_2 (Fig 4-7, Fig 4-15 ,Fig 4-21) had a more compact and smoother surface appearance, in contrast to the films formed in 0.5SF_6/air (Fig 4-4, Fig 4-11, Fig 4-18), indicating that the films formed in SF_6/air may have a more porous structure compared with the films produced in SF_6/CO_2. Thus a trapped gas of 0.5%SF_6/air in a Mg-alloy melt can be consumed faster than that of 0.5%SF_6/CO_2. In conjunction with films bonding phenomenon occurring in double oxide film defects (see Fig 4-108), it can be suggested that the use of 0.5%SF_6/air in the casting process allows more double oxide films to grow together, compared with 0.5%SF_6/CO_2. It can be therefore conjectured that the Mg-alloy castings produced in 0.5%SF_6/air may have a better reproducibility than those produced in 0.5%SF_6/CO_2.

However, this conjecture is not necessarily correct according to the Weibull modulus results shown in section 4.6 (Fig 4-97 ~ Fig 4-102). The AZ91 casting produced in 0.5%SF_6/air had a significantly higher Weibull moduli than that produced in 0.5%SF_6/CO_2 (see section 4.6.2), but the Weibull modulus of the Mg and Mg-Y alloy castings did not present any clear difference when using different carrier gases (see section 4.6.1, section 4.6.3).

This inconsistency between the conjecture and the actual Weibull moduli results may

be due to the compounds of the jointed area between the double oxide films. According to the evolution process suggested in section 5.1, SF_6 contained in the trapped gas with volume fraction of only 0.5%, would be preferentially depleted by the surrounding melt. Thus the jointed area between the double oxide films may mainly contain oxides and nitrides, which is supported by Fig 4-109. Thus the reason of the inconsistency between the conjecture and the actual Weibull modulus may be that not all of the oxides and nitrides are able to strongly bond with each other to confer an increase of strength, which will be further discussed in the following sections.

5.2.1 AZ91 alloy

For jointed double oxide films formed in an AZ91 alloy, according to section 5.1.3, the jointed area can occur mainly between $MgAl_2O_4$, AlN and MgO. Among them, the formation of $MgAl_2O_4$ was suggested as the main reaction causing a double oxide film defect formed in an A356-alloy melt to bond together in a holding time of less than 5 hours, and this bonding was demonstrated to be able to confer an increase of strength [39]. Therefore, the formation of $MgAl_2O_4$ may also confer an increase of strength to the jointed area of a double oxide film defect formed in AZ91 alloy. This may be the reason why the AZ91 castings gave a high Weibull modulus when the process was protected by SF_6/air (which allowed more double oxide films to bond together) compared with SF_6/CO_2.

Due to this improvement of the casting quality of AZ91 alloy, it can be suggested the European Mg industry, which did not use air as a carrier gas according to an EU commission survey [52] (as mentioned in section 2.7), to consider the application of air in the Mg-alloy casting process.

5.2.2 Commercial purity Mg alloy

However, for a double oxide film defect formed in commercial purity Mg castings, its jointed layers composed of MgO/Mg_3N_2 may not be strongly bonded with each other, due to the porous structure of the MgO/Mg_3N_2 layer (0.81 P-B ratio of MgO, and 0.89 P-B ratio for Mg_3N_2). As shown in Fig 4-4, the film surface of the double oxide films formed in a commercial purity Mg casting consisted of particles. When the double oxide films grew together, the jointed layers consisting of those particles may result in a porous structure, which accordingly may not be able to confer an increase of strength. Therefore, the negative effect of a double oxide film defect could not be deactivated by the bonding action in commercial purity Mg alloy. This can explain why the commercial purity Mg castings produced in different cover gases did not had a clear difference in Weibull modulus.

5.2.3 Mg-Y alloy

For Mg-Y alloy, the bonding layer of a double oxide films may mainly contain Y_2O_3, MgO, Mg_3N_2, YN. Although Y_2O_3 has a P-B ratio of 1.13 > 1, the film surface of a double oxide films, as shown in Fig 4-18, was also not compact compared with the

film surface of an AZ91 alloy as shown in Fig 4-11. Thus a Y_2O_3 jointed layer may not have a compact structure. In addition, Du et al. [143] reported that an yttrium chunk after nitridizing turned black and was easily fractured, indicating YN can not confer a good mechanical property to the bonded double oxide films. It can be therefore suggested that the bonded double oxide film defects formed in a Mg-Y alloy is also too weak to deactivate the defect, so that the quality of the Mg-Y castings protected by different carrier gases did not present a clear difference based on their Weibull modulus.

6. Conclusions

1. Double oxide film defects were found acting as a crack initiator on fracture surfaces of Mg-alloy castings. The film surface of the double oxide film defects formed in the three different alloys (i.e. commercial purity Mg, AZ91, Mg-Y) each cast with two cover gases (i.e. 0.5%SF_6/air, 0.5%SF_6/CO_2) were observed (see section 4.1).

2. The cross-sections of the double oxide film defects formed in the three different alloys (i.e. commercial purity Mg, AZ91, Mg-Y) each cast with two cover gases (i.e. 0.5%SF_6/air, 0.5%SF_6/CO_2) were observed (see section 4.2), indicating a double-layer structure of the oxide films. The cross-sectional observation also confirmed the Al and Y in the oxide films.

3. According to the experiment of the oxidation cell, the growth process of surfaces films formed on Mg-alloy melt has been concluded (see section 4.3). The growth process was consistent with the corresponding theoretical thermodynamic calculation (see section 4.4).

4. The evolution processes of the defects, occurring in the casting process, were suggested. According the evolution process, SF_6 in the entrained gas could be preferentially consumed compared to the carrier gas (i.e. air or CO_2), and the oxide films contained different combinations of compounds, depended on which stage the defect was in.

5, it was demonstrated that the difference between estimated and true cumulative probabilities of data points can be dramatically enlarged in the lower and upper trails of the linearized Weibull distribution, due to the linearized transformation occurring in the traditional Weibull moduli estimation using the LLS method. This is an underlying reason for the deviation from the linear regression line, which was previously widely reported in the Weibull modulus estimation of brittle and metal materials. It is therefore not appropriate to reject the Weibull behaviour of a dataset, according to the goodness-of-fit of the linear regression line, such as the popular method using R^2.

6. A new method (Non-LS method), which is demonstrated to be less biased compared with both the LLS and ML methods, is recommended for the Weibull moduli estimation.

7, a comparison of the film growth rates (section 4.3.7, Fig 4-73 ~ Fig 4-74) revealed that the oxide films grew faster in 0.5%SF_6/air than in 0.5%SF_6/CO_2. In addition, the double oxide films formed in 0.5%SF_6/air had a more porous surface appearance in contrast to that formed in 0.5%SF_6/CO_2. Thus it can be concluded that double oxide films formed in SF_6/air were easier to grow together compared with that formed in SF_6/CO_2, which may allow relatively more double oxide films formed in 0.5SF_6/air to

bond together, and may increase the quality of the corresponding Mg alloy castings.

8. In the actual casting results (see section 4.6), the AZ91 casting produced in 0.5%SF_6/air had a significantly higher Weibull moduli than that produced in 0.5%SF_6/CO_2, but the Weibull modulus of the Mg and Mg-Y alloy castings did not present a clear difference when using different carrier gases. This phenomenon may be due to the different combinations of compounds contained in the jointed area: some compounds can make the double oxide films strongly bond together (such the spinel formed in AZ91 alloy), while the others (such as MgO and YN formed in pure Mg and Mg-Y alloy) can not confer an increase in strength of the jointed area.

9, it was demonstrated that the use of air can improve the casting quality of AZ91 alloy, which is the one of most widely used Mg-alloy.

7. Future Work

1. The Monte Carlo simulation demonstrated the merit of non-linear least square method in Weibull moduli estimation, compared with the traditional linear least square method. However, the underlying distribution of the ratio between the estimated and true Weibull modulus (M) is still unknown. Accordingly, the confidence interval could not been proposed to test whether the Weibull moduli of one casting is significantly different to another. The study carried out in this thesis simply assumed M values following a normal distribution, but there is no evidence to support this assumption. Currently, the underlying distribution of M values has not been verified on a rigorous mathematical basis, and is a point for further study in order to improve the statistical analysis in Weibull moduli estimation.

2. Three cover gases (SO_2, HFC-134a, SF_6) are widely used in the magnesium casting industry to protect a Mg-alloy melt. However, only one of the cover gases (i.e. SF_6) was studied in the work reported here. Further investigation is required of the double oxide film defects formed in the protective gases SO_2 and HFC-134a.

3. In this work, the AZ91 casting formed with a cover gas of SF_6/air was suggested to have a better quality than that formed in SF_6/CO_2. However, this quality difference due to the use of protective gas was not found with commercial purity Mg and Mg-Y

castings. This phenomenon was probably caused by the different compounds of the jointed area of the double oxide film defects. To verify this hypothesis, further experiments are required to investigate how strongly double oxide film layers can be bonded together.

4. Although H porosity is widely found in Mg-alloy castings, the processes by which hydrogen diffuses into double oxide films has not been directly observed in Mg-alloy melts. It would be desirable to observe this process directly using a Synchrotron X-rays.

8. Reference

1. Kimball, S.M., (Acting Director) and S. Jewell, (Secretary), *Mineral Commodity Summaries 2015*, in *Magnesium, Compounds & Metal*. 2015, U.S. Geological Survey and U.S. Department of the Interior: Reston, Virginia.
2. Kimball, S.M., (Acting Director) and S. Jewell, (Secretary), *Mineral Commodity Summaries 2014*, in *Magnesium, Compounds & Metal*. 2014, U.S. Geological Survey and U.S. Department of the Interior: Reston, Virginia.
3. McNutt, M.K., (Director) and K. SALAZAR, (Secretary), *Mineral Commodity Summaries 2013*, in *Magnesium, Compounds & Metal*. 2013, U.S. Geological Survey and U.S. Department of the Interior: Reston, Virginia.
4. McNutt, M.K., (Director) and K. SALAZAR, (Secretary), *Mineral Commodity Summaries 2012*, in *Magnesium, Compounds & Metal*. 2012, U.S. Geological Survey and U.S. Department of the Interior: Reston, Virginia.
5. McNutt, M.K., (Director) and K. SALAZAR, (Secretary), *Mineral Commodity Summaries 2011*, in *Magnesium, Compounds & Metal*. 2011, U.S. Geological Survey and U.S. Department of the Interior: Reston, Virginia.
6. McNutt, M.K., (Director) and K. SALAZAR, (Secretary), *Mineral Commodity Summaries 2010*, in *Magnesium, Compounds & Metal*. 2010, U.S. Geological Survey and U.S. Department of the Interior: Reston, Virginia.
7. Kimball. S.M., A.D. and K. SALAZAR, (Secretary), *Mineral Commodity Summaries 2009*, in *Magnesium, Compounds & Metal*. 2009, U.S. Geological Survey and U.S. Department of the Interior: Reston, Virginia.
8. Myers, M.D., (Director) and D. KEMPTHORNE, (Secretary), *Mineral Commodity Summaries 2008*, in *Magnesium, Compounds & Metal*. 2008, U.S. Geological Survey and U.S. Department of the Interior: Reston, Virginia.
9. Myers, M.D., (Director) and D. KEMPTHORNE, (Secretary), *Mineral Commodity Summaries 2007*, in *Magnesium, Compounds & Metal*. 2007, U.S. Geological Survey and U.S. Department of the Interior: Reston, Virginia.
10. LEAHY, P.P., (Acting Director) and G.A. Norton, (Secretary), *Mineral Commodity Summaries 2006*, in *Magnesium, Compounds & Metal*. 2006, U.S. Geological Survey and U.S. Department of the Interior: Reston, Virginia.
11. GROAT, C.G., (Director) and G.A. NORTON, (Secretary), *Mineral Commodity Summaries 2005*, in *Magnesium, Compounds & Metal*. 2005, U.S. Geological Survey and U.S. Department of the Interior: Reston, Virginia.
12. GROAT, C.G., (Director) and G.A. NORTON, (Secretary), *Mineral Commodity Summaries 2004*, in *Magnesium, Compounds & Metal*. 2004, U.S. Geological Survey and U.S. Department of the Interior: Reston, Virginia.
13. GROAT, C.G., (Director) and G.A. NORTON, (Secretary), *Mineral Commodity Summaries 2003*, in *Magnesium, Compounds & Metal*. 2003, U.S. Geological Survey and U.S. Department of the Interior: Reston, Virginia.
14. GROAT, C.G., (Director) and G.A. NORTON, (Secretary), *Mineral Commodity Summaries 2002*, in *Magnesium, Compounds & Metal*. 2002, U.S. Geological Survey and U.S. Department of the Interior: Reston, Virginia.

15. GROAT, C.G., (Director) and B. BABBITT, (Secretary), *Mineral Commodity Summaries 2001*, in *Magnesium, Compounds & Metal*. 2001, U.S. Geological Survey and U.S. Department of the Interior: Reston, Virginia.
16. *Mineral Commodity Summaries 2000*, in *Magnesium, Compounds & Metal*. 2000, U.S. Geological Survey and U.S. Department of the Interior: Pittsburgh.
17. *Mineral Commodity Summaries 1999*, in *Magnesium, Compounds & Metal*. 1999, U.S. Geological Survey and U.S. Department of the Interior: Pittsburgh.
18. *Mineral Commodity Summaries 1998*, in *Magnesium, Compounds & Metal*. 1998, U.S. Geological Survey and U.S. Department of the Interior.
19. *Mineral Commodity Summaries 1997*, in *Magnesium, Compounds & Metal*. 1997, U.S. Geological Survey and U.S. Department of the Interior.
20. *Mineral Commodity Summaries 1996*, in *Magnesium, Compounds & Metal*. 1996, U.S. Geological Survey and U.S. Department of the Interior.
21. Ostrovsky, I. and Y. Henn, *PRESENT STATE AND FUTURE OF MAGNESIUM APPLICATION IN AEROSPACE INDUSTRY*, in *ASTEC'07 International Conference-NEW CHALLENGES IN AERONAUTICS*. Aug 19-22,2007: Moscow. p. 1-5.
22. Campbell, J., *Castings*. 2004, Oxford: Butterworth-Heinemann.
23. Griffiths, W.D. and N.W. Lai, *Double oxide film defects in cast magnesium alloy.* Metallurgical and Materials Transactions a-Physical Metallurgy and Materials Science, 2007. **38A**(1): p. 190-196.
24. Mirak, A.R., et al., *Oxide film characteristics of AZ91 magnesium alloy in casting conditions.* International Journal of Cast Metals Research, 2007. **20**(4): p. 215-220.
25. Fox, S. and J. Campbell, *Visualisation of oxide film defects during solidification of aluminium alloys.* Scripta Materialia, 2000. **43**(10): p. 881-886.
26. Cox, M., R.A. Harding, and J. Campbell, *Optimised running system design for bottom filled aluminium alloy 2L99 investment castings.* Materials Science and Technology, 2003. **19**(5): p. 613-625.
27. Cao, X. and J. Campbell, *Precipitation of primary intermetallic compounds in liquid Al 11.5Si 0.4Mg alloy.* International Journal of Cast Metals Research, 2000. **13**(3): p. 175-184.
28. Wang, Q.G., D. Apelian, and D.A. Lados, *Fatigue behavior of A356-T6 aluminum cast alloys. Part I. Effect of casting defect.* Journal of Light Metals, 2001. **1**(1): p. 73-84.
29. Pitcher, P.D. and P.J.E. Forsyth, *The Influence of Microstructure on the Fagtigure Properties of an Al Casting Alloy*, in *Royal Aircraft Establishment Technical Report 82107*. 1982, Royal Aircraft Establishment.
30. Nyahumwa, C., N.R. Green, and J. Campbell, *Influence of casting technique and hot isostatic pressing on the fatigue of an Al-7Si-Mg alloy.* Metallurgical and Materials Transactions a-Physical Metallurgy and Materials Science, 2001. **32**(2): p. 349-358.
31. Ardekhani, A. and R. Raiszadeh, *Removal of Double Oxide Film Defects by Ceramic Foam Filters.* Journal of Materials Engineering and Performance, 2012. **21**(7): p. 1352-1362.
32. Edelson, B.J. and W.M. Baldwin, *The effect of second phases on the mechanical properties of alloys.* Transactions of the American Society of Metals, 1962. **55**: p. 230-250.
33. Dai, X., et al., *Influence of oxide film defects generated in filling on mechanical strength of aluminium alloy castings.* Materials Science and Technology, 2004. **20**(4): p. 505-513.
34. Eisaabadi, B.G., et al., *Effect of oxide films, inclusions and Fe on reproducibility of tensile*

properties in cast Al-Si-Mg alloys: Statistical and image analysis. Materials Science and Engineering a-Structural Materials Properties Microstructure and Processing, 2012. **558**: p. 134-143.

35. Miller, D.N., L. Lu, and A.K. Dahle, *The role of oxides in the formation of primary iron intermetallics in an Al-11.6Si-0.37Mg alloy.* Metallurgical and Materials Transactions B-Process Metallurgy and Materials Processing Science, 2006. **37**(6): p. 873-878.
36. Zahedi, H., et al., *The effect of Fe-rich intermetallics on the Weibull distribution of tensile properties in a cast Al-5 pct Si-3 pct Cu-1 pct Fe-0.3 pct Mg alloy.* Metallurgical and Materials Transactions a-Physical Metallurgy and Materials Science, 2007. **38A**(3): p. 659-670.
37. Raiszadeh, R. and W.D. Griffiths, *A method to study the history of a double oxide film defect in liquid aluminum alloys.* Metallurgical and Materials Transactions B-Process Metallurgy and Materials Processing Science, 2006. **37**(6): p. 865-871.
38. Impey, S., D.J. Stephenson, and J.R. Nicholls, *A STUDY OF THE EFFECT OF MAGNESIUM ADDITIONS ON THE OXIDE-GROWTH MORPHOLOGIES ON LIQUID ALUMINUM-ALLOYS*. Microscopy of Oxidation, ed. M.J. Bennett and G.W. Lorimer. 1992, London: Inst Metals. 238-244.
39. Aryafar, M., R. Raiszadeh, and A. Shalbafzadeh, *Healing of double oxide film defects in A356 aluminium melt.* Journal of Materials Science, 2010. **45**(11): p. 3041-3051.
40. Raiszadeh, R. and W.D. Griffiths, *The Effect of Holding Liquid Aluminum Alloys on Oxide Film Content.* Metallurgical and Materials Transactions B-Process Metallurgy and Materials Processing Science, 2011. **42**(1): p. 133-143.
41. Scholz, H. and P. Greil, *NITRIDATION REACTIONS OF MOLTEN AL-(MG, SI) ALLOYS.* Journal of Materials Science, 1991. **26**(3): p. 669-677.
42. Yue, Y., et al., *IN SITU CHARACTERISATION OF ENTRAINMENT DEFECTS IN LIQUID Al-Si-Mg ALLOY.* Proceedings of the 1st International Conference on 3d Materials Science, 2012: p. 131-136.
43. Lin, R.Y. and M. Hoch, *THE SOLUBILITY OF HYDROGEN IN MOLTEN ALUMINUM-ALLOYS.* Metallurgical Transactions a-Physical Metallurgy and Materials Science, 1989. **20**(9): p. 1785-1791.
44. Liu, H., M. Bouchard, and L. Zhang, *AN EXPERIMENTAL-STUDY OF HYDROGEN SOLUBILITY IN LIQUID ALUMINUM.* Journal of Materials Science, 1995. **30**(17): p. 4309-4315.
45. Harvey, J.P. and P. Chartrand, *Modeling the Hydrogen Solubility in Liquid Aluminum Alloys.* Metallurgical and Materials Transactions B-Process Metallurgy and Materials Processing Science, 2010. **41**(4): p. 908-924.
46. Xu, S., et al., *Variation of hydrogen level in magnesium alloy melt.* China Foundry, 2006. **3**(4): p. 275-278.
47. Zhou, C.S., et al., *Thermodynamic Destabilization of Magnesium Hydride Using Mg-Based Solid Solution Alloys.* Journal of Physical Chemistry C, 2014. **118**(22): p. 11526-11535.
48. Ouyang, L.Z., et al., *Comparative investigation on the hydrogenation/dehydrogenation characteristics and hydrogen storage properties of Mg3Ag and Mg3Y.* International Journal of Hydrogen Energy, 2014. **39**(25): p. 13616-13621.
49. Liu, H.Z., et al., *Hydrogen Desorption Properties of the MgH2-AlH3 Composites.* Journal of Physical Chemistry C, 2014. **118**(1): p. 37-45.
50. Aarstad, K., *Protective Films on Molten Magnesium*. 2004, Norwegian University of Science

and Technology.

51. Cramer, S.D. and B.S. Covino, *ASM handbook. Vol.13A, Corrosion: fundamentals, testing, and protection / prepared under the direction of the ASM International Handbook Committee*. 2003, Materials Park, Ohio: ASM.
52. Schwarz, W., B. Gschrey, and O. Recherche, *Service contract to assess the feasibility of options to reduce emissions of SF6 from the EU non-ferrous metal industry and analyse their potential impacts*. 2009, Prepared for European Commission, DG Environment: Frankfurt.
53. Polmear, I.J., *Light alloys: metallurgy of the light metals*. 4 ed. 2006, Oxford: Butterworth-Heinemann.
54. Fruehling, J.W., *Protective Atmospheres for Molten Magnesium*. 1970, University of Michigan.
55. Cashion, S.P., N.J. Ricketts, and P.C. Hayes, *Characterisation of protective surface films formed on molten magnesium protected by air/SF6 atmospheres.* Journal of Light Metals, 2002. **2**(1): p. 37-42.
56. Cashion, S.P., N.J. Ricketts, and P.C. Hayes, *The mechanism of protection of molten magnesium by cover gas mixtures containing sulphur hexafluoride.* Journal of Light Metals, 2002. **2**(1): p. 43-47.
57. Pettersen, G., et al., *Characterisation of the surface films formed on molten magnesium in different protective atmospheres.* Materials Science and Engineering a-Structural Materials Properties Microstructure and Processing, 2002. **332**(1-2): p. 285-294.
58. Xiong, S.M. and X.L. Liu, *Microstructure, composition, and depth analysis of surface films formed on molten AZ91D alloy under protection of SF6 mixtures.* Metallurgical and Materials Transactions a-Physical Metallurgy and Materials Science, 2007. **38A**(2): p. 428-434.
59. Xiong, S.M. and X.F. Wang, *Protection behavior of fluorine-containing cover gases on molten magnesium alloys.* Transactions of Nonferrous Metals Society of China, 2010. **20**(7): p. 1228-1234.
60. Shih, T.S., J.B. Liu, and P.S. Wei, *Oxide films on magnesium and magnesium alloys.* Materials Chemistry and Physics, 2007. **104**(2-3): p. 497-504.
61. Wilkins, R.L., *THERMODYNAMICS OF SF6 AND ITS DECOMPOSITION AND OXIDATION PRODUCTS.* Journal of Chemical Physics, 1969. **51**(2): p. 853-&.
62. Tsang, W. and J.T. Herron, *KINETICS AND THERMODYNAMICS OF THE REACTION SF6-REVERSIBLE-SF5+F.* Journal of Chemical Physics, 1992. **96**(6): p. 4272-4282.
63. Hayashi, S., et al., *SF6 Pyrolysis Decomposition in N-2 or O-2 Bath Gas and the Influence of H2O Addition.* Kagaku Kogaku Ronbunshu, 2009. **35**(4): p. 411-415.
64. Bartos, S.C., *US EPA's SF6 emission reduction partnership for the magnesium industry: An update on early success.* Magnesium Technology 2001, 2001: p. 43-47.
65. Ricketts, N.J. and S.P. Cashion, *Hydrofluorocarbons as a replacement for sulphur hexafluoride in magnesium processing*. Magnesium Technology 2001, ed. J.N. Hryn. 2001, Warrendale: Minerals, Metals & Materials Soc. 31-36.
66. Ha, W. and Y.J. Kim, *Effects of cover gases on melt protection of Mg alloys.* Journal of Alloys and Compounds, 2006. **422**(1-2): p. 208-213.
67. Chen, H.K., J.R. Liu, and W.D. Huang, *Oxidation behavior of molten magnesium in air/HFC-134a atmospheres.* Journal of Materials Science, 2006. **41**(23): p. 8017-8024.
68. Liu, X.L. and S.M. Xiong, *Characterization of surface films formed on molten AZ91D magnesium alloy protected by HFC-134a mixtures.* Rare Metal Materials and Engineering,

2006. **35**(9): p. 1396-1399.

69. Cashion, S. and N. Ricketts, *The use of SO2 as a cover gas for molten magnesium.* Magnesium Technology 2000, 2000: p. 77-81.
70. Liang, W.Z., et al., *Protective behavior of an SO2/CO2 gas mixture for molten AZ91D alloy.* China Foundry, 2012. **9**(3): p. 226-230.
71. Wang, X.F. and S.M. Xiong, *CHARACTERIZATION OF THE SURFACE FILM FORMED ON MOLTEN AZ91D MAGNESIUM ALLOY PROTECTED BY SO2 MIXTURES.* Acta Metallurgica Sinica, 2010. **46**(12): p. 1529-1533.
72. Wang, X.F. and S.M. Xiong, *Oxidation behavior of molten magnesium in atmospheres containing SO2.* Corrosion Science, 2011. **53**(12): p. 4050-4057.
73. Wang, X.F. and S.M. Xiong, *Protection behavior of SO2-containing cover gases to molten magnesium alloy.* Transactions of Nonferrous Metals Society of China, 2011. **21**(4): p. 807-813.
74. Wang, X.F. and S.M. Xiong, *Characterization of surface films formed on molten magnesium in atmospheres containing SO2.* Materials Chemistry and Physics, 2012. **135**(2-3): p. 541-548.
75. Wang, X.F. and S.M. Xiong, *Characterization of the Surface Film Formed on Molten AZ91D Magnesium Alloy in Atmospheres Containing SO2.* Metallurgical and Materials Transactions a-Physical Metallurgy and Materials Science, 2012. **43A**(11): p. 4406-4413.
76. Wang, X.F. and S.M. Xiong, *Oxidation behavior of molten magnesium in atmospheres containing SO2 and air in a sealed furnace.* Corrosion Science, 2013. **66**: p. 300-307.
77. Hillis, J.E., *The International Program to Identify Alternatives to SF6 for Magnesium Melt Protection*, in *International Conference on SF6 and the Environment: Emission Reduction Strategies*. November 21-22, 2002, The International Magnesium Association: San Diego.
78. Bartos, S., *UPDATE ON EPA'S MAGNESIUM INDUSTRY PARTNERSHIP FOR CLIMATE PROTECTION*, in *131st TMS Annual Meeting*. February 17-21, 2002: Washington.
79. Biedenkopf, P., et al., *Protecting liquid Mg by solid CO2: New ways to avoid SF6 and SO2.* Magnesium Technology 2005, 2005: p. 39-42.
80. Kumari, S.S.S., U.T.S. Pillai, and B.C. Pai, *Synthesis and characterization of in situ Al-AlN composite by nitrogen gas bubbling method.* Journal of Alloys and Compounds, 2011. **509**(5): p. 2503-2509.
81. Swaminathan, S., B.S. Rao, and V. Jayaram, *The influence of oxygen impurities on the formation of AlN-Al composites by infiltration of molten Al-Mg.* Materials Science and Engineering a-Structural Materials Properties Microstructure and Processing, 2002. **337**(1-2): p. 134-139.
82. Couling, S.L., *USE OF GASEOUS AIR-CO2-SF6 MIXTURES TO IMPROVE THE PROTECTION OF LIQUID MAGNESIUM.* Fonderie, 1979. **34**(394): p. 369-374.
83. Hu, B., et al., *THERMODYNAMIC DESCRIPTION OF THE C-Ge AND C-Mg SYSTEMS.* Journal of Mining and Metallurgy Section B-Metallurgy, 2010. **46**(1): p. 97-103.
84. Gol'dshleger, U.I. and E.Y. Shafirovich, *Combustion regimes of magnesium in carbon oxides. 1. Combustion in CO2.* Combustion Explosion and Shock Waves, 1999. **35**(6): p. 637-644.
85. Lee, B.D., et al., *Protective Properties of SF6 under Various Carrier Gases for the Protection of Molten Mg.* Materials Transactions, 2013. **54**(1): p. 66-73.
86. Salas, O., et al., *NUCLEATION AND GROWTH OF AL2O3/METAL COMPOSITES BY OXIDATION OF ALUMINUM-ALLOYS.* Journal of Materials Research, 1991. **6**(9): p. 1964-1981.

87. Czerwinski, F., *The oxidation behaviour of an AZ91D magnesium alloy at high temperatures.* Acta Materialia, 2002. **50**(10): p. 2639-2654.
88. Barrena, M.I., et al., *Effect of heat treatments on oxidation kinetics in AZ91 and AM60 magnesium alloys.* Materials Characterization, 2011. **62**(10): p. 982-986.
89. Zeng, X.Q., et al., *Behavior of surface oxidation on molten Mg-9Al-0.5Zn-0.3Be alloy.* Materials Science and Engineering a-Structural Materials Properties Microstructure and Processing, 2001. **301**(2): p. 154-161.
90. Wang, X.M., et al., *Early oxidation behaviors of Mg-Y alloys at high temperatures.* Journal of Alloys and Compounds, 2008. **460**(1-2): p. 368-374.
91. Fan, J.F., et al., *Oxidation behavior of ignition-proof magnesium alloys with rare earth addition.* Journal of Alloys and Compounds, 2011. **509**(5): p. 2137-2142.
92. Fan, J.F., et al., *Surface oxidation behavior of Mg-Y-Ce alloys at high temperature.* Metallurgical and Materials Transactions a-Physical Metallurgy and Materials Science, 2005. **36A**(1): p. 235-239.
93. Guan, M., W. Hao, and J. Fan, *High Temperature Oxidation Behavior of Ignition-Proof Mg-Y-Ce Alloys.* Rare Metal Materials and Engineering, 2010. **39**(8): p. 1375-1379.
94. Zhou, N., et al., *Selective oxidation behavior of an ignition-proof Mg-Y-Ca-Ce alloy.* Journal of Rare Earths, 2013. **31**(10): p. 1003-1008.
95. Wan, D.Q., J.C. Wang, and G.C. Yang, *A study of the effect of Y on the mechanical properties, damping properties of high damping Mg-0.6%Zr based alloys.* Materials Science and Engineering a-Structural Materials Properties Microstructure and Processing, 2009. **517**(1-2): p. 114-117.
96. Green, N.R. and J. Campbell, *STATISTICAL DISTRIBUTIONS OF FRACTURE STRENGTHS OF CAST AL-7SI-MG ALLOY.* Materials Science and Engineering a-Structural Materials Properties Microstructure and Processing, 1993. **173**(1-2): p. 261-266.
97. Emamy, M., et al., *Statistical analysis of tensile properties of cast A357/Al2O3 MMCs.* Materials Science and Technology, 2010. **26**(2): p. 149-156.
98. Weibull, W., *A STATISTICAL DISTRIBUTION FUNCTION OF WIDE APPLICABILITY.* Journal of Applied Mechanics-Transactions of the Asme, 1951. **18**(3): p. 293-297.
99. Tiryakioglu, M. and D. Hudak, *On estimating Weibull modulus by the linear regression method.* Journal of Materials Science, 2007. **42**(24): p. 10173-10179.
100. Wu, D.F., J.C. Zhou, and Y.D. Li, *Methods for estimating Weibull parameters for brittle materials.* Journal of Materials Science, 2006. **41**(17): p. 5630-5638.
101. Wu, D.F., J.C. Zhou, and Y.D. Li, *Unbiased estimation of Weibull parameters with the linear regression method.* Journal of the European Ceramic Society, 2006. **26**(7): p. 1099-1105.
102. Khalili, A. and K. Kromp, *STATISTICAL PROPERTIES OF WEIBULL ESTIMATORS.* Journal of Materials Science, 1991. **26**(24): p. 6741-6752.
103. Zhang, L., et al., *Effect of high hydrostatic pressure on the viability of Streptococcus thermophilus bacteriophages isolated from cheese.* Innovative Food Science & Emerging Technologies, 2015. **29**: p. 113-118.
104. Fan, Z.T. and S. Ji, *Low pressure lost foam process for casting magnesium alloys.* Materials Science and Technology, 2005. **21**(6): p. 727-734.
105. Fisher, R.A., *On the mathematical foundations of theoretical statistics.* Philosophical Transactions of the Royal Society A, 1922. **222**: p. 309–368.

106. Edgeworth and F. Y., *On the probable errors of frequency-constants.* Journal of the Royal Statistical Society 1908. **71**(4): p. 651–678.
107. Butikofer, L., B. Stawarczyk, and M. Roos, *Two regression methods for estimation of a two-parameter Weibull distribution for reliability of dental materials.* Dental Materials, 2015. **31**(2): p. E33-E50.
108. Nakamura, N., K. Horie, and Y. Iijima, *Analysis of the strength data of wood structures on limit states design III. Reliability index and design point on bending strength of structural lumber.* Mokuzai Gakkaishi, 2000. **46**(1): p. 32-36.
109. Bantle, M., K. Kolsaker, and T.M. Eikevik, *Modification of the Weibull Distribution for Modeling Atmospheric Freeze-Drying of Food.* Drying Technology, 2011. **29**(10): p. 1161-1169.
110. Doremus, R.H., *FRACTURE STATISTICS - A COMPARISON OF THE NORMAL, WEIBULL, AND TYPE-I EXTREME VALUE DISTRIBUTIONS.* Journal of Applied Physics, 1983. **54**(1): p. 193-198.
111. Espinoza-Cuadra, J., G. Garcia-Garcia, and H. Mancha-Molinar, *Influence of defects on strength of industrial aluminum alloy Al-Si 319.* Materials & Design, 2007. **28**(3): p. 1038-1044.
112. Mbuya, T.O., et al., *Effect of runner design on mechanical properties of permanent mould aluminium castings.* International Journal of Cast Metals Research, 2006. **19**(6): p. 357-360.
113. Tiryakioglu, M., D. Hudak, and G. Oekten, *On evaluating Weibull fits to mechanical testing data.* Materials Science and Engineering a-Structural Materials Properties Microstructure and Processing, 2009. **527**(1-2): p. 397-399.
114. Kutner, M.H., et al., *Applied Linear Statistical Models*. 2005, Boston: McGraw-Hili.
115. Avsaroglu, M.D., et al., *Use of the Weibull model for lactococcal bacterlophage inactivation by high hydrostatic pressure.* International Journal of Food Microbiology, 2006. **108**(1): p. 78-83.
116. Buzrul, S., H. Alpas, and F. Bozoglu, *Use of Weibull frequency distribution model to describe the inactivation of Alicyclobacillus acidoterrestris by high pressure at different temperatures.* Food Research International, 2005. **38**(2): p. 151-157.
117. X., Y. and C. J., *Liquid Metal Flow in A Pouring Basin.* International Journal of Cast Metals Research, 1998. **10**: p. 239-253.
118. Wright T. C. and Campbell J., *Enhanced Solidification Rate in Castings by Use of Cooling Fins.* AFS Transactions, 1997. **105**: p. 639-644.
119. Takamori, S., et al., *Casting surface of AZ91 alloy and its reaction with sand mold.* Materials Transactions, 2008. **49**(5): p. 1089-1092.
120. Friedrich, H.E. and B.L. Mordike, eds. *Magnesium Technology: Metallurgy, Design Data, Applications*. 2006, Springer: Germany.
121. BSI, *BS EN 1753:1997 Magnesium and magnesium alloys-Magnesium alloy ingots and castings*. 1997, British Standards Institute: London.
122. BSI, *BS EN 12421: Magnesium and magnesium alloys-Unalloyed Magnesium*. 1998, British Standards Institute: London.
123. PETROVICH, V., W. MERCER, E., , and W. GREEN, G., *FLUXLESS MELTING AND REFINING OF MAGNESIUM AND/OR MAGNESIUM ALLOYS*, in *Patentscope,*

Espacenet, E.P. Office, Editor. 1993: U.S.

124. BSI, *BS EN ISO 6892-1 Metallic materials - Tensile testing, Part 1: Method of test at room temperature*. 2014, British Standards Institute: London.
125. Mahmoudi, M., *Double Oxide Film Defects and Mechanical Properties in Aluminium Alloys*, in

School of Metallurgy and Material. 2012, University of Birmingham: Birmingham.

126. Rolland, P., V. Carlino, and R. Vane, *Improved Carbon Analysis with Evactron Plasma Cleaning.* Microscopy and Microanalysis, 2004. **10**(Supplement S02): p. 964-965.
127. Czerwinski, F., *Oxidation Characteristics of Magnesium Alloys.* Jom, 2012. **64**(12): p. 1477-1483.
128. Yasui, S., et al., *High-temperature decomposition of SF6 gas and dry-fixation of the gaseous decomposition products.* Kagaku Kogaku Ronbunshu, 2004. **30**(2): p. 194-199.
129. Kubaschewski, O. and K. Hesselemam, *Thermo-chemical properties of Inorganic Substances*. 1991, Belin: Springer-Verlag.
130. Patnaik, P., *Handbook of Inorganic Chemicals*. 2002, New York: McGraw-Hill.
131. Tiryakioglu, M. and D. Hudak, *Guidelines for Two-Parameter Weibull Analysis for Flaw-Containing Materials.* Metallurgical and Materials Transactions B-Process Metallurgy and Materials Processing Science, 2011. **42**(6): p. 1130-1135.
132. Langlois, R., *ESTIMATION OF WEIBULL PARAMETERS.* Journal of Materials Science Letters, 1991. **10**(18): p. 1049-1051.
133. Keles, O., R.E. Garcia, and K.J. Bowman, *Deviations from Weibull statistics in brittle porous materials.* Acta Materialia, 2013. **61**(19): p. 7207-7215.
134. Meganck, J.A., et al., *Biaxial flexure testing of calcium phosphate bioceramics for use in tissue engineering.* Journal of Biomedical Materials Research Part A, 2005. **72A**(1): p. 115-126.
135. Kishimoto, A., et al., *MICROSTRUCTURE DEPENDENCE OF MECHANICAL AND DIELECTRIC STRENGTHS .1. POROSITY.* Engineering Fracture Mechanics, 1991. **40**(4-5): p. 927-930.
136. Tiryakioglu, M. and J. Campbell, *Weibull Analysis of Mechanical Data for Castings: A Guide to the Interpretation of Probability Plots.* Metallurgical and Materials Transactions a-Physical Metallurgy and Materials Science, 2010. **41A**(12): p. 3121-3129.
137. Tiryakioglu, M., *Weibull Analysis of Mechanical Data for Castings II: Weibull Mixtures and Their Interpretation.* Metallurgical and Materials Transactions a-Physical Metallurgy and Materials Science, 2015. **46A**(1): p. 270-280.
138. Rinne, H., *The Weibull Distributin: A Handbook*. 2009, U.S.: CRC Press.
139. Bergman, B., *ESTIMATION OF WEIBULL PARAMETERS USING A WEIGHT FUNCTION.* Journal of Materials Science Letters, 1986. **5**(6): p. 611-614.
140. Bozchaloei, G.E., et al., *Effect of oxide bifilms on the mechanical properties of cast Al-7Si-0.3Mg alloy and the roll of runner height after filter on their formation.* Materials Science and Engineering a-Structural Materials Properties Microstructure and Processing, 2012. **548**: p. 99-105.
141. Teng, X., H. Mae, and Y. Bai, *Probability characterization of tensile strength of an aluminum casting.* Materials Science and Engineering a-Structural Materials Properties Microstructure and Processing, 2010. **527**(16-17): p. 4169-4176.
142. Li, T. and W.D. Griffiths, *The behaviour of entrainment defects formed in commercial purity Mg alloy cast under a cover gas of.* IOP Conference Series: Materials Science and Engineering, 2016. **117**(1): p. 012065.
143. Du, L., et al., *Sublimation crystal growth of yttrium nitride.* Journal of Crystal Growth, 2010. **312**(20): p. 2896-2903.